BRAIN-METASTATIC MELANOMA MODELS UNCOVER IMMUNE AND MOLECULAR CORRELATES OF RESPONSE TO IMMUNOTHERAPY

Amélie Daugherty-Lopès[1,8], Eva Pérez-Guijarro[2,7,8], Vishaka Gopalan[3], Jessica Rappaport[1], Quanyi Chen[1,5], April Huang[1,5], Khiem C. Lam[1], Sung Chin[4], Jessica Ebersole[4], Emily Wu[2], Gabriel A. Needle[2], Isabella Church[2], George Kyriakopoulos[1,2], Yongmei Zhao[6], Charli Gruen[2], Antonella Sassano[2], Romina E. Araya[1], Andres Thorkelsson[2], Cari Smith[4], Maxwell P. Lee[2], Sridhar Hannenhalli[3], Chi-Ping Day[2,3], Glenn Merlino[2] and Romina S. Goldszmid[1,9*]

[1]Inflammatory Cell Dynamics Section, Laboratory of Integrative Cancer Immunology, Center for Cancer Research, National Cancer Institute, NIH, Bethesda, MD 20892, USA
[2]Laboratory of Cancer Biology and Genetics, Center for Cancer Research, National Cancer Institute, NIH, Bethesda, MD 20892, USA
[3]Cancer Data Science Laboratory, Center for Cancer Research, National Cancer Institute, NIH, Bethesda, MD 20892, USA
[4]Leidos Biomedical Research Inc., Frederick National Laboratory for Cancer Research, National Cancer Institute, Frederick, MD 21701, USA
[5]Kelly Government Solutions, Bethesda, MD, USA
[6]CCR-SF Bioinformatics Team, Bioinformatics and Computational Science Directorate, Frederick National Laboratory for Cancer Research, NIH, Frederick, MD 21701, USA
[7]Present address: Instituto de Investigaciones Biomédicas Sols-Morreale, Universidad Autónoma de Madrid, Consejo Superior de Investigaciones Científicas (IIBM, CSIC-UAM), Madrid, Spain.
[8]These authors contributed equally
[9]Lead contact
[*]Correspondence: rgoldszmid@mail.nih.gov

SUMMARY

Despite promising results with immune checkpoint blockade (ICB) therapy, outcomes of patients with brain metastasis (BrM) remain poor. Identifying determinant of resistance is crucial but has been hindered by limited access to patient samples and the scarcity of relevant preclinical models. Here, we developed two mouse melanoma BrM models that mirror the disparate response to ICB seen in patients. By characterizing their mutational landscape and performing single-cell phenotypic and transcriptomic analysis, we demonstrated that these models recapitulate both the cellular and molecular features of human disease. Through our comparative analysis, we identified key factors contributing to ICB response. In the responsive model, we found that tumor cells expressed inflammatory programs that polarized microglia toward reactive states, expressing high levels of MHC-I and -II and immunostimulatory molecules, eliciting robust T cell recruitment and activation, which favored anti-tumor immunity. Conversely, the resistant melanoma cells were characterized by neurological molecular signatures and expression of ligands that maintain microglia homeostatic states, resulting in poor T cell infiltration and therapy resistance. We validated our findings in BrM patients, showing that BR1 and BR3 signatures correlated with T cell infiltration and were associated with better and worse

patient outcomes, respectively. Our study fills a critical gap by providing clinically relevant models and revealing mechanistic insights into BrM ICB responses, identifying potential biomarkers and therapeutic targets.

INTRODUCTION

Cancer treatment has seen substantial improvement in the last decade. However, therapeutic options for patients with brain metastasis (BrM) are still limited and frequently ineffective, leading to a dismal prognosis[1,2]. Immune checkpoint blockade (ICB) has shown promising results in clinical trials, reaching up to 55% response rates in asymptomatic melanoma BrM but 6-22% in symptomatic patients or with leptomeningeal disease[3–7]. While ICB combination or in association with radiotherapy, in particular stereotactic radiation therapy (SRT), can enhance efficacy, the use of steroids – often prescribed to BrM patients to reduced inflammation – has proven to be detrimental for ICB response[6]. Therefore, there is an urgent need to identify optimal combinations and regimens to apply in each clinical scenario. Moreover, we still lack a clear understanding of the specific tumor microenvironment (TME) responses in BrMs that could lead to the identification of biomarkers strongly correlating with the clinical benefit of ICB.

The brain tumor microenvironment (BrTME) is highly specialized, containing unique resident cell types including microglia that constitute the majority of its immune components, and non-immune cells, such as neurons, astrocytes, and oligodendrocytes[8–10]. These are combined with specific extracellular matrix (ECM) networks and neurotransmitters[8–10], all of which contribute to brain homeostasis and distinguish the BrTME from non-brain TME. The BrTME is also controlled in part by the blood-brain barrier (BBB), which regulates the access and distribution of infiltrating immune cells, tumor cells, and drugs, to the brain[8–12]. Previous reports have shown clear differences in immune composition and tumor molecular profile between BrMs, extracranial metastases, and primary tumors in patients[13–16]. This raises the question of whether non-brain tumor determinants and mechanisms of ICB responses apply to BrM. Recent studies have expanded our knowledge regarding the diversity of the BrTME, demonstrating that heterogeneity in immune composition within the BrTME among patients is mainly driven by tumor types (e.g., primary brain tumor versus BrM) and subtypes (e.g., BrM tumor of origin such as melanoma, breast carcinoma, etc)[17–22] rather than the uniqueness of the brain environment. These studies showed that the largest discrepancies among BrM subtypes were in the T cell and myeloid compartments[17–22]. Nevertheless, how tumor cells regulate the BrTME and its impact on ICB responses remain to be elucidated.

Important limitations of these retrospective studies include the relatively small cohorts, the diverse treatments patients received, and the rare availability of biopsies from ICB responder patients. Additionally, the constraints of sample collection result in heterogeneous representation of the stroma in BrM biopsies, including an under-representation of microglia. Modeling BrM in mice is extremely challenging and the majority of models show low penetrance and/or long latencies[23,24]. Few BrM models are currently available, including an autochthonous model[23–26]. Many require intracranial injection of melanoma cells[27,28], which bypasses extravasation and artificially disrupts the BBB, thereby inducing inflammation. Altogether, these limitations preclude the comparative studies between responders and non-responders, thus preventing the identification of predictive biomarkers of ICB response and the discovery of new therapeutic targets.

The aim of this study was to address this unmet need by developing two syngeneic brain-metastatic models M4-BR1 (hereafter BR1) and M4-BR3 (BR3) derived from our previously established M4-B2905 (M4) melanoma mouse cell line[29]. We demonstrate that these models represent the molecular and cellular complexity and diversity of ICB responses observed in patients. Through comparative studies, we identify specific tumor molecular signatures associated with immune BrTME composition, ICB response or resistance, and patient outcomes. Therefore, this study provides a robust foundation for the necessary mechanistic studies to optimize BrM therapy.

RESULTS

Development of metastatic melanoma models with high brain penetrance.

To study BrM therapeutic response to ICB, we generated a panel of syngeneic immunocompetent preclinical models preserving BBB integrity by intracardiac (i.c.) injection of the M4 melanoma mouse cell line[29] into syngeneic C57BL/6 mice. We have previously demonstrated that this cell line, generated by neonatal UV-irradiation of hepatocyte growth factor transgenic mice (Hgf^{Tg}), faithfully recapitulates the etiology, histopathology, and molecular features of human cutaneous melanoma[29]. After recovering metastatic cells from the brain, we cycled them *in vivo* to enhance their brain-metastatic potential (see Methods) (Figure S1A). We obtained two polyclonal sublines, BR1 and BR3, that exhibit high penetrance to the brain and form numerous pigmented macroscopic metastases in up to 100% of injected animals on average per experiment (Figure 1A-B). We confirmed the presence of melanoma cells in the brains of mice from both models by dopachrome tautomerase (DCT)[30,31] immunostaining at day 18-20 post-implantation (model endpoint) (Figure S1B). To assess metastatic burden in an unbiased manner, we developed a machine learning approach that semi-automatically detects and counts metastatic foci on whole-brain stereomicroscope images[32]. Following optimization

(see Methods), we achieved a comparable number of BrM per mouse between BR1 and BR3 (Figure 1C). However, BR3 formed more extracranial metastases and displayed a lower BrM/extracranial metastases ratio compared to BR1, indicating different metastatic tropism between the two models (Figures S1C-D, 1C). Nevertheless, in both BR1 and BR3, the highest incidence of metastases was observed in the brain (Figure S1D). Thus, we successfully developed two immunocompetent BrM models with high brain penetrance while preserving a physiological BBB, providing a valuable platform for the comparative and mechanistic studies of BrM therapeutic responses.

BR1 and BR3 models exhibit mutational landscapes representative of human BrM melanomas.

To confirm that our models are translationally relevant, we interrogated their molecular resemblance with human disease. We first characterized the mutational landscape of cultured BR1 and BR3 cell lines in comparison to the M4 parental line using whole exome sequencing analysis. We found an elevated tumor mutation burden in both brain-metastatic lines compared with the parental M4 cells (432, 403 and 327 genes in BR1, BR3 and M4 parental, respectively; Figure S1E). This is in agreement with observations from clinical data showing higher mutational burden in BrM compared to primary tumors[14,33,34]. Not surprisingly, 90% and 86% of the genes mutated in the M4 parental line were also detected in BR1 and BR3, respectively. However, each of the brain-metastatic models presented approximately 30% of unique mutated genes (Figure S1E), which may partly explain their distinct metastatic behavior *in vivo*. Ingenuity Pathway Analysis (IPA) of the mutated genes in each model revealed significant enrichment of the PTEN and PI3K/AKT pathways, although the specific mutated genes varied between the models (Figure S1F and Table S1). We next explored the mutational landscape in metastatic patients using the publicly available MSK-MET-SKCM cohort[35] and the cBioportal platform[36–38]. We found that most of the mutated genes identified in our models that are related with these pathways, were also frequently mutated in BrMs from melanoma patients (Figure S1G). In line with our observation, while no specific mutations unique to melanoma BrM have been identified so far, AKT1E17K increases BrM incidence in mice, and patients with mutations in PI3K/AKT pathway (e.g., PTEN) have a higher risk of developing central nervous system (CNS) metastases[26,33,34]. Overall, these results show that our models recapitulate, at least in part, the molecular complexity of human melanomas.

Single-cell transcriptomic profiles of BR1 and BR3 BrMs show strong correlation with patient data sets.

To further corroborate the molecular similarities between BrMs from our two preclinical models and melanoma patients, we performed single-cell RNA sequencing (scRNAseq) of whole brains from

BR1- and BR3-bearing animals (Figure 1D, see Methods). After annotating CNS stromal, tumor, and immune cells (Figure 1D, see Methods), we focused on melanoma cells for downstream analysis. We then applied a Non-negative Matrix Factorization (NMF)[39] approach to identify the key molecular programs (referred to as metaprograms [MPs]) that characterize our models *in vivo* (see Fig S1H and Methods). NMF-based methods are able to identify gene expression patterns that highlight differences within tumors, as well as variations between different tumors[40–42]. A similar approach has been successfully used in BrM patients to discover tumor MPs[13]. Importantly, NMF allowed us to compare the features of our models with available clinical data. We identified seven different MPs (MP1-MP7) and characterized them using Metascape pathway analysis[43] (Figure 1E and Table S2, see Methods). MP1 and MP4 were enriched in pathways and genes previously found to be expressed in pan-cancer and melanoma BrM patients, such as cell cycle (MP1), and immune response and antigen presentation (MP4)[13,20] (Figure 1E and Table S2, see methods). Other MPs showed enrichment for melanin biosynthesis (MP2, MP7), translation and mitochondrial metabolism (MP5), and neuro-functions such as axon guidance and neurodevelopment (MP3, MP6), which have been recently shown to be increased in BrM compared to primary tumors or extra-BrM metastases in pan-cancer and melanoma patients[13–15,20] (Figure 1E and Table S2, see Methods). To validate that our mouse BrM MPs are representative of human disease, we computed correlations between these mouse-MP and human-MP from three patient cohorts Biermann et. al[13], Smalley et al.[44], and Alvarez-Breckenridge et al.[45] (Figure 1F-G, see Methods). Each mouse-MP identified in our study correlated with one or more patient-MP from at least one cohort (Figure 1F). For instance, mouse MP4 enriched for antigen presentation pathways mapped to the human MPs 1 and 2 characterized by similar pathways[13]. In all three patient cohorts, human-MP1 containing translation control pathways (e.g., MYC targets and mTORC1 signaling[13]), strongly correlated with mouse-MP5 (Figure 1F). Similarly, human-MP7, enriched in melanocytic genes and neuronal development and function positively correlated with mouse MPs involved in melanin production (MP2 and MP7) and neurodevelopment (MP6 and MP3) pathways (Figure 1F). Importantly, we verified that the correlations found between pairs of human- and mouse-MPs were consistent across all melanoma BrM human datasets[13,44,45] (Figure 1G). Overall, these results underscore the robustness, reliability, and clinical relevance of our murine brain-metastatic models, demonstrating their translational potential.

BR1 and BR3 BrM recapitulate the diversity of responses to ICB observed in the clinic.

To evaluate the ICB therapeutic response of the models, we treated syngeneic mice that were i.c.-injected with either BR1 or BR3 using anti-CTLA-4 or anti-PD-L1 monotherapies, or combination therapy (combo), dual isotype or vehicle controls (Figure 2A). We started dosing at day 3 or 4 with

each antibody, after verifying metastatic brain seeding on day 4 through microscopy, DCT immunostaining, and ex vivo culture of cells from the implanted brains (Figure S2 A-D). When control groups reached the endpoint, we assessed BrM burden using our machine-learning algorithm[32]. We observed striking response differences between the two models (Figure 2B-E). We found a significant reduction in total metastatic foci count and area in BR1 following treatment with both mono- and combo-therapies. Combo therapy was the most effective regimen, also reducing the size of individual metastases (Figure 2D). In addition, we observed significantly fewer extracranial metastases in this model, which disappeared in half of the monotherapy-treated and more than 90% of the combo-treated animals (Figure S2E). In marked contrast, BR3 BrM were resistant to ICB, showing no changes in the total metastatic area, BrM foci count, or individual lesion size in any therapeutic group (Figure 2E). Notably, we observed a modest decrease in total extracranial metastasis counts in BR3-bearing animals treated with ICB monotherapies, and a significant response with combo therapy (Figure S2F). These results align with clinical studies indicating that extracranial and BrM responses to ICB do not always correlate with each other[3].

Even at a more advanced metastatic stage (7 days after i.c. injection), the BR1 model remained significantly responsive to combo therapy and displayed a modest response to monotherapies (Figure S2B, S2G-H). Overall, our models recapitulate the diversity of clinical responses observed in melanoma BrM patients[3–5].

ICB-sensitive and resistant models display distinct BrTME and remodeling upon treatment.

Because we saw striking differences in the response to ICB between the two models, we interrogated the BrTME to identify potential immune correlates of BrM ICB response. We performed multiparametric spectral flow cytometry on brain leukocytes from both combo-treated, which yielded the strongest response, and untreated BR1 and BR3 models. Consistent with their ICB responsiveness, we observed a significantly higher number of total leukocytes in BR1 compared to BR3, independent of their treatment status (Figure 3A). To gain more granularity, we performed unsupervised clustering of immune cells followed by supervised cell annotation (Figure 3B, S3A-B; Table S3). Uniform Manifold Approximation and Projection (UMAP) visualization and Principal Component Analysis (PCA) using the frequency of the identified leukocyte populations revealed different BrTME compositions between the two models in both treated and untreated groups (Figure 3C-D).

To determine the specific immune populations driving the differences between untreated BR1 and BR3, we analyzed the PC1 loadings, which segregate these two groups (Figure 3D). These loadings revealed neutrophils, microglia, and Ly6C^{lo} monocytes as enriched in BR3 samples, which indeed had a higher proportion of these cells (Figure 3D-E and S3C-E). Both the proportion of microglia (> 90%

of total leukocytes) and the infiltrating cell populations in the BR3 ICB-resistant BrTME resembled that of non-tumor-bearing brains (PBS) (Figure 3E and S3F). In contrast to BR3, BR1 showed a higher frequency and number of various infiltrating cells, including natural killer (NK) cells, DCs, and T cells, which are known to favor ICB responses[46,47] (Figure 3E-H and S3G-H). This indicates a stronger immune cell recruitment in untreated BR1 BrM compared to untreated BR3.

We observed a therapy-induced increase of total leukocytes along with an enrichment of T-cells in both models (Figure 3A, 3E-H, S3G-H, 3J). This aligns with recently published clinical studies showing ICB-driven increase T cell infiltration[21,44,48]. Nevertheless, TME dissimilarities between BR1 and BR3 were still observed after combo therapy, as evidenced by their segregation along PC2 (Figure 3D, S3D, S3I). BR1 continued to display higher frequency and number of infiltrating cells compared to BR3, which after combo therapy was specifically due to a surge in $CD8^+$ T cells (Figure 3C-H, S3D-E, S3D, S3G-J). Additionally, a higher number of microglia was observed in treated BR1 compared to treated BR3 (Figure 3F). Altogether, these observations indicate BrTME immune compositional differences between ICB-sensitive and -resistant BrMs, with some differences, such as those in T cells and microglia, persisting after therapy.

A distinct T cell landscape is associated with ICB response.

The quantity and characteristics of infiltrating T cells play an important role in the response to ICB[49–52]. Therefore, we studied the specific T-cell characteristics associated with ICB-responses in our BrM models using our whole-brain scRNA-seq data from PBS, BR1-, and BR3-untreated samples (Figures S1D, S3K-L, 4A-E, and S4A-D). We performed differential gene expression analysis of total CD8 T cells between untreated ICB-sensitive BR1 and the resistant BR3. This analysis revealed a higher expression of activation/effector function-associated genes (*Nkg7*, *Pdcd1*, *Ifng*, *Gzmb*) in BR1, whereas the BR3 CD8 T cell pool displayed a naïve signature (*Sell*, *Lef1*, *Tcf7*, *Foxp1*) (Figure 4A). UMAP projection and unsupervised clustering of the T cells revealed six CD8 T cell clusters (CD8.sc1-6) and six CD4 T cell clusters (CD4.sc1-6) with different abundance between the two models (Figure 4B-C, S4A). Compared to BR1, BR3 was enriched in T cell subsets defined by a naïve gene signature (CD8.sc1, CD4.sc1) (Figures 4B-D, S4A-C, Tables S4-5). Projection of our T cell clusters onto a single-cell reference atlas for T cell states[49] confirmed that CD8.sc1 and CD4.sc1 correspond to the naïve compartments (Figures 4E, S4D). These clusters account for over 60% of the total $CD8^+$ and $CD4^+$ T cell populations in BR3 and PBS control, whereas they make up only 5-20% of T cells in BR1 (Figures 4C, S4A). BR3 also presented a higher proportion of cluster CD8.sc3, which mapped mostly onto $CD8^+$ effector memory T cells on the reference atlas (Figures 4B-E, S4B, Table S4).

In contrast to BR3, BR1 was characterized by a higher diversity of T cells, including various $CD8^+$ and $CD4^+$ T cell subsets expressing different levels of genes encoding for T cell degranulation/lysosomal activity (*Lamp1*, *Ctsl, Cd63;* CD8.sc2), activation/dysfunction (*Cd81*, *Ckb*, *Nr3c1;* CD8.sc2)[53,54], T cell regulatory function (*Foxp3, Il2ra, Ikzf2;* CD4.sc5-6), and immune checkpoint receptors previously described as activation and/or exhaustion markers (*Lag3*, *Pdcd1*, *Havcr2;* CD8.sc4-6 and CD4.sc3-4)[49,52,53] (Figures 4B-E, S4A-C, Tables S4-5). Among the latter, CD8.sc5, the most enriched cluster in BR1, displayed the highest level of genes encoding for cytotoxic molecules (e.g., *Ifng*, *Prf1*, *Gzmb*) (Figures 4B-D, S4B, Table S4). Similarly, the BR1-enriched CD4-sc3 exhibited the highest expression of *Ifng* and *Tbx21* (T-bet), consistent with a Th1-like signature (Figures S4A, S4C-D, 4E, Table S4). Notably, CD8.sc4, exclusively found in the BR1 BrTME, expressed the transcription factor TCF-1 (*Tcf-7*), the nuclear protein TOX (Tox), and low level of genes encoding for cytotoxic cytokines and immune checkpoint receptors (except *Havcr2*) (Figures 4B-E, S4A-C, Tables S4-5). This expression profile resembles that of the so-called "exhausted stem cell-like CD8 T cells", previously identified as essential for ICB response and associated with better clinical outcomes in melanoma patients[50,52] (Figures 4D-E, Table S4). Finally, the BR1 enriched clusters CD8.sc6 and CD4.sc6 displayed a proliferative profile (*Mki67*, *Cdk1*, *Ccnb2*), suggesting that local expansion contributes to the higher T cell number observed in this model (Figures 4B-D, S4A-C, Tables S4-5). We confirmed these T cell compositional differences between untreated BR1 and BR3 BrTME by spectral flow cytometry and showed higher number of activated T cells in BR1 (Figures 4F-J, S4E-G).

To determine if the T cell compositional differences between the two models are sustained after treatment, we analyzed the BrTMEof combo-treated BR1 and BR3 (Figures 4F-H, S4E-F). While all $CD8^+$ and $CD4^+$ T cell subsets slightly increased in BR3 after therapy, BR1 showed a specific 20-fold increase in CD8.F5 and a 10-fold increase in CD8.F4, both subsets marked by activation. Interestingly, CD8.F5 resembles tissue-resident memory T cells (T_{RM}), which have been associated with better ICB efficacy and improved patient outcomes for non-brain tumors[55–57] (Figure 4H). In addition, combo therapy in BR1 led to a significant increase in the $CD4^+$ T cell subset CD4.F5 displaying activation/exhaustion markers (Figures 4H, 4J, S4F, S4G). Together, these results demonstrate that the quantity and the quality of the T cells differ between the ICB-responder and resistant BrM models, highlighting the importance of the intrinsic BrTME T cell landscape in ICB response and aligning with immune correlates of response described for non-brain tumors[50–52].

Unique reactive microglia signatures are found in ICB-responder BrM.

Microglia, the predominant immune cell type in the CNS, are crucial in regulating brain homeostasis as well as response to tissue injury and pathogens[58–60]. While different studies have suggested their dual role in BrM development[10,61,62], their contribution to ICB response is unclear. As expected, microglia represented 80-95% of the immune BrTME in both of our models. We then inquired whether different microglia transcriptional states might be associated with BrM response to ICB. To do so, we turned to our whole-brain scRNA-seq dataset from untreated samples and extracted microglia for further analysis (Figure S3K-L). Differential gene expression and Gene Set Enrichment Analysis (GSEA) between BR1 and BR3 showed enrichment of homeostatic microglia genes and pathways such as neuronal development and synaptic remodeling[58–60] in BR3 (Figures 5A-B, S5A). In contrast, BR1 microglia upregulated genes and pathways associated with MHC class I and class II antigen presentation (MHC-I and MHC-II) (*H2-Aa*, *Cd74*, *B2m*), response to type I and type II interferons (IFN-I and IFN-II) (*Ifitm3*, *Ifi27l2a*, *Cxcl10*), and inflammatory proteins including T-cell attracting chemokines (*Cxcl10*, *Cxcl16*, *Cxcl9*) (Figures 5A-B), indicating a reactive microglia transcriptional signature in the responder model. We found similar pathways were enriched in BR1 relative to PBS, while, as expected, PBS samples were enriched in pathways associated with microglia homeostatic function (Figure S5B). Our analysis only revealed TNFα signaling via NF-κB enriched in BR3 microglia compared to PBS (Figure S5B).

Microglia are heterogeneous, particularly in disease conditions[58–60]. To investigate microglia heterogeneity in our BrM models, we performed unsupervised clustering and identified thirteen different microglia clusters (Figure 5D). Clusters Mg1-4 and Mg8, characterized by the highest level of homeostatic microglia genes and pathways (e.g., phagocytosis, regulation of cellular response to TGF_{β}, and neuronal function), represented the predominant microglia states in BR3 and PBS (Figure 5C-E, S5C). Clusters Mg5-6, also highly abundant in these groups, were enriched in pathways related to ribosomal and mitochondrial function, indicating a transcriptionally active state (Figure 5E). On the other hand, the overall reactive signature of BR1 microglia was driven by the combination of five different clusters, Mg9-Mg13, defined by reduced expression of homeostatic genes and pathways (Mg9-11 and Mg13), upregulation of IFN response genes (Mg12-13), antigen presentation (Mg9, Mg12-13), and pathways involved in T cell recruitment and regulation of adaptive immune responses (Mg12-13) (Figure 5C-E, S5C). These clusters constituted 70-80% of the total BR1 microglia, while representing less than 15% of BR3 and minimally present in PBS (Figure 5D). Clusters Mg11 and Mg13, almost absent in BR3 and PBS, expressed mitotic and proliferative genes (Figures 5E, S5C), explaining the higher number of microglia found in BR1 (Figure 3F). Using high-parametric spectral

flow cytometry, we confirmed the higher proportion and total number of microglia with various reactive states in BR1 (Mg.D-E) as compared to BR3 (Figure 5F-J, S5D). Taken together, our data suggest that reactive microglia states, characterized by high expression of MHC-I/II and T cell-attracting chemokines, are associated with response to ICB, while resistant BrMs are enriched in microglia that maintain homeostatic function.

Systemic ICB alters microglia functional state.

It is unclear whether systemic ICB treatment can impact microglia states. To address this question, we assessed the combo-treated BR1 and BR3 microglia phenotype using spectral flow cytometry. Surprisingly, therapy led to the disappearance of almost all homeostatic microglia states in both models (Mg.A-Mg.C; Figures 5F-I, S5D). Instead, they were replaced by various non-homeostatic states characterized by the absence of P2RY12 expression, a receptor essential for microglia homeostasis. The loss of this receptor has been previously linked with neuroinflammation[59,63] (Mg.F-Mg.J; Figures 5F-I, S5D). While the decrease of P2RY12 was a common therapy-induced feature, some phenotypic differences were still observed between BR1 and BR3 (Figure 5H-I, S5D). Only BR1 microglia maintained the expression of MHC-II, while reducing markers associated with macrophage pro-tumorigenic function such as ARG1, SIRPα[64–67] and the T cell inhibitory receptors TIM3 and LAG3[68–70] (clusters Mg.F-G; Figure 6F-J, S6D). Of note, we observed a reduced level of PD-L1, resulting from either phenotypic changes or the blockade of PD-L1 with anti-PD-L1 antibody included in the combo treatment, thus preventing its detection by flow cytometry. In contrast, the microglia state increased in BR3, but not in BR1, after therapy (Mg.J), expressed the highest levels of TIM3, LAG3, and SIRPα (Figure 5G, 5I-J, S5D). These results indicate that systemic ICB therapy alters microglia functional states. The key differences between microglia in ICB-responder and non-responder BrMs, regardless of treatment status, lie in the expression of genes, pathways, and proteins that can modulate T-cell activities.

BR1 tumor cell-intrinsic programs favor immune response while those in BR3 support brain homeostasis

We then sought to identify tumor cell-intrinsic molecular features that may be influencing the BrTME dissimilarities observed in our models. To do so, we compared BR1 and BR3 melanoma cells from *in vivo* established BrM in our whole brain scRNA-seq data set. Model-based analysis of single-cell transcriptomics (MAST)[71,72] followed by GSEA revealed that BR3 cells, compared to BR1, expressed higher levels of genes and pathways related to melanin biosynthesis (e.g., *Tyr, Dct, Slc45a2*), neuronal function (e.g., *Sema3a, Unc5c, Slc6a11, Pde1c/3a/4b, Cacna1d, Selenop*), and metabolic pathways

such as glutathione transferase activity (e.g., *Gsta4, Gstm1*), oxidative phosphorylation (OXPHOS, e.g., *Atp6v0d2, Cox7a1*), and lipid metabolism (e.g., *Apoe*) (Figures 6A, S6A). On the other hand, BR1 melanoma cells showed enrichment in MHC-I and MHC-II antigen presentation (e.g., *H2-K1/D1, B2m, Tap1, H2-Aa/Ab1/Eb1, Cd74,*), immune response and IFN signaling (e.g., *Ifng, Irf1, Stat1, Ifi203, Cxcl9*), cell cycle, DNA replication and repair (e.g., *Mki67, Aurka/b, Plk1, Top2a, Pdgfa, Chek1*) (Figures 6A, S6A). Notably, these differences were also observed when we analyzed the MP distributions in the two models, showing higher activity of MP2 (melanin biosynthesis), MP6 (neurofunction), and MP7 (melanin biosynthesis and fatty acid metabolism) in BR3, while BR1 tumor cells were enriched in MP1 (cell cycle) and MP4 (immune) (Figures 6B).

Given that the BR1 and BR3 cell lines are polyclonal, we investigated if the transcriptomic signatures distinguishing these two models were broadly expressed across cells within each model or specific to BrM cell sub-populations. To be able to align our findings with clinical data, we performed unsupervised clustering of tumor cells based on their expression of MPs (Figure 6C-D). We identified 5 clusters, T1-T5. BR3 samples were enriched in clusters T3-T5, with T4 being the predominant cluster in this model (Figure 6C, 6E and S6B). These clusters uniquely showed high activity of the melanin-MPs (MP2 and MP7), with T3 also expressing the highest level of neuro-MP activity (MP3 and MP6) (Figure 6D). In contrast, clusters T1 and T2, unique subpopulations exhibiting high immune-MP4 activity, constituted a higher proportion of tumor cells in BR1 compared to BR3 BrMs (Figure 6C-E and S6B). Cluster T2, the most abundant in BR1, displayed the highest activity for MP4 and the cell cycle-associated MP1 (Figure 6C-E and S6B). This data demonstrates that the distinct transcriptomic profiles of BR1 and BR3 are driven by differentially distributed tumor cell states. Furthermore, our results suggest that the expression of an immune response-related signature in BR1 could explain its ICB-favorable BrTME, whereas the enrichment of brain homeostasis-associated programs in BR3 cells likely results in a blunted immune response.

BR1 and BR3 tumor cell-intrinsic programs shape the microglia functional states that drive T cell phenotypes

Cell-cell interactions are essential to shape the TME and drive antitumor immunity. Based on the BR1 and BR3 cell-intrinsic programs, we hypothesized that tumor cells communicate with microglia, skewing their functional state and downstream interaction with T cells. To test this, we performed interactome analysis of tumor cell – microglia – T cells to infer ligand-receptor (L-R) pairs implicated in their crosstalk (Figures 6F-H; S6C-D). In agreement with our hypothesis, we observed the highest predicted interaction number and strength from tumor cells to microglia in both models (Figure 6F and S6C). This crosstalk occurred among distinct microglia and tumor states and involved different types

of interactions in BR1 compared to BR3 (Figure 6G-H). In BR3, we found stronger interactions from tumor clusters displaying the highest neuro-MP (T3) and melanin-MP activities (T3-T5) to homeostatic microglia (Mg1-2 and Mg8; Figure 6G). Among the most upregulated interactions in BR3 were L-R pairs previously associated microglia anti-inflammatory pathways (CD200_CD200R1, GAS6_MERTK)[73–75] as well as those involved in maintenance of microglia homeostatic function, including phagocytosis (e.g., APOE_TREM2_TYROBP)[76] and neuro-function (e.g., PTRM-PTRM)[77] (Figure 6H). The predominant predicted tumor-to-microglia interactions in this model were driven by tumor junctional adhesion molecule (JAM)[78] and extracellular matrix (ECM) ligands, such as collagens (e.g., COL4A2, COL6A3)[79,80] and laminins (e.g., LAMA3, LAMC1; Figure 6H)[79,80].In contrast, in the BR1 BrTME we observed enhanced communication from the tumor cell cluster enriched in immune and cell-cycle-MPs (T2) to reactive microglia states (Mg9, Mg12-13; Figure 6G-H), including upregulation of the microglia activating MIF_CD74_CD44 axis[81–83]. We also observed enrichment of the LGALS9 axis, known to induce MHCII expression on macrophages and DC and strong anti-tumor responses in murine melanoma models[84,85].

We then investigated the downstream microglia – T cell crosstalk. Although a similar number of microglia – T cell interactions were observed between BR1 and BR3, we found significantly stronger interactions from microglia to T cells, specifically $CD8^+$ T cells, in BR1 (Figures S6C and 6F). The reactive microglia states, which receive signals from BR1 tumor cells, were the ones predicted to preferentially interact with T cells in BR1 (Figure 6G). This crosstalk involved all the necessary signals to efficiently activate T cell responses, such as adhesion molecules, antigen presentation, TCR and co-stimulatory signaling (Figures 6G-H and S6D), explaining the T cell landscape observed in BR1. The inferred communications from microglia to $CD8^+$ T cells were also characterized by T cell-attracting chemokines (Figure 6H)[86–88], further suggesting that BR1- microglia are responsible for $CD8^+$ T cell recruitment . Importantly, we confirmed that these chemokine-encoding genes were predominantly expressed by BR1 microglia, with significantly higher protein levels found in BR1 compared to BR3 brains (Figures S5C, 6I-J, S6E). In marked contrast to BR1, the few microglia – T cell interactions predicted in BR3 involved only cell-cell adhesion processes between microglia homeostatic states (Mg1, Mg2, and Mg8) and naïve T cells (SELL) (Figures 6G-H and S6D).

To confirm these predicted interactions using a different approach, we performed a correlation analysis of cell populations identified by flow cytometry. Agreeing with the interactome analysis, we observed positive correlations between BR1-reactive microglia (Mg.D) and CD8+ T cells expressing activation markers (CD8.F3-F5) (Figures 6K, 4H). No correlations were observed between the BR3-associated microglia (Mg.A-C) and $CD8^+$ T cell (Figures 6G-H, 6K, S6D). Altogether, these findings support our

hypothesis that BR1 and BR3 tumor cell-intrinsic programs dictate microglia functional states, which in turn shape T cell phenotypes.

The molecular features identified in our preclinical models predict T cell infiltration and survival in BrM patients.

To further validate the clinical relevance of our findings, we interrogated the potential associations of our ICB-responder and ICB-resistant signatures with BrTME composition and patient survival in publicly available clinical datasets[13,21]. We first focused on the association between BR1 and BR3 BrM MPs and $CD8^+$ T cell infiltration in a small cohort of untreated melanoma patients[13]. To do so, we extracted $CD8^+$ T cells from their scRNA-seq dataset and re-analyzed them using unsupervised clustering (Figure S6F). Consistent with our preclinical data, we found that the frequency of total $CD8^+$ T cells within the biopsies positively correlated with BR1 immune-MP (MP4) activity and negatively correlated with BR3 neuro-MP (MP6) (Figure 7A). Out of the nine $CD8^+$ T cell clusters identified in the BrM patients, eight shared similarities with the subsets found in our BrM models (Figure S6F-G, 4B-D). Although not reaching statistical significance due to the small number of patients, we observed correlation trends consistent with our pre-clinical data. All BR3 enriched MPs (MP2, MP6, MP7) showed a trend toward positive correlation with the $CD8^+$ T cluster resembling BR3 $CD8^+$ T cells (Figures 7B, S6G, 4B-D). Conversely, $CD8^+$ T cell clusters resembling BR1 $CD8^+$ T cells showed a trend of positive correlation with BR1 MPs and negative with BR3 MPs (Figures 7B, S6G, 4B-D). Among these clusters, we identified a subset sharing molecular signatures with a population recently reported as "potential tumor reactive T cell" both in patients' BrM (BrM pTRT)[19] and non-brain tumors[89–93] (Figures 7C, 4C-D, S7H-I, and Table S6).

We corroborated our observations using pseudo-bulk RNA-seq analysis of data from a larger patient cohort of pan-cancer BrM, composed of individuals untreated or treated with various therapies, including ICB[21]. Total $CD8^+$ T and BrM pTRT $CD8^+$ T cell signatures showed a significant positive correlation with BR1 immune-MP4 and a negative correlation with BR3 neuro-MP6 (Figure 7D-E, S7J, and Table S6). Furthermore, we found that high expression of total $CD8^+$ T, BrM pTRT, and BR1 MP1 signatures associated with better progression-free survival (Figure 7F, Table S6). We further generated three other signatures based on interactome and DEGs between BR1 and BR3: "BR1 pro-inflammatory", "BR1 chemokine", "BR3 Neuro" (Table S6) We stratified patients based on high (>=median) or low expression (< median) of these signatures and found that "BR1-proinflammatory" and "BR1 chemokine" signatures significantly associated with better patient outcomes (Figure 7F, Table S6). In contrast, the "BR3 Neuro" signature significantly associated with poorer patient outcomes (Figure 7F, Table S6). Taken together, our data demonstrate that the ICB-responder and ICB-

resistant MPs and the signatures that we identified in our preclinical models are expressed in patient BrMs, correlate with their TME composition, and can predict patient outcomes.

DISCUSSION

BrM remains a critical challenge in cancer treatment with most cases being resistant to ICB[3–5,7,94,95]. Unfortunately, the restricted availability of patient biopsies and lack of representative preclinical models for diverse ICB responses observed in clinical settings[23–25,96] has hampered our ability to identify biomarkers and determinants of response. Here, we have developed two translationally relevant preclinical melanoma BrM mouse models that overcome these limitations, enabling us to identify tumor molecular signatures that influence the BrTME and therapy responses. In particular, we show that ICB-responder BrM (BR1) expresses a molecular program of response to IFN, antigen presentation, and inflammatory pathways that polarizes microglia into reactive states. These microglia are characterized by high expression of MHC, co-stimulatory molecules, and T cell recruiting chemokines, which enhance T cell recruitment and activation favoring ICB efficacy. In contrast resistant BrM (BR3) express neurological features and evade the immune response by preserving a homeostatic state within the BrTME. Importantly, we confirmed the translational relevance of our findings demonstrating that these ICB-responder and -resistant tumor signatures were present in human BrM. Agreeing with our preclinical data the BR1 responsive BrM signatures positively correlated with T cell infiltration, and were associated with improved patient outcome, whereas the BR3 resistant signature showed negative correlation with T cells and was associated with poorer patient outcome.

To date, the general assumption has been that circulating T cells play an important role in brain tumor control and therapy[28,97,98]. With respect to BrM, a previous study using a preclinical model in which melanoma cells were injected directly into the brain, has shown that the presence of extracranial disease – created by subcutaneous injection of the same cells – activated peripheral T cells promoting brain ICB response[28]. However, in our study, we found that naturally occurring extracranial metastases did not improve ICB efficacy. In contrast, BR1, which is associated with minimal extracranial disease, responded to therapy, while BR3, which has a higher systemic metastatic burden, did not. Although here we didn't explore the circulating T cell pool, we found striking differences between responders and resistant models in the BrTME T cell repertoire. The presence of a proliferative T cell subset in the responder model suggests that local expansion likely plays a role in the brain T cell landscape. An interesting finding from our study is that therapy induces an increase in T cell infiltration in both responder and non-responder models; however, the phenotypic characteristics of these cells were markedly distinct. These observations may help explain contradictory results observed from studies

showing a positive correlation between T-cell infiltration and improved patient outcomes vs. others that did not[21,100–103], stressing the importance of studying other immune populations that may influence T-cell function.

In the context of ICB therapy, the focus in the field has been mostly placed on the T cell compartment. However, our findings reveal that not only T cells but also microglia distinguish responders from non-responders. In fact, we show that specific reactive microglia states are significantly enriched in ICB responders and positively correlate with $CD8^+$ T cell infiltration. Although the relationship between microglia – T cell crosstalk and therapy responses has not been explored in patients, recent studies have reported positive correlations between MHC-II expression on microglia and $CD8^+$ T cells in BrM patients[19,100]. Supporting our results, previous data have shown that microglia sharing some of the BR1 signatures can attract or activate T cells in other contexts, such as CNS infection[104,106], Alzheimer's disease[108], or glioblastoma (GBM) treated with ICB[110]. Of note, CXCL9 alone or $MHCII^+$ reactive microglia, were recently found to be required for GBM response to PD-1 or CTLA-4 blockade, respectively[110,112]. In our study, reactive microglia had stronger interactions with $CD8^+$ T cells in both untreated and combo therapy conditions. In contrast, the GBM report observed these interactions uniquely after anti-CTLA-4 blockade, where they specifically controlled CD4 T cells[110].

Other studies using breast and lung BrM preclinical models have recently shown that microglia with some BR1-reactive characteristics could suppress T cell activity and support BrM development[61,115,120]. These dual microglia functions are not mutually exclusive and suggest a context-dependent role. We observed that BR1-microglia states express different T cell immune checkpoints, which can paradoxically both induce and limit T cell activation in the absence of treatment. When these inhibitor axes are targeted by ICB, they unleash the T cells' anti-tumor potential. Thus, our findings indicate that microglia can play different roles in BrM depending on the brain tumor subtype and the therapy utilized. Moreover, our observations can help explain the inconsistent pro- and anti-tumor impact of microglia depletion observed across independent preclinical studies[10,61,120]. While depleting microglia has been suggested as a potential therapeutic approach for brain tumors, our data indicate that such a strategy could be more harmful than beneficial depending on the context. Instead, modulating the balance between pro- and anti-tumor microglia states might be a more effective alternative.

Here we reveal three major types of interactions used preferentially by the ICB-resistant BR3 tumors to shape microglia states: (1) ligands known to inhibit microglia reactivity such as CD200 and Gas6[105,107,109,111], (2) components of the extra-cellular matrix such as collagens and laminins, and (3) neurological features such as neurotransmitter (e.g., glutamate) and axon guidance (e.g., semaphoring).

In the CNS, these three axes constitute crucial crosstalk involving microglia and other cells (e.g., neurons, astrocytes, and endothelial cells) to maintain brain homeostasis and resolve neuroinflammation[105,113,114,116–119]. Others have described the pro-carcinogenic effect of CD200-CD200R and Gas6-MertK in brain primary tumors[109], and a recent report implicated collagens in murine breast and lung BrM growth[120]. The latter study demonstrated that tumor-derived collagen polarizes pro-tumor microglia through TNFα-NF-κB signaling, suppressing T cell infiltration and activation[120]. We found this pathway upregulated in BR3 microglia, suggesting that similar interactions might contribute to the BR3 BrTME profile and its ICB-resistance. Additionally, while no direct link has been established between neurotransmitters and BrM response to therapy, independent studies have shown that glutamate can support GBM growth[127,129] and decrease microglia reactive states[118]. Thus, our findings suggest that the ICB-resistant BR3 BrM model hijacks natural CNS tolerance systems to support homeostatic microglia, inhibit reactive states, and promote pro-tumoral polarization. The molecular axes that we identified not only deepen our understanding of how BrM tumors shape the BrTME but also provide potential targets for overcoming therapy resistance.[127,129]

We extended our findings to a pan-cancer BrM cohort, confirming that the BR1 and BR3 signatures that we established can predict the BrTME and correlate with patient outcomes. These observations provide promising predictive biomarkers and valuable insights for treatment decision-making. Specifically, we show that BrM with proliferative and inflammatory signatures benefit from ICB therapies, whereas BrM subtypes enriched in neurological features such as axon guidance are less likely to respond and may require alternative or additional strategies, such as targeting myeloid cells or tumor ligands.

One of the most arduous obstacles to improving BrM therapy is the difficulty in accessing patient samples, underscoring the importance of relevant preclinical models to elucidate mechanisms of resistance. An important consideration when studying ICB therapy in BrM is maintaining a functional TME and physiological BBB to regulate tumor extravasation and drug distribution[95,131,133,135]. Our models not only meet this requirement but also recapitulate the cellular and molecular diversity of BrM tumors and TME observed in the clinic[13–15,17–20,44,45,99]. Moreover, they capture the differential ICB responses observed in patients. Therefore, the BR1 and BR3 models constitute a key resource to perform mechanistic studies. Using them, we conducted comparative studies identifying key molecular features associated with responses to ICB therapy. By offering critical insights into the mechanisms governing sensitivity and resistance to treatment, our study significantly contributes toward the development of more efficacious therapeutic options for BrM patients.

Limitations of the study

Here we focused on the immune and the tumor compartments, but we cannot rule out the role of other important BrTME actors, such as astrocytes and endothelial cells. Further studies should investigate how these cell types can influence ICB responses. An important limitation in the field, that persists in our study, is the to directly associate ICB response status and different BrM features in patients due to the scarcity of available human BrM samples. Although we demonstrated that the BR1 and BR3 signatures are associated with the patients' BrTME and survival in cohorts that included ICB treatment, it will be important to test our findings when larger cohorts of treated patients become available. A remaining unmet need is the ability to identify valuable predictors of response employing less invasive approaches, such as monitoring blood or cerebrospinal fluid. Despite these constraints, our report significantly enhances our understanding of the mechanisms by which BrM tumor cells can impact BrTME and ICB responses. We anticipate that our findings will facilitate the development of new therapeutic approaches and help inform clinical trials for melanoma patients with brain metastases.

ACKNOWLEDGMENTS

We thank Patricia Steeg's laboratory, particularly Alex Wu, for their advice and help with the BrM model development. We are grateful to the following NCI facilities: CCR Single Cell Analysis Facility, SpiTR Nanoscale Protein Analysis Section, LGI Flow Cytometry Core, NIH Animal Facility Bethesda and Frederick, and NCI LASP Small Animal Imaging Program (SAIP). We also thank Jennifer Dwyer (LCBG) and Katerina Grafanaki (University of Patras, School of Medicine) for technical help, Christophe Cataisson (LCBG) and Grégoire Atlan-Bonnet Lab (LICI) for access to equipment, and members of LICI and LCBG for their helpful discussion. This research was supported by the Intramural Research Program of the NIH (CCR-NCI), CCR FLEX Synergy Award, and a CCR Excellence in Postdoctoral Research Transition Award (2020) to EP-G. GK was founded by a Fulbright Foundation Visiting Research Fellowship from Greece (2023–2024). This work utilized the computational resources of the NIH HPC Biowulf cluster (https://hpc.nih.gov)

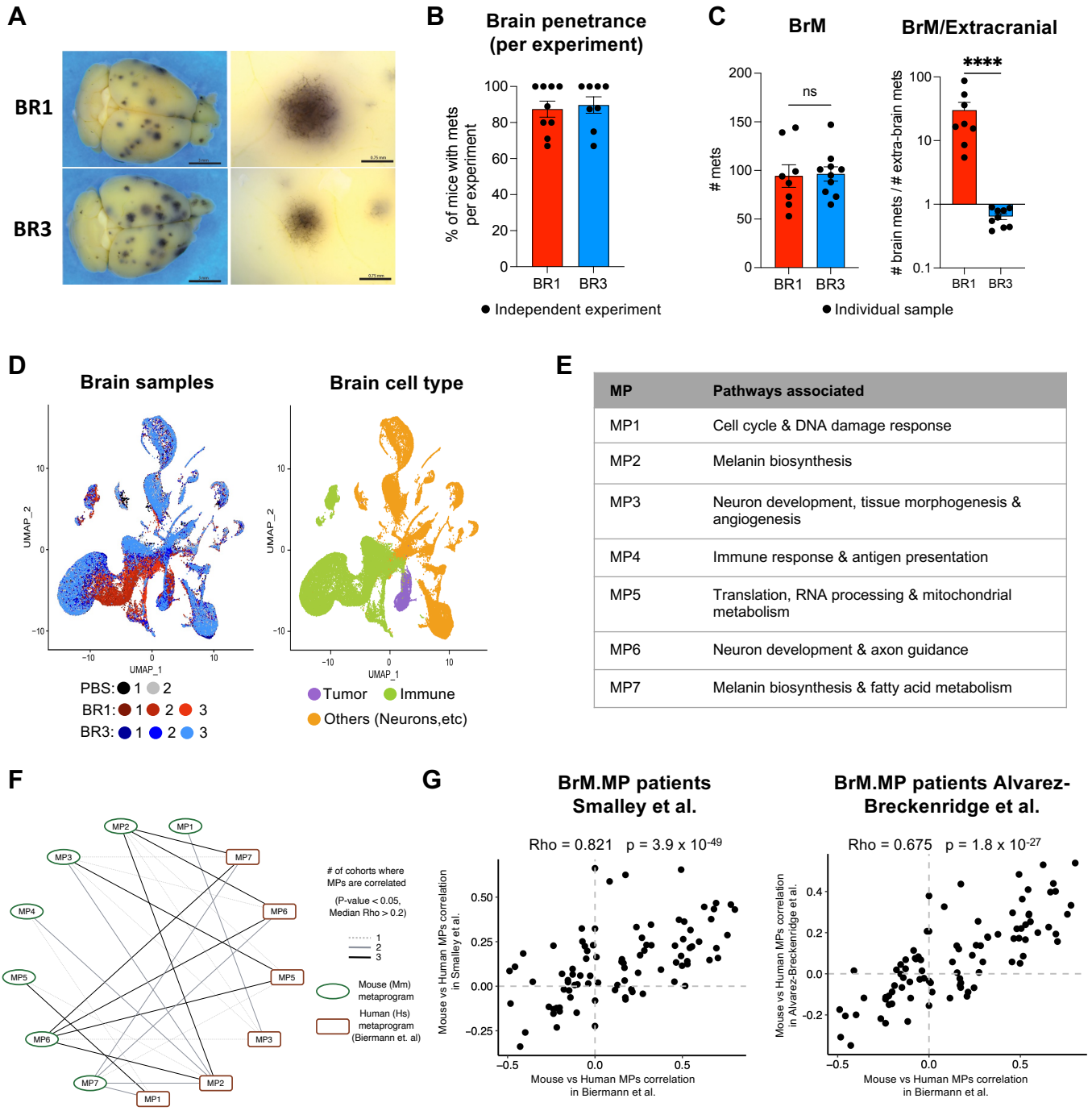

MP	Pathways associated
MP1	Cell cycle & DNA damage response
MP2	Melanin biosynthesis
MP3	Neuron development, tissue morphogenesis & angiogenesis
MP4	Immune response & antigen presentation
MP5	Translation, RNA processing & mitochondrial metabolism
MP6	Neuron development & axon guidance
MP7	Melanin biosynthesis & fatty acid metabolism

Figure 1. Generation of two syngeneic metastatic melanoma models that exhibit similar molecular features that BrM patients

(A) Representative stereomicroscope images of whole brains (left) and brain macrometastases (right) from BR1 and BR3 bearing animals (B) Proportion of mice with brain metastases (BrM) per independent experiment. (C) BrM count (left) and ratio of the count of metastases formed at the brain divided by the count of metastases formed in other organs (extracranial) (right) per mouse. (D-E) Single-cell RNA sequencing analysis of whole brain from BR1, BR3, and non-BrM control (PBS) animals. (D) UMAP projection showing the distribution of cells from PBS, BR1, and BR3 samples (left) and per cell type (right). (E) Tumor metaprograms from BR1 and BR3 tumor cells and summary of their associated pathways. (F) Correlation-based network analysis between mouse metaprograms (MP) derived in our study (green circles) with human MP derived in Biermann et. al (brown rectangles). The correlation between the activities of both sets of metaprograms are evaluated in malignant cells from three cohorts of patients (Biermann et al. 2022, Smalley et al. 2021, Alvarez-Breckenridge et al. 2022). Edges are drawn between human and mouse metaprogram pairs that have median Rho > 0.2 and $p < 0.05$ (see Methods). The thickness of the edge represents the number of cohorts in which a given metaprogram pair is correlated. (G) Spearman correlation between activities of our study mouse MP and Biermann et. al-derived MP evaluated in tumor cells in the Biermann et. al cohort (x-axis), Smalley et. al cohort (y-axis, left panel) and Alvarez-Breckenridge et. al cohort (y-axis, right panel).

A representative of 8-9 independent experiments, n=3-12 mouse/group/experiment. B-C shown as mean ± SEM, B data from 8-9 experiments combined, n=3-12 mouse/group/experiment. C data from 3 experiments combined, n=2-5 mouse/group/experiment. ****$p < 0.00001$. D-E n = 2-3/group. F-G n = 2-3 mouse/group (our study), n= 25 (Biermann et. al), 14 (Smalley et. al), 27 patients (Alvarez-Breckenridge et. al). See also Figure S1 and Table S2.

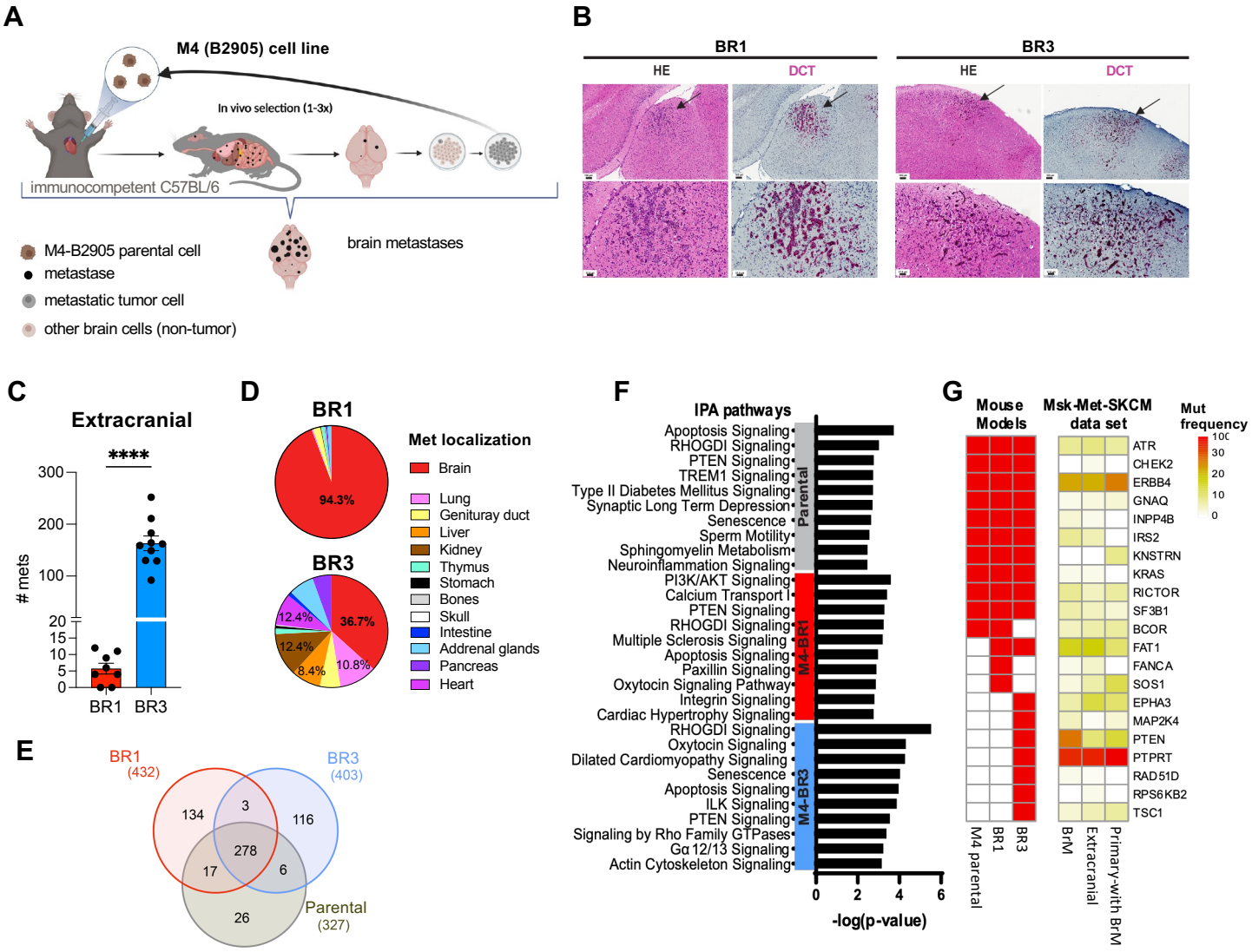
A
M4 (B2905) cell line
In vivo selection (1-3x)
immunocompetent C57BL/6
brain metastases
M4-B2905 parental cell
metastase
metastatic tumor cell
other brain cells (non-tumor)
B
BR1
BR3
HE
DCT
C
Extracranial
****
mets
BR1
BR3
D
BR1
94.3%
BR3
36.7%
10.8%
8.4%
12.4%
12.4%
Met localization
Brain
Lung
Genituray duct
Liver
Kidney
Thymus
Stomach
Bones
Skull
Intestine
Addrenal glands
Pancreas
Heart
E
BR1 (432)
BR3 (403)
Parental (327)
134
3
116
278
17
6
26
F
IPA pathways
Apoptosis Signaling
RHOGDI Signaling
PTEN Signaling
TREM1 Signaling
Type II Diabetes Mellitus Signaling
Synaptic Long Term Depression
Senescence
Sperm Motility
Sphingomyelin Metabolism
Neuroinflammation Signaling
PI3K/AKT Signaling
Calcium Transport I
PTEN Signaling
RHOGDI Signaling
Multiple Sclerosis Signaling
Apoptosis Signaling
Paxillin Signaling
Oxytocin Signaling Pathway
Integrin Signaling
Cardiac Hypertrophy Signaling
RHOGDI Signaling
Oxytocin Signaling
Dilated Cardiomyopathy Signaling
Senescence
Apoptosis Signaling
ILK Signaling
PTEN Signaling
Signaling by Rho Family GTPases
Gα12/13 Signaling
Actin Cytoskeleton Signaling
Parental
M4-BR1
M4-BR3
-log(p-value)
G
Mouse Models
Msk-Met-SKCM data set
Mut frequency
M4 parental
BR1
BR3
BrM
Extracranial
Primary-with BrM
ATR
CHEK2
ERBB4
GNAQ
INPP4B
IRS2
KNSTRN
KRAS
RICTOR
SF3B1
BCOR
FAT1
FANCA
SOS1
EPHA3
MAP2K4
PTEN
PTPRT
RAD51D
RPS6KB2
TSC1
H
Non-negative Matrix Factorization (NMF) pipeline
Cells from BR1
Genes
Factors
Cells
Retain genes in each factor co-expressed in BR1 cells
Cluster co-varying factors to form metaprograms
Score BR1 and BR3 cells with metaprogram genes using AUCell
Cluster cells based on metaprogram scores
Cells from BR3
Retain genes in each factor co-expressed in BR3 cells

Figure S1. Characterization of the metastatic potential of BR1 and BR3 models, related to Figure 1.

(A) Experimental design for the development strategy of brain-metastatic melanoma models. (B) Microscopical pictures of hematoxylin and eosin (HE) and dopachrome tautomerase (DCT, in pink) immunostaining of brain sagittal sections showing BR1 (left panels) and BR3 (right panels) metastases. Magnification 15x (top) and 40x (bottom). (C) Extracranial metastases count per mouse. (D) Percentage of metastases per organ in BR1 (top) and BR3 (bottom) models. (E) Venn diagram showing the number of genes mutated and their overlap between the indicated cell sublines (F) Top 10 signaling pathways obtained by Ingenuity Pathway Analysis (IPA, © QIAGEN 2013–24) of the genes mutated in each model. (G) Mutated genes related to MAPK and PI3K-PTEN-AKT pathways found in the brain-metastatic models (marked in red in the heatmap) and BrM, extracranial metastases and primary tumors from patients with BrM (primary-with BrM) from MSK MetTropism data set. Color scale represent the mutation frequency in the indicated group of samples (source: https://www.cbioportal.org). (H) Schematic of metaprogram discovery and their use in clustering malignant cells in BR1 and BR3 models. Step 1: NMF is carried out (k = 30 factors) separately in malignant cells from BR1 and BR3 models based on genes that are expressed in at least 1% of cells in either model. Step 2: Genes with a high weight in each factor are then filtered to retain genes that are co-expressed. Step 3: The activity of each filtered factor is computed across all malignant cells using AUCell. A correlation matrix between all factors is computed based on these activities, and after hierarchical clustering, correlated factors are grouped together. Genes occurring in at least 25% of constituent factors in a group are retained to form metaprograms. Step 4: AUCell is used to compute the activity of all metaprograms across all malignant cells. Step 5: Cluster cells using Louvain clustering based on metaprogram activity scores.

B is representative of 2 experiments. n=2-5 mouse/group/experiment. C data from 3 experiments combined, shown as mean ± SEM, n=2-5 mouse/group/experiment. ****$p < 0.00001$. D is representative of 3 experiments, n=2-5 mouse/group/experiment. E-G n = 2-3/group. See also Table S1-2.

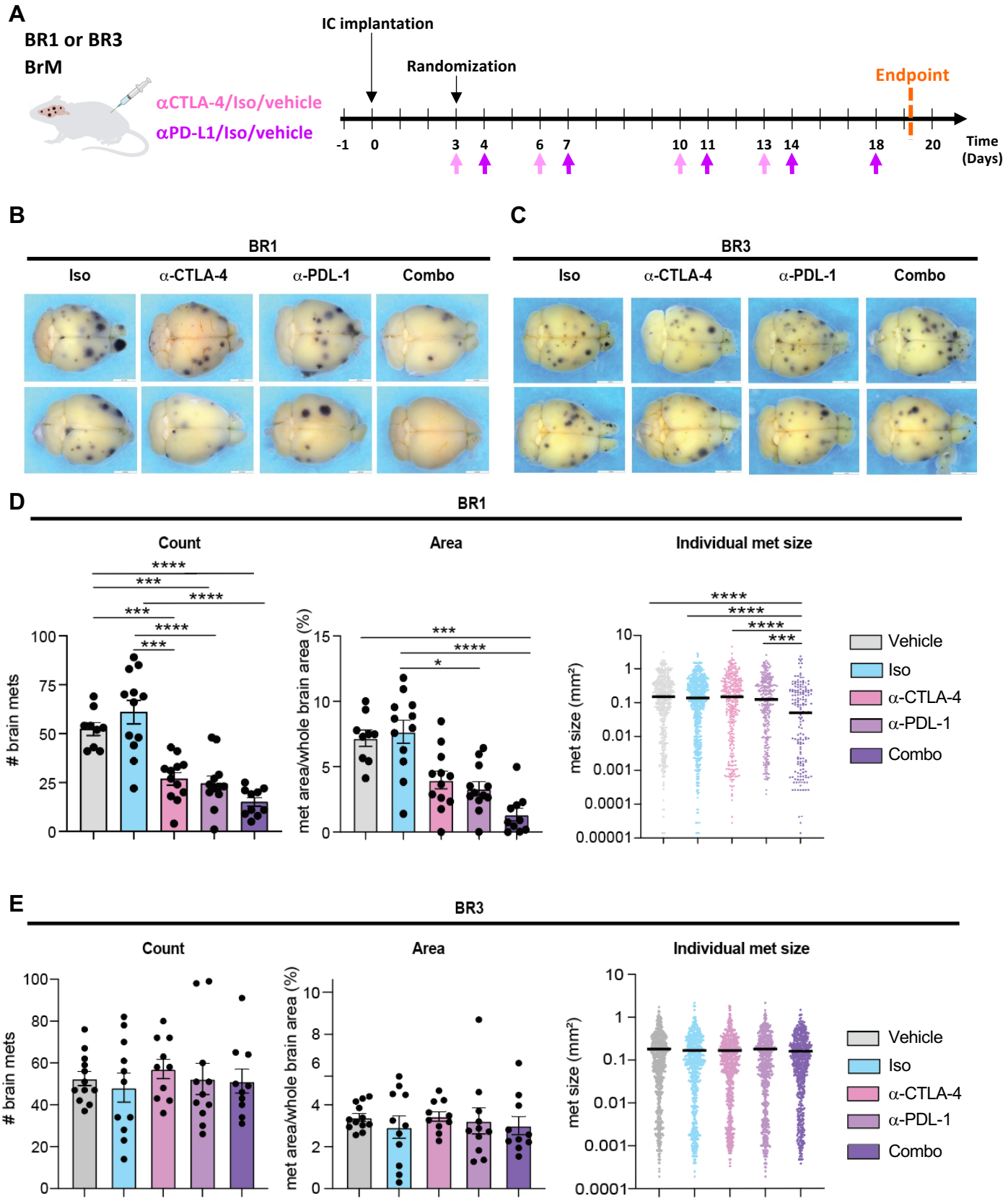
A
BR1 or BR3
BrM
αCTLA-4/Iso/vehicle
αPD-L1/Iso/vehicle
IC implantation
Randomization
Endpoint
-1 0 3 4 6 7 10 11 13 14 18 20
Time (Days)
B
BR1
Iso
α-CTLA-4
α-PDL-1
Combo
C
BR3
Iso
α-CTLA-4
α-PDL-1
Combo
D
BR1
Count
Area
Individual met size
brain mets
met area/whole brain area (%)
met size (mm²)
Vehicle
Iso
α-CTLA-4
α-PDL-1
Combo
E
BR3
Count
Area
Individual met size
brain mets
met area/whole brain area (%)
met size (mm²)
Vehicle
Iso
α-CTLA-4
α-PDL-1
Combo

Figure 2. BR1 and BR3 BrM recapitulate the diversity of responses to ICB observed in the clinic.

(A-E) Immune checkpoint blockade (ICB) therapeutic study of BR1 or BR3 bearing animals untreated or treated with isotype control (Iso), anti-CTLA-4 (α-CTLA-4) or anti-PD-L1 (α-PD-L1) alone, or anti-PD-L1 and anti-CTLA-4 combination therapy (Combo). (A) Experimental design. (B-C) Brain stereomicroscope images from BR1 (B) and BR3 (C) models. (D-E) Brain metastasis (BrM) count per individual brain (left), total brain metastatic area per individual brain (middle), and size of individual BrM lesion (right), from BR1 (D) and BR3 (E).

D-E representative of 2 independent experiments, data shown as mean ± SEM, n = 9-12/group/experiment. *$p < 0.05$, ***$p < 0.001$, ****$p < 0.00001$. See also Figure S2

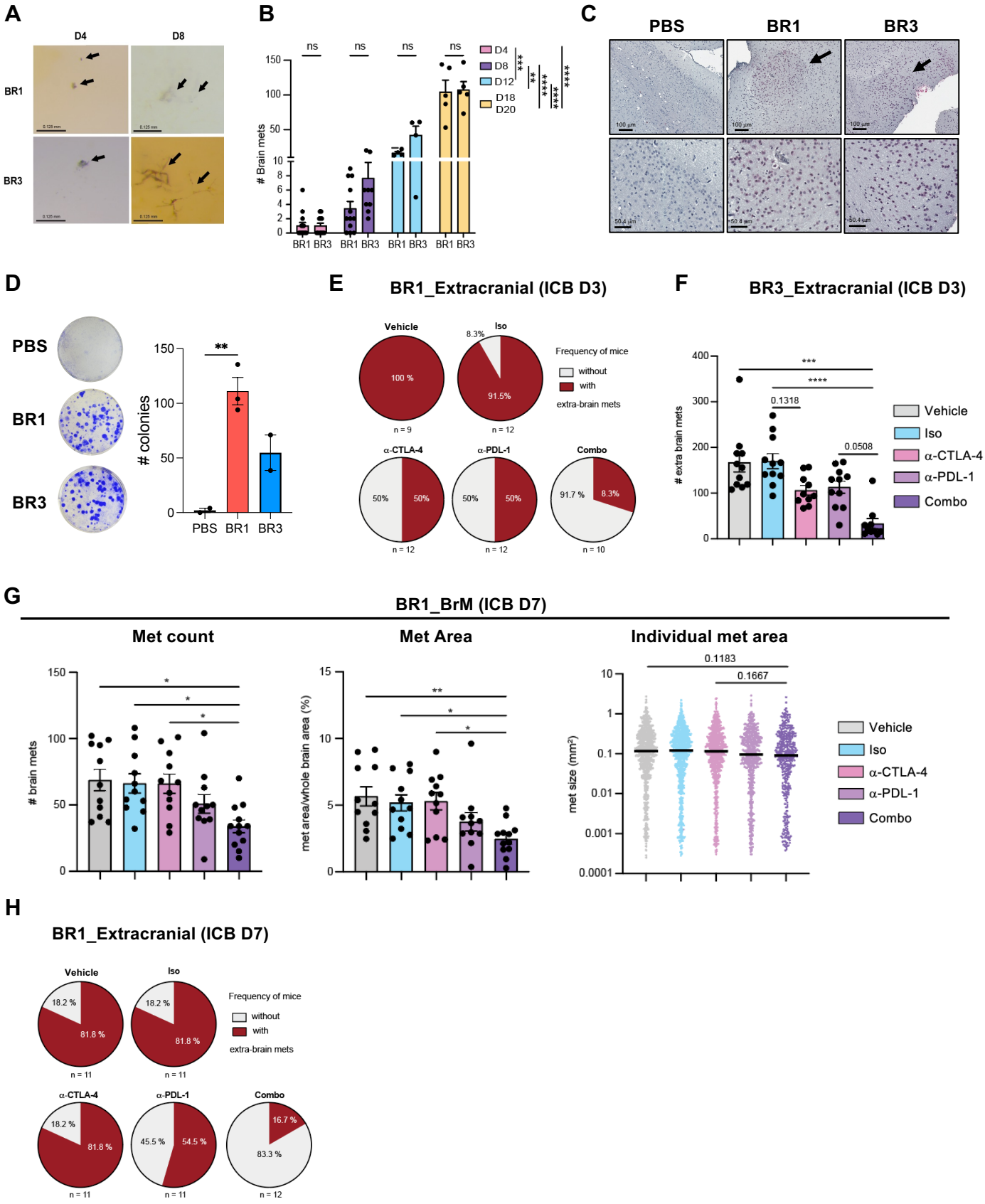
A
D4
D8
BR1
BR3
B
ns
D4
D8
D12
D18
D20
Brain mets
BR1 BR3 BR1 BR3 BR1 BR3 BR1 BR3
C
PBS
BR1
BR3
D
PBS
BR1
BR3
colonies
PBS BR1 BR3
E
BR1_Extracranial (ICB D3)
Vehicle
Iso
8.3%
100 %
91.5%
Frequency of mice
without
with
extra-brain mets
n = 9
n = 12
α-CTLA-4
α-PDL-1
Combo
50%
50%
91.7 %
8.3%
n = 12
n = 12
n = 10
F
BR3_Extracranial (ICB D3)
extra brain mets
0.1318
0.0508
Vehicle
Iso
α-CTLA-4
α-PDL-1
Combo
G
BR1_BrM (ICB D7)
Met count
brain mets
Met Area
met area/whole brain area (%)
Individual met area
0.1183
0.1667
met size (mm²)
Vehicle
Iso
α-CTLA-4
α-PDL-1
Combo
H
BR1_Extracranial (ICB D7)
Vehicle
Iso
18.2 %
81.8 %
Frequency of mice
without
with
extra-brain mets
n = 11
n = 11
α-CTLA-4
α-PDL-1
Combo
18.2 %
81.8 %
45.5 %
54.5 %
16.7 %
83.3 %
n = 11
n = 11
n = 12

Figure S2. Response to immune checkpoint blockades of the two new models, related to Figure 2.

(A-D) BR1 and BR3 BrM detection at day 4 (A-D), day 8 (A), or indicated time points (B) post-intracardiac injection (ic.). Mice receiving PBS by ic. are used as non-BrM bearing control (PBS). (A) Stereomicroscope images of individual micrometastases detected in mouse brains. (B) BrM counts (C) Microscopical pictures of hematoxylin and eosin (HE) and dopachrome tautomerase (DCT, in pink) immunostaining of brain sagittal sections showing BrM. Magnification 10x (top) and 40x (bottom). cultured cell colonies recovered from mouse brains. Macroscopic pictures (left). Cell colony counts (right). (E-H) Immune checkpoint blockade (ICB) therapeutic study of BR1 or BR3 bearing animals untreated (Vehicle) or treated with isotype control (Iso), anti-CTLA-4 (α-CTLA-4) or anti-PD-L1 (α-PD-L1) alone, or anti-PD-L1 and anti-CTLA-4 combination therapy (Combo). Therapy started at D3 (E-F) or D7 (G-H) post-ic. (E) Proportion of mice with and without BR1 extracranial metastases (F) BR3 extracranial metastatic count per mouse. (G) BR1 BrM count (left), total brain metastatic area per individual brain (middle), and size of individual BrM lesion (right). (H) Proportion of mice with and without BR1 extracranial metastases.

A and C showed representative images from 2 independent experiments. n=3-11/group/experiment. Showed data of 2 independent experiments combined, n=3-12 mouse/group/experiment. D n=2-3/group/experiment. E-G representative of 2 independent experiments, n = 9-12/group/experiment.

B, D, F-G data shown as mean ± SEM *$p < 0.05$, ***$p < 0.001$, ****$p < 0.00001$.

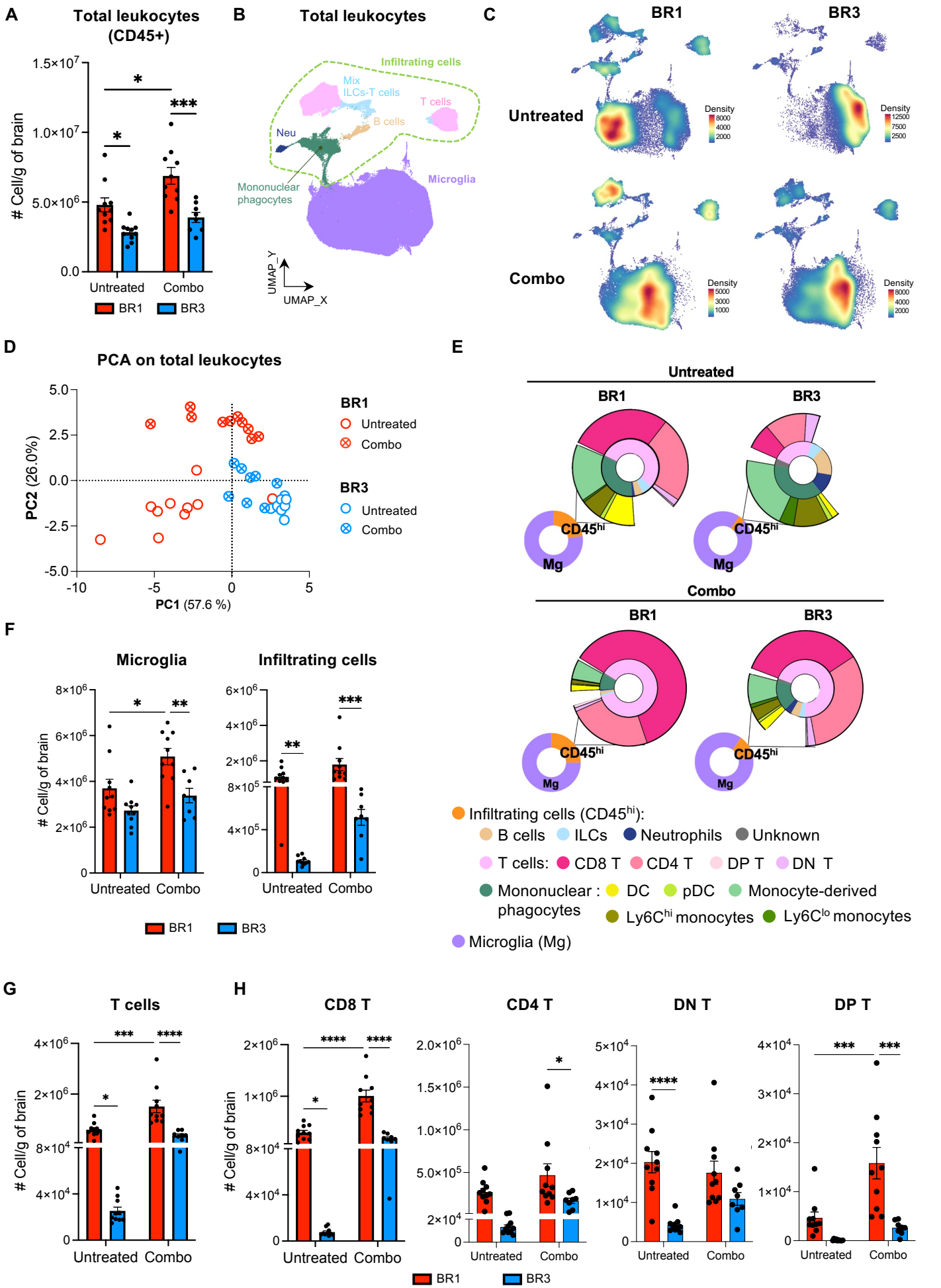
A
Total leukocytes (CD45+)
Cell/g of brain
1.5×10^7
1.0×10^7
5.0×10^6
0.0
Untreated
Combo
BR1
BR3
B
Total leukocytes
Infiltrating cells
Mix
ILCs-T cells
T cells
B cells
Neu
Mononuclear phagocytes
Microglia
UMAP_Y
UMAP_X
C
BR1
BR3
Untreated
Combo
Density
D
PCA on total leukocytes
PC2 (26.0%)
PC1 (57.6 %)
BR1
Untreated
Combo
BR3
Untreated
Combo
E
Untreated
BR1
BR3
CD45hi
Mg
Combo
Infiltrating cells (CD45hi):
B cells
ILCs
Neutrophils
Unknown
T cells:
CD8 T
CD4 T
DP T
DN T
Mononuclear phagocytes :
DC
pDC
Monocyte-derived
Ly6Chi monocytes
Ly6Clo monocytes
Microglia (Mg)
F
Microglia
Infiltrating cells
Cell/g of brain
Untreated
Combo
BR1
BR3
G
T cells
Cell/g of brain
Untreated
Combo
H
CD8 T
CD4 T
DN T
DP T
Cell/g of brain
Untreated
Combo
BR1
BR3

Figure 3. Distinct BrTME are associated with different responses to immune checkpoint blockade.

High-parametric spectral flow cytometry analysis of brain leukocytes from BR1 and BR3 bearing animals untreated or treated with anti-PD-L1 and anti-CTLA-4 combination therapy (combo). (A) Absolute number of leukocytes (live $CD45^{+}$) per gram of brain tissue. (B) UMAP projection of total BrM leukocytes: resident microglia, infiltrating mononuclear phagocytes, neutrophils (Neu), B cells, innate lymphoid cells (ILC), and T cells. (C) Density plots showing cell distribution in untreated (top) and treated (bottom) mice from BR1 (left) and BR3 (right) models. (D) PCA of the main immune cell population frequencies in total leukocytes for each sample. (E) Proportion of microglia (Mg) and infiltrating cells ($CD45^{hi}$) in total leukocytes (purple and orange circle respectively). Proportion of indicated cells in total infiltrating cells (inset). (F) Absolute number of microglia (left) and infiltrating cells (right) per gram of brain. (G) Absolute number of total T cells per gram of brain. (H) Absolute number of indicated T cell subsets per g of brain. A, F, G, and H data shown as mean ± SEM, n = 8-10/group/experiment. *$p < 0.05$, **$p < 0.01$, ***$p < 0.001$, ****$p < 0.00001$. See also Figure S3 and Table S3.

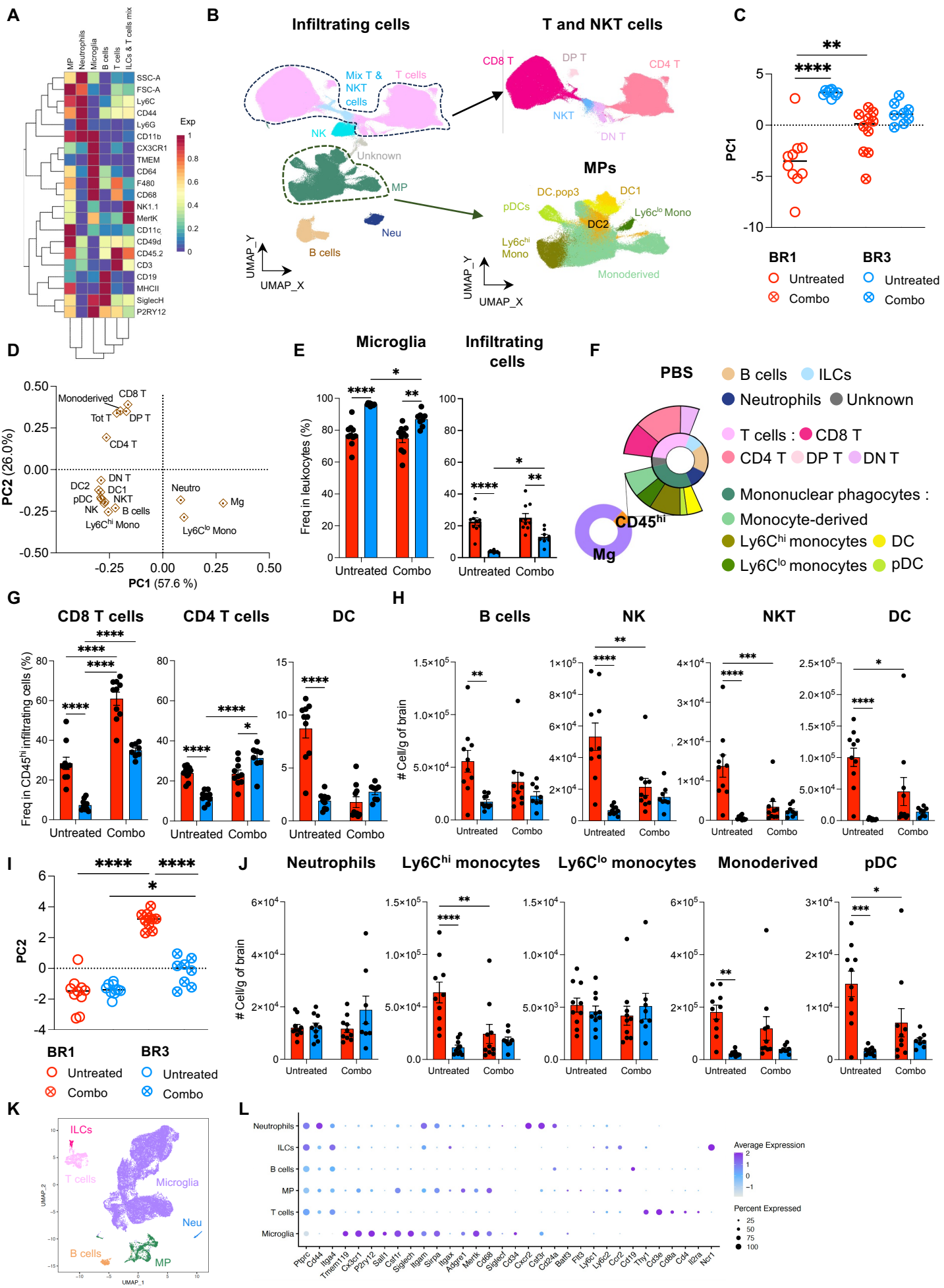
A
MP
Neutrophils
Microglia
B cells
T cells
ILCs & T cells mix
SSC-A
FSC-A
Ly6C
CD44
Ly6G
CD11b
CX3CR1
TMEM
CD64
F480
CD68
NK1.1
MertK
CD11c
CD49d
CD45.2
CD3
CD19
MHCII
SiglecH
P2RY12
Exp
B
Infiltrating cells
Mix T & NKT cells
T cells
NK
Unknown
MP
Neu
B cells
UMAP_Y
UMAP_X
T and NKT cells
CD8 T
DP T
CD4 T
NKT
DN T
MPs
DC.pop3
DC1
pDCs
Ly6c^lo Mono
DC2
Ly6c^hi Mono
Monoderived
C
PC1
BR1
Untreated
Combo
BR3
Untreated
Combo
D
Monoderived
CD8 T
Tot T
DP T
CD4 T
DN T
DC2
DC1
pDC
NKT
NK
B cells
Ly6C^hi Mono
Neutro
Mg
Ly6C^lo Mono
PC2 (26.0%)
PC1 (57.6 %)
E
Microglia
Infiltrating cells
Freq in leukocytes (%)
Untreated
Combo
F
PBS
CD45^hi
Mg
B cells
ILCs
Neutrophils
Unknown
T cells : CD8 T
CD4 T
DP T
DN T
Mononuclear phagocytes :
Monocyte-derived
Ly6C^hi monocytes
DC
Ly6C^lo monocytes
pDC
G
CD8 T cells
CD4 T cells
DC
Freq in CD45^hi infiltrating cells (%)
Untreated
Combo
H
B cells
NK
NKT
DC
Cell/g of brain
Untreated
Combo
I
PC2
BR1
Untreated
Combo
BR3
Untreated
Combo
J
Neutrophils
Ly6C^hi monocytes
Ly6C^lo monocytes
Monoderived
pDC
Cell/g of brain
Untreated
Combo
K
ILCs
T cells
Microglia
Neu
B cells
MP
UMAP_2
UMAP_1
L
Neutrophils
ILCs
B cells
MP
T cells
Microglia
Ptprc
Cd44
Itga4
Tmem119
Cx3cr1
P2ry12
Sall1
Csf1r
Siglech
Itgam
Sirpa
Itgax
Adgre1
MertK
Cd68
Siglecf
Cd34
Cxcr2
Csf3r
Cd24a
Batf3
Flt3
Ly6c1
Ly6c2
Ccr2
Cd19
Thy1
Cd3e
Cd8a
Cd4
Il2ra
Ncr1
Average Expression
Percent Expressed

Figure S3. Global immune BrTME characterization of untreated and treated BR1 and BR3 brains, related to Figure 3.

High-parametric spectral flow cytometry analysis of brain leukocytes from BR1 and BR3 bearing animals untreated or treated with anti-PD-L1 and anti-CTLA-4 combination therapy (combo). (A) Heatmap representing the level of expression of indicated markers (scaled by marker) for each immune cluster with hierarchical clustering indicated on left and markers on top. (B) UMAP projection of natural killer T (NKT) and T cell subsets: $CD8^{+}CD4^{-}$ (CD8 T), $CD8^{-}CD4^{+}$ (CD4 T), $CD8^{-}CD4^{-}$ (DN T), $CD8^{+}CD4^{+}$ (DP T) (top); clustering of MP subsets: dendritic cell subsets (DC1, DC2, DC.pop3), plasmacytoid DC (pDCs), monocytes subsets ($Ly6C^{hi}$ mono, $Ly6C^{lo}$ mono), and monoderived. (C) Quantification of principal component 1 (PC1) from Figure 3D. (D) Loading plot of PC1 and PC2 from Figure 3D. (E) Proportion of indicated immune cells. (F) Proportion of indicated cell subsets in total infiltrating leukocytes ($CD45^{hi}$). Proportion of microglia (Mg) and infiltrating cells ($CD45^{hi}$) in total leukocytes (bottom). Proportion of indicated cells in total infiltrating cells (inset). (G) Proportion of indicated immune cells. (H) Absolute number of indicated immune cells per gram of brain. (I) (C) Quantification of principal component 2 (PC2) from Figure 3D. (J) Absolute number of indicated immune cells per gram of brain. (K-L) Single-cell RNA sequencing analysis of immune BrM cells from untreated BR1, BR3, PBS brains. (K) UMAP projection. (L) Dot plot showing the expression of selected genes differentially expressed between clusters. C and J data shown as mean, n = 8-10/group/experiment. *$p < 0.05$, **$p < 0.01$, ****$p < 0.00001$. E, G, H and I data shown as mean ± SEM, n = 8-10/group/experiment. *$p < 0.05$, **$p < 0.01$, ***$p < 0.001$, ****$p < 0.00001$. See also Table S3.

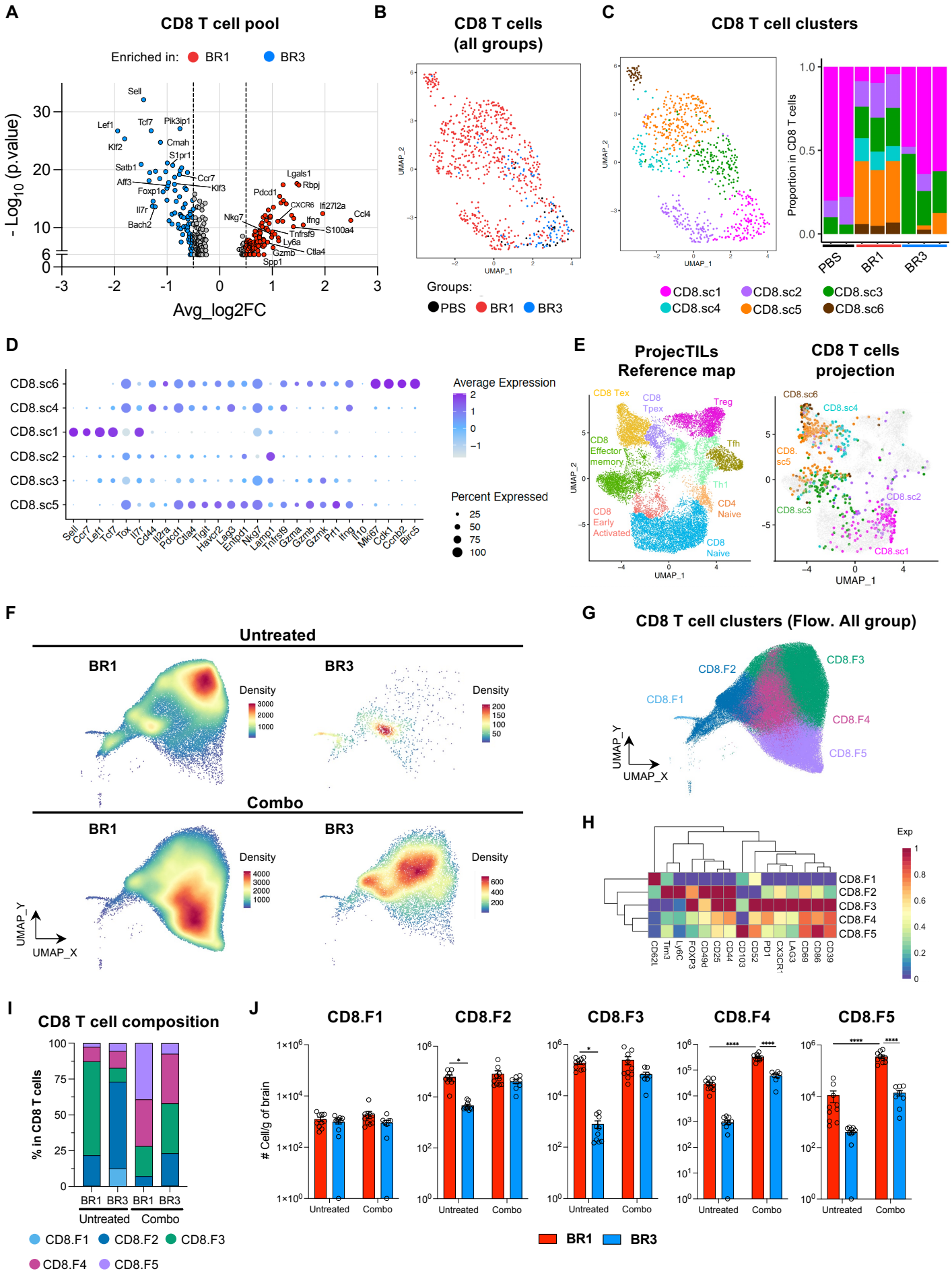
A
CD8 T cell pool
Enriched in: BR1 BR3
- Log10 (p.value)
Avg_log2FC
Sell
Lef1
Tcf7
Pik3ip1
Klf2
Cmah
S1pr1
Satb1
Ccr7
Aff3
Foxp1
Klf3
Il7r
Bach2
Lgals1
Rbpj
Pdcd1
CXCR6
Ifi27l2a
Ccl4
Nkg7
Ifng
S100a4
Tnfrsf9
Ly6a
Gzmb
Ctla4
Spp1
B
CD8 T cells (all groups)
UMAP_1
UMAP_2
Groups:
PBS BR1 BR3
C
CD8 T cell clusters
Proportion in CD8 T cells
PBS BR1 BR3
CD8.sc1 CD8.sc2 CD8.sc3
CD8.sc4 CD8.sc5 CD8.sc6
D
CD8.sc6
CD8.sc4
CD8.sc1
CD8.sc2
CD8.sc3
CD8.sc5
Sell Ccr7 Lef1 Tcf7 Tox Il7r Cd44 Il2ra Pdcd1 Ctla4 Tigit Havcr2 Lag3 Entpd1 Nkg7 Lamp1 Tnfrsf9 Gzma Gzmb Gzmk Prf1 Ifng Il10 Mki67 Cdk1 Ccnb2 Birc5
Average Expression
Percent Expressed
E
ProjecTILs Reference map
CD8 T cells projection
CD8 Tex
CD8 Tpex
Treg
CD8 Effector memory
Tfh
Th1
CD4 Naive
CD8 Early Activated
CD8 Naive
UMAP_1
UMAP_2
F
Untreated
BR1
BR3
Density
Combo
UMAP_Y
UMAP_X
G
CD8 T cell clusters (Flow. All group)
CD8.F1
CD8.F2
CD8.F3
CD8.F4
CD8.F5
H
Exp
CD62L Tim3 Ly6C FOXP3 CD49d CD25 CD44 CD103 CD52 PD1 CX3CR1 LAG3 CD69 CD86 CD39
I
CD8 T cell composition
% in CD8 T cells
BR1 BR3 BR1 BR3
Untreated Combo
CD8.F1 CD8.F2 CD8.F3
CD8.F4 CD8.F5
J
CD8.F1
CD8.F2
CD8.F3
CD8.F4
CD8.F5
Cell/g of brain
Untreated Combo
BR1 BR3

Figure 4. Distinct CD8 T cell subsets infiltrate ICB-responder compared to ICB-resistant BrM.

(A-E) Single-cell RNA sequencing analysis of CD8 T cells from untreated BR1, BR3, and non-BrM control (PBS) brains. (A) Volcano plot of BR1 versus BR3 differentially expressed genes. Significantly higher expressed genes in BR1 depicted in red and higher in BR3 depicted in blue (p-value adjusted <0.05 and average log2 fold change (Avg_log2FC)> 0.5). (B) UMAP projection showing cell distribution in PBS, BR1, and BR3 brain models. (C) UMAP projection; clustering (left) and proportion per sample (right) of indicated CD8 T cell clusters in total CD8 T cells per sample. (D) Dot plot showing the expression of selected genes differentially expressed between clusters. (E) Projection of our CD8 T cell clusters onto the single-cell reference atlas for T cell states ProjecTILs. Reference map (left), our CD8 T cell cluster projection (right). (F-J) High-parametric spectral flow cytometry analysis of CD8 T cells from BR1 and BR3 brains untreated or treated with anti-PD-L1 and anti-CTLA-4 combination therapy (combo). (F) Density plots showing cell distribution in untreated (top) and treated (bottom) BR1 (left) and BR3 (right) models. (G) UMAP projection, clustering of indicated CD8 T cell clusters among total CD8 T cells. (H) Heatmap representing the level of expression of indicated markers (scaled by marker) for each CD8 T cell cluster with hierarchical clustering indicated on left and markers on top. (I) Proportion of indicated CD8 T cell clusters in total CD8 T cells. (J) Absolute number of indicated T cell clusters per gram of brain. A-E n = 2-3/group. F-J n = 8-10/group/experiment. J data shown as mean ± SEM, *p <0.05, ****p < 0.00001. See also Figure S4 and Tables S4.

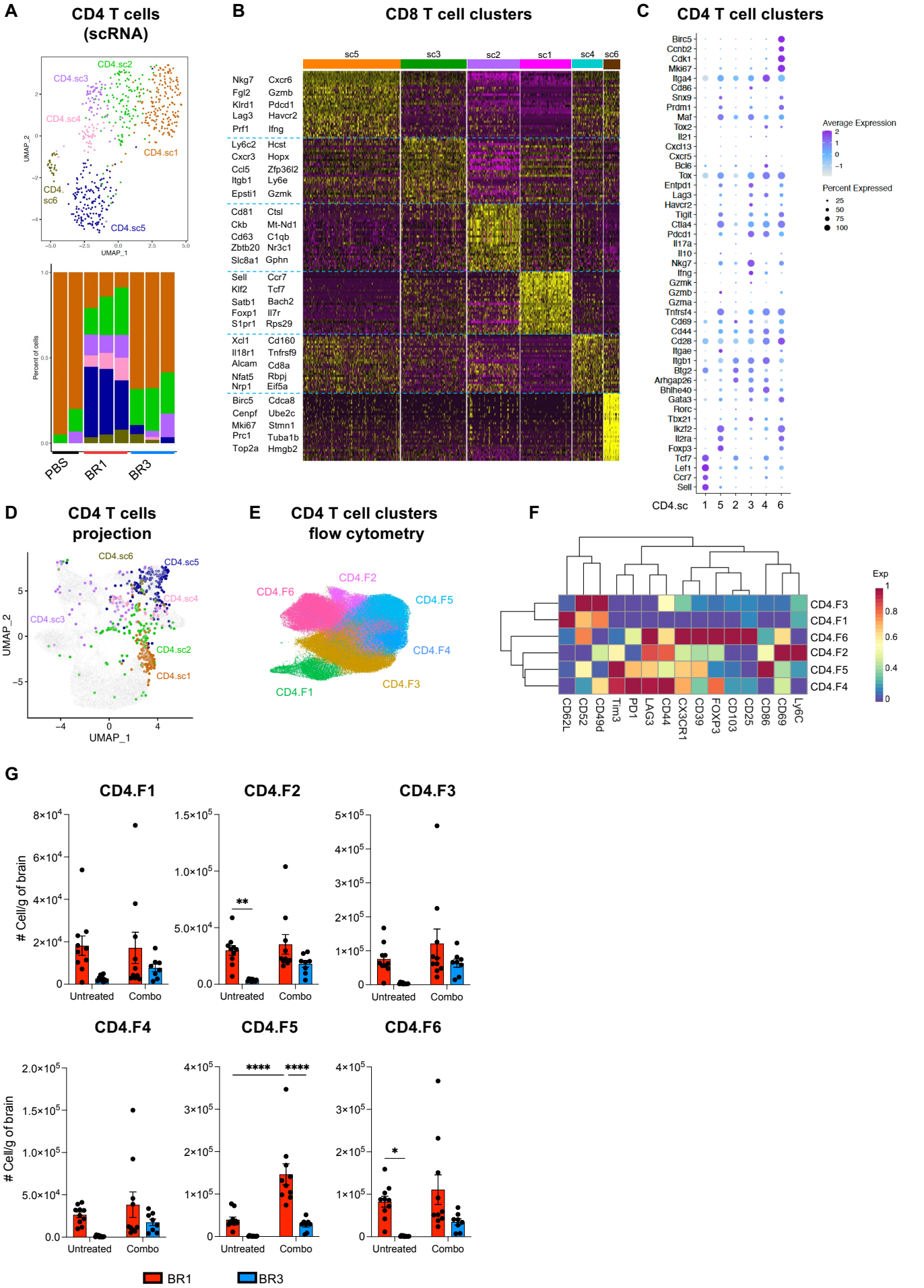
A
CD4 T cells (scRNA)
CD4.sc2
CD4.sc3
CD4.sc4
CD4.sc1
CD4. sc6
CD4.sc5
UMAP_1
UMAP_2
Percent of cells
PBS
BR1
BR3
B
CD8 T cell clusters
sc5
sc3
sc2
sc1
sc4
sc6
Nkg7 Cxcr6
Fgl2 Gzmb
Klrd1 Pdcd1
Lag3 Havcr2
Prf1 Ifng
Ly6c2 Hcst
Cxcr3 Hopx
Ccl5 Zfp36l2
Itgb1 Ly6e
Epsti1 Gzmk
Cd81 Ctsl
Ckb Mt-Nd1
Cd63 C1qb
Zbtb20 Nr3c1
Slc8a1 Gphn
Sell Ccr7
Klf2 Tcf7
Satb1 Bach2
Foxp1 Il7r
S1pr1 Rps29
Xcl1 Cd160
Il18r1 Tnfrsf9
Alcam Cd8a
Nfat5 Rbpj
Nrp1 Eif5a
Birc5 Cdca8
Cenpf Ube2c
Mki67 Stmn1
Prc1 Tuba1b
Top2a Hmgb2
C
CD4 T cell clusters
Birc5
Ccnb2
Cdk1
Mki67
Itga4
Cd86
Snx9
Prdm1
Maf
Tox2
Il21
Cxcl13
Cxcr5
Bcl6
Tox
Entpd1
Lag3
Havcr2
Tigit
Ctla4
Pdcd1
Il17a
Il10
Nkg7
Ifng
Gzmk
Gzmb
Gzma
Tnfrsf4
Cd69
Cd44
Cd28
Itgae
Itgb1
Btg2
Arhgap26
Bhlhe40
Gata3
Rorc
Tbx21
Ikzf2
Il2ra
Foxp3
Tcf7
Lef1
Ccr7
Sell
CD4.sc 1 5 2 3 4 6
Average Expression
Percent Expressed
D
CD4 T cells projection
CD4.sc6
CD4.sc5
CD4.sc4
CD4.sc3
CD4.sc2
CD4.sc1
UMAP_1
UMAP_2
E
CD4 T cell clusters flow cytometry
CD4.F6
CD4.F2
CD4.F5
CD4.F4
CD4.F3
CD4.F1
F
CD4.F3
CD4.F1
CD4.F6
CD4.F2
CD4.F5
CD4.F4
CD62L
CD52
CD49d
Tim3
PD1
LAG3
CD44
CX3CR1
CD39
FOXP3
CD103
CD25
CD86
CD69
Ly6C
Exp
G
CD4.F1
CD4.F2
CD4.F3
CD4.F4
CD4.F5
CD4.F6
Cell/g of brain
Untreated
Combo
**
****
*
BR1
BR3

Figure S4. Distinct T cell characteristics found in the ICB-responder model, related to Figure 4.

(A-D) scRNA-seq analysis of indicated brain T cell populations. (A) UMAP projection of indicated CD4 T cell clusters among total CD4 T cells (top). Proportion of indicated CD4 T cell clusters in total CD4 T cells, per sample (bottom). (B) Heatmap representing the level of expression of the top 30 CD8 T cell cluster-specific genes. (C) Dot plot showing the expression of selected genes differentially expressed between CD4 T cell clusters. (D) Projection of our CD4 T cell clusters onto the single-cell reference atlas for T cell states ProjecTILs. See figure 4E for the Reference map (left). (E-H) High-parametric flow cytometry analysis of CD4 T cells from BR1 and BR3 brains untreated or treated with anti-PD-L1 and anti-CTLA-4 combination therapy (combo). (E) UMAP projection of CD4 T cell populations. (F) Heatmap representing the level of expression of indicated markers (scaled by marker) for each CD4 cluster with hierarchical clustering indicated on left and markers on top. (G) Absolute number of indicated CD4 T cell clusters per gram of brain. A-D n = 2-3/group/experiment. F-G Data shown as mean ± SEM, n = 8-10/group/experiment. *$p < 0.05$, ***$p < 0.001$, ****$p < 0.00001$. See also Table S4-5.

Daugherty-Lopès et al. Fig5

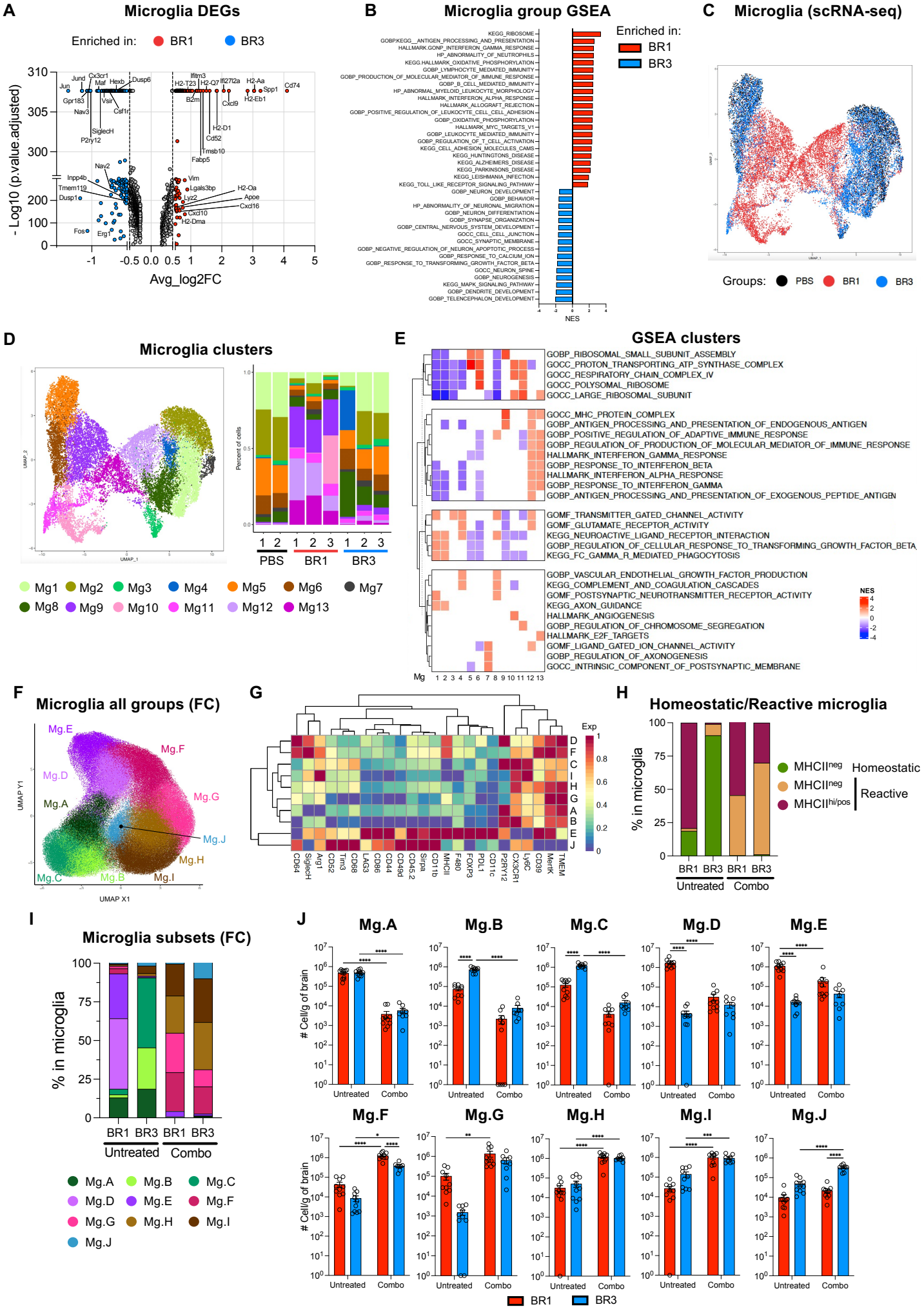

Figure 5. Unique reactive microglia signatures are found in ICB-responder.
(A-E) scRNA-seq analysis of microglia from untreated BR1, BR3, and non-BrM control (PBS) brains. (A) Volcano plot of BR1 versus BR3 differentially expressed genes. Significantly higher expressed genes in BR1 depicted in red and higher in BR3 depicted in blue (p-value adjusted <0.05 and average log2 fold change (Avg_log2FC)> 0.5). (B) Gene set enrichment analysis (GSEA) showing Hallmark, Gene Ontology (GO), and Kyoto Encyclopedia of Genes and Genomes (KEGG) pathways selected among the top 10 enriched in total BR1 microglia versus BR3 (see Methods). The distinct significantly enriched pathways by Normalized Enrichment Score (NES) in BR1 and BR3 melanoma cells were shown as red and blue bars, respectively. (C) UMAP projection of total microglia population showing cell distribution from PBS, BR1, and BR3 brains. (D) UMAP projection; clustering (left) and proportion per sample (right) of indicated microglia clusters in total microglia. (E) GSEA showing selected Hallmark, GO and KEGG top pathways enriched in each microglia cluster. (F-J) High-parametric spectral flow cytometry analysis of microglia from BR1 and BR3 bearing animals untreated or treated with anti-PD-L1 and anti-CTLA-4 combination therapy (combo). (F) Clustering on UMAP projection of indicated microglia clusters among total microglia. (G) Heatmap representing the level of expression of indicated markers (scaled by marker) for each cluster with hierarchical clustering indicated on left and markers on top. (H) Proportion of indicated microglia states in total microglia, per group. (I) Proportion of indicated microglia clusters in total microglia per group. (J) Absolute number of indicated microglia clusters per gram of brain. A-E n = 2-3/group/experiment. F-J n = 8-10/group/experiment. J data shown as mean ± SEM, n = 8-10/group/experiment. *p <0.05, **p < 0.01, ***p < 0.001, ****p < 0.00001. See also Figure S5.

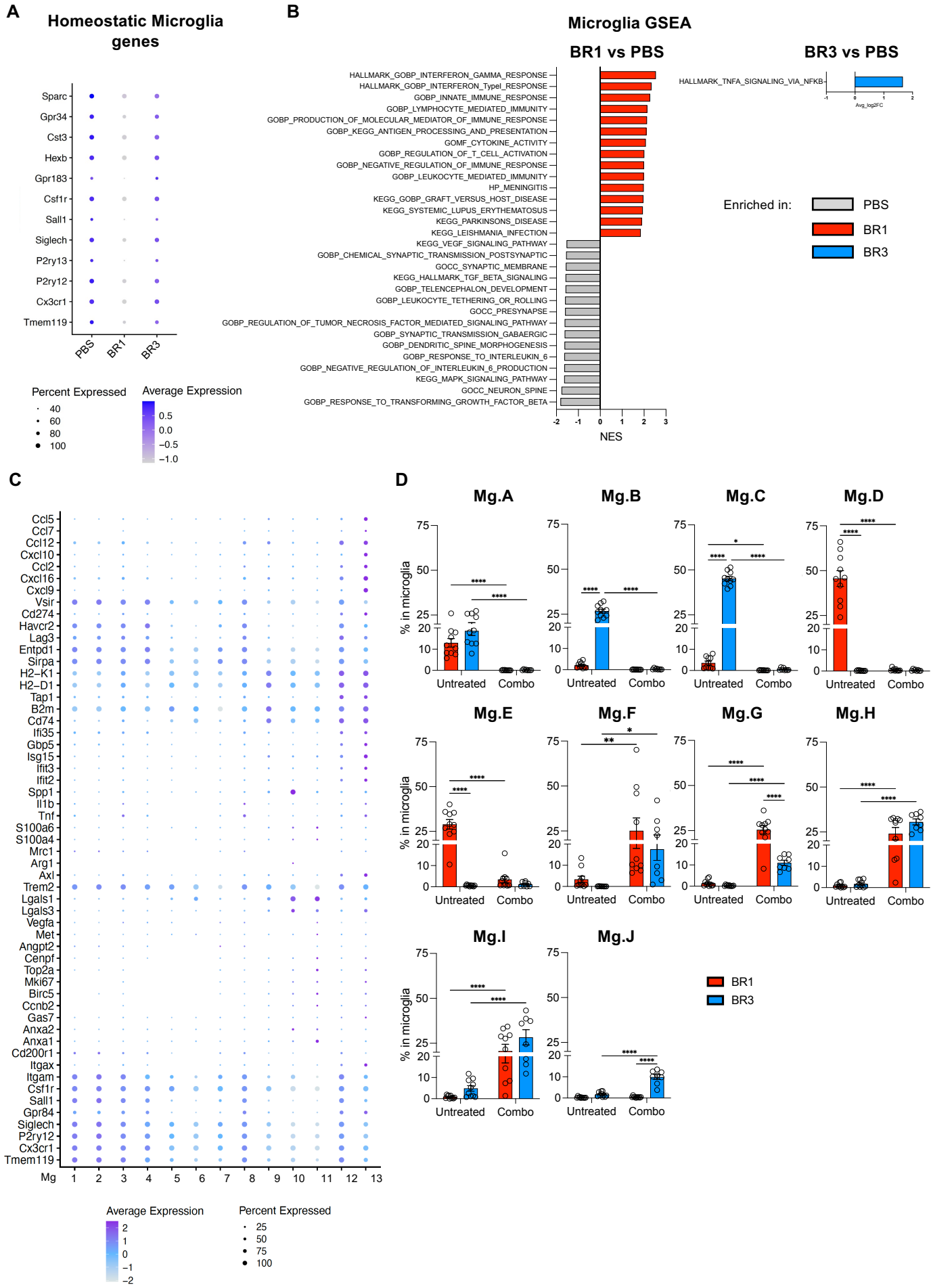
A
Homeostatic Microglia genes
Sparc
Gpr34
Cst3
Hexb
Gpr183
Csf1r
Sall1
Siglech
P2ry13
P2ry12
Cx3cr1
Tmem119
PBS
BR1
BR3
Percent Expressed
40
60
80
100
Average Expression
0.5
0.0
−0.5
−1.0
B
Microglia GSEA
BR1 vs PBS
BR3 vs PBS
HALLMARK_GOBP_INTERFERON_GAMMA_RESPONSE
HALLMARK_GOBP_INTERFERON_TypeI_RESPONSE
GOBP_INNATE_IMMUNE_RESPONSE
GOBP_LYMPHOCYTE_MEDIATED_IMMUNITY
GOBP_PRODUCTION_OF_MOLECULAR_MEDIATOR_OF_IMMUNE_RESPONSE
GOBP_KEGG_ANTIGEN_PROCESSING_AND_PRESENTATION
GOMF_CYTOKINE_ACTIVITY
GOBP_REGULATION_OF_T_CELL_ACTIVATION
GOBP_NEGATIVE_REGULATION_OF_IMMUNE_RESPONSE
GOBP_LEUKOCYTE_MEDIATED_IMMUNITY
HP_MENINGITIS
KEGG_GOBP_GRAFT_VERSUS_HOST_DISEASE
KEGG_SYSTEMIC_LUPUS_ERYTHEMATOSUS
KEGG_PARKINSONS_DISEASE
KEGG_LEISHMANIA_INFECTION
KEGG_VEGF_SIGNALING_PATHWAY
GOBP_CHEMICAL_SYNAPTIC_TRANSMISSION_POSTSYNAPTIC
GOCC_SYNAPTIC_MEMBRANE
KEGG_HALLMARK_TGF_BETA_SIGNALING
GOBP_TELENCEPHALON_DEVELOPMENT
GOBP_LEUKOCYTE_TETHERING_OR_ROLLING
GOCC_PRESYNAPSE
GOBP_REGULATION_OF_TUMOR_NECROSIS_FACTOR_MEDIATED_SIGNALING_PATHWAY
GOBP_SYNAPTIC_TRANSMISSION_GABAERGIC
GOBP_DENDRITIC_SPINE_MORPHOGENESIS
GOBP_RESPONSE_TO_INTERLEUKIN_6
GOBP_NEGATIVE_REGULATION_OF_INTERLEUKIN_6_PRODUCTION
KEGG_MAPK_SIGNALING_PATHWAY
GOCC_NEURON_SPINE
GOBP_RESPONSE_TO_TRANSFORMING_GROWTH_FACTOR_BETA
HALLMARK_TNFA_SIGNALING_VIA_NFKB
Avg_log2FC
NES
Enriched in:
PBS
BR1
BR3
C
Ccl5
Ccl7
Ccl12
Cxcl10
Ccl2
Cxcl16
Cxcl9
Vsir
Cd274
Havcr2
Lag3
Entpd1
Sirpa
H2−K1
H2−D1
Tap1
B2m
Cd74
Ifi35
Gbp5
Isg15
Ifit3
Ifit2
Spp1
Il1b
Tnf
S100a6
S100a4
Mrc1
Arg1
Axl
Trem2
Lgals1
Lgals3
Vegfa
Met
Angpt2
Cenpf
Top2a
Mki67
Birc5
Ccnb2
Gas7
Anxa2
Anxa1
Cd200r1
Itgax
Itgam
Csf1r
Sall1
Gpr84
Siglech
P2ry12
Cx3cr1
Tmem119
Mg
1 2 3 4 5 6 7 8 9 10 11 12 13
Average Expression
2
1
0
−1
−2
Percent Expressed
25
50
75
100
D
Mg.A
Mg.B
Mg.C
Mg.D
Mg.E
Mg.F
Mg.G
Mg.H
Mg.I
Mg.J
% in microglia
Untreated
Combo
BR1
BR3

Figure S5. Different microglia are found in ICB-responder and resistant BrM, related to Figure 5.

(A-C) scRNA-seq analysis of microglia from untreated BR1, BR3 and non-BrM control (PBS) brains. (A) Dot plot showing the expression of homeostatic microglia genes per group. (B) Gene set enrichment analysis (GSEA) showing Hallmark, Gene Ontology (GO), and Kyoto Encyclopaedia of Genes and Genomes (KEGG) pathways selected among the top 10 enriched in total BR1 microglia versus PBS (left) and in total BR3 microglia versus PBS (right) (see Methods). (C) Dot plot showing expression of selected genes differentially expressed between microglia clusters. (D) High-parametric spectral flow cytometry analysis of microglia from BR1 and BR3 bearing animals untreated or treated with anti-PD-L1 and anti-CTLA-4 combination therapy (combo). Proportion of indicated microglia clusters in total microglia. A-C n = 2-3/group/experiment. D n = 8-10/group/experiment. *$p < 0.05$, **$p < 0.01$, ***$p < 0.001$, ****$p < 0.00001$.

Daugherty-Lopès et al. Fig6

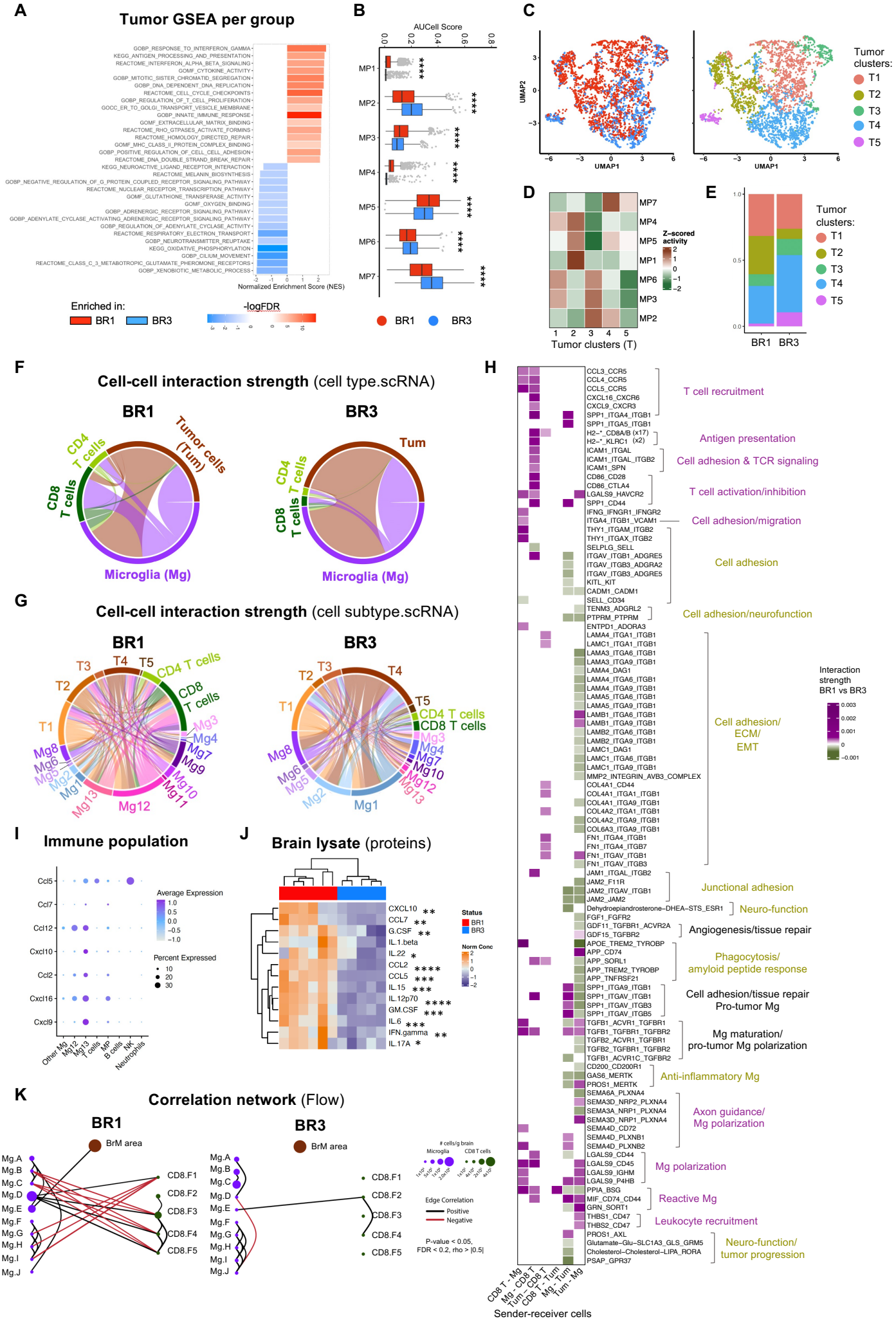

Figure 6. BrM tumor cells dictate the TME differences between ICB-responder BR1 and resistant BR3.

(A-E) scRNA-seq analysis of microglia from untreated BR1 and BR3 brains. (A) Gene set enrichment analysis (GSEA) showing selected Gene Ontology (GO), Kyoto Encyclopaedia of Genes and Genomes (KEGG) and REACTOME pathways of C2 curated datasets (see Methods). The distinct significantly enriched pathways by Normalized Enrichment Score (NES) in BR1 and BR3 melanoma cells were shown as red and blue bars, respectively. The $-Log_{10}$(FDR) value was shown as the intensity gradient. FDR, False Discovery Rate. (B) AUCell score of mouse metaprograms evaluated in malignant cells from BR1 (red) and BR3 (blue). (C) UMAP projection of total tumor cell population based on Z-scores of metaprogram activities, showing cell distribution from BR1 and BR3 brains (left) and cell cluster distribution (right). (D) Heatmap of Z-score of median activity of metaprograms (along rows) across malignant cells in each cluster (along columns). (E) Proportion per group of indicated tumor clusters in the total tumor population. (F-H) Cell-cell interaction analysis from scRNA-seq data of untreated BR1 and BR3 brains. (F-G) Circos plot showing the overall predicted interaction strength between CD8 T cells, CD4 T cells, microglia (Mg) and BrM tumor cells (Tum). The outside borders of the circos represent the sender and receiver cell populations. The width of the lines inside the circos plot indicates the interaction strength. The color of the lines indicates the sender cell population. (F) Circos showing interaction strength between each indicated cell type. (G) Circos showing interaction strength between each indicated cell subtype. (H) Heatmap showing the top and bottom 10% most differential interaction strength of ligand-receptor (L-R) pairs between BR1 versus BR3 (see methods) for each indicated cell type pair. Square and interaction family names colored in green indicate interaction stronger in BR3 versus BR1. Square and interaction family names colored in purple color indicates interactions stronger in BR1 versus BR3. Interaction family names in black indicate equal distribution between BR1 and BR3. Numbers in parentheses indicate the number of different L-R pairs. No number indicates that only one L-R pair is present. (I) Dot plot showing the expression of selected T-cell chemokines in each immune cell population. (J) Protein analysis. Cytokine/chemokine profile of whole untreated BR1 and BR3 brain lysates. Normalized measurement. (K) Correlation-based network analysis of brain metastasis (BrM) area measurement by machine learning algorithm, and microglia (Mg-A – Mg-J) and CD8 T cell clusters (CD8-F1 – CD8-F5) proportion among total leukocytes quantified from spectral high-parametric flow cytometry analysis, from untreated BR1 and BR3 brains. Purple and green circle sizes represent the number of cells per g of brain, brown circle sizes represent the BrM area in mm^2. Black and red lines respectively represent positive and negative spearman correlations.

A-I n = 2-3/group, **** $p < 0.0001$. J = 5-6/group, *$p < 0.05$, **$p < 0.01$, ***$p < 0.001$, ****$p < 0.00001$. K n = 8-10/group/experiment. See also Figure S6.

Daugherty-Lopès et al. FigS6

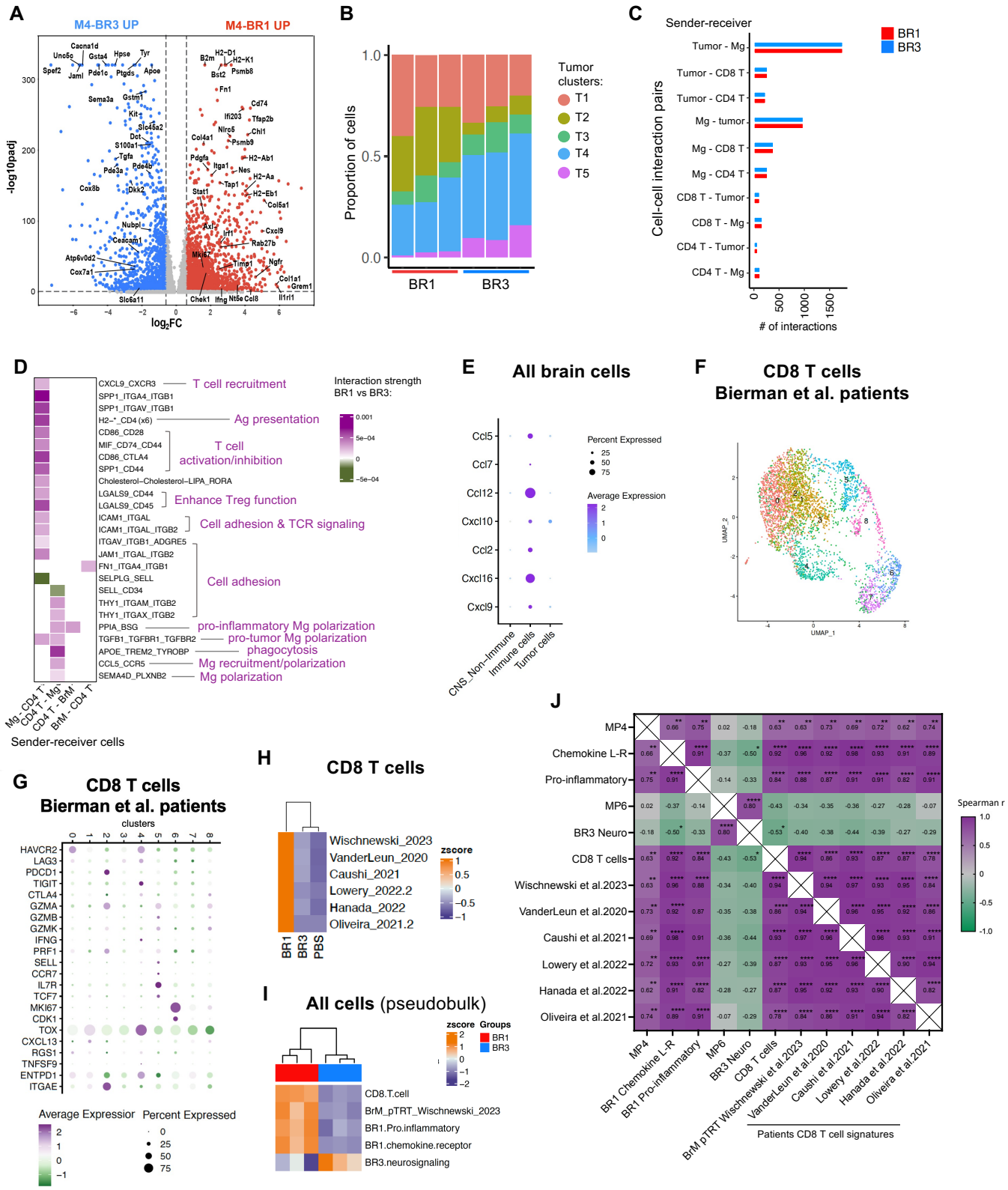

Figure S6. BR1 and BR3 tumor molecular features control BrM TME in mouse and patients
(A-B) scRNA-seq analysis of tumor cells from untreated BR1 and BR3 brains. (A) Volcano plot of BR1 versus BR3 differentially expressed genes. Significantly higher expressed genes in BR1 depicted in red and higher in BR3 depicted in blue (p-value <0.05 and average log2 fold change (Avg_log2FC)> 0.6). (B) Proportion per sample of indicated tumor clusters in the total tumor population. (C-D) Cell-cell interaction analysis from scRNA-seq data of untreated BR1 and BR3 brains. (C) Total number of interactions between the cell sender-cell receiver pairs indicated, per group. (D) Heatmap showing the top and bottom 10% most differential interaction strength of ligand-receptor (L-R) pairs between BR1 versus BR3 (see methods) for each indicated cell type pair. Square and interaction family names colored in green indicate interaction stronger in BR3 versus BR1. Square and interaction family names colored in purple color indicates interactions stronger in BR1 versus BR3. Interaction family names in black indicate equal distribution between BR1 and BR3. Numbers in parentheses indicate the number of different L-R pairs. No number indicates that only one L-R pair is present. (E) scRNA-seq analysis of all brain cells from untreated BR1 and BR3-bearing mice. Dot plot showing the expression of selected T-cell chemokines in each cell type. (F-G) scRNA-seq analysis of CD8 T cells from Biermann et al. 2022 BrM patient biopsies. (F) UMAP projection and clustering. (G) Dot plot showing the expression of selected differentially expressed T-cell markers. (H) scRNA-seq analysis of CD8 T cells from BR1, BR3 and non-tumor (PBS) bearing mice. Heatmap of Z-score expression of different published signatures described as "tumor-reactive" CD8 T cells. See supplementary table S6 for details. (I) Pseudo-bulk RNA-seq analysis of BR1 and BR3-bearing brains. Heatmap of Z-score expression of CD8 T cells, BR1, and BR3 signatures expression among total brain cells across samples. (J) Pseudo-bulk RNA-seq analysis of Sun et al. 2023 pan-cancer BrM cohort patient. Spearman correlation matrix between the different BR1 and BR3 signatures in patient biopsies.
A-E and H-I n = 2-3/group. F-G n= 10 patients. J n=17 patients. *p <0.05, **p < 0.01, ****p < 0.00001. See also Table S6.

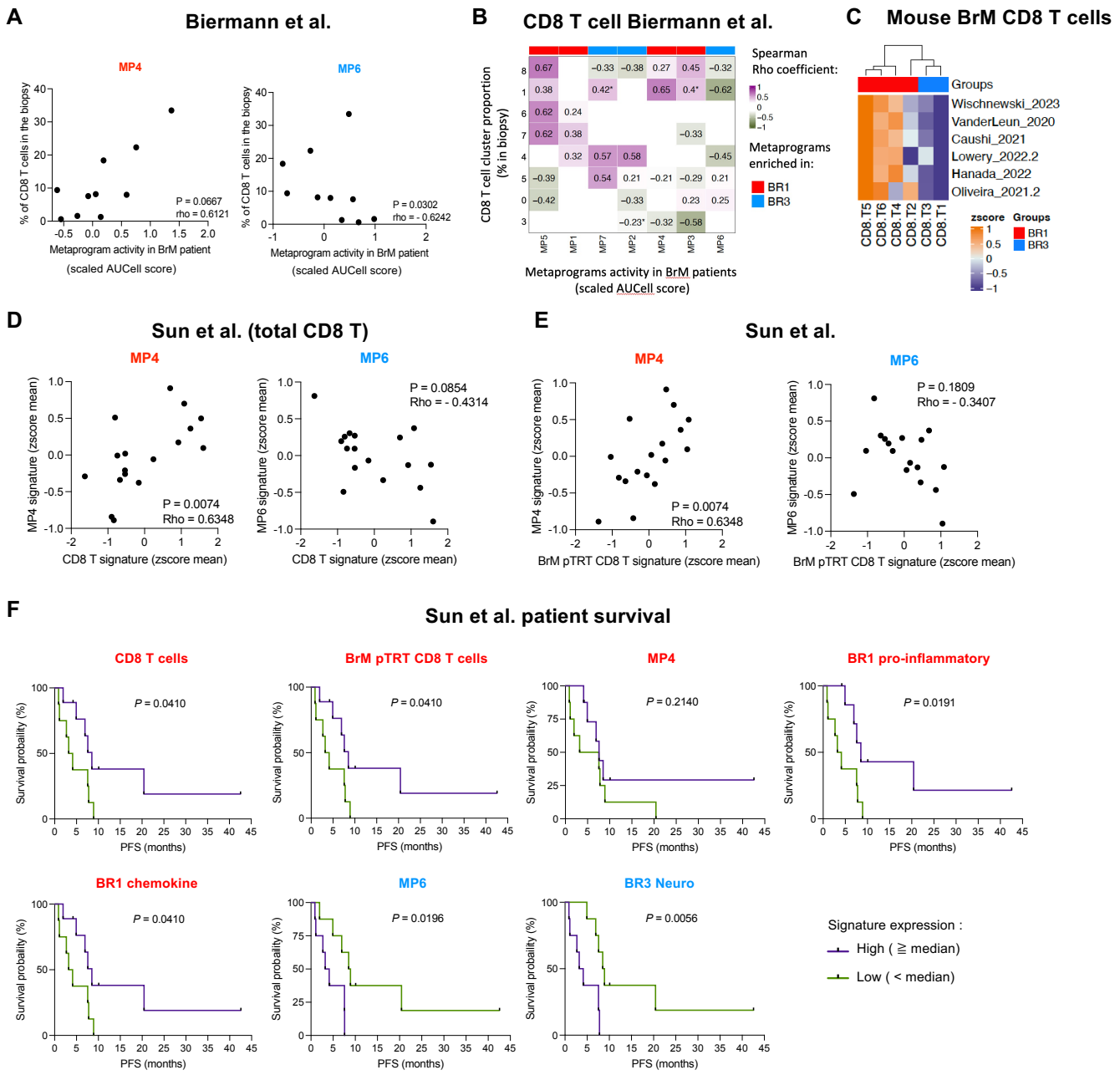
A
Biermann et al.
MP4
MP6
% of CD8 T cells in the biopsy
P = 0.0667
rho = 0.6121
P = 0.0302
rho = - 0.6242
Metaprogram activity in BrM patient
(scaled AUCell score)
B
CD8 T cell Biermann et al.
CD8 T cell cluster proportion
(% in biopsy)
Spearman
Rho coefficient:
Metaprograms
enriched in:
BR1
BR3
MP5
MP1
MP7
MP2
MP4
MP3
MP6
Metaprograms activity in BrM patients
(scaled AUCell score)
C
Mouse BrM CD8 T cells
Groups
Wischnewski_2023
VanderLeun_2020
Caushi_2021
Lowery_2022.2
Hanada_2022
Oliveira_2021.2
CD8.T5
CD8.T6
CD8.T4
CD8.T2
CD8.T3
CD8.T1
zscore
Groups
BR1
BR3
D
Sun et al. (total CD8 T)
MP4
MP6
MP4 signature (zscore mean)
MP6 signature (zscore mean)
P = 0.0074
Rho = 0.6348
P = 0.0854
Rho = - 0.4314
CD8 T signature (zscore mean)
E
Sun et al.
MP4
MP6
P = 0.0074
Rho = 0.6348
P = 0.1809
Rho = - 0.3407
BrM pTRT CD8 T signature (zscore mean)
F
Sun et al. patient survival
CD8 T cells
BrM pTRT CD8 T cells
MP4
BR1 pro-inflammatory
BR1 chemokine
MP6
BR3 Neuro
Survival probality (%)
PFS (months)
P = 0.0410
P = 0.0410
P = 0.2140
P = 0.0191
P = 0.0410
P = 0.0196
P = 0.0056
Signature expression :
High (≧ median)
Low (< median)

Figure 7. BR1 and BR3 signatures are associated with BrM patient CD8 T cell infiltration and survival.

(A-B) scRNA-seq analysis of untreated melanoma patient brain metastasis (BrM) biopsies from Biermann et al. 2022. (A) Spearman correlation of the proportion of CD8 T cells among total cells and the indicated BR1 (MP4) and BR3 (MP6) metaprogram activity in each biopsy. (B) Heatmap representing spearman correlation of the proportion of indicated CD8 T cell clusters in total CD8 T cells and the indicated BR1 (MP1, MP3, MP4, MP5) and BR3 (MP2, MP6, MP7) metaprograms activity in each biopsy. Cluster enriched in BR1 indicated in red and in BR3 in blue on top of the heatmap. (C) Heatmap of Z-score of "tumor-reactive" T cell signature expression from cancer patients (along rows) across each CD8 T cell cluster from our study (along columns). Cluster enriched in BR1 indicated in red and in BR3 in blue on top of the heatmap. (D-F) Pseudo-bulk RNA-seq analysis of untreated and treated patient pan-cancer BrM biopsies from Sun et al. 2023. (D) Spearman correlation of the expression of total CD8 T cell signature and the expression of the indicated BR1 (MP4) and BR3 (MP6) metaprogram signature in each biopsy. (E) Spearman correlation of the expression of the "potential tumor-reactive" CD8 T cells cell signature found in BrM patients (BrM pTRT) among total cells and the expression of the indicated BR1 (MP4) and BR3 (MP6) metaprogram signature in each biopsy. (F) Progression-free survival of BrM patients stratified by median expression of the indicated signatures. BR1 and BR3 signatures are indicated in red and blue respectively.

A-B n= 10 patients. C n = 2-3/group. D-F n=17 patients. See also Figure S6 and Table S6.

SUPPLEMENTARY TABLES

Table S1: Ingenuity Pathway Analysis (IPA) of mutated genes in M4, BR1 and BR3 cell lines.

Table S2: List of the genes associated to each metaprogram.

Table S3: Immune cell annotations.

Table S4: CD8 T cell cluster defining genes.

Table S5: CD4 T cell cluster defining genes.

Table S6: patient T cell signatures and BR1 and BR3 genes signatures.

METHODS

RESOURCE AVAILABILITY

Lead contact

Further information and requests for resources and reagents should be directed to and will be fulfilled by the lead contact, Romina S. Goldszmid (rgoldszmid@mail.nih.gov).

Materials availability

Cell lines generated in this study will be made available from the lead contact upon request but may require a completed Materials Transfer Agreement. It may also require payment if there is potential for commercial application.

Data and code availability.

Single-cell RNA-seq and whole exosome sequencing data generated by this study will be deposited at GEO and are publicly available as of the date of publication. This paper also analyzes existing, publicly available data. All accession numbers are listed in the key resources table and method section. Any additional information required to reanalyze the data reported in this paper is available from the lead contact upon request.

EXPERIMENTAL MODEL AND STUDY PARTICIPANT DETAILS

Animals

All animal studies were approved by the Institutional Animal Care and Use Committee of National Cancer Institute and were conducted in accordance with the IACUC guidelines at the National Institutes of Health Guide for the Care and Use of Laboratory Animals. C57BL6/J female mice were obtained from Charles River Laboratories (CRL) and were group-housed with up to 5 mice per cage, in a specific pathogen-free environment in the Center for Cancer Research (CCR) animal facility at the NCI Bethesda or the NCI Frederick. In both facilities, mice were housed under standard conditions with *ad libitum* access to food and water and under a 12/12h light/dark cycle. In all studies, 6-8 weeks-old mice were used. For experiments in which brain metastatic untreated mice were compared, the mice distribution per group was randomized to obtain similar weight per group, as weight can impact the success of the tumor implantation by intracardiac injection. Additional randomization was performed for brain metastatic therapy studies after tumor implantation but before the administration of the immunotherapy, considering the order of injection, as this factor might also influence tumor implantation.

Cell lines

M4-BR1 (BR1) and M4-BR3 (BR3) brain metastatic cell lines were generated by intracardiac (i.c.) injection of $5x10^5$ M4-B2905 (M4) cells, which originated in a hepatocyte growth factor (Hgf^{tg}) transgenic C57BL/6J male mouse as described before[29]. Successive *in-vivo* selection for homing to the brain was done for one (BR1) or three (BR3) cycles. Briefly, brains from 5-10 mice i.c. implanted were cut separately in small pieces and homogenized in 0.25% trypsin (Gibco #25200056) for less than 10 min. Whole brain homogenates were plated and maintained in culture for 2 weeks or until expanded in enough cell numbers. Successful cultures were harvested and injected i.c. again to repeat the cycle.

M4 cell line was cultured in RPMI medium supplemented with 10% FBS and 1% l-Glutamine (200 mM); BR1 and BR3 melanoma cell lines were cultured in high glucose, GlutaMAX™ supplement, HEPES DMEM medium (Gibco #10564011) supplemented with 10% heat inactivated FBS at 37°C, 5% CO_2 in air atmosphere. All cells were tested and found negative for specific mouse pathogens (MTBM test) and were confirmed as Mycoplasma negative using a Mycoplasma detection kit (Lonza, LT07-418).

Publicly available patient dataset

The single-cell read-count matrix of the single-cell RNA-sequencing (scRNA-seq) dataset from BrM patient biopsies used in this manuscript were downloaded from Gene Expression Omnibus (GEO): Smalley et al. 2021 (GSE174401) 14 melanoma patients untreated or treated with immune-checkpoint blockade (ICB) and/or targeted therapy, and/or radiotherapy (RT); Sun et al. 2023 (GSE193745), 17 pan-cancer patients untreated or treated with ICB and/or targeted therapies and/or RT. Alvarez-Breckenridge et al. 2023, was downloaded from Broad Single Cell Portal (SCP1493) and composed of 27 melanoma patients untreated or treated with ICB and/or targeted therapies and/or RT. Biermann et al. 2022 (GSE200218), single-nucleus RNA-seq from 25 untreated melanoma patients (15 BrM biopsies and 10 extra-BrM biospies) were downloaded from GEO.

Experimental brain metastasis

C57BL/6J mice were shaved at the chest and intracardially (i.c.) injected with $5x10^5$ BR1 cells or $7.5x10^4$ BR3 cells per mouse. Animals were kept under anesthesia (2-3% isoflurane in oxygen) and continuous monitoring during the whole procedure. The endpoint of the model was set when the animal weight loss reached 5% of the initial weight and/or any behavior changes were observed such as shortness of breath or slow motion, and was reached around 18-20 days after i.c. injection. When, in

some rare cases, animals did not show any brain metastasis implantation at endpoint, they were excluded from the study.

Immune checkpoint inhibitor treatment

To test and compare ICB monotherapy and combination efficacy between the models we implanted BR1 and BR3 cells by ultrasound-guided intracardiac injection. Mice were treated with monotherapy anti-CTLA-4 (BioXcell, BP0164) and anti-gp120 IgG1 isotype control (BioXcell, BE0154), or anti-PD-L1 (Genentech, clone 6E11) and anti-IgG2b isotype control (BioXcell, BP0086), or anti-CTLA-4 and anti-PDL-1 combination therapy, or a mix of anti-gp120 IgG1 and anti-IgG2b isotype control, or with PBS as a supplementary control. Anti-CTLA-4 and anti-IgG2b antibodies were administered twice per week for a total of 4 doses. The first dose was administered intravenously (IV) at 200mg per mouse, and the following 3 doses were administered intraperitoneally (IP) at 200mg per mouse. Anti-PD-L1 and anti-gp120 IgG1 antibodies were administered twice per week for a total of 5 doses. The first dose was administered intravenously (IV) at 200mg per mouse, and the following 4 doses were administered intraperitoneally (IP) at 100mg per mouse. Depending on the studies this treatment regimen started 3 days or 7 days post-tumor implantation.

Tissue collection

Mice were euthanized in CO_2 chambers following the American Veterinary Medical Association (AVMA) guidelines at endpoint or as indicated for kinetic studies (4, 8 or 12 days after ic. injection). Mice were then intracardially perfused with 20 mL of ice-cold 1X PBS supplemented with 2 mM EDTA. Lungs, thymus, livers, kidneys, adrenal glands, digestive and reproductive ducts were harvested, fixed for 24h in 10% formalin at room temperature, and then kept in ethanol 70% at room temperature until metastasis quantification. Brains were harvested, immediately imaged using a stereomicroscope, and prepared for immunohistochemistry, immunophenotyping, or single-cell RNA-sequencing (scRNA-seq) experiments.

Microscopy imaging

Macroscopic whole-brain pictures were acquired using a Leica M165 FC stereomicroscope (LEICA, USA) equipped with a Leica LED5000 ring light illumination (RL-80/40) and a digital color FLEXACAM C1 camera, as previously described[32]. Briefly, two pictures per brain were acquired: the whole ventral surface and the whole dorsal surface, at 4X magnification using the camera set on brightfield. Pictures focusing on individual brain metastases were acquired using the same microscopic platform and settings but at 12.5X magnification. All images were acquired with the Leica Application Suite X (LAS X) software, version 5.1.0.

Metastasis burden quantification

Extracranial metastasis burden was assessed by manual counting on fresh organs using a SMZ745T Nikon (Nikon, USA) stereomicroscope trinocular system at 2-4X magnification range. Brain metastasis burden was assessed using a machine learning algorithm that we developed to detect, count and measure size of each metastatic lesions and total metastatic area on whole brain LEICA stereomicroscope pictures, as previously described[32] using the software QuPath[121].

Colony formation assay

BR1, BR3-BrM bearing, and PBS (non-tumor bearing controls) brains were harvested at 4 days post-ic injection (as described above) and were processed using Adult Brain Dissociation Kit (Miltenyi, #130-107-677) following the manufacturer's instruction. Each single cell suspension obtained were seeded in duplicate in 6-well plates and cultured in high glucose, GlutaMAX™ supplement, HEPES DMEM medium (Gibco #10564011) supplemented with 10% heat inactivated FBS and 50 mg/mL of gentamicin, at 37°C, 5% CO_2 in air atmosphere. Media was renewed and dead cell remove every 2 days. After 10 days, the cells were washed with 1X PBS, fixed for 5 min at room temperature in ice cold methanol (VWR Chemicals, 85800.290P), washed with 1X PBS and then stained with a 2.3% crystal violet solution (Sigma-Aldrich, HT90132). After removing the excess stain, the cells were washed in molecular biology water (Vita scientific, 351-029-101) and the well were air-dried overnight at room temperature and protected from light. The wells were then imaged using a Nikon D90 camera (Nikon, USA) and single colonies were counted using Image J software.

Histology and Immunohistochemistry

Formalin-fixed and paraffin-embedded 5µm sagittal or longitudinal sections of brains from BR1 or BR3 BrM-bearing mice or injected with PBS as non-BrM control were stained with hematoxylin and eosin (HE) or DCT (Pep8h58[122]) antibody using standard immunohistochemistry methods. Antigen retrieval was performed at 95ºC for 20 minutes in a pressure cooker using target retrieval buffer pH6 (Dako, S1699). Protein Blocking reagent (Dako, X0909) and Bloxall blocking solution (Vector, SP-6000-100) were used to block nonspecific proteins and endogenous peroxidase and alkaline phosphatase activities following provider recommendations. DCT antibody (dilution 1:5000) was incubated overnight at 4˚C in a humidity chamber. Antibody detection was performed using Impress AP Reagent anti-rabbit Ig (Vector, MP-5401) and ImPACT Vector Red (Vector, SK-5105) following provider protocol. Slides were counterstained with Mayer's Hematoxylin (Electron Microscopy Sciences, 26043-06) and GIEMSA (New Comer Supply, 1120A)) for 2-5 minutes each at RT. Slides were counterstained with Mayer's Hematoxylin (Electron Microscopy Sciences, 26043-06) and

GIEMSA (New Comer Supply, 1120A) for 2-5 minutes each at RT. Whole slides were scanned using an AT2 Leica scanner (Leica, USA) at 20X magnification and digital image files were visualized using HALO link (Indica labs).

Whole exome sequencing of brain metastatic cell lines

Mouse genomic DNA concentration was measured using Quant-iT PicoGreen dsDNA Assay Kit (Thermofisher scientific, P11496).200ng of DNA was sheared by Covaris Instrument (E210) to ~150-200bp fragments. Shearing was done in a Covaris snap cap tube (microTUBE Covaris p/n 520045) with the following parameters: duty cycle, 10%; intensity, 5; cycle burst, 200; time, 360 seconds at 4°C. Samples quality assessment/size was validated by Bioanalyzer DNA-High sensitivity kit (Agilent # 5067-4626).

Agilent SureSelectXT library prep ILM Kit (Agilent Technologies, #G9611A) was used to prepare the library for each sheared mouse DNA sample. DNA fragment's ends were repaired, followed by Adenylation of the 3' end and then ligation of paired-end adaptor. Adaptor-ligated libraries were then amplified (Pre-capture PCR amplification: 98°C 2 minutes, 10 cycles; 98°C 30 seconds; 65°C 30 seconds; 72°C 1 minute; then 72°C 10 minutes, 4°C hold) by Herculase II fusion enzyme (Agilent Technologies, #600679). After each step DNA was purified by Ampure XP beads (Beckmann Coulter Genomics #A63882). DNA Lo Bind Tubes, 1.5mL PCR clean (Eppendorf # 022431021) or 96 well plates were used to process the samples.

Samples were analyzed by bioanalyzer using DNA-1000 kit (Agilent #5067-1504). Concentration of each library was determined by integrating under the peak of approximately 225-275bp. Then each gDNA library (~750-1000ng) was hybridized with biotinylated mouse specific capture RNA baits (SureSelectXT Mouse All Exon, catalog #5190-4641, 16 reactions) in the presence of blocking oligonucleotides. Hybridization was done at 65°C for 16 hours using SureSelectXT kit reagents. Bait-target hybrids were captured by streptavidin-coated magnetic beads (Dynabeads MyOne Streptavidin T1, Life Technologies, #6560) for 30 minutes at room temperature. Then after a series of washes to remove the non-specifically bound DNA, the captured library was eluted in nuclease free water and half volume was amplified with individual index (Post-capture PCR amplification: 98°C 2 minutes; 10 cycles, 98°C 30 seconds; 57°C 30 seconds; 72°C 1 minute; then 72°C 10 minutes, 4°C hold). The Bioanalyzer High sensitivity kit was used to validate the size of the libraries prior to sequencing. The libraries were sequenced in a NovaSeq S2-300 chip.

Single nucleotide variant (SNV) analysis

Fastq sequence reads were mapped to the mouse reference genome mm10 (https://www.ncbi.nlm.nih.gov/datasets/genome/GCF_000001635.20) with BWA or Bowtie. Single nucleotide variants (SNV) were identified using samtools mpileup or GATK HaplotypeCaller. Mouse germline single nucleotide polymorphisms (SNPs) were filtered out using the Sanger Mouse Genomes Project database for variants identified from whole genome sequencing of 36 mouse strains (ftp://ftp-mouse.sanger.ac.uk/current_snps/mgp.v5.merged.snps_all.dbSNP142.vcf.gz). Variants with a Phred-scaled quality score of <30 were removed. Variants that are present in normal spleen samples (in-house collection) were also removed. Variants were annotated with Annovar software to identify non-synonymous mutations. All analyses were carried out on NIH biowulf2 high performance computing environment. Statistical analysis was carried out in R environment.

For pathway analysis of the genes mutated in each cell line we used Ingenuity Pathway Analysis (QIAGEN Digital Insights). For comparison with human BrM we selected 21 genes involved in MAPK and PI3K/mTOR pathways that were mutated in at least one of the BR cell lines and retrieved mutation data from cBioportal (https://www.cbioportal.org/). We used MSK MetTropism data set[35] selecting the samples from metastatic cutaneous melanoma patients and sorted the data in three groups: 1) brain metastases (BrM), 2) all other extracranial metastases, and 3) primary melanomas from patients with BrM. The heatmaps were generated using R package Ggplot2.

Flow cytometry on leucocytes

For immunophenotyping experiments, freshly harvested brains were processed to obtain single-cell suspension following a previously described protocol[123] with some adaptations. Briefly, whole brain tissues were mechanically disrupted using a dounce homogenizer in plain RPMI media. Brain leukocytes were enriched by a 70%/30% Percoll gradient centrifugation and then washed in 10 mL of 1X PBS. After centrifugation. Single cell suspensions were resuspended in 1X PBS and stained with LIVE/DEAD™ Fixable Dead Cell Stain Kit (Invitrogen). FC receptors were blocked with anti-CD16/32 antibody (2.4G2, BioXcell) and the cell suspensions were successively stained in Brilliant Stain Buffer (BD Biosciences) with one or a combination of the following anti-mouse antibodies: Ly6G (1A8, BD Biosciences) , P2RY12 (S16007D, Biolegend), Sirpα (P84, BD Biosciences), CD86 (GL1, BD Biosciences), CD4 (GK1.5, BD Biosciences), CD45.2 (104, BD Biosciences), CD11b (M1/70, BD Biosciences), CX3CR1 (SA011F12, Biolegend), CD8α (MCD0826, ThermoFisher scientific), Arg1 (A1exF5, ThermoFisher scientific), MHCII (M5/114.15.2, BD Biosciences), CD103 (M290, BD Biosciences), CD62L (MEL-14, Biolegend), PD1 (J43, BD Biosciences), CD24 (M1/69, BD Biosciences), PD-L1 (MIH5, BD Biosciences), SiglecH (440C, BD Biosciences), CD64 (X54-

5/7.1, BD Biosciences), TMEM119 (106-6, abcam), CD3 (17A2, Biolegend), CD68 (FA-11, Biolegend), CD49d (9C10, BD Biosciences), LAG3 (ebioC9B7W, Invitrogen), CD44 (IM7, Biolegend), FOXP3 (FJK.16s, Invitrogen), CD69 (H1.2F3, Biolegend), CD25 (PC1, Biolegend), NK1.1 (PK136, Biolegend), CD11c (N418, ThermoFisher scientific), CD39 (Duha59, Biolegend), MertK (DS5MMER, ThermoFisher scientific), Tim3 (RMT4-54, BD Biosciences), F4/80 (BM8, Invitrogen), Ly6C (AL-21, BD Biosciences), CD52 (4C8, BD Biosciences), CD19 (6D5, Biolegend). When unlabeled primary rabbit antibodies or biotinylated antibodies were used, cells were subsequently incubated with anti-rabbit IgG antibodies or fluorochrome-conjugated streptavidin. For intracellular staining, the cell suspension was fixed and permeabilized with the eBioscience™ FOXP3/Transcription Factor Staining Buffer Set (eBioscience) after the cell surface staining, following the manufacturer's instruction.

The cell suspension was then filtered through a 40 mm filter and each sample was acquired using the spectral flow cytometer Cytek® Aurora (5 lasers, 5L UV-V-B-YG-R) and the SpectroFlo® software (v.3.3.0) (Cytek® Biosciences). For data analysis initial gating strategy were performed as previously described[124] with FlowJo software (v.10.10.0): (1) FSC-A versus SSC-A to exclude debris; (2) FSC-A versus FSC-H to select singlet; (3) SSC-A versus Live/Dead for dead cell exclusion; (4) SSC-A versus CD45 to select $CD45^+$ leukocytes. They were then followed by unsupervised high parametric analysis using Spectre package[125] (v.1.0.0) on R software (v.4.2.1). Uniform Manifold Approximation and Projection (UMAP) and density UMAP was run with a concatenation of all samples per group simultaneously. For cluster analysis, Rphenograph was selected (k= 25-45) and the clusters were annotated based on expression level of the markers of interest. Cell populations were defined as indicated in Supplementary Table S3. Frequencies of total leukocytes and subpopulations were determined using FlowJo and Spectre respectively and total leukocytes and subpopulation absolute numbers per g of brain were calculated. Principal component analysis (PCA) was performed in R using the singular value decomposition and visualized using GraphPadPrism (v.10.2.3). Spearman correlation network between CD8 T cell subsets, microglia subsets and brain metastatic area were calculated within each group using the R package Hmisc_5.1.0 and multiple hypothesis correction was performed using FDR. Correlations that passed p-value < 0.05, FDR < 0.2, spearman rho > |0.5| were visualized using the R package igraph_1.5.1.

Single-cell RNA sequencing (scRNAseq) of mouse BrM

- **Brain dissociation, cell capture and sequencing**

Single cell suspension from BR1 or BR3-BrM bearing or PBS (non-implanted controls) brains were obtained using Adult Brain Dissociation Kit (Miltenyi, #130-107-677) following manufacturer's protocol. Library preparation, captures and sequencing were performed by Single Cell Analysis Facility (SCAF, CCR, NCI). The sample concentration and viability were assessed using the LunaFx7 fluorescent cell counter. The cellular samples were loaded in the lanes according to the 10X Genomics 3' v3.1 Single Cell User Guide with a single capture lane per sample targeting recovery of up to 6,000 cells per lane. Cell partitioning completed successfully with uniform emulsion consistency and the reverse transcription PCR was run overnight. All subsequent steps and quality control was performed as described in the 10X Genomics 3' v3.1 Single Cell User Guide. Two NovaSeq runs for GEX were performed: NovaSeq 2k S1 100-cycle and NovaSeq 6k S1 100-cycle.

- **ScRNA-seq data preprocessing (10x chromium single cell 3' v3) and analysis**

10x Genomics Cell Ranger (v.7.0.1) was used to perform demultiplexing, alignment to mouse reference mm10 (refdata-gex-mm10-2020-A), gene and transcript quantification. The parameters –include-introns –force-cells were applied in Cell Ranger count step. Seurat (v.4.2.0)[126] was used for preprocessing, normalization and clustering. Genes detected in fewer than 3 cells and cells containing less than 100 genes were removed from the data sets prior to further filtering. Doublets and background cells were filtered based on negative binomial distribution to determine the upper and lower limit of UMI count per cell (9-93,348) and gene count per cell (33-16,472). Mitochondrial percentages in cells were calculated in Seurat, we set up the filtering threshold as 15.46% (median + 4 x median absolute deviation), cells with higher mitochondrial expression than the selected threshold were filtered out. After removing unwanted cells from the dataset, the data was normalized by SCTransform from Seurat. Seurat RunPCA and ElbowPlot were used to find the optimal number of principal components (PCs), Seurat FindClusters function was called to use the first 20 PCs at the resolution of 0.6 and identified 37 distinct cell clusters. Uniform manifold approximation and (UMAP)[128] was used for data visualization in two-dimensional space. These upstream analyses were performed by CCR-SF Bioinformatics Team (NIH-CCR).

Then all downstream analysis were performed using Seurat package (v.5.1.0)[130] in R software. Cell type identifications were performed using the reference cell type gene expression databases: Allen brain atlas (https://portal.brain-map.org/), Immgen (https://www.immgen.org/) and PanglaoDB (https://panglaodb.se/) and the automated annotation algorithm: Azimuth (https://azimuth.hubmapconsortium.org/) and SC_Type[132].

Re-clusterings on immune cell subsets were performed using FindNeighbors (dimension 1:30) and FindClusters (resolution 0.5), and visualized using RunUMAP (dimension 1:30). Cluster specific genes were identified using the FindMarkers function with a fold change of > 0.25. Re-clustering for immune cells analysis were performed following the same approach. Re-clustering on tumor cells were performed using non-negative matrix (NMF) as described in the next section. For all immune cell analysis, the differentially expressed genes (DEGs) between groups and cluster was performed using the FindMarkers function (p_adj < 0.05 and Avg_Log2FC > 0.25). For volcano plot the thresholds of significance used were: p_adj < 0.05 and Avg_Log2FC > 0.5 For melanoma cells the DEGs between BR1 and BR3 groups were analyzed using MAST (Model-based Analysis of Single-cell Transcriptomics)[71]. Log_2 values of BR1 vs. BR3 fold change of gene expression levels (Log_2FC) and Log_{10} of p values of t-test ($-Log_{10}$p-value) were analyzed to make the volcano plot. The threshold of significance used is $Log_2FC > 0.6$ and $p < 0.05$. Gene Set Enrichment Analysis (GSEA) (https://www.gsea-msigdb.org/gsea/index.jsp) were then performed and using GO, KEGG and Hallmark for microglia (group comparison and clusters), and using Gene Ontology (GO), Kyoto Encyclopedia of Genes and Genomes (KEGG) and REACTOME datasets for melanoma BrM cells, The top pathways determined by the highest Normalized Enrichment Score (NES) were used to select those represented on the figures.

Non-negative matrix factorization and metaprogram discovery

We retained genes expressed in at least 1% of all malignant cells from both BR1 and BR3 mouse models and ran a fast NMF implementation[39] separately on malignant cells from each model with no L1 or L2 penalty specified. We chose to obtain 30 factors for cells from each mouse model based on the change in reconstruction error of the gene expression matrix as the number of factors was increased. For a given NMF run within BR1 or BR3 models, we prioritized genes that contributed to each factor using a two-step procedure. We first z-scored the loadings of each gene across all factors and for a given factor, retained those genes with z > 1.5. Second, for a given factor, we computed the Spearman correlation coefficient of all gene pairs and used those pairs whose correlation was greater than 0.4 and constructed a gene co-expression graph. The final prioritized gene list (referred to as prioritized genes) consists of only those genes in the largest component of the co-expression graph. Any factor with less than ten prioritized genes is discarded. For each factor, we then use AUCell[134] to score the activity of prioritized genes across malignant cells from both the mouse models and compute the Pearson correlation coefficient between all pairs of factors including both models. We hierarchically clustered the factors based on the inter-factor correlations and grouped all factors into eight clusters or metaprograms (this number maximized the Silhouette coefficient of the clustering). Within each

metaprogram, we only retained those genes that were present in at least 25% of all constituent factors. The metaprograms that were active (based on the Global_k1 AUCell threshold) in less than 10% of cells from each model were discarded. This procedure yielded seven metaprograms spanning the cells in the two mouse models. Each metaprogram functional implication was characterized by pathway analysis using Metascape[43].

Since NMF factorizations are non-unique i.e., can yield different factors when re-run, we repeated the above procedure 100 times. For each run, we trained a logistic regression classifier to distinguish BR1 and BR3 tumor cells (using five-fold cross-validation) based on the metaprograms obtained from the procedure outlined above and computed its area under the ROC (auROC) value. We chose this criterion to ensure that our pipeline to derive metaprograms from an NMF run is able to capture differences between BR1 and BR3 models. The metaprograms derived in this paper were based on the NMF run whose auROC (auROC = 0.927) was the median auROC value amongst all NMF runs.

To cluster all malignant cells, we first scored the activity of these seven metaprograms using AUCell. We then z-scored each metaprogram activity across all cells and constructed a k-nearest neighbor graph (k=30) based on the seven z-scores for each cell. The Mahalanobis distance was used to compute distances between cells for neighborhood graph construction as this distance metric takes into account potential correlations between metaprogram scores. We ran 100 parallel iterations of Louvain clustering (with a resolution of 0.4) on this graph and kept the clustering with the highest Silhouette coefficient (where cell-cell distances were computed using the Mahalanobis distance metric). For visualization, we computed UMAP coordinates of each malignant cell based on the activity across the seven metaprograms.

Correlation analysis of mouse tumor metaprograms with tumor metaprograms derived in Biermann et. al

We used AUCell to compute the activity of our metaprograms as well as metaprograms derived by Biermann et al. 2022 in every malignant cell from Biermann et al. 2022, Smalley et al. 2023, Alvarez-Breckenridge et al. 2023. We then computed the pair-wise Spearman correlation coefficient between every mouse metaprogram and every Biermann et al. 2022 metaprogram across cells in each tumor biopsy. Within a given cohort, the median correlation coefficients computed for a given pair of metaprograms across all tumors was retained for further analyses. A metaprogram pair was considered to be significantly and positively correlated within a cohort if the set of tumor-wise correlations were significantly above 0.2 (Wilcoxon one-sided p-value < 0.05). We then counted the number of cohorts

in which a metaprogram pair were significantly positively correlated and only visualized those that were correlated in at least one cohort.

Cell-cell interaction discovery using Cellchat

We used Cellchat[136] to infer cell-cell communications between microglia, CD4 T cells, CD8 T cells and malignant cells in BR1 and BR3 samples separately. Given the relatively lower numbers of CD4 and CD8 T cells in the data, we grouped all sub-clusters of those two cell types while keeping CD4 and CD8 T cells separated and detected interactions between them and sub-clusters of microglia and up-regulated ($p_adj < 0.05$) in the sender and receiver cell type, respectively and (b) the ligand and receptor were expressed in at least 10% of cells in the sender and receiver cell type, respectively. Interactions amongst the top 10% most different in strength (which is defined by Cellchat as the product of ligand and receptor expression in sender and receiver cell types and weighted by the proportion of cells in each cell type) between BR1 and BR3 was labelled as either BR1-specific or BR3-specific.

Whole metastatic brain protein expression

Brain hemispheres were mechanically disrupted in 500 µL ProcartaPlex™ cell lysis buffer (ThermoFisher scientific, EPX-99999-000) for every 100mg of tissue, using an Omni Tissue Master 125 Homogenizer (Omni international). Supernatants were extracted and total concentration of protein was measured using the Pierce™ BCA Protein Assay Kit (ThermoFisher scientific, 23227). Samples were diluted to 10mg/mL protein with PBS and cytokines concentration were measured using the ProcartaPlexTM Mouse Cytokine & Chemokine Panel 1A, 36plex (ThermoFisher scientific, EPX360-26092-901) according to manufacturer's instructions.

Patient single-cell transcriptomic analysis on T cells

The single-cell read-count matrix of Biermann et al.2022 dataset were processed using Seurat (v4.3.0) [130].We chose only brain metastatic biopsies and normalized read counts using the NormalizeData function. The 5000 most variable genes were chosen to compute 50 principal components, which were then clustered using the FindClusters function (with a resolution of 0.8). We then subset the data to those clusters with high expression of CD45 for re-analysis. Based on the expression of *CD3D*, *CD3E*, *NCR1*, *CD8A*, *CD8B*, *CD4*, *GZMA*, *GZMB*, *IFNG*, *GZMK*, *PRF1*, *ITGAM*, *ITGAX*, *CD14*, *NCAM1*, *FCGR3A*, *P2RY12*, *HBB*, we separated lymphoid cells from other CD45+ sub-populations. We then retained only those samples from BrM patients (n=15) with at least 50 lymphoid cells (resulting in a set of cells from 10 patients) and carried out batch-correction and integration in Seurat (using 30 PCs and k.weight = 50). The expression of *HAVCR2*, *LAG3*, *PDCD1*, *TIGIT*, *CTLA4*, *GZMA*, *GZMB*,

GZMK, *IFNG*, *PRF1*, *SELL*, *CCR7*, *IL7R*, *TCF7*, *MKI67*, *CDK1*, *CD45RO*, *TOX*, *CXCL13*, *RGS1*, *TNFSF9*, *ENTPD1*, *ITGAE* was used to annotate all CD8 T-cell subclusters.

Patient bulk-RNA sequencing and survival analysis

To yield a single gene expression vector for each biopsy in Sun et al. 2023 dataset, bulk RNA expression was calculated per sample by summing counts for all cells using the AggregateExpression function from the R package Seurat[130](v.5.0.1). Counts were normalized per sample using log2(CPM+0.001). Mouse metaprogram genes were converted to human homologs using R software and the Jackson laboratory database (http://www.informatics.jax.org/downloads/reports/HOM_MouseHumanSequence.rpT); genes without direct homologs or that were not contained in the dataset was omitted from signature calculations. Z-scores were calculated for genes of interest across all samples and mean z-score for each gene signatures were performed. Spearman correlation between the different Z-score signature in patients were performed using GraphPadPrism. For survival analysis: for each signature, patients were separated based on median into High (≥ median) and Low (< median) expression. Log-rank (Mantel-Cox) test was performed to calculate the correlation of the gene signature expression and the patient progression free survival after surgery, and p-value reported using GraphPadPrism.

QUANTIFICATION AND STATISTICAL ANALYSIS

Statistical analysis

Statistical analyses were performed using GraphPadPrism or R. Data were analyzed for normal distribution prior to comparisons. Outliers were detected using ROUT' test and excluded from the analysis. Values are presented as the mean ± SEM; individual values (representing individual samples when non indicated or individual experiment when indicated) are presented as scatterplots with column bar graphs or box plot. Data in pie charts represent mean of samples in group. Statistical significance between two groups was determined by two-tailed unpaired Student's t test (parametric) or Mann-Whitney (non-parametric). For the comparison of multiple groups, comparing different treatment in one unique model, one-way ANOVA followed by Tukey's multiple comparison correction test (parametric) or Mann-Whitney (non-parametric) followed by Dunn's multiple comparison correction test were used). For the comparison of multiple groups, comparing BR1 and BR3 in untreated and treated conditions, two-way ANOVA followed by Tukey's multiple comparison correction test (parametric) or Mann-Whitney (non-parametric) followed by Dunn's multiple comparison correction test were used.

REFERENCES

1. Sperduto, P.W., Mesko, S., Li, J., Cagney, D., Aizer, A., Lin, N.U., Nesbit, E., Kruser, T.J., Chan, J., Braunstein, S., et al. (2020). Survival in Patients With Brain Metastases: Summary Report on the Updated Diagnosis-Specific Graded Prognostic Assessment and Definition of the Eligibility Quotient. J Clin Oncol *38*, 3773–3784. https://doi.org/10.1200/JCO.20.01255.

2. Bander, E.D., Yuan, M., Carnevale, J.A., Reiner, A.S., Panageas, K.S., Postow, M.A., Tabar, V., and Moss, N.S. (2021). Melanoma brain metastasis presentation, treatment, and outcomes in the age of targeted and immunotherapies. Cancer *127*, 2062–2073. https://doi.org/10.1002/cncr.33459.

3. Long, G.V., Atkinson, V., Lo, S., Sandhu, S., Guminski, A.D., Brown, M.P., Wilmott, J.S., Edwards, J., Gonzalez, M., Scolyer, R.A., et al. (2018). Combination nivolumab and ipilimumab or nivolumab alone in melanoma brain metastases: a multicentre randomised phase 2 study. The Lancet Oncology *19*, 672–681. https://doi.org/10.1016/S1470-2045(18)30139-6.

4. Tawbi, H.A., Forsyth, P.A., Hodi, F.S., Algazi, A.P., Hamid, O., Lao, C.D., Moschos, S.J., Atkins, M.B., Lewis, K., Postow, M.A., et al. (2021). Long-term outcomes of patients with active melanoma brain metastases treated with combination nivolumab plus ipilimumab (CheckMate 204): final results of an open-label, multicentre, phase 2 study. The Lancet Oncology *22*, 1692–1704. https://doi.org/10.1016/S1470-2045(21)00545-3.

5. Tawbi, H.A., Forsyth, P.A., Algazi, A., Hamid, O., Hodi, F.S., Moschos, S.J., Khushalani, N.I., Lewis, K., Lao, C.D., Postow, M.A., et al. (2018). Combined Nivolumab and Ipilimumab in Melanoma Metastatic to the Brain. N Engl J Med *379*, 722–730. https://doi.org/10.1056/NEJMoa1805453.

6. Tawbi, H.A., Forsyth, P.A., Hodi, F.S., Lao, C.D., Moschos, S.J., Hamid, O., Atkins, M.B., Lewis, K., Thomas, R.P., Glaspy, J.A., et al. (2021). Safety and efficacy of the combination of nivolumab plus ipilimumab in patients with melanoma and asymptomatic or symptomatic brain metastases (CheckMate 204). Neuro Oncol *23*, 1961–1973. https://doi.org/10.1093/neuonc/noab094.

7. Brastianos, P.K., Kim, A.E., Giobbie-Hurder, A., Lee, E.Q., Lin, N.U., Overmoyer, B., Wen, P.Y., Nayak, L., Cohen, J.V., Dietrich, J., et al. (2023). Pembrolizumab in brain metastases of diverse histologies: phase 2 trial results. Nat Med *29*, 1728–1737. https://doi.org/10.1038/s41591-023-02392-7.

8. Quail, D.F., and Joyce, J.A. (2017). The Microenvironmental Landscape of Brain Tumors. Cancer Cell *31*, 326–341. https://doi.org/10.1016/j.ccell.2017.02.009.

9. Aili, Y., Maimaitiming, N., Qin, H., Ji, W., Fan, G., Wang, Z., and Wang, Y. (2022). Tumor microenvironment and exosomes in brain metastasis: Molecular mechanisms and clinical application. Front. Oncol. *12*. https://doi.org/10.3389/fonc.2022.983878.

10. Caffarel, M.M., and Braza, M.S. (2022). Microglia and metastases to the central nervous system: victim, ravager, or something else? J Exp Clin Cancer Res *41*, 1–13. https://doi.org/10.1186/s13046-022-02535-7.

11. Arvanitis, C.D., Ferraro, G.B., and Jain, R.K. (2020). The blood–brain barrier and blood–tumour barrier in brain tumours and metastases. Nat Rev Cancer *20*, 26–41. https://doi.org/10.1038/s41568-019-0205-x.

12. Wu, D., Chen, Q., Chen, X., Han, F., Chen, Z., and Wang, Y. (2023). The blood-brain barrier: structure, regulation, and drug delivery. Signal Transduct Target Ther *8*, 217. https://doi.org/10.1038/s41392-023-01481-w.

13. Biermann, J., Melms, J.C., Amin, A.D., Wang, Y., Caprio, L.A., Karz, A., Tagore, S., Barrera, I., Ibarra-Arellano, M.A., Andreatta, M., et al. (2022). Dissecting the treatment-naive ecosystem of human melanoma brain metastasis. Cell *185*, 2591-2608.e30. https://doi.org/10.1016/j.cell.2022.06.007.

14. Fischer, G.M., Jalali, A., Kircher, D.A., Lee, W.-C., McQuade, J.L., Haydu, L.E., Joon, A.Y., Reuben, A., de Macedo, M.P., Carapeto, F.C.L., et al. (2019). Molecular Profiling Reveals Unique Immune and Metabolic Features of Melanoma Brain Metastases. Cancer Discov *9*, 628–645. https://doi.org/10.1158/2159-8290.CD-18-1489.

15. Lusby, R., Carl, S., and Tiwari, V.K. (2024). Integrating single-cell transcriptomics with Artificial Intelligence reveals pan-cancer biomarkers of brain metastasis. bioRxiv, 2024.03.08.584083. https://doi.org/10.1101/2024.03.08.584083.

16. Ikarashi, D., Okimoto, T., Shukuya, T., Onagi, H., Hayashi, T., Sinicropi-Yao, S.L., Amann, J.M., Nakatsura, T., Kitano, S., and Carbone, D.P. (2021). Comparison of Tumor Microenvironments Between Primary Tumors and Brain Metastases in Patients With NSCLC. JTO Clin Res Rep *2*, 100230. https://doi.org/10.1016/j.jtocrr.2021.100230.

17. Friebel, E., Kapolou, K., Unger, S., Núñez, N.G., Utz, S., Rushing, E.J., Regli, L., Weller, M., Greter, M., Tugues, S., et al. (2020). Single-Cell Mapping of Human Brain Cancer Reveals Tumor-Specific Instruction of Tissue-Invading Leukocytes. Cell *181*, 1626-1642.e20. https://doi.org/10.1016/j.cell.2020.04.055.

18. Klemm, F., Maas, R.R., Bowman, R.L., Kornete, M., Soukup, K., Nassiri, S., Brouland, J.-P., Iacobuzio-Donahue, C.A., Brennan, C., Tabar, V., et al. (2020). Interrogation of the Microenvironmental Landscape in Brain Tumors Reveals Disease-Specific Alterations of Immune Cells. Cell *181*, 1643-1660.e17. https://doi.org/10.1016/j.cell.2020.05.007.

19. Wischnewski, V., Maas, R.R., Aruffo, P.G., Soukup, K., Galletti, G., Kornete, M., Galland, S., Fournier, N., Lilja, J., Wirapati, P., et al. (2023). Phenotypic diversity of T cells in human primary and metastatic brain tumors revealed by multiomic interrogation. Nat Cancer *4*, 908–924. https://doi.org/10.1038/s43018-023-00566-3.

20. Gonzalez, H., Mei, W., Robles, I., Hagerling, C., Allen, B.M., Hauge Okholm, T.L., Nanjaraj, A., Verbeek, T., Kalavacherla, S., van Gogh, M., et al. (2022). Cellular architecture of human brain metastases. Cell *185*, 729-745.e20. https://doi.org/10.1016/j.cell.2021.12.043.

21. Sun, L., Kienzler, J.C., Reynoso, J.G., Lee, A., Shiuan, E., Li, S., Kim, J., Ding, L., Monteleone, A.J., Owens, G.C., et al. (2023). Immune checkpoint blockade induces distinct alterations in the microenvironments of primary and metastatic brain tumors. J Clin Invest *133*, e169314. https://doi.org/10.1172/JCI169314.

22. Álvarez-Prado, Á.F., Maas, R.R., Soukup, K., Klemm, F., Kornete, M., Krebs, F.S., Zoete, V., Berezowska, S., Brouland, J.-P., Hottinger, A.F., et al. (2023). Immunogenomic analysis of human brain metastases reveals diverse immune landscapes across genetically distinct tumors. Cell Reports Medicine *4*, 100900. https://doi.org/10.1016/j.xcrm.2022.100900.

23. Valiente, M., Van Swearingen, A.E.D., Anders, C.K., Bairoch, A., Boire, A., Bos, P.D., Cittelly, D.M., Erez, N., Ferraro, G.B., Fukumura, D., et al. (2020). Brain Metastasis Cell Lines Panel: A Public Resource of Organotropic Cell Lines. Cancer Research *80*, 4314–4323. https://doi.org/10.1158/0008-5472.CAN-20-0291.

24. Miarka, L., and Valiente, M. (2021). Animal models of brain metastasis. Neurooncol Adv *3*, v144–v156. https://doi.org/10.1093/noajnl/vdab115.

25. Cho, J.H., Robinson, J.P., Arave, R.A., Burnett, W.J., Kircher, D.A., Chen, G., Davies, M.A., Grossmann, A.H., VanBrocklin, M.W., McMahon, M., et al. (2015). AKT1 Activation Promotes Development of Melanoma Metastases. Cell Rep *13*, 898–905. https://doi.org/10.1016/j.celrep.2015.09.057.

26. Kircher, D.A., Trombetti, K.A., Silvis, M.R., Parkman, G.L., Fischer, G.M., Angel, S.N., Stehn, C.M., Strain, S.C., Grossmann, A.H., Duffy, K.L., et al. (2019). AKT1E17K Activates Focal Adhesion Kinase and Promotes Melanoma Brain Metastasis. Mol Cancer Res *17*, 1787–1800. https://doi.org/10.1158/1541-7786.MCR-18-1372.

27. Phadke, M.S., Li, J., Chen, Z., Rodriguez, P.C., Mandula, J.K., Karapetyan, L., Forsyth, P.A., Chen, Y.A., and Smalley, K.S.M. (2023). Differential requirements for CD4+ T cells in the efficacy of the anti-PD-1+LAG-3 and anti-PD-1+CTLA-4 combinations in melanoma flank and brain metastasis models. J Immunother Cancer *11*, e007239. https://doi.org/10.1136/jitc-2023-007239.

28. Taggart, D., Andreou, T., Scott, K.J., Williams, J., Rippaus, N., Brownlie, R.J., Ilett, E.J., Salmond, R.J., Melcher, A., and Lorger, M. (2018). Anti-PD-1/anti-CTLA-4 efficacy in melanoma brain metastases depends on extracranial disease and augmentation of CD8+ T cell trafficking. Proc Natl Acad Sci U S A *115*, E1540–E1549. https://doi.org/10.1073/pnas.1714089115.

29. Pérez-Guijarro, E., Yang, H.H., Araya, R.E., El Meskini, R., Michael, H.T., Vodnala, S.K., Marie, K.L., Smith, C., Chin, S., Lam, K.C., et al. (2020). Multimodel preclinical platform predicts clinical response of melanoma to immunotherapy. Nat Med *26*, 781–791. https://doi.org/10.1038/s41591-020-0818-3.

30. Bloom, M.B., Perry-Lalley, D., Robbins, P.F., Li, Y., El-Gamil, M., Rosenberg, S.A., and Yang, J.C. (1997). Identification of Tyrosinase-related Protein 2 as a Tumor Rejection Antigen for the B16 Melanoma. J Exp Med *185*, 453–460.

31. Tímár, J., Mészáros, L., Ladányi, A., Puskás, L.G., and Rásó, E. (2006). Melanoma genomics reveals signatures of sensitivity to bio- and targeted therapies. Cell Immunol *244*, 154–157. https://doi.org/10.1016/j.cellimm.2006.12.009.

32. Rappaport, J., Chen, Q., McGuire, T., Daugherty-Lopes, A., and Goldszmid, R.S. (2024). Development of an optimized machine learning approach to enhance brain metastatic burden assessment in preclinical models. bioRxiv, 2024.08.21.608131. https://doi.org/10.1101/2024.08.21.608131.

33. Chen, G., Chakravarti, N., Aardalen, K., Lazar, A.J., Tetzlaff, M.T., Wubbenhorst, B., Kim, S.-B., Kopetz, S., Ledoux, A.A., Gopal, Y.N.V., et al. (2014). Molecular Profiling of Patient-Matched Brain and Extracranial Melanoma Metastases Implicates the PI3K Pathway as a Therapeutic Target. Clin Cancer Res *20*, 5537–5546. https://doi.org/10.1158/1078-0432.CCR-13-3003.

34. Brastianos, P.K., Carter, S.L., Santagata, S., Cahill, D.P., Taylor-Weiner, A., Jones, R.T., Van Allen, E.M., Lawrence, M.S., Horowitz, P.M., Cibulskis, K., et al. (2015). Genomic Characterization of Brain Metastases Reveals Branched Evolution and Potential Therapeutic Targets. Cancer Discov *5*, 1164–1177. https://doi.org/10.1158/2159-8290.CD-15-0369.

35. Nguyen, B., Fong, C., Luthra, A., Smith, S.A., DiNatale, R.G., Nandakumar, S., Walch, H., Chatila, W.K., Madupuri, R., Kundra, R., et al. (2022). Genomic characterization of metastatic patterns from prospective clinical sequencing of 25,000 patients. Cell *185*, 563-575.e11. https://doi.org/10.1016/j.cell.2022.01.003.

36. Cerami1, E., Gao, J., Dogrusoz, U., Gross, B.E., Sumer, S.O., Aksoy, B.A., Jacobsen, A., Byrne, C.J., Heuer, M.L., Larsson, E., et al. (2012). The cBio Cancer Genomics Portal: An Open Platform for Exploring

Multidimensional Cancer Genomics Data. Cancer Discov *2*, 401–404. https://doi.org/10.1158/2159-8290.CD-12-0095.

37. Gao, J., Aksoy, B.A., Dogrusoz, U., Dresdner, G., Gross, B., Sumer, S.O., Sun, Y., Jacobsen, A., Sinha, R., Larsson, E., et al. (2013). Integrative Analysis of Complex Cancer Genomics and Clinical Profiles Using the cBioPortal. Science Signaling. https://doi.org/10.1126/scisignal.2004088.

38. de Bruijn, I., Kundra, R., Mastrogiacomo, B., Tran, T.N., Sikina, L., Mazor, T., Li, X., Ochoa, A., Zhao, G., Lai, B., et al. (2023). Analysis and Visualization of Longitudinal Genomic and Clinical Data from the AACR Project GENIE Biopharma Collaborative in cBioPortal. Cancer Res *83*, 3861–3867. https://doi.org/10.1158/0008-5472.CAN-23-0816.

39. Lin, X., and Boutros, P.C. (2020). Optimization and expansion of non-negative matrix factorization. BMC Bioinformatics *21*, 7. https://doi.org/10.1186/s12859-019-3312-5.

40. Tirosh, I., Venteicher, A.S., Hebert, C., Escalante, L.E., Patel, A.P., Yizhak, K., Fisher, J.M., Rodman, C., Mount, C., Filbin, M.G., et al. (2016). Single-cell RNA-seq supports a developmental hierarchy in human oligodendroglioma. Nature *539*, 309–313. https://doi.org/10.1038/nature20123.

41. Kinker, G.S., Greenwald, A.C., Tal, R., Orlova, Z., Cuoco, M.S., McFarland, J.M., Warren, A., Rodman, C., Roth, J.A., Bender, S.A., et al. (2020). Pan-cancer single-cell RNA-seq identifies recurring programs of cellular heterogeneity. Nat Genet *52*, 1208–1218. https://doi.org/10.1038/s41588-020-00726-6.

42. Gavish, A., Tyler, M., Greenwald, A.C., Hoefflin, R., Simkin, D., Tschernichovsky, R., Galili Darnell, N., Somech, E., Barbolin, C., Antman, T., et al. (2023). Hallmarks of transcriptional intratumour heterogeneity across a thousand tumours. Nature *618*, 598–606. https://doi.org/10.1038/s41586-023-06130-4.

43. Zhou, Y., Zhou, B., Pache, L., Chang, M., Khodabakhshi, A.H., Tanaseichuk, O., Benner, C., and Chanda, S.K. (2019). Metascape provides a biologist-oriented resource for the analysis of systems-level datasets. Nat Commun *10*, 1523. https://doi.org/10.1038/s41467-019-09234-6.

44. Smalley, I., Chen, Z., Phadke, M., Li, J., Yu, X., Wyatt, C., Evernden, B., Messina, J.L., Sarnaik, A., Sondak, V.K., et al. (2021). Single-Cell Characterization of the Immune Microenvironment of Melanoma Brain and Leptomeningeal Metastases. Clin Cancer Res *27*, 4109–4125. https://doi.org/10.1158/1078-0432.CCR-21-1694.

45. Alvarez-Breckenridge, C., Markson, S.C., Stocking, J.H., Nayyar, N., Lastrapes, M., Strickland, M.R., Kim, A.E., de Sauvage, M., Dahal, A., Larson, J.M., et al. (2022). Microenvironmental Landscape of Human Melanoma Brain Metastases in Response to Immune Checkpoint Inhibition. Cancer Immunol Res *10*, 996–1012. https://doi.org/10.1158/2326-6066.CIR-21-0870.

46. Morad, G., Helmink, B.A., Sharma, P., and Wargo, J.A. (2021). Hallmarks of response, resistance, and toxicity to immune checkpoint blockade. Cell *184*, 5309–5337. https://doi.org/10.1016/j.cell.2021.09.020.

47. Petitprez, F., Meylan, M., de Reyniès, A., Sautès-Fridman, C., and Fridman, W.H. (2020). The Tumor Microenvironment in the Response to Immune Checkpoint Blockade Therapies. Front Immunol *11*, 784. https://doi.org/10.3389/fimmu.2020.00784.

48. Zakaria, R., Jenkinson, M.D., Radon, M., Das, K., Poptani, H., Rathi, N., and Rudland, P.S. (2023). Immune checkpoint inhibitor treatment of brain metastasis associated with a less invasive growth pattern, higher

T-cell infiltration and raised tumor ADC on diffusion weighted MRI. Cancer Immunol Immunother *72*, 3387–3393. https://doi.org/10.1007/s00262-023-03499-z.

49. Andreatta, M., Corria-Osorio, J., Müller, S., Cubas, R., Coukos, G., and Carmona, S.J. (2021). Interpretation of T cell states from single-cell transcriptomics data using reference atlases. Nat Commun *12*, 2965. https://doi.org/10.1038/s41467-021-23324-4.

50. Sade-Feldman, M., Yizhak, K., Bjorgaard, S.L., Ray, J.P., de Boer, C.G., Jenkins, R.W., Lieb, D.J., Chen, J.H., Frederick, D.T., Barzily-Rokni, M., et al. (2018). Defining T cell states associated with response to checkpoint immunotherapy in melanoma. Cell *175*, 998-1013.e20. https://doi.org/10.1016/j.cell.2018.10.038.

51. Giles, J.R., Globig, A.-M., Kaech, S.M., and Wherry, E.J. (2023). CD8+ T cells in the cancer-immunity cycle. Immunity *56*, 2231–2253. https://doi.org/10.1016/j.immuni.2023.09.005.

52. Miller, B.C., Sen, D.R., Al Abosy, R., Bi, K., Virkud, Y.V., LaFleur, M.W., Yates, K.B., Lako, A., Felt, K., Naik, G.S., et al. (2019). Subsets of exhausted CD8+ T cells differentially mediate tumor control and respond to checkpoint blockade. Nat Immunol *20*, 326–336. https://doi.org/10.1038/s41590-019-0312-6.

53. Jiang, W., He, Y., He, W., Wu, G., Zhou, X., Sheng, Q., Zhong, W., Lu, Y., Ding, Y., Lu, Q., et al. (2021). Exhausted CD8+T Cells in the Tumor Immune Microenvironment: New Pathways to Therapy. Front. Immunol. *11*, 622509. https://doi.org/10.3389/fimmu.2020.622509.

54. Acharya, N., Madi, A., Zhang, H., Klapholz, M., Escobar, G., Dulberg, S., Christian, E., Ferreira, M., Dixon, K.O., Fell, G., et al. (2020). Endogenous Glucocorticoid Signaling Regulates CD8+ T Cell Differentiation and Development of Dysfunction in the Tumor Microenvironment. Immunity *53*, 658-671.e6. https://doi.org/10.1016/j.immuni.2020.08.005.

55. Damei, I., Trickovic, T., Mami-Chouaib, F., and Corgnac, S. (2023). Tumor-resident memory T cells as a biomarker of the response to cancer immunotherapy. Front. Immunol. *14*, 1205984. https://doi.org/10.3389/fimmu.2023.1205984.

56. Corgnac, S., Malenica, I., Mezquita, L., Auclin, E., Voilin, E., Kacher, J., Halse, H., Grynszpan, L., Signolle, N., Dayris, T., et al. (2020). CD103+CD8+ TRM Cells Accumulate in Tumors of Anti-PD-1-Responder Lung Cancer Patients and Are Tumor-Reactive Lymphocytes Enriched with Tc17. Cell Reports Medicine *1*. https://doi.org/10.1016/j.xcrm.2020.100127.

57. Edwards, J., Wilmott, J.S., Madore, J., Gide, T.N., Quek, C., Tasker, A., Ferguson, A., Chen, J., Hewavisenti, R., Hersey, P., et al. (2018). CD103+ Tumor-Resident CD8+ T Cells Are Associated with Improved Survival in Immunotherapy-Naïve Melanoma Patients and Expand Significantly During Anti–PD-1 Treatment. Clinical Cancer Research *24*, 3036–3045. https://doi.org/10.1158/1078-0432.CCR-17-2257.

58. Colonna, M., and Butovsky, O. (2017). Microglia Function in the Central Nervous System During Health and Neurodegeneration. Annu Rev Immunol *35*, 441–468. https://doi.org/10.1146/annurev-immunol-051116-052358.

59. Borst, K., Dumas, A.A., and Prinz, M. (2021). Microglia: Immune and non-immune functions. Immunity *54*, 2194–2208. https://doi.org/10.1016/j.immuni.2021.09.014.

60. Paolicelli, R.C., Sierra, A., Stevens, B., Tremblay, M.-E., Aguzzi, A., Ajami, B., Amit, I., Audinat, E., Bechmann, I., Bennett, M., et al. (2022). Microglia states and nomenclature: A field at its crossroads. Neuron *110*, 3458. https://doi.org/10.1016/j.neuron.2022.10.020.

61. Guldner, I.H., Wang, Q., Yang, L., Golomb, S.M., Zhao, Z., Lopez, J.A., Brunory, A., Howe, E.N., Zhang, Y., Palakurthi, B., et al. (2020). CNS-Native Myeloid Cells Drive Immune Suppression in the Brain Metastatic Niche through Cxcl10. Cell *183*, 1234-1248.e25. https://doi.org/10.1016/j.cell.2020.09.064.

62. You, H., Baluszek, S., and Kaminska, B. (2019). Immune Microenvironment of Brain Metastases—Are Microglia and Other Brain Macrophages Little Helpers? Front. Immunol. *10*, 1941. https://doi.org/10.3389/fimmu.2019.01941.

63. Lin, S.-S., Tang, Y., Illes, P., and Verkhratsky, A. (2021). The Safeguarding Microglia: Central Role for P2Y12 Receptors. Front Pharmacol *11*, 627760. https://doi.org/10.3389/fphar.2020.627760.

64. Huang, C., Wang, X., Wang, Y., Feng, Y., Wang, X., Chen, S., Yan, P., Liao, J., Zhang, Q., Mao, C., et al. (2024). Sirpα on tumor-associated myeloid cells restrains antitumor immunity in colorectal cancer independent of its interaction with CD47. Nat Cancer *5*, 500–516. https://doi.org/10.1038/s43018-023-00691-z.

65. Hutter, G., Theruvath, J., Graef, C.M., Zhang, M., Schoen, M.K., Manz, E.M., Bennett, M.L., Olson, A., Azad, T.D., Sinha, R., et al. (2019). Microglia are effector cells of CD47-SIRPα antiphagocytic axis disruption against glioblastoma. Proceedings of the National Academy of Sciences *116*, 997–1006. https://doi.org/10.1073/pnas.1721434116.

66. Bian, Z., Shi, L., Kidder, K., Zen, K., Garnett-Benson, C., and Liu, Y. (2021). Intratumoral SIRPα-deficient macrophages activate tumor antigen-specific cytotoxic T cells under radiotherapy. Nat Commun *12*, 1–16. https://doi.org/10.1038/s41467-021-23442-z.

67. Niu, F., Yu, Y., Li, Z., Ren, Y., Li, Z., Ye, Q., Liu, P., Ji, C., Qian, L., and Xiong, Y. (2022). Arginase: An emerging and promising therapeutic target for cancer treatment. Biomed Pharmacother *149*, 112840. https://doi.org/10.1016/j.biopha.2022.112840.

68. Dixon, K.O., Lahore, G.F., and Kuchroo, V.K. (2024). Beyond T cell exhaustion: TIM-3 regulation of myeloid cells. Science Immunology. https://doi.org/10.1126/sciimmunol.adf2223.

69. Ausejo-Mauleon, I., Labiano, S., de la Nava, D., Laspidea, V., Zalacain, M., Marrodán, L., García-Moure, M., González-Huarriz, M., Hervás-Corpión, I., Dhandapani, L., et al. (2023). TIM-3 blockade in diffuse intrinsic pontine glioma models promotes tumor regression and antitumor immune memory. Cancer Cell *41*, 1911-1926.e8. https://doi.org/10.1016/j.ccell.2023.09.001.

70. Ocaña-Guzman, R., Torre-Bouscoulet, L., and Sada-Ovalle, I. (2016). TIM-3 Regulates Distinct Functions in Macrophages. Front Immunol *7*, 229. https://doi.org/10.3389/fimmu.2016.00229.

71. Finak, G., McDavid, A., Yajima, M., Deng, J., Gersuk, V., Shalek, A.K., Slichter, C.K., Miller, H.W., McElrath, M.J., Prlic, M., et al. (2015). MAST: a flexible statistical framework for assessing transcriptional changes and characterizing heterogeneity in single-cell RNA sequencing data. Genome Biol *16*, 278. https://doi.org/10.1186/s13059-015-0844-5.

72. Wang, T., Li, B., Nelson, C.E., and Nabavi, S. (2019). Comparative analysis of differential gene expression analysis tools for single-cell RNA sequencing data. BMC Bioinformatics *20*, 40. https://doi.org/10.1186/s12859-019-2599-6.

73. Gheibihayat, S.M., Cabezas, R., Nikiforov, N.G., Jamialahmadi, T., Johnston, T.P., and Sahebkar, A. (2021). CD47 in the Brain and Neurodegeneration: An Update on the Role in Neuroinflammatory Pathways. Molecules *26*, 3943. https://doi.org/10.3390/molecules26133943.

74. Burstyn-Cohen, T., and Fresia, R. (2023). TAM receptors in phagocytosis: Beyond the mere internalization of particles. Immunol Rev *319*, 7–26. https://doi.org/10.1111/imr.13267.

75. Gilchrist, S.E., Pennelli, G.M., and Hafizi, S. (2021). Gas6/TAM Signalling Negatively Regulates Inflammatory Induction of GM-CSF in Mouse Brain Microglia. Cells *10*, 3281. https://doi.org/10.3390/cells10123281.

76. Li, Y., Xu, H., Wang, H., Yang, K., Luan, J., and Wang, S. (2023). TREM2: Potential therapeutic targeting of microglia for Alzheimer's disease. Biomedicine & Pharmacotherapy *165*, 115218. https://doi.org/10.1016/j.biopha.2023.115218.

77. Mo, X., Liu, M., Gong, J., Mei, Y., Chen, H., Mo, H., Yang, X., and Li, J. (2022). PTPRM Is Critical for Synapse Formation Regulated by Zinc Ion. Front Mol Neurosci *15*, 822458. https://doi.org/10.3389/fnmol.2022.822458.

78. Czubak-Prowizor, K., Babinska, A., and Swiatkowska, M. (2022). The F11 Receptor (F11R)/Junctional Adhesion Molecule-A (JAM-A) (F11R/JAM-A) in cancer progression. Mol Cell Biochem *477*, 79–98. https://doi.org/10.1007/s11010-021-04259-2.

79. Scott, L.E., Weinberg, S.H., and Lemmon, C.A. (2019). Mechanochemical Signaling of the Extracellular Matrix in Epithelial-Mesenchymal Transition. Front. Cell Dev. Biol. *7*. https://doi.org/10.3389/fcell.2019.00135.

80. Yurchenco, P.D. (2011). Basement Membranes: Cell Scaffoldings and Signaling Platforms. Cold Spring Harb Perspect Biol *3*, a004911. https://doi.org/10.1101/cshperspect.a004911.

81. Jin, C., Shao, Y., Zhang, X., Xiang, J., Zhang, R., Sun, Z., Mei, S., Zhou, J., Zhang, J., and Shi, L. (2021). A Unique Type of Highly-Activated Microglia Evoking Brain Inflammation via Mif/Cd74 Signaling Axis in Aged Mice. Aging Dis *12*, 2125–2139. https://doi.org/10.14336/AD.2021.0520.

82. Potru, P.S., and Spittau, B. (2023). CD74: a prospective marker for reactive microglia? Neural Regen Res *18*, 2673–2674. https://doi.org/10.4103/1673-5374.371350.

83. Jahn, J., Bollensdorf, A., Kalischer, C., Piecha, R., Weiß-Müller, J., Potru, P.S., Ruß, T., and Spittau, B. (2022). Microglial CD74 Expression Is Regulated by TGFβ Signaling. Int J Mol Sci *23*, 10247. https://doi.org/10.3390/ijms231810247.

84. Wiersma, V.R., de Bruyn, M., Helfrich, W., and Bremer, E. (2013). Therapeutic potential of Galectin-9 in human disease. Medicinal Research Reviews *33*, E102–E126. https://doi.org/10.1002/med.20249.

85. Nobumoto, A., Oomizu, S., Arikawa, T., Katoh, S., Nagahara, K., Miyake, M., Nishi, N., Takeshita, K., Niki, T., Yamauchi, A., et al. (2009). Galectin-9 expands unique macrophages exhibiting plasmacytoid dendritic cell-like phenotypes that activate NK cells in tumor-bearing mice. Clinical Immunology *130*, 322–330. https://doi.org/10.1016/j.clim.2008.09.014.

86. Ozga, A.J., Chow, M.T., and Luster, A.D. (2021). Chemokines and the immune response to cancer. Immunity *54*, 859. https://doi.org/10.1016/j.immuni.2021.01.012.

87. Harlin, H., Meng, Y., Peterson, A.C., Zha, Y., Tretiakova, M., Slingluff, C., McKee, M., and Gajewski, T.F. (2009). Chemokine Expression in Melanoma Metastases Associated with CD8+ T-Cell Recruitment. Cancer Res *69*, 3077–3085. https://doi.org/10.1158/0008-5472.CAN-08-2281.

88. Allen, F., Bobanga, I.D., Rauhe, P., Barkauskas, D., Teich, N., Tong, C., Myers, J., and Huang, A.Y. (2017). CCL3 augments tumor rejection and enhances CD8+ T cell infiltration through NK and CD103+ dendritic cell recruitment via IFNγ. Oncoimmunology *7*, e1393598. https://doi.org/10.1080/2162402X.2017.1393598.

89. Caushi, J.X., Zhang, J., Ji, Z., Vaghasia, A., Zhang, B., Hsiue, E.H.-C., Mog, B.J., Hou, W., Justesen, S., Blosser, R., et al. (2021). Transcriptional programs of neoantigen-specific TIL in anti-PD-1-treated lung cancers. Nature *596*, 126–132. https://doi.org/10.1038/s41586-021-03752-4.

90. Lowery, F.J., Krishna, S., Yossef, R., Parikh, N.B., Chatani, P.D., Zacharakis, N., Parkhurst, M.R., Levin, N., Sindiri, S., Sachs, A., et al. (2022). Molecular signatures of antitumor neoantigen-reactive T cells from metastatic human cancers. Science *375*, 877–884. https://doi.org/10.1126/science.abl5447.

91. Hanada, K.-I., Zhao, C., Gil-Hoyos, R., Gartner, J.J., Chow-Parmer, C., Lowery, F.J., Krishna, S., Prickett, T.D., Kivitz, S., Parkhurst, M.R., et al. (2022). A phenotypic signature that identifies neoantigen-reactive T cells in fresh human lung cancers. Cancer Cell *40*, 479-493.e6. https://doi.org/10.1016/j.ccell.2022.03.012.

92. Oliveira, G., Stromhaug, K., Klaeger, S., Kula, T., Frederick, D.T., Le, P.M., Forman, J., Huang, T., Li, S., Zhang, W., et al. (2021). Phenotype, specificity and avidity of antitumour CD8+ T cells in melanoma. Nature *596*, 119–125. https://doi.org/10.1038/s41586-021-03704-y.

93. van der Leun, A.M., Thommen, D.S., and Schumacher, T.N. (2020). CD8+ T cell states in human cancer: insights from single-cell analysis. Nat Rev Cancer *20*, 218–232. https://doi.org/10.1038/s41568-019-0235-4.

94. Tan, X.-L., Le, A., Scherrer, E., Tang, H., Kiehl, N., Han, J., Jiang, R., Diede, S.J., and Shui, I.M. (2022). Systematic literature review and meta-analysis of clinical outcomes and prognostic factors for melanoma brain metastases. Frontiers in Oncology *12*.

95. Achrol, A.S., Rennert, R.C., Anders, C., Soffietti, R., Ahluwalia, M.S., Nayak, L., Peters, S., Arvold, N.D., Harsh, G.R., Steeg, P.S., et al. (2019). Brain metastases. Nat Rev Dis Primers *5*, 5. https://doi.org/10.1038/s41572-018-0055-y.

96. Lee, J.E., and Yang, S.H. (2023). Advances in Brain Metastasis Models. Brain Tumor Res Treat *11*, 16–21. https://doi.org/10.14791/btrt.2022.0037.

97. Arrieta, V.A., Dmello, C., McGrail, D.J., Brat, D.J., Lee-Chang, C., Heimberger, A.B., Chand, D., Stupp, R., and Sonabend, A.M. (2023). Immune checkpoint blockade in glioblastoma: from tumor heterogeneity to personalized treatment. Journal of Clinical Investigation *133*, e163447. https://doi.org/10.1172/JCI163447.

98. Lee, A.H., Sun, L., Mochizuki, A.Y., Reynoso, J.G., Orpilla, J., Chow, F., Kienzler, J.C., Everson, R.G., Nathanson, D.A., Bensinger, S.J., et al. (2021). Neoadjuvant PD-1 blockade induces T cell and cDC1 activation but fails to overcome the immunosuppressive tumor associated macrophages in recurrent glioblastoma. Nat Commun *12*, 6938. https://doi.org/10.1038/s41467-021-26940-2.

99. Sudmeier, L.J., Hoang, K.B., Nduom, E.K., Wieland, A., Neill, S.G., Schniederjan, M.J., Ramalingam, S.S., Olson, J.J., Ahmed, R., and Hudson, W.H. (2022). Distinct phenotypic states and spatial distribution of CD8+ T cell clonotypes in human brain metastases. Cell Reports Medicine *3*, 100620. https://doi.org/10.1016/j.xcrm.2022.100620.

100. Jansen, C.S., Prabhu, R.S., Pagadala, M.S., Chappa, P., Goyal, S., Zhou, C., Neill, S.G., Prokhnevska, N., Cardenas, M., Hoang, K.B., et al. (2023). Immune niches in brain metastases contain TCF1+ stem-like T cells, are associated with disease control and are modulated by preoperative SRS. Res Sq, rs.3.rs-2722744. https://doi.org/10.21203/rs.3.rs-2722744/v1.

101. Zakaria, R., Platt-Higgins, A., Rathi, N., Radon, M., Das, S., Das, K., Bhojak, M., Brodbelt, A., Chavredakis, E., Jenkinson, M.D., et al. (2018). T-Cell Densities in Brain Metastases Are Associated with Patient Survival Times and Diffusion Tensor MRI Changes. Cancer Res *78*, 610–616. https://doi.org/10.1158/0008-5472.CAN-17-1720.

102. Harter, P.N., Bernatz, S., Scholz, A., Zeiner, P.S., Zinke, J., Kiyose, M., Blasel, S., Beschorner, R., Senft, C., Bender, B., et al. (2015). Distribution and prognostic relevance of tumor-infiltrating lymphocytes (TILs) and PD-1/PD-L1 immune checkpoints in human brain metastases. Oncotarget *6*. https://doi.org/10.18632/oncotarget.5696.

103. Berghoff, A.S., Ricken, G., Wilhelm, D., Rajky, O., Widhalm, G., Dieckmann, K., Birner, P., Bartsch, R., and Preusser, M. (2016). Tumor infiltrating lymphocytes and PD-L1 expression in brain metastases of small cell lung cancer (SCLC). J Neurooncol *130*, 19–29. https://doi.org/10.1007/s11060-016-2216-8.

104. Schetters, S.T.T., Gomez-Nicola, D., Garcia-Vallejo, J.J., and Van Kooyk, Y. (2018). Neuroinflammation: Microglia and T Cells Get Ready to Tango. Front Immunol *8*, 1905. https://doi.org/10.3389/fimmu.2017.01905.

105. Nguyen, L.T., Aprico, A., Nwoke, E., Walsh, A.D., Blades, F., Avneri, R., Martin, E., Zalc, B., Kilpatrick, T.J., and Binder, M.D. (2023). Mertk-expressing microglia influence oligodendrogenesis and myelin modelling in the CNS. Journal of Neuroinflammation *20*, 253. https://doi.org/10.1186/s12974-023-02921-8.

106. Rodríguez, A.M., Rodríguez, J., and Giambartolomei, G.H. (2022). Microglia at the Crossroads of Pathogen-Induced Neuroinflammation. ASN Neuro *14*, 17590914221104566. https://doi.org/10.1177/17590914221104566.

107. Gilchrist, S.E., Goudarzi, S., and Hafizi, S. (2020). Gas6 Inhibits Toll-Like Receptor-Mediated Inflammatory Pathways in Mouse Microglia via Axl and Mer. Front Cell Neurosci *14*, 576650. https://doi.org/10.3389/fncel.2020.576650.

108. Chen, X., Firulyova, M., Manis, M., Herz, J., Smirnov, I., Aladyeva, E., Wang, C., Bao, X., Finn, M.B., Hu, H., et al. (2023). Microglia-mediated T cell Infiltration Drives Neurodegeneration in Tauopathy. Nature *615*, 668–677. https://doi.org/10.1038/s41586-023-05788-0.

109. Moertel, C.L., Xia, J., LaRue, R., Waldron, N.N., Andersen, B.M., Prins, R.M., Okada, H., Donson, A.M., Foreman, N.K., Hunt, M.A., et al. (2014). CD200 in CNS tumor-induced immunosuppression: the role for CD200 pathway blockade in targeted immunotherapy. J Immunother Cancer *2*, 46. https://doi.org/10.1186/s40425-014-0046-9.

110. Chen, D., Varanasi, S.K., Hara, T., Traina, K., Sun, M., McDonald, B., Farsakoglu, Y., Clanton, J., Xu, S., Garcia-Rivera, L., et al. (2023). CTLA-4 blockade induces a microglia-Th1 cell partnership that stimulates microglia phagocytosis and anti-tumor function in glioblastoma. Immunity *56*, 2086-2104.e8. https://doi.org/10.1016/j.immuni.2023.07.015.

111. Ngwa, C., and Liu, F. (2019). CD200-CD200R signaling and diseases: a potential therapeutic target? Int J Physiol Pathophysiol Pharmacol *11*, 297–309.

112. von Roemeling, C.A., Patel, J.A., Carpenter, S.L., Yegorov, O., Yang, C., Bhatia, A., Doonan, B.P., Russell, R., Trivedi, V.S., Klippel, K., et al. (2024). Adeno-associated virus delivered CXCL9 sensitizes glioblastoma to anti-PD-1 immune checkpoint blockade. Nat Commun *15*, 5871. https://doi.org/10.1038/s41467-024-49989-1.

113. Timmerman, R., Zuiderwijk-Sick, E.A., Baron, W., and Bajramovic, J.J. (2023). In silico-in vitro modeling to uncover cues involved in establishing microglia identity: TGF-β3 and laminin can drive microglia signature gene expression. Front Cell Neurosci *17*, 1178504. https://doi.org/10.3389/fncel.2023.1178504.

114. Rigby, M.J., Gomez, T.M., and Puglielli, L. (2020). Glial Cell-Axonal Growth Cone Interactions in Neurodevelopment and Regeneration. Front Neurosci *14*, 203. https://doi.org/10.3389/fnins.2020.00203.

115. Feng, Y., Hu, X., Zhang, Y., and Wang, Y. (2024). The Role of Microglia in Brain Metastases: Mechanisms and Strategies. Aging Dis *15*, 169–185. https://doi.org/10.14336/AD.2023.0514.

116. Lee, W.S., Lee, W.-H., Bae, Y.C., and Suk, K. (2019). Axon Guidance Molecules Guiding Neuroinflammation. Exp Neurobiol *28*, 311–319. https://doi.org/10.5607/en.2019.28.3.311.

117. Tang, J., Jin, Y., Jia, F., Lv, T., Manaenko, A., Zhang, L.-F., Zhang, Z., Qi, X., Xue, Y., Zhao, B., et al. (2023). Gas6 Promotes Microglia Efferocytosis and Suppresses Inflammation Through Activating Axl/Rac1 Signaling in Subarachnoid Hemorrhage Mice. Transl Stroke Res *14*, 955–969. https://doi.org/10.1007/s12975-022-01099-0.

118. Fazio, F., Ulivieri, M., Volpi, C., Gargaro, M., and Fallarino, F. (2018). Targeting metabotropic glutamate receptors for the treatment of neuroinflammation. Current Opinion in Pharmacology *38*, 16–23. https://doi.org/10.1016/j.coph.2018.01.010.

119. Szepesi, Z., Manouchehrian, O., Bachiller, S., and Deierborg, T. (2018). Bidirectional Microglia-Neuron Communication in Health and Disease. Front Cell Neurosci *12*, 323. https://doi.org/10.3389/fncel.2018.00323.

120. Wang, L., Li, C., Zhan, H., Li, S., Zeng, K., Xu, C., Zou, Y., Xie, Y., Zhan, Z., Yin, S., et al. (2024). Targeting the HSP47-collagen axis inhibits brain metastasis by reversing M2 microglial polarization and restoring anti-tumor immunity. CR Med *5*. https://doi.org/10.1016/j.xcrm.2024.101533.

121. Bankhead, P., Loughrey, M.B., Fernández, J.A., Dombrowski, Y., McArt, D.G., Dunne, P.D., McQuaid, S., Gray, R.T., Murray, L.J., Coleman, H.G., et al. (2017). QuPath: Open source software for digital pathology image analysis. Sci Rep *7*, 16878. https://doi.org/10.1038/s41598-017-17204-5.

122. Virador, V., Matsunaga, N., Matsunaga, J., Valencia, J., Oldham, R.J., Kameyama, K., Peck, G.L., Ferrans, V.J., Vieira, W.D., Abdel-Malek, Z.A., et al. (2001). Production of Melanocyte-Specific Antibodies to Human Melanosomal Proteins: Expression Patterns in Normal Human Skin and in Cutaneous Pigmented Lesions. Pigment Cell Research *14*, 289–297. https://doi.org/10.1034/j.1600-0749.2001.140410.x.

123. Korin, B., Dubovik, T., and Rolls, A. (2018). Mass cytometry analysis of immune cells in the brain. Nat Protoc *13*, 377–391. https://doi.org/10.1038/nprot.2017.155.

124. Araya, R.E., and Goldszmid, R.S. (2020). Characterization of the tumor immune infiltrate by multiparametric flow cytometry and unbiased high-dimensional data analysis. Methods Enzymol *632*, 309–337. https://doi.org/10.1016/bs.mie.2019.11.012.

125. Ashhurst, T.M., Marsh-Wakefield, F., Putri, G.H., Spiteri, A.G., Shinko, D., Read, M.N., Smith, A.L., and King, N.J.C. (2022). Integration, exploration, and analysis of high-dimensional single-cell cytometry data using Spectre. Cytometry Part A *101*, 237–253. https://doi.org/10.1002/cyto.a.24350.

126. Hao, Y., Hao, S., Andersen-Nissen, E., Mauck, W.M., Zheng, S., Butler, A., Lee, M.J., Wilk, A.J., Darby, C., Zager, M., et al. (2021). Integrated analysis of multimodal single-cell data. Cell *184*, 3573-3587.e29. https://doi.org/10.1016/j.cell.2021.04.048.

127. So, J.-S., Kim, H., and Han, K.-S. (2021). Mechanisms of Invasion in Glioblastoma: Extracellular Matrix, Ca2+ Signaling, and Glutamate. Frontiers in Cellular Neuroscience *15*. https://doi.org/10.3389/fncel.2021.663092.

128. McInnes, L., Healy, J., Saul, N., and Großberger, L. (2018). UMAP: Uniform Manifold Approximation and Projection. Journal of Open Source Software *3*, 861. https://doi.org/10.21105/joss.00861.

129. Huang, Q., Chen, L., Liang, J., Huang, Q., and Sun, H. (2022). Neurotransmitters: Potential Targets in Glioblastoma. Cancers (Basel) *14*, 3970. https://doi.org/10.3390/cancers14163970.

130. Hao, Y., Stuart, T., Kowalski, M.H., Choudhary, S., Hoffman, P., Hartman, A., Srivastava, A., Molla, G., Madad, S., Fernandez-Granda, C., et al. (2024). Dictionary learning for integrative, multimodal and scalable single-cell analysis. Nat Biotechnol *42*, 293–304. https://doi.org/10.1038/s41587-023-01767-y.

131. Wang, S., Feng, Y., Chen, L., Yu, J., Van Ongeval, C., Bormans, G., Li, Y., and Ni, Y. (2022). Towards updated understanding of brain metastasis. Am J Cancer Res *12*, 4290–4311.

132. Ianevski, A., Giri, A.K., and Aittokallio, T. (2022). Fully-automated and ultra-fast cell-type identification using specific marker combinations from single-cell transcriptomic data. Nat Commun *13*, 1246. https://doi.org/10.1038/s41467-022-28803-w.

133. Masmudi-Martín, M., Zhu, L., Sanchez-Navarro, M., Priego, N., Casanova-Acebes, M., Ruiz-Rodado, V., Giralt, E., and Valiente, M. (2021). Brain metastasis models: What should we aim to achieve better treatments? Advanced Drug Delivery Reviews *169*, 79–99. https://doi.org/10.1016/j.addr.2020.12.002.

134. Aibar, S., González-Blas, C.B., Moerman, T., Huynh-Thu, V.A., Imrichova, H., Hulselmans, G., Rambow, F., Marine, J.-C., Geurts, P., Aerts, J., et al. (2017). SCENIC: Single-cell regulatory network inference and clustering. Nature methods *14*, 1083. https://doi.org/10.1038/nmeth.4463.

135. Strickland, M.R., Alvarez-Breckenridge, C., Gainor, J.F., and Brastianos, P.K. (2022). Tumor Immune Microenvironment of Brain Metastases: Toward Unlocking Antitumor Immunity. Cancer Discov *12*, 1199–1216. https://doi.org/10.1158/2159-8290.CD-21-0976.

136. Jin, S., Guerrero-Juarez, C.F., Zhang, L., Chang, I., Ramos, R., Kuan, C.-H., Myung, P., Plikus, M.V., and Nie, Q. (2021). Inference and analysis of cell-cell communication using CellChat. Nat Commun *12*, 1088. https://doi.org/10.1038/s41467-021-21246-9.

Table S1_Ingenuity Pathway Analysis (IPA) of mutated genes from M4, BR1 and I

© 2000-2023 QIAGEN. All rights reserved.

M4 Parental			
Ingenuity Canonical Pathways	-log(p-value)	Ratio	Molecules
Apoptosis Signaling	3.73	0.0673	AIFM1,CAPN3,IKBKB,KRAS,LMNA,MAP4K4,Naip1 (includes others)
RHOGDI Signaling	3.02	0.0409	ACTC1,CDH15,CDH23,CDH8,GNAQ,GNAZ,ITGAD,ITGB1,MYH6
PTEN Signaling	2.77	0.0464	BCAR1,IKBKB,INPP5B,ITGAD,ITGB1,KRAS,SHARPIN
TREM1 Signaling	2.74	0.0649	ITGB1,Naip1 (includes others),NLRP4,NOD1,TLR2
Type II Diabetes Mellitus Signaling	2.73	0.0458	CACNA1I,CD36,ENPP7,IKBKB,IRS2,NSMAF,SMPD4
Synaptic Long Term Depression	2.71	0.0404	CACNA1I,GNAQ,GNAZ,GRIA1,GRID1,KRAS,PLA2G4D,PNPLA3
Senescence Pathway	2.64	0.0334	ANAPC1,ATR,CAPN3,CBX2,CHEK2,HBP1,IKBKB,KRAS,MAPK7,TLR2
Sperm Motility	2.56	0.035	AATK,CACNA1I,CSF2RA,ERBB4,FES,GNAQ,GNAZ,PLA2G4D,PNPLA3
Sphingomyelin Metabolism	2.47	0.25	ENPP7,SMPD4
Neuroinflammation Signaling Pathway	2.46	0.0315	AGER,GRIA1,IKBKB,IRAK3,KCNJ3,MAPK7,Naip1 (includes others),PLA2G4D,TLR2,ZBTB12
Pathogen Induced Cytokine Storm Signaling Pathway	2.45	0.0296	C5,COL24A1,COL6A2,COL7A1,CSF2RA,Il3,MAPK7,Naip1 (includes others),NLRP4,NOD1,TLR2
Multiple Sclerosis Signaling Pathway	2.4	0.036	AIFM1,ASIC1,C5,CAPN3,IL17RC,Il3,PLP1,TLR2
Protein Ubiquitination Pathway	2.39	0.033	AMFR,ANAPC1,CUL2,NEDD4L,PSMD13,USO1,USP13,USP9Y,ZBTB12
Gα12/13 Signaling	2.38	0.0451	CDH15,CDH23,CDH8,IKBKB,KRAS,MAPK7
Death Receptor Signaling	2.32	0.0521	ACTC1,IKBKB,LMNA,MAP4K4,Naip1 (includes others)
Oxytocin Signaling Pathway	2.3	0.0319	ATP2B1,ATP2B4,CD36,EEF2,GNAQ,KRAS,MAPK7,MYH6,PLA2G4D

Calcium Transport I	2.27	0.2	ATP2B1,ATP2B4
Hereditary Breast Cancer Signaling	2.25	0.0423	ATR,CHEK2,KRAS,POLR2A,SLC19A1,SMARCC1
Actin Cytoskeleton Signaling	2.16	0.0328	ACTC1,BCAR1,ITGAD,ITGB1,KRAS,MYH6,TRIO,TTN
Endocannabinoid Neuronal Synapse Pathway	2.15	0.0403	CACNA1I,GNAQ,GRIA1,KCNJ3,MAPK7,RIMS1
WNK Renal Signaling Pathway	2.14	0.0472	AMFR,ANAPC1,ASIC1,CUL2,IRS2
Paxillin Signaling	2.13	0.0467	ACTC1,BCAR1,ITGAD,ITGB1,KRAS
Oxytocin In Brain Signaling Pathway	2.11	0.0352	CACNA1I,GNAQ,KRAS,MAPK7,NLRP4,PLA2G4D,PNPLA3
Agrin Interactions at Neuromuscular Junction	2.11	0.058	ACTC1,ERBB4,ITGB1,KRAS
Ephrin Receptor Signaling	2.08	0.0347	BCAR1,GNAQ,GNAZ,ITGAD,ITGB1,KRAS,MAP4K4
Role of Tissue Factor in Cancer	2.02	0.0338	GNAQ,IKBKB,ITGB1,KRAS,MAPK7,PDXP,SNAI1
Caveolar-mediated Endocytosis Signaling	1.98	0.0533	ACTC1,ITGAD,ITGB1,ZBTB12
Role of IL-17A in Psoriasis	1.97	0.143	IL17RC,S100A9
Integrin Signaling	1.97	0.033	ACTC1,BCAR1,CAPN3,ITGAD,ITGB1,KRAS,TTN
Neuregulin Signaling	1.97	0.0427	ERBB4,ITGAD,ITGB1,KRAS,TMEFF2
Signaling by Rho Family GTPases	1.94	0.03	ACTC1,CDH15,CDH23,CDH8,GNAQ,GNAZ,ITGAD,ITGB1
NGF Signaling	1.92	0.0417	IKBKB,KRAS,MAPK7,SMPD4,TRIO
Toll-like Receptor Signaling	1.92	0.0513	IKBKB,IRAK3,MAP4K4,TLR2
Role of BRCA1 in DNA Damage Response	1.89	0.05	ATR,CHEK2,SLC19A1,SMARCC1
G Beta Gamma Signaling	1.8	0.0388	CACNA1I,GNAQ,GNAZ,KCNJ3,KRAS
nNOS Signaling in Skeletal Muscle Cells	1.77	0.0625	CACNA1I,CAPN3,SNTA1
Glutaryl-CoA Degradation	1.76	0.111	ACAA2,TBXAS1

Cell Cycle: G2/M DNA Damage Checkpoint Regulation	1.72	0.06	ATR,CHEK2,TOP2A
Regulation of Cellular Mechanics by Calpain Protease	1.72	0.0444	CAPN3,ITGAD,ITGB1,KRAS
Ceramide Signaling	1.7	0.044	ENPP7,KRAS,NSMAF,SMPD4
UVC-Induced MAPK Signaling	1.7	0.0588	ATR,KRAS,SMPD4
NOD1/2 Signaling Pathway	1.68	0.0317	IKBKB,Il3,MAP4K4,NOD1,SHARPIN,TLR2
Insulin Receptor Signaling	1.66	0.0357	ASIC1,INPP5B,IRS2,KRAS,PDE3B
Endothelin-1 Signaling	1.63	0.0309	GNAQ,GNAZ,KRAS,MAPK7,PLA2G4D,PNPLA3
IL-1 Signaling	1.62	0.0417	GNAQ,GNAZ,IKBKB,IRAK3
PPARα/RXRα Activation	1.62	0.0308	ABCA1,CD36,GNAQ,IKBKB,KRAS,MAP4K4
Wound Healing Signaling Pathway	1.6	0.0278	COL24A1,COL6A2,COL7A1,IKBKB,Il3,ITGB1,KRAS
CSDE1 Signaling Pathway	1.59	0.0536	AGO4,SNAI1,TRIO
PI3K/AKT Signaling	1.57	0.03	IKBKB,IL17RC,INPP5B,ITGAD,ITGB1,KRAS
ILK Signaling	1.56	0.0299	ACTC1,IRS2,ITGB1,MYH6,RICTOR,SNAI1
Phagosome Formation	1.56	0.0201	BCAR1,CD36,CRHR2,GPR83,ITGAD,ITGB1,KRAS,MAPK7,MRC1,MYH6,PLA2G4D,PNPLA3,TLR2,TTN
Role of CHK Proteins in Cell Cycle Checkpoint Control	1.55	0.0517	ATR,CHEK2,SLC19A1
Dilated Cardiomyopathy Signaling Pathway	1.55	0.0333	ACTC1,CACNA1I,LMNA,MYH6,TTN
Sertoli Cell-Sertoli Cell Junction Signaling	1.52	0.0291	ACTC1,BCAR1,IGSF5,ITGAD,ITGB1,KRAS
Tryptophan Degradation III (Eukaryotic)	1.49	0.08	ACAA2,TBXAS1
IL-8 Signaling	1.48	0.0286	GNAQ,GNAZ,IKBKB,IRAK3,KRAS,MAP4K4
Pulmonary Fibrosis Idiopathic Signaling Pathway	1.48	0.0245	ACTC1,COL24A1,COL6A2,COL7A1,ITGB1,KRAS,POLR2A,SNAI1
Diphthamide Biosynthesis	1.47	0.333	EEF2

5-aminoimidazole Ribonucleotide Biosynthesis I	1.47	0.333	PFAS
Role of Macrophages, Fibroblasts and Endothelial Cells in Rheumatoid Arthritis	1.44	0.0241	C5,GNAQ,IKBKB,IL17RC,IRAK3,KRAS,SELE,TLR2
Inhibition of ARE-Mediated mRNA Degradation Pathway	1.43	0.0309	AGO4,DIS3L,MAPK7,PSMD13,XRN1
Neutrophil Extracellular Trap Signaling Pathway	1.41	0.0226	AGER,C5,COL24A1,COL6A2,COL7A1,ITGB1,PLA2G4D,PNPLA3,TLR2
Calcium Signaling	1.4	0.0273	ACTC1,ATP2B1,ATP2B4,CACNA1I,GRIA1,MYH6
Antioxidant Action of Vitamin C	1.39	0.0351	CSF2RA,IKBKB,PLA2G4D,PNPLA3
Role of MAPK Signaling in Promoting the Pathogenesis of Influenza	1.39	0.0351	ATP6V1A,KRAS,PLA2G4D,PNPLA3
Amyotrophic Lateral Sclerosis Signaling	1.37	0.0345	CAPN3,GRIA1,GRID1,Naip1 (includes others)
Role of JAK1 and JAK3 in γc Cytokine Signaling	1.36	0.0435	FES,IRS2,KRAS
Androgen Signaling	1.36	0.0296	CACNA1I,GNAQ,GNAZ,POLR2A,TAF5L
Eicosanoid Signaling	1.34	0.0429	PLA2G4D,PNPLA3,TBXAS1
Virus Entry via Endocytic Pathways	1.34	0.0339	ACTC1,ITGB1,KRAS,ZBTB12
Cholecystokinin/Gastrin-mediated Signaling	1.33	0.0336	BCAR1,GNAQ,KRAS,MAPK7
Neurovascular Coupling Signaling Pathway	1.31	0.0259	CACNA1I,GNAQ,GRIA1,KCNJ3,PLA2G4D,PNPLA3
TNFR2 Signaling	1.29	0.0625	IKBKB,Naip1 (includes others)
IL-15 Production	1.29	0.0325	AATK,CSF2RA,ERBB4,FES
ERK5 Signaling	1.29	0.0405	GNAQ,KRAS,MAPK7
NRF2-mediated Oxidative Stress Response	1.27	0.0253	ABCC4,ACTC1,Cyp2d9 (includes others),CYP2F1,KRAS,MAPK7
Macropinocytosis Signaling	1.26	0.0395	ITGB1,KRAS,MRC1
Creatine-phosphate Biosynthesis	1.26	0.2	MAP4K4
Tetrapyrrole Biosynthesis II	1.26	0.2	ALAS1

Regulation of eIF4 and p70S6K Signaling	1.26	0.0276	AGO4,ITGAD,ITGB1,KRAS,RPS12
NF-κB Activation by Viruses	1.23	0.0385	IKBKB,ITGB1,KRAS
MicroRNA Biogenesis Signaling Pathway	1.21	0.0267	AGO4,DIS3L,KRAS,POLR2A,XRN1
Macrophage Alternative Activation Signaling Pathway	1.19	0.0265	ABCA1,CD36,IRS2,LLGL1,MRC1
Atherosclerosis Signaling	1.19	0.0301	CD36,PLA2G4D,PNPLA3,SELE
TWEAK Signaling	1.18	0.0541	IKBKB,Naip1 (includes others)
Serotonin and Melatonin Biosynthesis	1.18	0.167	Asmt
CCR3 Signaling in Eosinophils	1.18	0.0299	GNAQ,GNAZ,KRAS,PLA2G4D
IL-17A Signaling in Fibroblasts	1.16	0.0526	IKBKB,IL17RC
Role of MAPK Signaling in the Pathogenesis of Influenza	1.15	0.0357	KRAS,PLA2G4D,PNPLA3
LPS/IL-1 Mediated Inhibition of RXR Function	1.15	0.0235	ABCA1,ABCC4,ALAS1,Cyp2d9 (includes others),CYP2F1,HS3ST5
Gap Junction Signaling	1.12	0.0253	ACTC1,GNAQ,GRIA1,KRAS,MAPK7
Adrenomedullin signaling pathway	1.12	0.0251	GNAQ,KRAS,MAPK7,TFAP2A,TTN
Role Of Chondrocytes In Rheumatoid Arthritis Signaling Pathway	1.11	0.0284	ASIC1,IL17RC,ITGB1,TLR2
Mechanisms of Viral Exit from Host Cells	1.1	0.0488	ACTC1,PDCD6IP
NER (Nucleotide Excision Repair, Enhanced Pathway)	1.08	0.0333	POLR2A,SLC19A1,TOP2A
Serotonin Receptor Signaling	1.06	0.0192	CACNA1I,GNAQ,ITGB1,KCNJ3,KRAS,PLA2G4D,PNPLA3,SNAI1,TTN
Actin Nucleation by ARP-WASP Complex	1.05	0.0323	ITGAD,ITGB1,KRAS
Cardiac Hypertrophy Signaling (Enhanced)	1.04	0.0185	GNAQ,IKBKB,IL17RC,Il3,ITGAD,ITGB1,KRAS,MAPK7,PDE11A,PDE3B
Agranulocyte Adhesion and Diapedesis	1.04	0.0238	ACTC1,C5,ITGB1,MYH6,SELE
Cellular Effects of Sildenafil (Viagra)	1.04	0.0267	ACTC1,MYH6,PDE3B,SLC4A11

Corticotropin Releasing Hormone Signaling	1.02	0.0263	CACNA1I,CRHR2,GNAQ,NR4A1
tRNA Splicing	1.02	0.0435	PDE11A,PDE3B
DNA damage-induced 14-3-3σ Signaling	1.02	0.0435	ATR,CHEK2
Protein Kinase A Signaling	1.01	0.0195	ANAPC1,GNAQ,PDE11A,PDE3B,PTPN3,PTPRO,TTN,UBASH3B
Sucrose Degradation V (Mammalian)	1.01	0.111	KHK
Heme Biosynthesis II	1.01	0.111	ALAS1
ERK/MAPK Signaling	1.01	0.0233	BCAR1,ITGAD,ITGB1,KRAS,PLA2G4D
iNOS Signaling	1	0.0426	IKBKB,IRAK3
Opioid Signaling Pathway	1	0.0214	CACNA1I,GNAQ,GNAZ,KCNJ3,KRAS,MAPK7
Relaxin Signaling	1	0.0258	GNAQ,GNAZ,PDE11A,PDE3B
p53 Signaling	0.999	0.0306	ATR,CHEK2,TP53BP2
Role of Pattern Recognition Receptors in Recognition of Bacteria and Viruses	0.992	0.0256	C5,Il3,NOD1,TLR2
Necroptosis Signaling Pathway	0.992	0.0256	CAPN3,IKBKB,PLA2G4D,SHARPIN
Dermatan Sulfate Biosynthesis (Late Stages)	0.988	0.0417	DSE,HS3ST5
Apelin Muscle Signaling Pathway	0.988	0.0417	GNAQ,GNAZ
Prostanoid Biosynthesis	0.968	0.1	TBXAS1
Ketolysis	0.968	0.1	ACAA2
Hepatic Fibrosis Signaling Pathway	0.961	0.0189	IKBKB,IRAK3,IRS2,ITGAD,ITGB1,KRAS,SNAI1,TTN
Assembly of RNA Polymerase II Complex	0.958	0.04	POLR2A,TAF5L
TNFR1 Signaling	0.944	0.0392	IKBKB,Naip1 (includes others)
Phagosome Maturation	0.941	0.0245	ATP6V1A,DYNC1LI2,EEA1,ZBTB12

Ketogenesis	0.929	0.0909	ACAA2
Purine Nucleotides De Novo Biosynthesis II	0.929	0.0909	PFAS
PPAR Signaling	0.914	0.028	IKBKB,KRAS,MAP4K4
HMGB1 Signaling	0.913	0.024	AGER,Il3,KRAS,SELE
CXCR4 Signaling	0.906	0.0238	BCAR1,GNAQ,GNAZ,KRAS
α-Adrenergic Signaling	0.897	0.0275	GNAQ,GNAZ,KRAS
Glucocorticoid Receptor Signaling	0.896	0.0172	IKBKB,IL17RC,KRAS,PLA2G4D,POLR2A,SELE,SMARCC1,TAF5L,TLR2,ZBTB12
Axonal Guidance Signaling	0.896	0.0176	ADAMTS19,ADAMTS20,BCAR1,FES,GNAQ,GNAZ,ITGAD,ITGB1,KRAS
Ribonucleotide Reductase Signaling Pathway	0.893	0.0235	ATR,KRAS,SMARCC1,SNAI1
Germ Cell-Sertoli Cell Junction Signaling	0.893	0.0235	ACTC1,BCAR1,ITGB1,KRAS
Osteoarthritis Pathway	0.882	0.0212	AGER,ITGAD,ITGB1,S100A9,TLR2
Cell Cycle Control of Chromosomal Replication	0.878	0.0357	CHEK2,TOP2A
Oxidative Ethanol Degradation III	0.865	0.0351	Cyp2d9 (includes others),CYP2F1
Role Of Osteoclasts In Rheumatoid Arthritis Signaling Pathway	0.854	0.0194	COL24A1,COL6A2,COL7A1,IKBKB,KRAS,Naip1 (includes others)
MSP-RON Signaling Pathway	0.853	0.0345	ACTC1,TLR2
Molecular Mechanisms of Cancer	0.852	0.0178	ATR,CHEK2,GNAQ,GNAZ,ITGAD,ITGB1,KRAS,Naip1 (includes others)
AMPK Signaling	0.85	0.0207	EEF2,GNAQ,GNAZ,IRS2,SMARCC1
Regulation of Actin-based Motility by Rho	0.847	0.0261	ACTC1,ITGAD,ITGB1
CDK5 Signaling	0.847	0.0261	ITGB1,KRAS,MAPK7
Nicotine Degradation III	0.841	0.0339	Aox3,CYP2F1
Tight Junction Signaling	0.835	0.0223	ACTC1,IGSF5,LLGL1,MYH6

Mevalonate Pathway I	0.831	0.0714	ACAA2
Phenylalanine Degradation IV (Mammalian, via Side Chain)	0.831	0.0714	ACSF3
PAK Signaling	0.831	0.0256	ITGAD,ITGB1,KRAS
Cardiac β-adrenergic Signaling	0.829	0.0222	GNAQ,GNAZ,PDE11A,PDE3B
Fc Epsilon RI Signaling	0.823	0.0254	INPP5B,KRAS,PLA2G4D
Semaphorin Signaling in Neurons	0.818	0.0328	FES,ITGB1
Dermatan Sulfate Biosynthesis	0.818	0.0328	DSE,HS3ST5
Acute Phase Response Signaling	0.799	0.0216	C5,IKBKB,KRAS,SERPINA3
Thrombopoietin Signaling	0.796	0.0317	IRS2,KRAS
LXR/RXR Activation	0.786	0.0244	ABCA1,CD36,PON3
D-myo-inositol (1,4,5)-trisphosphate Degradation	0.778	0.0625	INPP5B
Induction of Apoptosis by HIV1	0.775	0.0308	IKBKB,Naip1 (includes others)
Glutamate Receptor Signaling	0.765	0.0303	GRIA1,GRID1
Hepatic Cholestasis	0.764	0.0209	IKBKB,Il3,IRAK3,SLC22A6
GNRH Signaling	0.764	0.0209	CACNA1I,GNAQ,KRAS,MAPK7
3-phosphoinositide Degradation	0.764	0.0209	INPP4B,INPP5B,PDXP,PTPRO
GP6 Signaling Pathway	0.757	0.0236	COL24A1,COL6A2,COL7A1
Mitotic Roles of Polo-Like Kinase	0.755	0.0299	ANAPC1,CHEK2
IL-17A Signaling in Airway Cells	0.755	0.0299	IKBKB,IL17RC
Nicotine Degradation II	0.755	0.0299	Aox3,CYP2F1
Isoleucine Degradation I	0.754	0.0588	ACAA2

1D-myo-inositol Hexakisphosphate Biosynthesis II (Mammalian)	0.754	0.0588	INPP5B
D-myo-inositol (1,3,4)-trisphosphate Biosynthesis	0.754	0.0588	INPP5B
Hepatic Fibrosis / Hepatic Stellate Cell Activation	0.748	0.0206	COL24A1,COL6A2,COL7A1,MYH6
ERBB4 Signaling	0.745	0.0294	ERBB4,KRAS
IL-6 Signaling	0.744	0.0233	IKBKB,KRAS,MAP4K4
Phospholipases	0.735	0.029	PLA2G4D,PNPLA3
Mismatch Repair in Eukaryotes	0.732	0.0556	SLC19A1
Superpathway of Geranylgeranyldiphosphate Biosynthesis I (via Mevalonate)	0.732	0.0556	ACAA2
fMLP Signaling in Neutrophils	0.73	0.0229	GNAQ,GNAZ,KRAS
GM-CSF Signaling	0.725	0.0286	CSF2RA,KRAS
Synaptic Long Term Potentiation	0.724	0.0227	GNAQ,GRIA1,KRAS
HGF Signaling	0.724	0.0227	ITGAD,ITGB1,KRAS
GABA Receptor Signaling	0.724	0.0227	CACNA1I,GNAQ,GNAZ
Ferroptosis Signaling Pathway	0.724	0.0227	ABCA1,KRAS,SREBF2
Ephrin B Signaling	0.707	0.0278	GNAQ,GNAZ
Gustation Pathway	0.701	0.0197	ASIC1,CACNA1I,CD36,PDE3B
DHCR24 Signaling Pathway	0.692	0.0219	KRAS,PON3,SREBF2
RAC Signaling	0.692	0.0219	ITGAD,ITGB1,KRAS
Gαi Signaling	0.673	0.0214	GNAQ,GNAZ,KRAS
Angiopoietin Signaling	0.672	0.0263	IKBKB,KRAS
GDNF Family Ligand-Receptor Interactions	0.672	0.0263	IRS2,KRAS

RAR Activation	0.67	0.0164	GNAQ,GRIA1,Il3,PDE11A,PDE3B,RAB11FIP3,SMARCC1
Apelin Endothelial Signaling Pathway	0.667	0.0213	GNAQ,GNAZ,KRAS
Superpathway of D-myo-inositol (1,4,5)-trisphosphate Metabolism	0.654	0.0455	INPP5B
CLEAR Signaling Pathway	0.652	0.0175	ATP6V1A,IKBKB,KRAS,MAPK7,TLR2
Renal Cell Carcinoma Signaling	0.647	0.0253	CUL2,KRAS
Thyroid Cancer Signaling	0.647	0.0253	IRS2,KRAS
Role of MAPK Signaling in Inhibiting the Pathogenesis of Influenza	0.647	0.0253	PLA2G4D,PNPLA3
Activin Inhibin Signaling Pathway	0.634	0.0184	IKBKB,MAPK7,SNAI1,TLR2
Endocannabinoid Cancer Inhibition Pathway	0.633	0.0204	GNAQ,NSMAF,SMPD4
Chemokine Signaling	0.631	0.0247	GNAQ,KRAS
JAK/STAT Signaling	0.624	0.0244	GNAQ,KRAS
Tumoricidal Function of Hepatic Natural Killer Cells	0.621	0.0417	AIFM1
Semaphorin Neuronal Repulsive Signaling Pathway	0.616	0.02	FES,ITGAD,ITGB1
NAD Signaling Pathway	0.611	0.0199	AIFM1,POLR2A,SLC29A4
TR/RXR Activation	0.608	0.0238	PDE3B,SREBF2
VEGF Family Ligand-Receptor Interactions	0.608	0.0238	KRAS,PLA2G4D
PEDF Signaling	0.608	0.0238	IKBKB,KRAS
Bupropion Degradation	0.606	0.04	CYP2F1
Glycolysis I	0.606	0.04	GAPDHS
Gluconeogenesis I	0.606	0.04	GAPDHS
LPS-stimulated MAPK Signaling	0.601	0.0235	IKBKB,KRAS

Thrombin Signaling	0.599	0.0178	GNAQ,GNAZ,IKBKB,KRAS
CREB Signaling in Neurons	0.598	0.0148	CACNA1I,CRHR2,GNAQ,GNAZ,GPR83,GRIA1,GRID1,KRAS,POLR2A
HIPPO signaling	0.594	0.0233	LLGL1,TP53BP2
IL-17A Signaling in Gastric Cells	0.591	0.0385	IL17RC
EIF2 Signaling	0.59	0.0176	ACTC1,AGO4,KRAS,RPS12
PDGF Signaling	0.587	0.023	INPP5B,KRAS
S100 Family Signaling Pathway	0.583	0.0142	AGER,CACNA1I,CD36,CRHR2,GPR83,IKBKB,IRAK3,MAPK7,PLA2G4D,S100A9,VDR
Pregnenolone Biosynthesis	0.577	0.037	Cyp2d9 (includes others)
Aryl Hydrocarbon Receptor Signaling	0.57	0.0189	ATR,CHEK2,NCOA7
Unfolded protein response	0.566	0.0222	AMFR,SREBF2
CDP-diacylglycerol Biosynthesis I	0.563	0.0357	PNPLA3
Histidine Degradation VI	0.563	0.0357	Cyp2d9 (includes others)
Acute Myeloid Leukemia Signaling	0.56	0.022	CSF2RA,KRAS
G-Protein Coupled Receptor Signaling	0.559	0.0142	CRHR2,GNAQ,GNAZ,GPR83,IKBKB,KRAS,MAPK7,PDE11A,PDE3B,TTN
IL-12 Signaling and Production in Macrophages	0.554	0.0169	IKBKB,SELE,TLR2,VDR
ABRA Signaling Pathway	0.553	0.0217	ACTC1,ITGB1
Superpathway of Cholesterol Biosynthesis	0.55	0.0345	ACAA2
Pyroptosis Signaling Pathway	0.547	0.0215	NLRP4,TLR2
ERBB Signaling	0.547	0.0215	ERBB4,KRAS
Synaptogenesis Signaling Pathway	0.543	0.0159	CDH15,CDH23,CDH8,GRIA1,KRAS
Phosphatidylglycerol Biosynthesis II (Non-plastidic)	0.538	0.0333	PNPLA3

TGF-β Signaling	0.528	0.0208	KRAS,VDR
Ubiquinol-10 Biosynthesis (Eukaryotic)	0.526	0.0323	Cyp2d9 (includes others)
Gαq Signaling	0.518	0.0176	GNAQ,GNAZ,IKBKB
UVA-Induced MAPK Signaling	0.516	0.0204	KRAS,SMPD4
VEGF Signaling	0.51	0.0202	ACTC1,KRAS
Myelination Signaling Pathway	0.505	0.0153	ERBB4,ITGB1,KRAS,PLP1,SREBF2
ATM Signaling	0.504	0.02	ATR,CHEK2
4-1BB Signaling in T Lymphocytes	0.493	0.0294	IKBKB
Inhibition of Angiogenesis by TSP1	0.493	0.0294	CD36
Fatty Acid β-oxidation I	0.493	0.0294	ACAA2
Erythropoietin Signaling Pathway	0.488	0.0169	Il3,IRS2,KRAS
IL-9 Signaling	0.483	0.0286	IRS2
Nucleotide Excision Repair Pathway	0.483	0.0286	POLR2A
D-myo-inositol (1,4,5,6)-Tetrakisphosphate Biosynthesis	0.476	0.0167	INPP5B,PDXP,PTPRO
D-myo-inositol (3,4,5,6)-tetrakisphosphate Biosynthesis	0.476	0.0167	INPP5B,PDXP,PTPRO
IGF-1 Signaling	0.476	0.019	IRS2,KRAS
MIF-mediated Glucocorticoid Regulation	0.473	0.0278	PLA2G4D
Complement System	0.463	0.027	C5
Mitochondrial Dysfunction	0.455	0.0145	AIFM1,CACNA1I,CAPN3,MAPK7,MFN1
IL-17 Signaling	0.449	0.016	IL17RC,Il3,KRAS
Circadian Rhythm Signaling	0.443	0.0149	CACNA1I,GNAQ,GRIA1,KRAS

Granulocyte Adhesion and Diapedesis	0.441	0.0159	C5,ITGB1,SELE
Colorectal Cancer Metastasis Signaling	0.433	0.0148	GNAQ,GNAZ,KRAS,TLR2
Regulation Of The Epithelial Mesenchymal Transition By Growth Factors Pathway	0.431	0.0156	IKBKB,KRAS,SNAI1
Insulin Secretion Signaling Pathway	0.43	0.0147	AGO4,ASIC1,CACNA1I,GNAQ
Leukocyte Extravasation Signaling	0.427	0.0155	ACTC1,BCAR1,ITGB1
IL-13 Signaling Pathway	0.421	0.0172	CD36,IL17RC
April Mediated Signaling	0.42	0.0238	IKBKB
Acetone Degradation I (to Methylglyoxal)	0.42	0.0238	CYP2F1
D-myo-inositol-5-phosphate Metabolism	0.416	0.0153	INPP5B,PDXP,PTPRO
GPCR-Mediated Nutrient Sensing in Enteroendocrine Cells	0.412	0.0169	CACNA1I,GNAQ
B Cell Activating Factor Signaling	0.412	0.0233	IKBKB
Oncostatin M Signaling	0.412	0.0233	KRAS
MSP-RON Signaling In Macrophages Pathway	0.408	0.0168	IKBKB,KRAS
MIF Regulation of Innate Immunity	0.404	0.0227	PLA2G4D
BER (Base Excision Repair) Pathway	0.404	0.0227	SLC19A1
Sphingosine-1-phosphate Signaling	0.403	0.0167	GNAQ,SMPD4
p38 MAPK Signaling	0.403	0.0167	IRAK3,PLA2G4D
ID1 Signaling Pathway	0.399	0.0149	KRAS,S100A9,TFAP2A
Renin-Angiotensin Signaling	0.399	0.0165	GNAQ,KRAS
Huntington's Disease Signaling	0.399	0.0141	CAPN3,GNAQ,POLR2A,PSMD13
CDX Gastrointestinal Cancer Signaling Pathway	0.396	0.0149	IKBKB,Il3,SNAI1

Coronavirus Pathogenesis Pathway	0.39	0.0147	ATP6V1A,IKBKB,RPS12
Role of RIG1-like Receptors in Antiviral Innate Immunity	0.389	0.0217	IKBKB
Apelin Pancreas Signaling Pathway	0.389	0.0217	PDE3B
RHOA Signaling	0.386	0.0161	ACTC1,TTN
3-phosphoinositide Biosynthesis	0.383	0.0146	INPP5B,PDXP,PTPRO
Role of IL-17F in Allergic Inflammatory Airway Diseases	0.382	0.0213	IL17RC
nNOS Signaling in Neurons	0.382	0.0213	CAPN3
Ephrin A Signaling	0.382	0.0213	BCAR1
Estrogen Biosynthesis	0.382	0.0213	CYP2F1
Retinol Biosynthesis	0.382	0.0213	PNPLA3
Gαs Signaling	0.378	0.0159	GNAQ,GNAZ
14-3-3-mediated Signaling	0.374	0.0157	KRAS,PDCD6IP
Endocannabinoid Developing Neuron Pathway	0.374	0.0157	KRAS,MAPK7
Spliceosomal Cycle	0.368	0.0204	SF3B1
Melanoma Signaling	0.362	0.02	KRAS
MYC Mediated Apoptosis Signaling	0.362	0.02	IKBKB
FAT10 Cancer Signaling Pathway	0.362	0.02	IKBKB
mTOR Signaling	0.359	0.014	KRAS,RICTOR,RPS12
Chondroitin Sulfate Biosynthesis (Late Stages)	0.355	0.0196	HS3ST5
Amyloid Processing	0.355	0.0196	CAPN3
P2Y Purigenic Receptor Signaling Pathway	0.351	0.015	GNAQ,KRAS

STAT3 Pathway	0.343	0.0148	IL17RC,KRAS
SNARE Signaling Pathway	0.34	0.0147	MYH6,RIMS1
Role of PKR in Interferon Induction and Antiviral Response	0.34	0.0147	IKBKB,NLRP4
Iron homeostasis signaling pathway	0.333	0.0145	ATP6V1A,SLC48A1
Lymphotoxin β Receptor Signaling	0.332	0.0182	IKBKB
Triacylglycerol Biosynthesis	0.332	0.0182	PNPLA3
Role of NFAT in Cardiac Hypertrophy	0.33	0.0134	CACNA1I,GNAQ,KRAS
FAT10 Signaling Pathway	0.326	0.0179	PSMD13
MSP-RON Signaling In Cancer Cells Pathway	0.326	0.0143	ITGB1,KRAS
HER-2 Signaling in Breast Cancer	0.322	0.0132	IKBKB,ITGB1,KRAS
CD27 Signaling in Lymphocytes	0.32	0.0175	IKBKB
CNTF Signaling	0.32	0.0175	KRAS
Role of IL-17A in Arthritis	0.32	0.0175	IL17RC
Triacylglycerol Degradation	0.32	0.0175	PNPLA3
Xenobiotic Metabolism General Signaling Pathway	0.316	0.014	KRAS,MAPK7
Cancer Drug Resistance By Drug Efflux	0.315	0.0172	KRAS
Polyamine Regulation in Colon Cancer	0.31	0.0169	KRAS
Chondroitin Sulfate Biosynthesis	0.31	0.0169	HS3ST5
Estrogen Receptor Signaling	0.306	0.0122	GNAQ,GNAZ,KRAS,MED13,SNAI1
Endometrial Cancer Signaling	0.305	0.0167	KRAS
GADD45 Signaling	0.305	0.0167	ATR

Superpathway of Inositol Phosphate Compounds	0.304	0.0128	INPP5B,PDXP,PTPRO
Role of JAK2 in Hormone-like Cytokine Signaling	0.295	0.0161	IRS2
IL-2 Signaling	0.295	0.0161	KRAS
Melatonin Degradation I	0.29	0.0159	CYP2F1
IL-10 Signaling	0.282	0.013	IKBKB,MAP4K4
PXR/RXR Activation	0.281	0.0154	ALAS1
Activation of IRF by Cytosolic Pattern Recognition Receptors	0.281	0.0154	IKBKB
ERB2-ERBB3 Signaling	0.281	0.0154	KRAS
Pyridoxal 5'-phosphate Salvage Pathway	0.281	0.0154	MAPK7
Epithelial Adherens Junction Signaling	0.273	0.0127	KRAS,SNAI1
CD40 Signaling	0.272	0.0149	IKBKB
Superpathway of Melatonin Degradation	0.268	0.0147	CYP2F1
Remodeling of Epithelial Adherens Junctions	0.268	0.0147	ACTC1
Cell Cycle: G1/S Checkpoint Regulation	0.268	0.0147	ATR
Stearate Biosynthesis I (Animals)	0.264	0.0145	TBXAS1
SPINK1 General Cancer Pathway	0.264	0.0145	KRAS
Melatonin Signaling	0.252	0.0139	GNAQ
Netrin Signaling	0.252	0.0139	CACNA1I
Glioma Invasiveness Signaling	0.248	0.0137	KRAS
Cardiac Hypertrophy Signaling	0.244	0.0115	GNAQ,GNAZ,KRAS
Granzyme A Signaling	0.24	0.0133	HMGB2

GPCR-Mediated Integration of Enteroendocrine Signaling Exemplified by an L Cell	0.24	0.0133	GNAQ
Leptin Signaling in Obesity	0.237	0.0132	PDE3B
Aldosterone Signaling in Epithelial Cells	0.235	0.0116	ASIC1,KRAS
Antiproliferative Role of Somatostatin Receptor 2	0.233	0.013	KRAS
VDR/RXR Activation	0.23	0.0128	VDR
Neurotrophin/TRK Signaling	0.23	0.0128	KRAS
IL-3 Signaling	0.226	0.0127	KRAS
Role of JAK family kinases in IL-6-type Cytokine Signaling	0.226	0.0127	SERPINA3
Heparan Sulfate Biosynthesis (Late Stages)	0.223	0.0125	HS3ST5
FLT3 Signaling in Hematopoietic Progenitor Cells	0.216	0.0122	KRAS
Estrogen-Dependent Breast Cancer Signaling	0.213	0.012	KRAS
BAG2 Signaling Pathway	0.21	0.0119	PSMD13
Cyclins and Cell Cycle Regulation	0.207	0.0118	ATR
Heparan Sulfate Biosynthesis	0.201	0.0115	HS3ST5
Regulation Of The Epithelial Mesenchymal Transition In Development Pathway	0.201	0.0115	SNAI1
Pulmonary Healing Signaling Pathway	0	0.0101	KRAS,TLR2
Immunogenic Cell Death Signaling Pathway	0	0.0111	GZMH
Macrophage Classical Activation Signaling Pathway	0	0.0106	IKBKB,Il3
Role Of Osteoblasts In Rheumatoid Arthritis Signaling Pathway	0	0.0041	Il3
Natural Killer Cell Signaling	0	0.0101	ITGB1,KRAS
Chaperone Mediated Autophagy Signaling Pathway	0	0.00622	ATP6V1A,IKBKB,IL17RC,RICTOR

IL-33 Signaling Pathway	0	0.0108	IKBKB,SELE
FXR/RXR Activation	0	0.00794	PON3
Clathrin-mediated Endocytosis Signaling	0	0.00962	ACTC1,ITGB1
Fcγ Receptor-mediated Phagocytosis in Macrophages and Monocytes	0	0.0106	ACTC1
Role of NFAT in Regulation of the Immune Response	0	0.00386	GNAQ,GNAZ,IKBKB,KRAS
FcγRIIB Signaling in B Lymphocytes	0	0.00375	CACNA1I,KRAS
CCR5 Signaling in Macrophages	0	0.00601	CACNA1I,GNAQ,GNAZ
Calcium-induced T Lymphocyte Apoptosis	0	0.00217	NR4A1
Cytotoxic T Lymphocyte-mediated Apoptosis of Target Cells	0	0.00235	ZBTB12
Airway Pathology in Chronic Obstructive Pulmonary Disease	0	0.00847	Il3
CTLA4 Signaling in Cytotoxic T Lymphocytes	0	0.00658	IDO2,ITGB1,KRAS,ZBTB12
CD28 Signaling in T Helper Cells	0	0.00193	IKBKB
IL-15 Signaling	0	0.00189	KRAS
Dendritic Cell Maturation	0	0.00503	IKBKB,TLR2,ZBTB12
Reelin Signaling in Neurons	0	0.00725	ITGB1
HIF1α Signaling	0	0.00962	CUL2,KRAS
Neuropathic Pain Signaling In Dorsal Horn Neurons	0	0.0099	GRIA1
Factors Promoting Cardiogenesis in Vertebrates	0	0.00654	MYH6
ICOS-ICOSL Signaling in T Helper Cells	0	0.00197	IKBKB
Human Embryonic Stem Cell Pluripotency	0	0.00498	KRAS
Melanocyte Development and Pigmentation Signaling	0	0.0102	KRAS

Role of NANOG in Mammalian Embryonic Stem Cell Pluripotency	0	0.00806	KRAS
Prolactin Signaling	0	0.0105	KRAS
Prostate Cancer Signaling	0	0.00877	KRAS
Type I Diabetes Mellitus Signaling	0	0.00196	IKBKB
Small Cell Lung Cancer Signaling	0	0.0104	IKBKB
Glioma Signaling	0	0.008	KRAS
Bladder Cancer Signaling	0	0.00862	KRAS
Chronic Myeloid Leukemia Signaling	0	0.0108	IKBKB,ITGB1,KRAS
Non-Small Cell Lung Cancer Signaling	0	0.0106	KRAS
Production of Nitric Oxide and Reactive Oxygen Species in Macrophages	0	0.0105	IKBKB,TLR2
p70S6K Signaling	0	0.00516	EEF2,GNAQ,KRAS
Pancreatic Adenocarcinoma Signaling	0	0.00794	KRAS
G Protein Signaling Mediated by Tubby	0	0.00427	GNAQ,GNAZ
Communication between Innate and Adaptive Immune Cells	0	0.00214	TLR2,ZBTB12
Crosstalk between Dendritic Cells and Natural Killer Cells	0	0.011	ACTC1
Systemic Lupus Erythematosus Signaling	0	0.00281	C5,KRAS,PRPF38A
CDC42 Signaling	0	0.00521	ITGAD,ITGB1,LLGL1
FAK Signaling	0	0.00865	BCAR1,CAPN3,CRHR2,GPR83,IL17RC,ITGAD,ITGB1,KRAS,MAPK7
Role of Osteoblasts, Osteoclasts and Chondrocytes in Rheumatoid Arthritis	0	0.00877	IKBKB,Naip1 (includes others)
Phospholipase C Signaling	0	0.00446	GNAQ,ITGAD,ITGB1,KRAS,PLA2G4D
Ovarian Cancer Signaling	0	0.00633	KRAS

Altered T Cell and B Cell Signaling in Rheumatoid Arthritis	0	0.00106	TLR2
Breast Cancer Regulation by Stathmin1	0	0.00842	ANKHD1/ANKHD1-EIF4EBP3,CRHR2,GNAQ,GPR83,KRAS
RANK Signaling in Osteoclasts	0	0.011	IKBKB
Glioblastoma Multiforme Signaling	0	0.00585	KRAS
Neuroprotective Role of THOP1 in Alzheimer's Disease	0	0.00826	SERPINA3
Regulation of IL-2 Expression in Activated and Anergic T Lymphocytes	0	0.00433	IKBKB,KRAS
NUR77 Signaling in T Lymphocytes	0	0.00585	MAPK7,NR4A1,ZBTB12
PKCθ Signaling in T Lymphocytes	0	0.00538	CACNA1I,IKBKB,KRAS
PI3K Signaling in B Lymphocytes	0	0.00508	IKBKB,IRS2,KRAS
Dopamine-DARPP32 Feedback in cAMP Signaling	0	0.0108	GNAQ,KCNJ3
Telomerase Signaling	0	0.00926	KRAS
Mouse Embryonic Stem Cell Pluripotency	0	0.00962	KRAS
Transcriptional Regulatory Network in Embryonic Stem Cells	0	0.0061	KRAS
eNOS Signaling	0	0.00641	GNAQ
Salvage Pathways of Pyrimidine Ribonucleotides	0	0.0103	MAPK7
Regulation of the Epithelial-Mesenchymal Transition Pathway	0	0.0103	KRAS,SNAI1
TEC Kinase Signaling	0	0.00865	ACTC1,GNAQ,GNAZ,ITGAD,ITGB1
SAPK/JNK Signaling	0	0.00398	KRAS,MAP4K4
Nitric Oxide Signaling in the Cardiovascular System	0	0.00833	PDE3B
Xenobiotic Metabolism Signaling	0	0.0103	HS3ST5,KRAS,MAPK7
IL-4 Signaling	0	0.0104	COL24A1,COL6A2,COL7A1,IRS2,KRAS,RICTOR

B Cell Receptor Signaling	0	0.00472	IKBKB,INPP5B,KRAS
WNT/β-catenin Signaling	0	0.00575	GNAQ
cAMP-mediated signaling	0	0.00847	PDE11A,PDE3B
NF-κB Signaling	0	0.00876	IKBKB,IRAK3,KRAS,MAP4K4,TLR2
T Cell Receptor Signaling	0	0.00649	IKBKB,ITGB1,KRAS,ZBTB12
BMP signaling pathway	0	0.011	KRAS
Autophagy	0	0.00926	ATR,IRS2
PD-1, PD-L1 cancer immunotherapy pathway	0	0.00935	ZBTB12
Sumoylation Pathway	0	0.00971	SLC19A1
Sirtuin Signaling Pathway	0	0.00683	ABCA1,MAPK7
Th17 Activation Pathway	0	0.00207	IRAK3
Apelin Adipocyte Signaling Pathway	0	0.011	MAPK7
Apelin Cardiomyocyte Signaling Pathway	0	0.0101	MAPK7
T Cell Exhaustion Signaling Pathway	0	0.00176	KRAS
Systemic Lupus Erythematosus In T Cell Signaling Pathway	0	0.00311	KRAS,ZBTB12
Systemic Lupus Erythematosus In B Cell Signaling Pathway	0	0.00552	Il3,INPP5B,KRAS,MAP4K4
White Adipose Tissue Browning Pathway	0	0.00725	CACNA1I
HOTAIR Regulatory Pathway	0	0.00613	AGO4
Xenobiotic Metabolism CAR Signaling Pathway	0	0.00521	HS3ST5
Xenobiotic Metabolism PXR Signaling Pathway	0	0.00518	HS3ST5
Kinetochore Metaphase Signaling Pathway	0	0.00901	ANAPC1

Tumor Microenvironment Pathway	0	0.0112	IDO2,KRAS
BR1			
Ingenuity Canonical Pathways	-log(p-value)	Ratio	Molecules
PI3K/AKT Signaling	3.59	0.055	GAB2,IKBKB,IL13RA2,IL17RC,IL17RD,INPP5B,ITGAD,ITGB1,ITGB8,KRAS,SOS1
Calcium Transport I	3.41	0.3	ATP2B1,ATP2B2,ATP2B4
PTEN Signaling	3.28	0.0596	BCAR1,IKBKB,INPP5B,ITGAD,ITGB1,ITGB8,KRAS,SHARPIN,SOS1
RHOGDI Signaling	3.24	0.05	ACTC1,CDH15,CDH23,CDH8,GNAQ,GNAZ,ITGAD,ITGB1,ITGB8,MYH6,PIKFYVE
Multiple Sclerosis Signaling Pathway	3.2	0.0495	AIFM1,ASIC1,C5,CAPN3,IL17D,IL17RC,IL1F10,Il3,NFATC2,PLP1,TLR2
Apoptosis Signaling	2.97	0.0673	AIFM1,CAPN3,IKBKB,KRAS,LMNA,MAP4K4,Naip1 (includes others)
Paxillin Signaling	2.9	0.0654	ACTC1,BCAR1,ITGAD,ITGB1,ITGB8,KRAS,SOS1
Oxytocin Signaling Pathway	2.87	0.0426	ATP2B1,ATP2B2,ATP2B4,CACNA1B,CD36,EEF2,GNAQ,KRAS,MAPK7,MYH6,PLA2G4D,SOS1
Integrin Signaling	2.8	0.0472	ACTC1,BCAR1,CAPN3,ITGAD,ITGB1,ITGB8,KRAS,PIKFYVE,SOS1,TTN
Cardiac Hypertrophy Signaling (Enhanced)	2.76	0.0332	AKAP13,CACNA1B,GNAQ,IKBKB,IL13RA2,IL17D,IL17RC,IL17RD,IL1F10,Il3,ITGAD,ITGB1,ITGB8,KRAS,MAPK7,NFATC2,PDE11A,PDE3B
Calcium Signaling	2.68	0.0455	ACTC1,ATP2B1,ATP2B2,ATP2B4,CACNA1B,CACNA1I,GRIA1,MYH6,NFATC2,TRPM8
Neuregulin Signaling	2.68	0.0598	ERBB4,ITGAD,ITGB1,ITGB8,KRAS,SOS1,TMEFF2
Senescence Pathway	2.65	0.0401	ANAPC1,ATR,CACNA1B,CAPN3,CBX2,CHEK2,HBP1,IKBKB,KRAS,MAPK7,NFATC2,TLR2
Creatine-phosphate Biosynthesis	2.65	0.4	CKM,MAP4K4

Synaptic Long Term Depression	2.47	0.0455	CACNA1B,CACNA1I,GNAQ,GNAZ,GRIA1,GRID1,KRAS,PLA2G4D,PNPLA3
G Beta Gamma Signaling	2.44	0.0543	CACNA1B,CACNA1I,GNAQ,GNAZ,KCNJ3,KRAS,SOS1
Ephrin Receptor Signaling	2.41	0.0446	BCAR1,GNAQ,GNAZ,ITGAD,ITGB1,ITGB8,KRAS,MAP4K4,SOS1
Actin Cytoskeleton Signaling	2.36	0.041	ACTC1,BCAR1,ITGAD,ITGB1,ITGB8,KRAS,MYH6,SOS1,TRIO,TTN
Pathogen Induced Cytokine Storm Signaling Pathway	2.33	0.035	C5,COL24A1,COL6A2,COL7A1,CSF2RA,IL17D,IL1F10,Il3,MAPK7,Naip1 (includes others),NLRP4,NOD1,TLR2
Phagosome Formation	2.29	0.0288	BCAR1,CD36,CHRM2,CRHR2,ELMO2,GAB2,GPR83,ITGAD,ITGB1,ITGB8,KRAS,MAPK7,MRC1,MYH6,PIKFYVE,PLA2G4D,PNPLA3,SOS1,TLR2,TTN
Wound Healing Signaling Pathway	2.26	0.0397	COL24A1,COL6A2,COL7A1,IKBKB,IL17D,IL1F10,Il3,ITGB1,KRAS,SOS1
Caveolar-mediated Endocytosis Signaling	2.24	0.0667	ACTC1,ITGAD,ITGB1,ITGB8,ZBTB12
nNOS Signaling in Skeletal Muscle Cells	2.22	0.0833	CACNA1B,CACNA1I,CAPN3,SNTA1
Sphingomyelin Metabolism	2.22	0.25	ENPP7,SGMS2
Hereditary Breast Cancer Signaling	2.21	0.0493	ATR,CHEK2,FANCA,FANCG,KRAS,POLR2A,SLC19A1
TREM1 Signaling	2.19	0.0649	ITGB1,Naip1 (includes others),NLRP4,NOD1,TLR2
Toll-like Receptor Signaling	2.17	0.0641	IKBKB,IL1F10,IRAK3,MAP4K4,TLR2
Cell Cycle: G2/M DNA Damage Checkpoint Regulation	2.16	0.08	ATR,CHEK2,TOP2A,TRIP12
Role of BRCA1 in DNA Damage Response	2.13	0.0625	ATR,CHEK2,FANCA,FANCG,SLC19A1
Endocannabinoid Neuronal Synapse Pathway	2.1	0.047	CACNA1B,CACNA1I,GNAQ,GRIA1,KCNJ3,MAPK7,RIMS1
Signaling by Rho Family GTPases	2.09	0.0375	ACTC1,CDH15,CDH23,CDH8,GNAQ,GNAZ,ITGAD,ITGB1,ITGB8,PIKFYVE
NOD1/2 Signaling Pathway	2.07	0.0423	IKBKB,IL17D,IL1F10,Il3,MAP4K4,NOD1,SHARPIN,TLR2
Type II Diabetes Mellitus Signaling	2.04	0.0458	CACNA1B,CACNA1I,CD36,ENPP7,IKBKB,IRS2,NSMAF

Protein Ubiquitination Pathway	2.03	0.0366	AMFR,ANAPC1,CUL2,NEDD4L,PSMD13,SMURF1,USO1,USP13,USP9Y,ZBTB12
Neurovascular Coupling Signaling Pathway	2.03	0.0388	CACNA1B,CACNA1I,CHRM2,GNAQ,GRIA1,KCNJ3,KCNU1,PLA2G4D,PNPLA3
Virus Entry via Endocytic Pathways	2.03	0.0508	ACTC1,CXADR,ITGB1,ITGB8,KRAS,ZBTB12
Neuroinflammation Signaling Pathway	2.02	0.0347	AGER,GRIA1,IKBKB,IRAK3,KCNJ3,MAPK7,Naip1 (includes others),NFATC2,PLA2G4D,TLR2,ZBTB12
Cholecystokinin/Gastrin-mediated Signaling	2.01	0.0504	BCAR1,GNAQ,IL1F10,KRAS,MAPK7,SOS1
Oxytocin In Brain Signaling Pathway	1.94	0.0402	CACNA1B,CACNA1I,GNAQ,KRAS,MAPK7,NLRP4,PLA2G4D,PNPLA3
Regulation of Cellular Mechanics by Calpain Protease	1.92	0.0556	CAPN3,ITGAD,ITGB1,ITGB8,KRAS
Actin Nucleation by ARP-WASP Complex	1.86	0.0538	ITGAD,ITGB1,ITGB8,KRAS,SOS1
Thrombopoietin Signaling	1.81	0.0635	GAB2,IRS2,KRAS,SOS1
Death Receptor Signaling	1.8	0.0521	ACTC1,IKBKB,LMNA,MAP4K4,Naip1 (includes others)
Gα12/13 Signaling	1.79	0.0451	CDH15,CDH23,CDH8,IKBKB,KRAS,MAPK7
Sperm Motility	1.76	0.035	AATK,CACNA1I,CSF2RA,ERBB4,FES,GNAQ,GNAZ,PLA2G4D,PNPLA3
Role of IL-17A in Psoriasis	1.73	0.143	IL17RC,S100A9
Insulin Receptor Signaling	1.69	0.0429	ASIC1,INPP5B,IRS2,KRAS,PDE3B,SOS1
Agrin Interactions at Neuromuscular Junction	1.68	0.058	ACTC1,ERBB4,ITGB1,KRAS
Regulation of eIF4 and p70S6K Signaling	1.68	0.0387	AGO4,ITGAD,ITGB1,ITGB8,KRAS,RPS12,SOS1
WNK Renal Signaling Pathway	1.64	0.0472	AMFR,ANAPC1,ASIC1,CUL2,IRS2
Acute Phase Response Signaling	1.63	0.0378	C5,IKBKB,IL1F10,KRAS,RBP3,SERPINA3,SOS1
PPAR Signaling	1.62	0.0467	IKBKB,IL1F10,KRAS,MAP4K4,SOS1

Axonal Guidance Signaling	1.6	0.0275	ADAM19,ADAMTS19,ADAMTS20,ADAMTS9,BCAR1,FES,GNAQ,GNAZ,ITGAD,ITGB1,ITGB8,KRAS,NFATC2,SOS1
Hepatic Cholestasis	1.56	0.0366	ABCC2,IKBKB,IL17D,IL1F10,Il3,IRAK3,SLC22A6
Dilated Cardiomyopathy Signaling Pathway	1.56	0.04	ACTC1,CACNA1B,CACNA1I,LMNA,MYH6,TTN
Macropinocytosis Signaling	1.54	0.0526	ITGB1,ITGB8,KRAS,MRC1
Endothelin-1 Signaling	1.53	0.0361	GNAQ,GNAZ,KRAS,MAPK7,PLA2G4D,PNPLA3,SOS1
Glutaryl-CoA Degradation	1.52	0.111	ACAA2,TBXAS1
PPARα/RXRα Activation	1.52	0.0359	ABCA1,CD36,GNAQ,IKBKB,KRAS,MAP4K4,SOS1
Role of MAPK Signaling in Promoting the Pathogenesis of Influenza	1.52	0.0439	ATP6V0D2,ATP6V1A,KRAS,PLA2G4D,PNPLA3
Regulation of Actin-based Motility by Rho	1.5	0.0435	ACTC1,ITGAD,ITGB1,ITGB8,PIKFYVE
Role of Macrophages, Fibroblasts and Endothelial Cells in Rheumatoid Arthritis	1.5	0.0301	C5,GNAQ,IKBKB,IL17RC,IL1F10,IRAK3,KRAS,NFATC2,SELE,TLR2
Amyotrophic Lateral Sclerosis Signaling	1.49	0.0431	CACNA1B,CAPN3,GRIA1,GRID1,Naip1 (includes others)
Role of Pattern Recognition Receptors in Recognition of Bacteria and Viruses	1.49	0.0385	C5,IL17D,IL1F10,Il3,NOD1,TLR2
Adrenomedullin signaling pathway	1.48	0.0352	GNAQ,IL1F10,KRAS,MAPK7,SOS1,TFAP2A,TTN
PAK Signaling	1.48	0.0427	ITGAD,ITGB1,ITGB8,KRAS,SOS1
JAK/STAT Signaling	1.44	0.0488	GNAQ,KRAS,PIAS2,SOS1
NGF Signaling	1.44	0.0417	IKBKB,KRAS,MAPK7,SOS1,TRIO
Sertoli Cell-Sertoli Cell Junction Signaling	1.41	0.034	ACTC1,BCAR1,IGSF5,ITGAD,ITGB1,ITGB8,KRAS
Phagosome Maturation	1.41	0.0368	ATP6V0D2,ATP6V1A,DYNC1LI2,EEA1,PIKFYVE,ZBTB12
LPS/IL-1 Mediated Inhibition of RXR Function	1.38	0.0314	ABCA1,ABCC2,ABCC4,ALAS1,Cyp2d9 (includes others),GSTK1,HS3ST5,IL1F10
HMGB1 Signaling	1.37	0.0359	AGER,IL17D,IL1F10,Il3,KRAS,SELE

Androgen Signaling	1.35	0.0355	CACNA1B,CACNA1I,GNAQ,GNAZ,POLR2A,TAF5L
Diphthamide Biosynthesis	1.35	0.333	EEF2
5-aminoimidazole Ribonucleotide Biosynthesis I	1.35	0.333	PFAS
ERK/MAPK Signaling	1.33	0.0326	BCAR1,ITGAD,ITGB1,ITGB8,KRAS,PLA2G4D,SOS1
The Visual Cycle	1.33	0.087	RBP3,RDH13
IL-6 Signaling	1.32	0.0388	IKBKB,IL1F10,KRAS,MAP4K4,SOS1
HGF Signaling	1.29	0.0379	ITGAD,ITGB1,ITGB8,KRAS,SOS1
Synaptogenesis Signaling Pathway	1.28	0.0286	CACNA1B,CDH15,CDH23,CDH8,GRIA1,KRAS,NLGN3,SOS1,SYT10
Atherosclerosis Signaling	1.28	0.0376	CD36,IL1F10,PLA2G4D,PNPLA3,SELE
Erythropoietin Signaling Pathway	1.27	0.0339	IL17D,IL1F10,Il3,IRS2,KRAS,SOS1
Tryptophan Degradation III (Eukaryotic)	1.26	0.08	ACAA2,TBXAS1
Cardiac β-adrenergic Signaling	1.24	0.0333	AKAP13,CACNA1B,GNAQ,GNAZ,PDE11A,PDE3B
Role of CHK Proteins in Cell Cycle Checkpoint Control	1.23	0.0517	ATR,CHEK2,SLC19A1
RAC Signaling	1.23	0.0365	ITGAD,ITGB1,ITGB8,KRAS,PIKFYVE
IL-1 Signaling	1.23	0.0417	GNAQ,GNAZ,IKBKB,IRAK3
TGF-β Signaling	1.23	0.0417	KRAS,SMURF1,SOS1,VDR
2-ketoglutarate Dehydrogenase Complex	1.23	0.25	OGDH
Hepatic Fibrosis Signaling Pathway	1.22	0.026	CACNA1B,IKBKB,IL1F10,IRAK3,IRS2,ITGAD,ITGB1,ITGB8,KRAS,SOS1,TTN
p53 Signaling	1.2	0.0408	ATR,CHEK2,JMY,TP53BP2
Glucocorticoid Receptor Signaling	1.2	0.0241	IKBKB,IL13RA2,IL17RC,IL17RD,KRAS,KRT82,NFATC2,PLA2G4D,POLR2A,SELE,SOS1,TAF5L,TLR2,ZBTB12

Gαi Signaling	1.2	0.0357	CHRM2,GNAQ,GNAZ,KRAS,SOS1
Pregnenolone Biosynthesis	1.2	0.0741	Cyp2b23,Cyp2d9 (includes others)
RAR Activation	1.19	0.0257	GNAQ,GRIA1,IL17D,IL1F10,Il3,KLF2,PDE11A,PDE3B,RAB11FIP3,RBP3,RDH13
Role Of Chondrocytes In Rheumatoid Arthritis Signaling Pathway	1.19	0.0355	ASIC1,IL17RC,IL1F10,ITGB1,TLR2
Opioid Signaling Pathway	1.19	0.0286	CACNA1B,CACNA1I,GNAQ,GNAZ,KCNJ3,KRAS,MAPK7,SOS1
CDP-diacylglycerol Biosynthesis I	1.17	0.0714	AGPAT4,PNPLA3
Histidine Degradation VI	1.17	0.0714	Cyp2b23,Cyp2d9 (includes others)
Macrophage Alternative Activation Signaling Pathway	1.16	0.0317	ABCA1,CD36,IL1F10,IRS2,LLGL1,MRC1
NRF2-mediated Oxidative Stress Response	1.15	0.0295	ABCC2,ABCC4,ACTC1,Cyp2d9 (includes others),GSTK1,KRAS,MAPK7
GNRH Signaling	1.14	0.0314	CACNA1B,CACNA1I,GNAQ,KRAS,MAPK7,SOS1
Tetrapyrrole Biosynthesis II	1.13	0.2	ALAS1
Phosphatidylglycerol Biosynthesis II (Non-plastidic)	1.12	0.0667	AGPAT4,PNPLA3
AMPK Signaling	1.11	0.0289	AK2,CKM,EEF2,GNAQ,GNAZ,IRS2,PPM1G
Cellular Effects of Sildenafil (Viagra)	1.1	0.0333	ACTC1,CACNA1B,MYH6,PDE3B,SLC4A11
Ubiquinol-10 Biosynthesis (Eukaryotic)	1.1	0.0645	Cyp2b23,Cyp2d9 (includes others)
Mitochondrial Dysfunction	1.09	0.0262	AIFM1,ATPAF2,CACNA1B,CACNA1I,CAPN3,GSTK1,MAPK7,MFN1,OGDH
Gap Junction Signaling	1.08	0.0303	ACTC1,GNAQ,GRIA1,KRAS,MAPK7,SOS1
Corticotropin Releasing Hormone Signaling	1.08	0.0329	CACNA1B,CACNA1I,CRHR2,GNAQ,NR4A1
Molecular Mechanisms of Cancer	1.08	0.0244	ATR,CHEK2,GAB2,GNAQ,GNAZ,ITGAD,ITGB1,ITGB8,KRAS,Naip1 (includes others),SOS1
TNFR2 Signaling	1.07	0.0625	IKBKB,Naip1 (includes others)

ERBB4 Signaling	1.07	0.0441	ERBB4,KRAS,SOS1
ILK Signaling	1.06	0.0299	ACTC1,IRS2,ITGB1,ITGB8,MYH6,RICTOR
Role of JAK1 and JAK3 in γc Cytokine Signaling	1.06	0.0435	FES,IRS2,KRAS
Gustation Pathway	1.04	0.0296	ASIC1,CACNA1B,CACNA1I,CD36,LIPI,PDE3B
GM-CSF Signaling	1.04	0.0429	CSF2RA,KRAS,SOS1
Eicosanoid Signaling	1.04	0.0429	PLA2G4D,PNPLA3,TBXAS1
Antioxidant Action of Vitamin C	1.02	0.0351	CSF2RA,IKBKB,PLA2G4D,PNPLA3
Netrin Signaling	1.01	0.0417	CACNA1B,CACNA1I,NFATC2
Role of Tissue Factor in Cancer	1.01	0.029	GNAQ,IKBKB,ITGB1,KRAS,MAPK7,PDXP
Protein Kinase A Signaling	1.01	0.0243	AKAP13,ANAPC1,GNAQ,NFATC2,PDE11A,PDE3B,PTPN3,PTPRO,TTN,UBASH3B
Role Of Osteoclasts In Rheumatoid Arthritis Signaling Pathway	0.997	0.0259	ADAM19,COL24A1,COL6A2,COL7A1,IKBKB,KRAS,Naip1 (includes others),SOS1
IL-8 Signaling	0.991	0.0286	GNAQ,GNAZ,IKBKB,IRAK3,KRAS,MAP4K4
Agranulocyte Adhesion and Diapedesis	0.991	0.0286	ACTC1,C5,IL1F10,ITGB1,MYH6,SELE
ERK5 Signaling	0.987	0.0405	GNAQ,KRAS,MAPK7
Fc Epsilon RI Signaling	0.976	0.0339	INPP5B,KRAS,PLA2G4D,SOS1
MSP-RON Signaling In Macrophages Pathway	0.966	0.0336	GAB2,IKBKB,KRAS,SOS1
TWEAK Signaling	0.964	0.0541	IKBKB,Naip1 (includes others)
Angiopoietin Signaling	0.961	0.0395	IKBKB,KRAS,SOS1
GDNF Family Ligand-Receptor Interactions	0.961	0.0395	IRS2,KRAS,SOS1
IL-17A Signaling in Fibroblasts	0.945	0.0526	IKBKB,IL17RC

CXCR4 Signaling	0.943	0.0298	BCAR1,ELMO2,GNAQ,GNAZ,KRAS
NF-κB Activation by Viruses	0.936	0.0385	IKBKB,ITGB1,KRAS
LXR/RXR Activation	0.927	0.0325	ABCA1,CD36,IL1F10,PON3
IL-15 Production	0.927	0.0325	AATK,CSF2RA,ERBB4,FES
IL-3 Signaling	0.924	0.038	GAB2,KRAS,SOS1
Renal Cell Carcinoma Signaling	0.924	0.038	CUL2,KRAS,SOS1
Aldosterone Signaling in Epithelial Cells	0.912	0.0291	ASIC1,KCNU1,KRAS,PIKFYVE,SOS1
Pulmonary Fibrosis Idiopathic Signaling Pathway	0.9	0.0245	ACTC1,COL24A1,COL6A2,COL7A1,ITGB1,KRAS,POLR2A,SOS1
Myelination Signaling Pathway	0.895	0.0245	ERBB4,ITGB1,ITGB8,KRAS,NFATC2,PLP1,SOS1,SREBF2
Mechanisms of Viral Exit from Host Cells	0.891	0.0488	ACTC1,PDCD6IP
Sucrose Degradation V (Mammalian)	0.89	0.111	KHK
Heme Biosynthesis II	0.89	0.111	ALAS1
FLT3 Signaling in Hematopoietic Progenitor Cells	0.889	0.0366	GAB2,KRAS,SOS1
EIF2 Signaling	0.874	0.0264	ACTC1,AGO4,EIF5,KRAS,RPS12,SOS1
April Mediated Signaling	0.874	0.0476	IKBKB,NFATC2
Role of MAPK Signaling in the Pathogenesis of Influenza	0.866	0.0357	KRAS,PLA2G4D,PNPLA3
VEGF Family Ligand-Receptor Interactions	0.866	0.0357	KRAS,PLA2G4D,SOS1
Tight Junction Signaling	0.86	0.0279	ACTC1,IGSF5,LLGL1,MYH6,SMURF1
B Cell Activating Factor Signaling	0.857	0.0465	IKBKB,NFATC2
Oncostatin M Signaling	0.857	0.0465	KRAS,SOS1
fMLP Signaling in Neutrophils	0.855	0.0305	GNAQ,GNAZ,KRAS,NFATC2

Prostanoid Biosynthesis	0.847	0.1	TBXAS1
Ketolysis	0.847	0.1	ACAA2
GABA Receptor Signaling	0.847	0.0303	CACNA1B,CACNA1I,GNAQ,GNAZ
HIPPO signaling	0.844	0.0349	DLG5,LLGL1,TP53BP2
BER (Base Excision Repair) Pathway	0.841	0.0455	HUWE1,SLC19A1
PDGF Signaling	0.834	0.0345	INPP5B,KRAS,SOS1
CCR3 Signaling in Eosinophils	0.83	0.0299	GNAQ,GNAZ,KRAS,PLA2G4D
STAT3 Pathway	0.822	0.0296	IL13RA2,IL17RC,IL17RD,KRAS
IL-12 Signaling and Production in Macrophages	0.819	0.0254	IKBKB,NFATC2,PIAS2,SELE,TLR2,VDR
Osteoarthritis Pathway	0.819	0.0254	AGER,ITGAD,ITGB1,ITGB8,S100A9,TLR2
SNARE Signaling Pathway	0.814	0.0294	CACNA1B,MYH6,RIMS1,SYT10
tRNA Splicing	0.811	0.0435	PDE11A,PDE3B
DNA damage-induced 14-3-3σ Signaling	0.811	0.0435	ATR,CHEK2
Ketogenesis	0.809	0.0909	ACAA2
Purine Nucleotides De Novo Biosynthesis II	0.809	0.0909	PFAS
Neutrophil Extracellular Trap Signaling Pathway	0.806	0.0226	AGER,C5,COL24A1,COL6A2,COL7A1,ITGB1,PLA2G4D,PNPLA3,TLR2
IL-17 Signaling	0.804	0.0267	IL17D,IL17RC,IL1F10,Il3,KRAS
NER (Nucleotide Excision Repair, Enhanced Pathway)	0.803	0.0333	POLR2A,SLC19A1,TOP2A
iNOS Signaling	0.796	0.0426	IKBKB,IRAK3
Retinol Biosynthesis	0.796	0.0426	PNPLA3,RDH13
Ceramide Signaling	0.793	0.033	ENPP7,KRAS,NSMAF

Acute Myeloid Leukemia Signaling	0.793	0.033	CSF2RA,KRAS,SOS1
BMP signaling pathway	0.793	0.033	KRAS,SMURF1,SOS1
ABRA Signaling Pathway	0.783	0.0326	ACTC1,CKM,ITGB1
Dermatan Sulfate Biosynthesis (Late Stages)	0.781	0.0417	DSE,HS3ST5
Apelin Muscle Signaling Pathway	0.781	0.0417	GNAQ,GNAZ
3-phosphoinositide Degradation	0.778	0.0262	INPP4B,INPP5B,PDXP,PIKFYVE,PTPRO
Apelin Endothelial Signaling Pathway	0.775	0.0284	GNAQ,GNAZ,KLF2,KRAS
ERBB Signaling	0.773	0.0323	ERBB4,KRAS,SOS1
Prolactin Signaling	0.754	0.0316	KCNU1,KRAS,SOS1
Assembly of RNA Polymerase II Complex	0.754	0.04	POLR2A,TAF5L
Serotonin Receptor Signaling	0.746	0.0213	CACNA1B,CACNA1I,GNAQ,ITGB1,KCNJ3,KRAS,PLA2G4D,PNPLA3,TRPM8,TTN
TNFR1 Signaling	0.741	0.0392	IKBKB,Naip1 (includes others)
UVC-Induced MAPK Signaling	0.741	0.0392	ATR,KRAS
VEGF Signaling	0.718	0.0303	ACTC1,KRAS,SOS1
Mevalonate Pathway I	0.714	0.0714	ACAA2
Phenylalanine Degradation IV (Mammalian, via Side Chain)	0.714	0.0714	ACSF3
ATM Signaling	0.71	0.03	ATR,CHEK2,SMC2
Semaphorin Neuronal Repulsive Signaling Pathway	0.71	0.0267	FES,ITGAD,ITGB1,ITGB8
Triacylglycerol Biosynthesis	0.691	0.0364	AGPAT4,PNPLA3
CSDE1 Signaling Pathway	0.679	0.0357	AGO4,TRIO
Cell Cycle Control of Chromosomal Replication	0.679	0.0357	CHEK2,TOP2A

Relaxin Signaling	0.676	0.0258	GNAQ,GNAZ,PDE11A,PDE3B
Necroptosis Signaling Pathway	0.67	0.0256	CAPN3,IKBKB,PLA2G4D,SHARPIN
IGF-1 Signaling	0.668	0.0286	IRS2,KRAS,SOS1
CNTF Signaling	0.668	0.0351	KRAS,SOS1
Oxidative Ethanol Degradation III	0.668	0.0351	Cyp2b23,Cyp2d9 (includes others)
CREB Signaling in Neurons	0.666	0.0198	CACNA1B,CACNA1I,CHRM2,CRHR2,GNAQ,GNAZ,GPR83,GRIA1,GRID1,KRAS,POLR2A,SOS1
D-myo-inositol (1,4,5)-trisphosphate Degradation	0.663	0.0625	INPP5B
MSP-RON Signaling Pathway	0.657	0.0345	ACTC1,TLR2
Cancer Drug Resistance By Drug Efflux	0.657	0.0345	ABCC2,KRAS
Aryl Hydrocarbon Receptor Signaling	0.651	0.0252	ATR,CHEK2,GSTK1,NCOA7
Isoleucine Degradation I	0.639	0.0588	ACAA2
1D-myo-inositol Hexakisphosphate Biosynthesis II (Mammalian)	0.639	0.0588	INPP5B
D-myo-inositol (1,3,4)-trisphosphate Biosynthesis	0.639	0.0588	INPP5B
α-Adrenergic Signaling	0.637	0.0275	GNAQ,GNAZ,KRAS
Endometrial Cancer Signaling	0.635	0.0333	KRAS,SOS1
Inhibition of ARE-Mediated mRNA Degradation Pathway	0.632	0.0247	AGO4,DIS3L,MAPK7,PSMD13
Semaphorin Signaling in Neurons	0.625	0.0328	FES,ITGB1
Dermatan Sulfate Biosynthesis	0.625	0.0328	DSE,HS3ST5
Mismatch Repair in Eukaryotes	0.618	0.0556	SLC19A1
Superpathway of Geranylgeranyldiphosphate Biosynthesis I (via Mevalonate)	0.618	0.0556	ACAA2

IL-2 Signaling	0.614	0.0323	KRAS,SOS1
Chronic Myeloid Leukemia Signaling	0.603	0.0216	GAB2,IKBKB,ITGB1,KRAS,NFATC2,SOS1
CDK5 Signaling	0.594	0.0261	ITGB1,KRAS,MAPK7
Role of NFAT in Cardiac Hypertrophy	0.593	0.0223	CACNA1B,CACNA1I,GNAQ,KRAS,SOS1
Thrombin Signaling	0.588	0.0222	GNAQ,GNAZ,IKBKB,KRAS,SOS1
IL-13 Signaling Pathway	0.587	0.0259	CD36,IL13RA2,IL17RC
Germ Cell-Sertoli Cell Junction Signaling	0.586	0.0235	ACTC1,BCAR1,ITGB1,KRAS
Gαq Signaling	0.586	0.0235	GNAQ,GNAZ,IKBKB,NFATC2
PXR/RXR Activation	0.585	0.0308	ABCC2,ALAS1
Induction of Apoptosis by HIV1	0.585	0.0308	IKBKB,Naip1 (includes others)
ERB2-ERBB3 Signaling	0.585	0.0308	KRAS,SOS1
Huntington's Disease Signaling	0.581	0.0212	CACNA1B,CAPN3,GNAQ,POLR2A,PSMD13,SOS1
HER-2 Signaling in Breast Cancer	0.578	0.022	IKBKB,ITGB1,ITGB8,KRAS,SOS1
Glutamate Receptor Signaling	0.576	0.0303	GRIA1,GRID1
Role of Osteoblasts, Osteoclasts and Chondrocytes in Rheumatoid Arthritis	0.574	0.0219	IKBKB,IL1F10,Naip1 (includes others),NFATC2,SMURF1
Airway Pathology in Chronic Obstructive Pulmonary Disease	0.573	0.0254	IL17D,IL1F10,Il3
GPCR-Mediated Nutrient Sensing in Enteroendocrine Cells	0.573	0.0254	CACNA1B,CACNA1I,GNAQ
CLEAR Signaling Pathway	0.573	0.0211	ATP6V0D2,ATP6V1A,IKBKB,KRAS,MAPK7,TLR2
Mitotic Roles of Polo-Like Kinase	0.567	0.0299	ANAPC1,CHEK2
IL-17A Signaling in Airway Cells	0.567	0.0299	IKBKB,IL17RC
G-Protein Coupled Receptor Signaling	0.561	0.0185	CHRM2,CRHR2,GNAQ,GNAZ,GPR83,IKBKB,KRAS,MAPK7,NFATC2,PDE11A,PDE3B,SOS1,TTN

p38 MAPK Signaling	0.56	0.025	IL1F10,IRAK3,PLA2G4D
Renin-Angiotensin Signaling	0.553	0.0248	GNAQ,KRAS,SOS1
Phospholipases	0.549	0.029	PLA2G4D,PNPLA3
Superpathway of D-myo-inositol (1,4,5)-trisphosphate Metabolism	0.543	0.0455	INPP5B
RHOA Signaling	0.535	0.0242	ACTC1,PIKFYVE,TTN
D-myo-inositol (1,4,5,6)-Tetrakisphosphate Biosynthesis	0.533	0.0222	INPP5B,PDXP,PIKFYVE,PTPRO
D-myo-inositol (3,4,5,6)-tetrakisphosphate Biosynthesis	0.533	0.0222	INPP5B,PDXP,PIKFYVE,PTPRO
TCA Cycle II (Eukaryotic)	0.527	0.0435	OGDH
Ephrin B Signaling	0.524	0.0278	GNAQ,GNAZ
FXR/RXR Activation	0.522	0.0238	ABCC2,IL1F10,PON3
GP6 Signaling Pathway	0.517	0.0236	COL24A1,COL6A2,COL7A1
Tumoricidal Function of Hepatic Natural Killer Cells	0.512	0.0417	AIFM1
GPCR-Mediated Integration of Enteroendocrine Signaling Exemplified by an L Cell	0.5	0.0267	CHRM2,GNAQ
MicroRNA Biogenesis Signaling Pathway	0.499	0.0214	AGO4,DIS3L,KRAS,POLR2A
Glycolysis I	0.497	0.04	GAPDHS
Gluconeogenesis I	0.497	0.04	GAPDHS
Macrophage Classical Activation Signaling Pathway	0.489	0.0212	IKBKB,IL17D,IL1F10,Il3
Granulocyte Adhesion and Diapedesis	0.489	0.0212	C5,IL1F10,ITGB1,SELE
Synaptic Long Term Potentiation	0.488	0.0227	GNAQ,GRIA1,KRAS
Ferroptosis Signaling Pathway	0.488	0.0227	ABCA1,KRAS,SREBF2
IL-17A Signaling in Gastric Cells	0.483	0.0385	IL17RC

D-myo-inositol (1,4,5)-Trisphosphate Biosynthesis	0.483	0.0385	PIKFYVE
Neurotrophin/TRK Signaling	0.478	0.0256	KRAS,SOS1
Xenobiotic Metabolism CAR Signaling Pathway	0.476	0.0208	ABCC2,Cyp2b23,GSTK1,HS3ST5
Regulation Of The Epithelial Mesenchymal Transition By Growth Factors Pathway	0.476	0.0208	IKBKB,KRAS,SMURF1,SOS1
Maturity Onset Diabetes of Young (MODY) Signaling	0.47	0.0253	CACNA1B,OGDH
Thyroid Cancer Signaling	0.47	0.0253	IRS2,KRAS
Role of MAPK Signaling in Inhibiting the Pathogenesis of Influenza	0.47	0.0253	PLA2G4D,PNPLA3
Hepatic Fibrosis / Hepatic Stellate Cell Activation	0.467	0.0206	COL24A1,COL6A2,COL7A1,MYH6
DHCR24 Signaling Pathway	0.461	0.0219	KRAS,PON3,SREBF2
D-myo-inositol-5-phosphate Metabolism	0.458	0.0204	INPP5B,PDXP,PIKFYVE,PTPRO
Glutathione Redox Reactions I	0.457	0.0357	GSTK1
Chemokine Signaling	0.457	0.0247	GNAQ,KRAS
Iron homeostasis signaling pathway	0.456	0.0217	ATP6V0D2,ATP6V1A,SLC48A1
Natural Killer Cell Signaling	0.45	0.0202	ITGB1,KRAS,NFATC2,SOS1
MSP-RON Signaling In Cancer Cells Pathway	0.446	0.0214	ITGB1,KRAS,SOS1
Superpathway of Cholesterol Biosynthesis	0.445	0.0345	ACAA2
Cardiac Hypertrophy Signaling	0.438	0.0192	CACNA1B,GNAQ,GNAZ,KRAS,SOS1
TR/RXR Activation	0.437	0.0238	PDE3B,SREBF2
PEDF Signaling	0.437	0.0238	IKBKB,KRAS
CDX Gastrointestinal Cancer Signaling Pathway	0.433	0.0198	IKBKB,IL17D,IL1F10,Il3
Xenobiotic Metabolism General Signaling Pathway	0.431	0.021	GSTK1,KRAS,MAPK7

LPS-stimulated MAPK Signaling	0.43	0.0235	IKBKB,KRAS
Coronavirus Pathogenesis Pathway	0.425	0.0196	ATP6V1A,IKBKB,PIKFYVE,RPS12
3-phosphoinositide Biosynthesis	0.417	0.0194	INPP5B,PDXP,PIKFYVE,PTPRO
Circadian Rhythm Signaling	0.413	0.0187	CACNA1B,CACNA1I,GNAQ,GRIA1,KRAS
S100 Family Signaling Pathway	0.405	0.0168	AGER,CACNA1B,CACNA1I,CD36,CHRM2,CRHR2,GPR83,IKBKB,IRAK3,MAPK7,PLA2G4D,S100A9,VDR
Colorectal Cancer Metastasis Signaling	0.403	0.0185	GNAQ,GNAZ,KRAS,SOS1,TLR2
Insulin Secretion Signaling Pathway	0.4	0.0184	AGO4,ASIC1,CACNA1B,CACNA1I,GNAQ
Unfolded protein response	0.4	0.0222	AMFR,SREBF2
NAD Signaling Pathway	0.394	0.0199	AIFM1,POLR2A,SLC29A4
RANK Signaling in Osteoclasts	0.394	0.022	IKBKB,NFATC2
Apelin Adipocyte Signaling Pathway	0.394	0.022	GSTK1,MAPK7
4-1BB Signaling in T Lymphocytes	0.391	0.0294	IKBKB
Inhibition of Angiogenesis by TSP1	0.391	0.0294	CD36
Fatty Acid β-oxidation I	0.391	0.0294	ACAA2
Pyroptosis Signaling Pathway	0.383	0.0215	NLRP4,TLR2
IL-9 Signaling	0.382	0.0286	IRS2
Nucleotide Excision Repair Pathway	0.382	0.0286	POLR2A
IL-10 Signaling	0.381	0.0195	IKBKB,IL1F10,MAP4K4
Fcγ Receptor-mediated Phagocytosis in Macrophages and Monocytes	0.377	0.0213	ACTC1,GAB2
Non-Small Cell Lung Cancer Signaling	0.377	0.0213	KRAS,SOS1
Activin Inhibin Signaling Pathway	0.376	0.0184	IKBKB,IL1F10,MAPK7,TLR2

MIF-mediated Glucocorticoid Regulation	0.372	0.0278	PLA2G4D
Glutathione-mediated Detoxification	0.364	0.027	GSTK1
Complement System	0.364	0.027	C5
Melanocyte Development and Pigmentation Signaling	0.356	0.0204	KRAS,SOS1
Xenobiotic Metabolism Signaling	0.34	0.0171	ABCC2,GSTK1,HS3ST5,KRAS,MAPK7
Mouse Embryonic Stem Cell Pluripotency	0.327	0.0192	KRAS,SOS1
Retinoate Biosynthesis I	0.323	0.0238	RDH13
Superpathway of Inositol Phosphate Compounds	0.321	0.0171	INPP5B,PDXP,PIKFYVE,PTPRO
cAMP-mediated signaling	0.315	0.0169	AKAP13,CHRM2,PDE11A,PDE3B
Telomerase Signaling	0.309	0.0185	KRAS,SOS1
MIF Regulation of Innate Immunity	0.309	0.0227	PLA2G4D
Role of RIG1-like Receptors in Antiviral Innate Immunity	0.296	0.0217	IKBKB
Role of OCT4 in Mammalian Embryonic Stem Cell Pluripotency	0.296	0.0217	TDRD7
Apelin Pancreas Signaling Pathway	0.296	0.0217	PDE3B
Role Of Osteoblasts In Rheumatoid Arthritis Signaling Pathway	0.293	0.0164	IL17D,IL1F10,Il3,SMURF1
Role of IL-17F in Allergic Inflammatory Airway Diseases	0.289	0.0213	IL17RC
nNOS Signaling in Neurons	0.289	0.0213	CAPN3
Ephrin A Signaling	0.289	0.0213	BCAR1
Prostate Cancer Signaling	0.285	0.0175	KRAS,SOS1
Spliceosomal Cycle	0.277	0.0204	SF3B1
Melanoma Signaling	0.271	0.02	KRAS

MYC Mediated Apoptosis Signaling	0.271	0.02	IKBKB
FAT10 Cancer Signaling Pathway	0.271	0.02	IKBKB
IL-33 Signaling Pathway	0.268	0.0161	IKBKB,IL1F10,SELE
Dopamine-DARPP32 Feedback in cAMP Signaling	0.268	0.0161	CACNA1B,GNAQ,KCNJ3
Chondroitin Sulfate Biosynthesis (Late Stages)	0.266	0.0196	HS3ST5
Amyloid Processing	0.266	0.0196	CAPN3
Nitric Oxide Signaling in the Cardiovascular System	0.262	0.0167	CACNA1B,PDE3B
Neuroprotective Role of THOP1 in Alzheimer's Disease	0.259	0.0165	PRSS50,SERPINA3
Role of Cytokines in Mediating Communication between Immune Cells	0.249	0.0185	IL1F10
Leukocyte Extravasation Signaling	0.248	0.0155	ACTC1,BCAR1,ITGB1
Xenobiotic Metabolism PXR Signaling Pathway	0.248	0.0155	ABCC2,GSTK1,HS3ST5
Role of NANOG in Mammalian Embryonic Stem Cell Pluripotency	0.248	0.0161	KRAS,SOS1
Glioma Signaling	0.245	0.016	KRAS,SOS1
Lymphotoxin β Receptor Signaling	0.244	0.0182	IKBKB
Regulation of the Epithelial-Mesenchymal Transition Pathway	0.243	0.0154	KRAS,SMURF1,SOS1
Gαs Signaling	0.242	0.0159	GNAQ,GNAZ
EGF Signaling	0.239	0.0179	SOS1
FAT10 Signaling Pathway	0.239	0.0179	PSMD13
14-3-3-mediated Signaling	0.238	0.0157	KRAS,PDCD6IP
Endocannabinoid Developing Neuron Pathway	0.238	0.0157	KRAS,MAPK7
CD27 Signaling in Lymphocytes	0.234	0.0175	IKBKB

Role of IL-17A in Arthritis	0.234	0.0175	IL17RC
Triacylglycerol Degradation	0.234	0.0175	PNPLA3
Polyamine Regulation in Colon Cancer	0.225	0.0169	KRAS
Nicotine Degradation III	0.225	0.0169	Aox3
Chondroitin Sulfate Biosynthesis	0.225	0.0169	HS3ST5
GADD45 Signaling	0.221	0.0167	ATR
SPINK1 Pancreatic Cancer Pathway	0.221	0.0167	CPZ
Role of JAK2 in Hormone-like Cytokine Signaling	0.212	0.0161	IRS2
Activation of IRF by Cytosolic Pattern Recognition Receptors	0.2	0.0154	IKBKB
Pyridoxal 5'-phosphate Salvage Pathway	0.2	0.0154	MAPK7
Pulmonary Healing Signaling Pathway	0	0.0151	KRAS,SOS1,TLR2
ID1 Signaling Pathway	0	0.0149	KRAS,S100A9,TFAP2A
Immunogenic Cell Death Signaling Pathway	0	0.0111	GZMH
Ribonucleotide Reductase Signaling Pathway	0	0.0118	ATR,KRAS
Chaperone Mediated Autophagy Signaling Pathway	0	0.00933	ATP6V0D2,ATP6V1A,IKBKB,IL17RC, NFATC2,RICTOR
VDR/RXR Activation	0	0.0128	VDR
Clathrin-mediated Endocytosis Signaling	0	0.0144	ACTC1,ITGB1,ITGB8
Role of PKR in Interferon Induction and Antiviral Response	0	0.0147	IKBKB,NLRP4
Role of NFAT in Regulation of the Immune Response	0	0.00579	GNAQ,GNAZ,IKBKB,KRAS,NFATC2,SOS1
FcγRIIB Signaling in B Lymphocytes	0	0.0075	CACNA1B,CACNA1I,KRAS,SOS1
CCR5 Signaling in Macrophages	0	0.00802	CACNA1B,CACNA1I,GNAQ,GNAZ

CD40 Signaling	0	0.0149	IKBKB
Calcium-induced T Lymphocyte Apoptosis	0	0.00435	NFATC2,NR4A1
Cytotoxic T Lymphocyte-mediated Apoptosis of Target Cells	0	0.00235	ZBTB12
CTLA4 Signaling in Cytotoxic T Lymphocytes	0	0.00822	IDO2,ITGB1,KRAS,NFATC2,ZBTB12
CD28 Signaling in T Helper Cells	0	0.00387	IKBKB,NFATC2
IL-15 Signaling	0	0.00189	KRAS
Dendritic Cell Maturation	0	0.00671	IKBKB,IL1F10,TLR2,ZBTB12
Reelin Signaling in Neurons	0	0.00725	ITGB1
HIF1α Signaling	0	0.00962	CUL2,KRAS
Melatonin Signaling	0	0.0139	GNAQ
Neuropathic Pain Signaling In Dorsal Horn Neurons	0	0.0099	GRIA1
Factors Promoting Cardiogenesis in Vertebrates	0	0.00654	MYH6
ICOS-ICOSL Signaling in T Helper Cells	0	0.00592	GAB2,IKBKB,NFATC2
Human Embryonic Stem Cell Pluripotency	0	0.0149	KLF2,KRAS,SOS1
Antiproliferative Role of Somatostatin Receptor 2	0	0.013	KRAS
Type I Diabetes Mellitus Signaling	0	0.00196	IKBKB
Small Cell Lung Cancer Signaling	0	0.0104	IKBKB
Bladder Cancer Signaling	0	0.00862	KRAS
Graft-versus-Host Disease Signaling	0	0.00224	IL1F10
Production of Nitric Oxide and Reactive Oxygen Species in Macrophages	0	0.0105	IKBKB,TLR2
p70S6K Signaling	0	0.00688	EEF2,GNAQ,KRAS,SOS1

mTOR Signaling	0	0.014	KRAS,RICTOR,RPS12
Pancreatic Adenocarcinoma Signaling	0	0.00794	KRAS
G Protein Signaling Mediated by Tubby	0	0.00427	GNAQ,GNAZ
Communication between Innate and Adaptive Immune Cells	0	0.00322	IL1F10,TLR2,ZBTB12
Sphingosine-1-phosphate Signaling	0	0.00833	GNAQ
Crosstalk between Dendritic Cells and Natural Killer Cells	0	0.011	ACTC1
Systemic Lupus Erythematosus Signaling	0	0.00562	C5,IL1F10,KRAS,NFATC2,PRPF38A, SOS1
CDC42 Signaling	0	0.00694	ITGAD,ITGB1,ITGB8,LLGL1
FAK Signaling	0	0.0134	BCAR1,CAPN3,CHRM2,CRHR2,GPR83,IL13RA2,IL17RC,IL17RD,ITGAD,ITGB1,ITGB8,KRAS,MAPK7,SOS1
Phospholipase C Signaling	0	0.00714	GNAQ,ITGAD,ITGB1,ITGB8,KRAS,NFATC2,PLA2G4D,SOS1
Ovarian Cancer Signaling	0	0.00633	KRAS
Altered T Cell and B Cell Signaling in Rheumatoid Arthritis	0	0.00213	IL1F10,TLR2
Estrogen-Dependent Breast Cancer Signaling	0	0.012	KRAS
Leptin Signaling in Obesity	0	0.0132	PDE3B
Glioma Invasiveness Signaling	0	0.0137	KRAS
Breast Cancer Regulation by Stathmin1	0	0.0118	ANKHD1/ANKHD1-EIF4EBP3,CHRM2,CRHR2,GNAQ,GPR83,KRAS,SOS1
Glioblastoma Multiforme Signaling	0	0.0117	KRAS,SOS1
Regulation of IL-2 Expression in Activated and Anergic T Lymphocytes	0	0.00866	IKBKB,KRAS,NFATC2,SOS1
Granzyme A Signaling	0	0.0133	HMGB2
NUR77 Signaling in T Lymphocytes	0	0.00585	MAPK7,NR4A1,ZBTB12

PKCθ Signaling in T Lymphocytes	0	0.0108	CACNA1B,CACNA1I,IKBKB,KRAS,NFATC2,SOS1
Role of Hypercytokinemia/hyperchemokinemia in the Pathogenesis of	0	0.0116	IL1F10
PI3K Signaling in B Lymphocytes	0	0.00677	IKBKB,IRS2,KRAS,NFATC2
P2Y Purigenic Receptor Signaling Pathway	0	0.015	GNAQ,KRAS
Cyclins and Cell Cycle Regulation	0	0.0118	ATR
Role of JAK family kinases in IL-6-type Cytokine Signaling	0	0.0127	SERPINA3
Transcriptional Regulatory Network in Embryonic Stem Cells	0	0.0061	KRAS
eNOS Signaling	0	0.00641	GNAQ
Heparan Sulfate Biosynthesis	0	0.0115	HS3ST5
Heparan Sulfate Biosynthesis (Late Stages)	0	0.0125	HS3ST5
Nicotine Degradation II	0	0.0149	Aox3
Salvage Pathways of Pyrimidine Ribonucleotides	0	0.0103	MAPK7
Stearate Biosynthesis I (Animals)	0	0.0145	TBXAS1
Epithelial Adherens Junction Signaling	0	0.00637	KRAS
Remodeling of Epithelial Adherens Junctions	0	0.0147	ACTC1
TEC Kinase Signaling	0	0.0104	ACTC1,GNAQ,GNAZ,ITGAD,ITGB1,ITGB8
UVA-Induced MAPK Signaling	0	0.0102	KRAS
Oxidative Phosphorylation	0	0.00901	ATPAF2
WNT/Ca+ pathway	0	0.0152	NFATC2
Estrogen Receptor Signaling	0	0.0147	CACNA1B,GNAQ,GNAZ,KRAS,MED13,SOS1
Cell Cycle: G1/S Checkpoint Regulation	0	0.0147	ATR

SAPK/JNK Signaling	0	0.00598	KRAS,MAP4K4,SOS1
FGF Signaling	0	0.0116	SOS1
IL-4 Signaling	0	0.0139	COL24A1,COL6A2,COL7A1,IRS2,KRAS,NFATC2,RICTOR,SOS1
B Cell Receptor Signaling	0	0.00945	GAB2,IKBKB,INPP5B,KRAS,NFATC2,SOS1
WNT/β-catenin Signaling	0	0.00575	GNAQ
NF-κB Signaling	0	0.0105	IKBKB,IL1F10,IRAK3,KRAS,MAP4K4,TLR2
T Cell Receptor Signaling	0	0.00974	IKBKB,ITGB1,KRAS,NFATC2,SOS1,ZBTB12
Autophagy	0	0.00926	ATR,IRS2
PD-1, PD-L1 cancer immunotherapy pathway	0	0.00935	ZBTB12
Sumoylation Pathway	0	0.00971	SLC19A1
Th1 and Th2 Activation Pathway	0	0.00581	NFATC2
Th1 Pathway	0	0.0082	NFATC2
Th2 Pathway	0	0.0073	NFATC2
IL-7 Signaling Pathway	0	0.0128	SOS1
Sirtuin Signaling Pathway	0	0.00683	ABCA1,MAPK7
Th17 Activation Pathway	0	0.00413	IRAK3,NFATC2
SPINK1 General Cancer Pathway	0	0.0145	KRAS
Endocannabinoid Cancer Inhibition Pathway	0	0.0136	GNAQ,NSMAF
Apelin Cardiomyocyte Signaling Pathway	0	0.0101	MAPK7
BAG2 Signaling Pathway	0	0.0119	PSMD13
T Cell Exhaustion Signaling Pathway	0	0.00353	KRAS,NFATC2

Systemic Lupus Erythematosus In T Cell Signaling Pathway	0	0.00622	KRAS,NFATC2,SOS1,ZBTB12
Systemic Lupus Erythematosus In B Cell Signaling Pathway	0	0.011	IL17D,IL1F10,Il3,INPP5B,KRAS,MAP4K4,NFATC2,SOS1
White Adipose Tissue Browning Pathway	0	0.0145	CACNA1B,CACNA1I
HOTAIR Regulatory Pathway	0	0.00613	AGO4
Xenobiotic Metabolism AHR Signaling Pathway	0	0.0115	GSTK1
Kinetochore Metaphase Signaling Pathway	0	0.00901	ANAPC1
Tumor Microenvironment Pathway	0	0.0112	IDO2,KRAS
BR3			
Ingenuity Canonical Pathways	-log(p-value)	Ratio	Molecules
RHOGDI Signaling	5.52	0.0636	ACTC1,CDH15,CDH23,CDH26,CDH8,DGKZ,GNAQ,GNAZ,ITGAD,ITGB1,MYH6,MYH7B,MYH8,MYO18A
Oxytocin Signaling Pathway	4.31	0.0496	ATP2B1,ATP2B4,CD36,EEF2,GNAQ,KRAS,MAP2K4,MAPK7,MFN2,MYH6,MYH7B,MYH8,MYO18A,PLA2G4D
Dilated Cardiomyopathy Signaling Pathway	4.27	0.0667	ACTC1,CACNA1I,DMD,LMNA,MYH6,MYH7B,MYH8,MYO18A,PDE3A,TTN
Senescence Pathway	4.03	0.0468	ANAPC1,ATR,CAPN3,CBX2,CDC25C,CHEK2,DMTF1,HBP1,IKBKB,KRAS,MAP2K4,MAPK7,PTEN,TLR2
Apoptosis Signaling	3.96	0.0769	AIFM1,CAPN3,IKBKB,KRAS,LMNA,MAP2K4,MAP4K4,Naip1 (includes others)
ILK Signaling	3.87	0.0547	ACTC1,IRS2,ITGB1,MAP2K4,MYH6,MYH7B,MYH8,MYO18A,PTEN,RICTOR,VIM
PTEN Signaling	3.54	0.0596	BCAR1,IKBKB,INPP5B,ITGAD,ITGB1,KRAS,PTEN,RPS6KB2,SHARPIN
Signaling by Rho Family GTPases	3.38	0.0449	ACTC1,CDH15,CDH23,CDH26,CDH8,CIT,GNAQ,GNAZ,ITGAD,ITGB1,MAP2K4,VIM

Gα12/13 Signaling	3.23	0.0602	CDH15,CDH23,CDH26,CDH8,IKBKB,KRAS,MAP2K4,MAPK7
Actin Cytoskeleton Signaling	3.15	0.0451	ACTC1,BCAR1,ITGAD,ITGB1,KRAS,MYH6,MYH7B,MYH8,MYO18A,TRIO,TTN
TREM1 Signaling	3.13	0.0779	ITGB1,Naip1 (includes others),NLRP4,NOD1,TLR2,TREM1
Insulin Receptor Signaling	3.08	0.0571	ASIC1,INPP5B,IRS2,KRAS,PDE3B,PTEN,RPS6KB2,TSC1
Tight Junction Signaling	3	0.0503	ACTC1,LLGL1,MPDZ,MYH6,MYH7B,MYH8,MYO18A,PTEN,STX16
Sperm Motility	2.97	0.0428	AATK,CACNA1I,CSF2RA,EPHA3,ERBB4,FES,GNAQ,GNAZ,MAP2K4,PLA2G4D,PNPLA3
Neuregulin Signaling	2.88	0.0598	ERBB4,ITGAD,ITGB1,KRAS,PTEN,RPS6KB2,TMEFF2
Type II Diabetes Mellitus Signaling	2.83	0.0523	CACNA1I,CD36,ENPP7,IKBKB,IRS2,MAP2K4,NSMAF,SMPD4
NGF Signaling	2.81	0.0583	IKBKB,KRAS,MAP2K4,MAPK7,RPS6KB2,SMPD4,TRIO
PI3K/AKT Signaling	2.67	0.045	IKBKB,IL17RC,INPP5B,ITGAD,ITGB1,KRAS,PTEN,RPS6KB2,TSC1
Ephrin Receptor Signaling	2.64	0.0446	BCAR1,EFNB2,EPHA3,GNAQ,GNAZ,ITGAD,ITGB1,KRAS,MAP4K4
Pulmonary Fibrosis Idiopathic Signaling Pathway	2.63	0.0368	ACTC1,COL24A1,COL6A2,COL7A1,EFNB2,ITGB1,KRAS,MAP2K4,POLR2A,PTEN,RPS6KB2,VIM
Death Receptor Signaling	2.63	0.0625	ACTC1,IKBKB,LMNA,MAP2K4,MAP4K4,Naip1 (includes others)
Role of Tissue Factor in Cancer	2.57	0.0435	GNAQ,IKBKB,ITGB1,KRAS,MAP2K4,MAPK7,PDXP,PTEN,RPS6KB2
Agrin Interactions at Neuromuscular Junction	2.55	0.0725	ACTC1,ERBB4,ITGB1,KRAS,MAP2K4
Integrin Signaling	2.5	0.0425	ACTC1,BCAR1,CAPN3,ITGAD,ITGB1,KRAS,MAP2K4,PTEN,TTN
WNK Renal Signaling Pathway	2.42	0.0566	AMFR,ANAPC1,ASIC1,CUL2,IRS2,SLC12A6
Hereditary Breast Cancer Signaling	2.4	0.0493	ATR,CDC25C,CHEK2,KRAS,POLR2A,PTEN,SLC19A1
Paxillin Signaling	2.4	0.0561	ACTC1,BCAR1,ITGAD,ITGB1,KRAS,MAP2K4
nNOS Signaling in Skeletal Muscle Cells	2.34	0.0833	CACNA1I,CAPN3,DMD,SNTA1

Phagosome Formation	2.34	0.0273	BCAR1,CD36,CRHR2,GPR83,ITGAD,ITGB1,KRAS,MAP2K4,MAPK7,MRC1,MYH6,MYH7B,MYH8,MYO18A,PLA2G4D,PNPLA3,RPS6KB2,TLR2,TTN
Toll-like Receptor Signaling	2.32	0.0641	IKBKB,IRAK3,MAP2K4,MAP4K4,TLR2
Sphingomyelin Metabolism	2.28	0.25	ENPP7,SMPD4
Cell Cycle: G2/M DNA Damage Checkpoint Regulation	2.28	0.08	ATR,CDC25C,CHEK2,TOP2A
Cellular Effects of Sildenafil (Viagra)	2.27	0.0467	ACTC1,MYH6,MYH7B,MYH8,MYO18A,PDE3A,PDE3B
UVC-Induced MAPK Signaling	2.25	0.0784	ATR,KRAS,MAP2K4,SMPD4
IL-15 Production	2.1	0.0488	AATK,CSF2RA,EPHA3,ERBB4,FES,MAP2K4
CSDE1 Signaling Pathway	2.1	0.0714	AGO4,PTEN,TRIO,VIM
Calcium Transport I	2.09	0.2	ATP2B1,ATP2B4
Regulation of Cellular Mechanics by Calpain Protease	2.06	0.0556	CAPN3,CAST,ITGAD,ITGB1,KRAS
Sertoli Cell-Sertoli Cell Junction Signaling	2.05	0.0388	ACTC1,BCAR1,CTNNA2,ITGAD,ITGB1,KRAS,MAP2K4,PTEN
Role of CHK Proteins in Cell Cycle Checkpoint Control	2.05	0.069	ATR,CDC25C,CHEK2,SLC19A1
Ceramide Signaling	2.04	0.0549	ENPP7,KRAS,MAP2K4,NSMAF,SMPD4
Wound Healing Signaling Pathway	2.02	0.0357	COL24A1,COL6A2,COL7A1,IKBKB,Il3,ITGB1,KRAS,MAP2K4,VIM
Agranulocyte Adhesion and Diapedesis	2.01	0.0381	ACTC1,C5,ITGB1,MYH6,MYH7B,MYH8,MYO18A,SELE
TNFR2 Signaling	2	0.0938	IKBKB,MAP2K4,Naip1 (includes others)
IL-1 Signaling	1.94	0.0521	GNAQ,GNAZ,IKBKB,IRAK3,MAP2K4
SNARE Signaling Pathway	1.9	0.0441	MYH6,MYH7B,MYH8,MYO18A,RIMS1,STX16
Calcium Signaling	1.89	0.0364	ACTC1,ATP2B1,ATP2B4,CACNA1I,MYH6,MYH7B,MYH8,MYO18A
Multiple Sclerosis Signaling Pathway	1.87	0.036	AIFM1,ASIC1,C5,CAPN3,IL17RC,Il3,PLP1,TLR2

Protein Kinase A Signaling	1.86	0.0292	ANAPC1,CDC25C,GNAQ,PDE11A,PDE3A,PDE3B,PTEN,PTPN3,PTPRO,PTPRT,TTN,UBASH3B
Neuroinflammation Signaling Pathway	1.84	0.0315	AGER,IKBKB,IRAK3,KCNJ3,MAP2K4,MAPK7,Naip1 (includes others),PLA2G4D,TLR2,ZBTB12
IL-17A Signaling in Airway Cells	1.84	0.0597	IKBKB,IL17RC,MAP2K4,PTEN
Protein Ubiquitination Pathway	1.81	0.033	AMFR,ANAPC1,CUL2,HSPA12B,NEDD4L,PSMD13,USO1,USP13,ZBTB12
Role of IL-17A in Psoriasis	1.8	0.143	IL17RC,S100A9
Pathogen Induced Cytokine Storm Signaling Pathway	1.79	0.0296	C5,COL24A1,COL6A2,COL7A1,CSF2RA,Il3,MAPK7,Naip1 (includes others),NLRP4,NOD1,TLR2
NOD1/2 Signaling Pathway	1.75	0.037	IKBKB,Il3,MAP2K4,MAP4K4,NOD1,SHARPIN,TLR2
3-phosphoinositide Degradation	1.73	0.0366	CA3,CDC25C,INPP4B,INPP5B,PDXP,PTEN,PTPRO
Endocannabinoid Neuronal Synapse Pathway	1.73	0.0403	CACNA1I,DNAH10,GNAQ,KCNJ3,MAPK7,RIMS1
Hepatic Fibrosis / Hepatic Stellate Cell Activation	1.7	0.0361	COL24A1,COL6A2,COL7A1,MYH6,MYH7B,MYH8,MYO18A
ERK5 Signaling	1.69	0.0541	GNAQ,KRAS,MAPK7,RPS6KB2
PPARα/RXRα Activation	1.69	0.0359	ABCA1,CD36,GNAQ,IKBKB,KRAS,MAP2K4,MAP4K4
Caveolar-mediated Endocytosis Signaling	1.67	0.0533	ACTC1,ITGAD,ITGB1,ZBTB12
Cardiac Hypertrophy Signaling (Enhanced)	1.67	0.0258	GNAQ,IKBKB,IL17RC,Il3,ITGAD,ITGB1,KRAS,MAP2K4,MAPK7,PDE11A,PDE3A,PDE3B,PTEN,RPS6KB2
Synaptic Long Term Depression	1.66	0.0354	CACNA1I,GNAQ,GNAZ,GRID1,KRAS,PLA2G4D,PNPLA3
Antioxidant Action of Vitamin C	1.65	0.0439	CSF2RA,IKBKB,MAP2K4,PLA2G4D,PNPLA3
Oxytocin In Brain Signaling Pathway	1.65	0.0352	CACNA1I,GNAQ,KRAS,MAPK7,NLRP4,PLA2G4D,PNPLA3
D-myo-inositol (1,3,4)-trisphosphate Biosynthesis	1.63	0.118	INPP5B,PTEN
PAK Signaling	1.61	0.0427	EPHA3,ITGAD,ITGB1,KRAS,MAP2K4

Glutaryl-CoA Degradation	1.59	0.111	ACAA2,TBXAS1
Neutrophil Extracellular Trap Signaling Pathway	1.58	0.0276	AGER,C5,COL24A1,COL6A2,COL7A1,ITGB1,MAP2K4,PLA2G4D,PNPLA3,TLR2,TOMM40
Cholecystokinin/Gastrin-mediated Signaling	1.58	0.042	BCAR1,GNAQ,KRAS,MAP2K4,MAPK7
tRNA Splicing	1.57	0.0652	PDE11A,PDE3A,PDE3B
DNA damage-induced 14-3-3σ Signaling	1.57	0.0652	ATR,CDC25C,CHEK2
Phagosome Maturation	1.56	0.0368	Ctsq,DYNC1LI2,DYNC2H1,EEA1,STX16,ZBTB12
Alanine Degradation III	1.56	0.5	GPT2
Alanine Biosynthesis II	1.56	0.5	GPT2
IL-8 Signaling	1.54	0.0333	GNAQ,GNAZ,IKBKB,IRAK3,KRAS,MAP2K4,MAP4K4
Role of MAPK Signaling in the Pathogenesis of Influenza	1.51	0.0476	KRAS,MAP2K4,PLA2G4D,PNPLA3
Germ Cell-Sertoli Cell Junction Signaling	1.48	0.0353	ACTC1,BCAR1,CTNNA2,ITGB1,KRAS,MAP2K4
14-3-3-mediated Signaling	1.47	0.0394	KRAS,MAP2K4,PDCD6IP,TSC1,VIM
Serotonin Receptor Signaling	1.47	0.0256	CACNA1I,GNAQ,ITGB1,KCNJ3,KRAS,MAP2K4,MPDZ,PLA2G4D,PNPLA3,PSD4,RPS6KB2,TTN
Synaptogenesis Signaling Pathway	1.46	0.0286	CDH15,CDH23,CDH26,CDH8,EFNB2,EPHA3,KRAS,RPS6KB2,STX16
TNFR1 Signaling	1.46	0.0588	IKBKB,MAP2K4,Naip1 (includes others)
G Beta Gamma Signaling	1.45	0.0388	CACNA1I,GNAQ,GNAZ,KCNJ3,KRAS
Superpathway of D-myo-inositol (1,4,5)-trisphosphate Metabolism	1.42	0.0909	INPP5B,PTEN
Acute Myeloid Leukemia Signaling	1.41	0.044	CSF2RA,KRAS,MAP2K4,RPS6KB2
ABRA Signaling Pathway	1.39	0.0435	ACTC1,DMD,ITGB1,MAP2K4
Diphthamide Biosynthesis	1.38	0.333	EEF2

5-aminoimidazole Ribonucleotide Biosynthesis I	1.38	0.333	PFAS
D-myo-inositol (1,4,5,6)-Tetrakisphosphate Biosynthesis	1.38	0.0333	CA3,CDC25C,INPP5B,PDXP,PTEN,PTPRO
D-myo-inositol (3,4,5,6)-tetrakisphosphate Biosynthesis	1.38	0.0333	CA3,CDC25C,INPP5B,PDXP,PTEN,PTPRO
Opioid Signaling Pathway	1.35	0.0286	CACNA1I,GNAQ,GNAZ,KCNJ3,KRAS,MAP2K4,MAPK7,RPS6KB2
Role of Macrophages, Fibroblasts and Endothelial Cells in Rheumatoid Arthritis	1.34	0.0271	C5,GNAQ,IKBKB,IL17RC,IRAK3,KRAS,MAP2K4,SELE,TLR2
Tryptophan Degradation III (Eukaryotic)	1.32	0.08	ACAA2,TBXAS1
Role Of Chondrocytes In Rheumatoid Arthritis Signaling Pathway	1.31	0.0355	ASIC1,IL17RC,ITGB1,MAP2K4,TLR2
Apelin Endothelial Signaling Pathway	1.31	0.0355	GNAQ,GNAZ,KRAS,MAP2K4,RPS6KB2
p53 Signaling	1.31	0.0408	ATR,CHEK2,PTEN,TP53BP2
UVA-Induced MAPK Signaling	1.31	0.0408	KRAS,MAP2K4,RPS6KB2,SMPD4
NRF2-mediated Oxidative Stress Response	1.3	0.0295	ABCC4,ACTC1,Cyp2d9 (includes others),Cyp2t4,KRAS,MAP2K4,MAPK7
IL-17A Signaling in Gastric Cells	1.29	0.0769	IL17RC,MAP2K4
Endometrial Cancer Signaling	1.28	0.05	CTNNA2,KRAS,PTEN
ATM Signaling	1.28	0.04	ATR,CDC25C,CHEK2,MAP2K4
Molecular Mechanisms of Cancer	1.27	0.0244	ATR,CDC25C,CHEK2,CTNNA2,GNAQ,GNAZ,ITGAD,ITGB1,KRAS,MAP2K4,Naip1 (includes others)
Endothelin-1 Signaling	1.25	0.0309	GNAQ,GNAZ,KRAS,MAPK7,PLA2G4D,PNPLA3
Endocannabinoid Cancer Inhibition Pathway	1.25	0.034	GNAQ,MAP2K4,NSMAF,SMPD4,VIM
D-myo-inositol-5-phosphate Metabolism	1.23	0.0306	CA3,CDC25C,INPP5B,PDXP,PTEN,PTPRO
Adrenomedullin signaling pathway	1.21	0.0302	GNAQ,KRAS,MAP2K4,MAPK7,TFAP2A,TTN
Induction of Apoptosis by HIV1	1.2	0.0462	IKBKB,MAP2K4,Naip1 (includes others)

Gustation Pathway	1.17	0.0296	ASIC1,CACNA1I,CD36,PDE3A,PDE3B,SCN9A
Relaxin Signaling	1.17	0.0323	GNAQ,GNAZ,PDE11A,PDE3A,PDE3B
Mitotic Roles of Polo-Like Kinase	1.17	0.0448	ANAPC1,CDC25C,CHEK2
Creatine-phosphate Biosynthesis	1.17	0.2	MAP4K4
Tetrapyrrole Biosynthesis II	1.17	0.2	ALAS1
LPS/IL-1 Mediated Inhibition of RXR Function	1.16	0.0275	ABCA1,ABCC4,ALAS1,Cyp2d9 (includes others),Cyp2t4,HS3ST5,MAP2K4
Role of Pattern Recognition Receptors in Recognition of Bacteria and Viruses	1.16	0.0321	C5,Il3,MAP2K4,NOD1,TLR2
Necroptosis Signaling Pathway	1.16	0.0321	CAPN3,IKBKB,PLA2G4D,SHARPIN,TOMM40
Role Of Osteoclasts In Rheumatoid Arthritis Signaling Pathway	1.15	0.0259	COL24A1,COL6A2,COL7A1,CTNNA2,IKBKB,KRAS,MAP2K4,Naip1 (includes others)
3-phosphoinositide Biosynthesis	1.15	0.0291	CA3,CDC25C,INPP5B,PDXP,PTEN,PTPRO
Role of JAK1 and JAK3 in γc Cytokine Signaling	1.14	0.0435	FES,IRS2,KRAS
Eicosanoid Signaling	1.12	0.0429	PLA2G4D,PNPLA3,TBXAS1
Hepatic Fibrosis Signaling Pathway	1.12	0.0236	IKBKB,IRAK3,IRS2,ITGAD,ITGB1,KRAS,MAP2K4,PTEN,RPS6KB2,TTN
Role of MAPK Signaling in Promoting the Pathogenesis of Influenza	1.11	0.0351	KRAS,MAP2K4,PLA2G4D,PNPLA3
Inhibition of ARE-Mediated mRNA Degradation Pathway	1.11	0.0309	AGO4,CNOT1,DIS3L,MAPK7,PSMD13
Ephrin B Signaling	1.09	0.0417	EFNB2,GNAQ,GNAZ
mTOR Signaling	1.09	0.028	DGKZ,KRAS,RICTOR,RPS12,RPS6KB2,TSC1
4-1BB Signaling in T Lymphocytes	1.09	0.0588	IKBKB,MAP2K4
Inhibition of Angiogenesis by TSP1	1.09	0.0588	CD36,MAP2K4
Fc Epsilon RI Signaling	1.07	0.0339	INPP5B,KRAS,MAP2K4,PLA2G4D
Virus Entry via Endocytic Pathways	1.07	0.0339	ACTC1,ITGB1,KRAS,ZBTB12

HMGB1 Signaling	1.06	0.0299	AGER,Il3,KRAS,MAP2K4,SELE
CXCR4 Signaling	1.05	0.0298	BCAR1,GNAQ,GNAZ,KRAS,MAP2K4
p38 MAPK Signaling	1.05	0.0333	IRAK3,MAP2K4,PLA2G4D,RPS6KB2
Androgen Signaling	1.05	0.0296	CACNA1I,GNAQ,GNAZ,POLR2A,TAF5L
Myelination Signaling Pathway	1.04	0.0245	ERBB4,ITGB1,KRAS,PLP1,PTEN,RPS6KB2,SREBF2,TSC1
GDNF Family Ligand-Receptor Interactions	1.04	0.0395	IRS2,KRAS,MAP2K4
Macropinocytosis Signaling	1.04	0.0395	ITGB1,KRAS,MRC1
TWEAK Signaling	1.02	0.0541	IKBKB,Naip1 (includes others)
NF-κB Activation by Viruses	1.01	0.0385	IKBKB,ITGB1,KRAS
IL-17A Signaling in Fibroblasts	1	0.0526	IKBKB,IL17RC
Thyroid Cancer Signaling	1	0.038	IRS2,KRAS,PTEN
Role of MAPK Signaling in Inhibiting the Pathogenesis of Influenza	1	0.038	MAP2K4,PLA2G4D,PNPLA3
HER-2 Signaling in Breast Cancer	0.995	0.0264	IKBKB,ITGB1,KRAS,PTEN,RPS6KB2,TSC1
Role of BRCA1 in DNA Damage Response	0.989	0.0375	ATR,CHEK2,SLC19A1
Axonal Guidance Signaling	0.975	0.0216	ADAMTS19,ADAMTS20,BCAR1,EFNB2,EPHA3,FES,GNAQ,GNAZ,ITGAD,ITGB1,KRAS
CLEAR Signaling Pathway	0.968	0.0246	HEXA,IKBKB,KRAS,MAPK7,TLR2,TSC1,WDR59
BEX2 Signaling Pathway	0.965	0.0366	MAP2K4,PTEN,TSC1
IL-6 Signaling	0.965	0.031	IKBKB,KRAS,MAP2K4,MAP4K4
Neurovascular Coupling Signaling Pathway	0.962	0.0259	CACNA1I,GNAQ,KCNJ3,LRRC52,PLA2G4D,PNPLA3
Cardiac β-adrenergic Signaling	0.959	0.0278	GNAQ,GNAZ,PDE11A,PDE3A,PDE3B
Regulation of eIF4 and p70S6K Signaling	0.951	0.0276	AGO4,ITGAD,ITGB1,KRAS,RPS12

Superpathway of Inositol Phosphate Compounds	0.949	0.0256	CA3,CDC25C,INPP5B,PDXP,PTEN,PTPRO
Mechanisms of Viral Exit from Host Cells	0.948	0.0488	ACTC1,PDCD6IP
Mitochondrial Dysfunction	0.948	0.0233	AIFM1,CACNA1I,CAPN3,MAP2K4,MAPK7,MFN1,MFN2,TOMM40
HGF Signaling	0.939	0.0303	ITGAD,ITGB1,KRAS,MAP2K4
Osteoarthritis Pathway	0.936	0.0254	AGER,CTNNA2,ITGAD,ITGB1,S100A9,TLR2
April Mediated Signaling	0.931	0.0476	IKBKB,MAP2K4
LPS-stimulated MAPK Signaling	0.931	0.0353	IKBKB,KRAS,MAP2K4
Atherosclerosis Signaling	0.93	0.0301	CD36,PLA2G4D,PNPLA3,SELE
Sucrose Degradation V (Mammalian)	0.923	0.111	KHK
Heme Biosynthesis II	0.923	0.111	ALAS1
Acute Phase Response Signaling	0.922	0.027	C5,IKBKB,KRAS,MAP2K4,SERPINA3
CCR3 Signaling in Eosinophils	0.921	0.0299	GNAQ,GNAZ,KRAS,PLA2G4D
B Cell Activating Factor Signaling	0.914	0.0465	IKBKB,MAP2K4
PDGF Signaling	0.909	0.0345	INPP5B,KRAS,MAP2K4
MicroRNA Biogenesis Signaling Pathway	0.908	0.0267	AGO4,DIS3L,KRAS,PNPT1,POLR2A
MIF Regulation of Innate Immunity	0.898	0.0455	MAP2K4,PLA2G4D
BER (Base Excision Repair) Pathway	0.898	0.0455	MAP2K4,SLC19A1
RAC Signaling	0.896	0.0292	ITGAD,ITGB1,KRAS,MAP2K4
Macrophage Alternative Activation Signaling Pathway	0.894	0.0265	ABCA1,CD36,IRS2,LLGL1,MRC1
Prostanoid Biosynthesis	0.88	0.1	TBXAS1
Ketolysis	0.88	0.1	ACAA2

Hepatic Cholestasis	0.88	0.0262	IKBKB,Il3,IRAK3,MAP2K4,SLC22A6
GNRH Signaling	0.88	0.0262	CACNA1I,GNAQ,KRAS,MAP2K4,MAPK7
NER (Nucleotide Excision Repair, Enhanced Pathway)	0.877	0.0333	POLR2A,SLC19A1,TOP2A
Leukocyte Extravasation Signaling	0.867	0.0259	ACTC1,BCAR1,CTNNA2,ITGB1,MAP2K4
Apelin Pancreas Signaling Pathway	0.866	0.0435	MAP2K4,PDE3B
iNOS Signaling	0.851	0.0426	IKBKB,IRAK3
Ephrin A Signaling	0.851	0.0426	BCAR1,EPHA3
Actin Nucleation by ARP-WASP Complex	0.846	0.0323	ITGAD,ITGB1,KRAS
ERBB Signaling	0.846	0.0323	ERBB4,KRAS,MAP2K4
Ketogenesis	0.842	0.0909	ACAA2
Purine Nucleotides De Novo Biosynthesis II	0.842	0.0909	PFAS
Dermatan Sulfate Biosynthesis (Late Stages)	0.837	0.0417	DSE,HS3ST5
Apelin Muscle Signaling Pathway	0.837	0.0417	GNAQ,GNAZ
Fcγ Receptor-mediated Phagocytosis in Macrophages and Monocytes	0.837	0.0319	ACTC1,PTEN,RPS6KB2
TGF-β Signaling	0.817	0.0312	KRAS,MAP2K4,VDR
ID1 Signaling Pathway	0.815	0.0249	KRAS,PTEN,S100A9,TFAP2A,VIM
Melanoma Signaling	0.809	0.04	KRAS,PTEN
Assembly of RNA Polymerase II Complex	0.809	0.04	POLR2A,TAF5L
Semaphorin Neuronal Repulsive Signaling Pathway	0.795	0.0267	FES,ITGAD,ITGB1,MAP2K4
Corticotropin Releasing Hormone Signaling	0.781	0.0263	CACNA1I,CRHR2,GNAQ,NR4A1
Oleate Biosynthesis II (Animals)	0.775	0.0769	PTPRT

HIF1α Signaling	0.772	0.024	CUL2,KRAS,MAP2K4,RPS6KB2,VIM
Mevalonate Pathway I	0.746	0.0714	ACAA2
Phenylalanine Degradation IV (Mammalian, via Side Chain)	0.746	0.0714	ACSF3
IGF-1 Signaling	0.737	0.0286	IRS2,KRAS,RPS6KB2
Insulin Secretion Signaling Pathway	0.734	0.0221	AGO4,ASIC1,CACNA1I,GNAQ,RPS6KB2,STX16
Aryl Hydrocarbon Receptor Signaling	0.733	0.0252	ATR,CHEK2,NCOA7,TRIP11
Cell Cycle Control of Chromosomal Replication	0.732	0.0357	CHEK2,TOP2A
ERK/MAPK Signaling	0.732	0.0233	BCAR1,ITGAD,ITGB1,KRAS,PLA2G4D
Autophagy	0.726	0.0231	ATR,IRS2,MAP2K4,PTEN,TSC1
PPAR Signaling	0.721	0.028	IKBKB,KRAS,MAP4K4
CD27 Signaling in Lymphocytes	0.72	0.0351	IKBKB,MAP2K4
CNTF Signaling	0.72	0.0351	KRAS,RPS6KB2
Role of IL-17A in Arthritis	0.72	0.0351	IL17RC,MAP2K4
MSP-RON Signaling Pathway	0.709	0.0345	ACTC1,TLR2
Cancer Drug Resistance By Drug Efflux	0.709	0.0345	KRAS,PTEN
Glucocorticoid Receptor Signaling	0.706	0.0189	DNAH10,IKBKB,IL17RC,KRAS,MAP2K4,PLA2G4D,POLR2A,SELE,TAF5L,TLR2,ZBTB12
α-Adrenergic Signaling	0.705	0.0275	GNAQ,GNAZ,KRAS
Polyamine Regulation in Colon Cancer	0.698	0.0339	KRAS,MAP2K4
Chondroitin Sulfate Degradation (Metazoa)	0.694	0.0625	HEXA
D-myo-inositol (1,4,5)-trisphosphate Degradation	0.694	0.0625	INPP5B
GADD45 Signaling	0.687	0.0333	ATR,MAP2K4

Huntington's Disease Signaling	0.682	0.0212	CAPN3,GNAQ,MAP2K4,POLR2A,PSMD13,STX16
Semaphorin Signaling in Neurons	0.676	0.0328	FES,ITGB1
Dermatan Sulfate Biosynthesis	0.676	0.0328	DSE,HS3ST5
Isoleucine Degradation I	0.671	0.0588	ACAA2
1D-myo-inositol Hexakisphosphate Biosynthesis II (Mammalian)	0.671	0.0588	INPP5B
Dermatan Sulfate Degradation (Metazoa)	0.671	0.0588	HEXA
Regulation of Actin-based Motility by Rho	0.66	0.0261	ACTC1,ITGAD,ITGB1
CDK5 Signaling	0.66	0.0261	ITGB1,KRAS,MAPK7
Thrombopoietin Signaling	0.655	0.0317	IRS2,KRAS
Aldosterone Signaling in Epithelial Cells	0.653	0.0233	ASIC1,HSPA12B,KRAS,LRRC52
Amyotrophic Lateral Sclerosis Signaling	0.652	0.0259	CAPN3,GRID1,Naip1 (includes others)
Mismatch Repair in Eukaryotes	0.649	0.0556	SLC19A1
Superpathway of Geranylgeranyldiphosphate Biosynthesis I (via Mevalonate)	0.649	0.0556	ACAA2
Activation of IRF by Cytosolic Pattern Recognition Receptors	0.635	0.0308	IKBKB,MAP2K4
ERB2-ERBB3 Signaling	0.635	0.0308	KRAS,PTEN
Pyridoxal 5'-phosphate Salvage Pathway	0.635	0.0308	MAP2K4,MAPK7
Renin-Angiotensin Signaling	0.618	0.0248	GNAQ,KRAS,MAP2K4
CD40 Signaling	0.616	0.0299	IKBKB,MAP2K4
Valine Degradation I	0.609	0.05	HIBCH
ERBB4 Signaling	0.607	0.0294	ERBB4,KRAS
Remodeling of Epithelial Adherens Junctions	0.607	0.0294	ACTC1,CTNNA2

LXR/RXR Activation	0.604	0.0244	ABCA1,CD36,PON3
Phospholipases	0.598	0.029	PLA2G4D,PNPLA3
Stearate Biosynthesis I (Animals)	0.598	0.029	PTGR1,TBXAS1
RHOA Signaling	0.598	0.0242	ACTC1,CIT,TTN
AMPK Signaling	0.596	0.0207	EEF2,GNAQ,GNAZ,IRS2,TSC1
RAR Activation	0.595	0.0187	GNAQ,Il3,MAP2K4,PDE11A,PDE3A,PDE3B,PTEN,RAB11FIP3
GM-CSF Signaling	0.589	0.0286	CSF2RA,KRAS
GP6 Signaling Pathway	0.579	0.0236	COL24A1,COL6A2,COL7A1
Endocannabinoid Developing Neuron Pathway	0.579	0.0236	KRAS,MAP2K4,MAPK7
Melatonin Signaling	0.572	0.0278	GNAQ,MAP2K4
IL-17 Signaling	0.572	0.0214	IL17RC,Il3,KRAS,MAP2K4
fMLP Signaling in Neutrophils	0.554	0.0229	GNAQ,GNAZ,KRAS
GABA Receptor Signaling	0.549	0.0227	CACNA1I,GNAQ,GNAZ
Ferroptosis Signaling Pathway	0.549	0.0227	ABCA1,KRAS,SREBF2
Regulation Of The Epithelial Mesenchymal Transition By Growth Factors Pathway	0.547	0.0208	IKBKB,KRAS,MAP2K4,VIM
G-Protein Coupled Receptor Signaling	0.546	0.0171	CRHR2,GNAQ,GNAZ,GPR83,IKBKB,KRAS,MAP2K4,MAPK7,PDE11A,PDE3A,PDE3B,TTN
IL-22 Signaling	0.541	0.0417	MAP2K4
Tumoricidal Function of Hepatic Natural Killer Cells	0.541	0.0417	AIFM1
Angiopoietin Signaling	0.54	0.0263	IKBKB,KRAS
Leptin Signaling in Obesity	0.54	0.0263	PDE3A,PDE3B

STAT3 Pathway	0.531	0.0222	IL17RC,KRAS,MAP2K4
Glycolysis I	0.526	0.04	GAPDHS
Gluconeogenesis I	0.526	0.04	GAPDHS
Role of PKR in Interferon Induction and Antiviral Response	0.526	0.0221	IKBKB,MAP2K4,NLRP4
Neurotrophin/TRK Signaling	0.524	0.0256	KRAS,MAP2K4
DHCR24 Signaling Pathway	0.52	0.0219	KRAS,PON3,SREBF2
Gap Junction Signaling	0.519	0.0202	ACTC1,GNAQ,KRAS,MAPK7
Renal Cell Carcinoma Signaling	0.517	0.0253	CUL2,KRAS
Role of JAK family kinases in IL-6-type Cytokine Signaling	0.517	0.0253	MAP2K4,SERPINA3
Pulmonary Healing Signaling Pathway	0.515	0.0201	CDC25C,KRAS,MAP2K4,TLR2
Reelin Signaling in Neurons	0.515	0.0217	DNAH10,ITGB1,MAP2K4
Gαi Signaling	0.504	0.0214	GNAQ,GNAZ,KRAS
MSP-RON Signaling In Cancer Cells Pathway	0.504	0.0214	ITGB1,KRAS,VIM
Chemokine Signaling	0.502	0.0247	GNAQ,KRAS
Pregnenolone Biosynthesis	0.499	0.037	Cyp2d9 (includes others)
Apelin Liver Signaling Pathway	0.499	0.037	MAP2K4
JAK/STAT Signaling	0.495	0.0244	GNAQ,KRAS
Circadian Rhythm Signaling	0.49	0.0187	CACNA1I,GNAQ,HLF,KRAS,MAP2K4
Xenobiotic Metabolism General Signaling Pathway	0.488	0.021	KRAS,MAP2K4,MAPK7
CDP-diacylglycerol Biosynthesis I	0.486	0.0357	PNPLA3
Histidine Degradation VI	0.486	0.0357	Cyp2d9 (includes others)

TR/RXR Activation	0.481	0.0238	PDE3B,SREBF2
VEGF Family Ligand-Receptor Interactions	0.481	0.0238	KRAS,PLA2G4D
PEDF Signaling	0.481	0.0238	IKBKB,KRAS
Colorectal Cancer Metastasis Signaling	0.479	0.0185	GNAQ,GNAZ,KRAS,MAP2K4,TLR2
Superpathway of Cholesterol Biosynthesis	0.473	0.0345	ACAA2
HIPPO signaling	0.468	0.0233	LLGL1,TP53BP2
Phosphatidylglycerol Biosynthesis II (Non-plastidic)	0.461	0.0333	PNPLA3
Ubiquinol-10 Biosynthesis (Eukaryotic)	0.45	0.0323	Cyp2d9 (includes others)
Methylglyoxal Degradation III	0.45	0.0323	PTGR1
NAD Signaling Pathway	0.449	0.0199	AIFM1,POLR2A,SLC29A4
Unfolded protein response	0.443	0.0222	AMFR,SREBF2
Activin Inhibin Signaling Pathway	0.441	0.0184	IKBKB,MAP2K4,MAPK7,TLR2
RANK Signaling in Osteoclasts	0.437	0.022	IKBKB,MAP2K4
BMP signaling pathway	0.437	0.022	KRAS,MAP2K4
IL-10 Signaling	0.435	0.0195	IKBKB,MAP2K4,MAP4K4
Pyroptosis Signaling Pathway	0.425	0.0215	NLRP4,TLR2
Epithelial Adherens Junction Signaling	0.422	0.0191	CTNNA2,KRAS,PTEN
Fatty Acid β-oxidation I	0.418	0.0294	ACAA2
Ovarian Cancer Signaling	0.418	0.019	KRAS,PTEN,RPS6KB2
Role of NFAT in Cardiac Hypertrophy	0.415	0.0179	CACNA1I,GNAQ,KRAS,MAP2K4
Prolactin Signaling	0.414	0.0211	KRAS,LRRC52

Thrombin Signaling	0.411	0.0178	GNAQ,GNAZ,IKBKB,KRAS
IL-9 Signaling	0.409	0.0286	IRS2
Nucleotide Excision Repair Pathway	0.409	0.0286	POLR2A
Small Cell Lung Cancer Signaling	0.408	0.0208	IKBKB,PTEN
EIF2 Signaling	0.404	0.0176	ACTC1,AGO4,KRAS,RPS12
Salvage Pathways of Pyrimidine Ribonucleotides	0.403	0.0206	MAP2K4,MAPK7
MIF-mediated Glucocorticoid Regulation	0.399	0.0278	PLA2G4D
S100 Family Signaling Pathway	0.398	0.0155	AGER,CACNA1I,CD36,CRHR2,GPR83,IKBKB,IRAK3,MAP2K4,MAPK7,PLA2G4D,S100A9,VDR
Melanocyte Development and Pigmentation Signaling	0.397	0.0204	KRAS,RPS6KB2
HOTAIR Regulatory Pathway	0.397	0.0184	AGO4,PTEN,VIM
VEGF Signaling	0.392	0.0202	ACTC1,KRAS
Complement System	0.39	0.027	C5
IL-12 Signaling and Production in Macrophages	0.374	0.0169	IKBKB,SELE,TLR2,VDR
Sumoylation Pathway	0.372	0.0194	MAP2K4,SLC19A1
Ribonucleotide Reductase Signaling Pathway	0.369	0.0176	ATR,KRAS,MAP2K4
Gαq Signaling	0.369	0.0176	GNAQ,GNAZ,IKBKB
Glioblastoma Multiforme Signaling	0.366	0.0175	KRAS,PTEN,TSC1
PD-1, PD-L1 cancer immunotherapy pathway	0.353	0.0187	PTEN,ZBTB12
Acetone Degradation I (to Methylglyoxal)	0.349	0.0238	PTGR1
Erythropoietin Signaling Pathway	0.344	0.0169	Il3,IRS2,KRAS

Oncostatin M Signaling	0.342	0.0233	KRAS
Kinetochore Metaphase Signaling Pathway	0.335	0.018	ANAPC1,DNAH10
Prostate Cancer Signaling	0.322	0.0175	KRAS,PTEN
Role of RIG1-like Receptors in Antiviral Innate Immunity	0.32	0.0217	IKBKB
IL-33 Signaling Pathway	0.314	0.0161	IKBKB,MAP2K4,SELE
Role of IL-17F in Allergic Inflammatory Airway Diseases	0.314	0.0213	IL17RC
nNOS Signaling in Neurons	0.314	0.0213	CAPN3
Retinol Biosynthesis	0.314	0.0213	PNPLA3
IL-13 Signaling Pathway	0.314	0.0172	CD36,IL17RC
PFKFB4 Signaling Pathway	0.307	0.0208	MAP2K4
GPCR-Mediated Nutrient Sensing in Enteroendocrine Cells	0.306	0.0169	CACNA1I,GNAQ
Granulocyte Adhesion and Diapedesis	0.305	0.0159	C5,ITGB1,SELE
MSP-RON Signaling In Macrophages Pathway	0.302	0.0168	IKBKB,KRAS
Cardiac Hypertrophy Signaling	0.302	0.0153	GNAQ,GNAZ,KRAS,MAP2K4
Spliceosomal Cycle	0.301	0.0204	SF3B1
Production of Nitric Oxide and Reactive Oxygen Species in Macrophages	0.298	0.0157	IKBKB,MAP2K4,TLR2
Sphingosine-1-phosphate Signaling	0.298	0.0167	GNAQ,SMPD4
MYC Mediated Apoptosis Signaling	0.295	0.02	IKBKB
FAT10 Cancer Signaling Pathway	0.295	0.02	IKBKB
Estrogen Receptor Signaling	0.29	0.0147	GNAQ,GNAZ,KRAS,MED13,PTEN,RPS6KB2
Chondroitin Sulfate Biosynthesis (Late Stages)	0.289	0.0196	HS3ST5

Amyloid Processing	0.289	0.0196	CAPN3
UVB-Induced MAPK Signaling	0.283	0.0192	MAP2K4
Glioma Signaling	0.28	0.016	KRAS,PTEN
Natural Killer Cell Signaling	0.278	0.0152	ITGB1,Klra7 (includes others),KRAS
FXR/RXR Activation	0.276	0.0159	MAP2K4,PON3
Pancreatic Adenocarcinoma Signaling	0.276	0.0159	KRAS,MAP2K4
Gαs Signaling	0.276	0.0159	GNAQ,GNAZ
Lymphotoxin β Receptor Signaling	0.267	0.0182	IKBKB
Triacylglycerol Biosynthesis	0.267	0.0182	PNPLA3
CDX Gastrointestinal Cancer Signaling Pathway	0.267	0.0149	IKBKB,Il3,PTEN
EGF Signaling	0.262	0.0179	MAP2K4
FAT10 Signaling Pathway	0.262	0.0179	PSMD13
Coronavirus Pathogenesis Pathway	0.262	0.0147	IKBKB,MAP2K4,RPS12
Chronic Myeloid Leukemia Signaling	0.261	0.0144	IKBKB,ITGB1,KRAS,PTEN
Triacylglycerol Degradation	0.257	0.0175	PNPLA3
Oxidative Ethanol Degradation III	0.257	0.0175	Cyp2d9 (includes others)
Synaptic Long Term Potentiation	0.256	0.0152	GNAQ,KRAS
P2Y Purigenic Receptor Signaling Pathway	0.253	0.015	GNAQ,KRAS
Nicotine Degradation III	0.247	0.0169	Aox3
Chondroitin Sulfate Biosynthesis	0.247	0.0169	HS3ST5
PCP (Planar Cell Polarity) Pathway	0.243	0.0167	MAP2K4

Role of JAK2 in Hormone-like Cytokine Signaling	0.234	0.0161	IRS2
IL-2 Signaling	0.234	0.0161	KRAS
PXR/RXR Activation	0.221	0.0154	ALAS1
Glutamate Receptor Signaling	0.217	0.0152	GRID1
Nicotine Degradation II	0.213	0.0149	Aox3
Cell Cycle: G1/S Checkpoint Regulation	0.209	0.0147	ATR
SPINK1 General Cancer Pathway	0.205	0.0145	KRAS
Growth Hormone Signaling	0.198	0.0141	RPS6KB2
Immunogenic Cell Death Signaling Pathway	0	0.0111	GZMH
Macrophage Classical Activation Signaling Pathway	0	0.0106	IKBKB,Il3
Role Of Osteoblasts In Rheumatoid Arthritis Signaling Pathway	0	0.0082	Ctsq,Il3
Chaperone Mediated Autophagy Signaling Pathway	0	0.00622	IKBKB,IL17RC,MAP2K4,RICTOR
VDR/RXR Activation	0	0.0128	VDR
Clathrin-mediated Endocytosis Signaling	0	0.00962	ACTC1,ITGB1
Role of NFAT in Regulation of the Immune Response	0	0.00386	GNAQ,GNAZ,IKBKB,KRAS
FcγRIIB Signaling in B Lymphocytes	0	0.00563	CACNA1I,KRAS,MAP2K4
CCR5 Signaling in Macrophages	0	0.00802	CACNA1I,GNAQ,GNAZ,MAP2K4
Calcium-induced T Lymphocyte Apoptosis	0	0.00217	NR4A1
Cytotoxic T Lymphocyte-mediated Apoptosis of Target Cells	0	0.00235	ZBTB12
IL-3 Signaling	0	0.0127	KRAS
Airway Pathology in Chronic Obstructive Pulmonary Disease	0	0.00847	Il3

CTLA4 Signaling in Cytotoxic T Lymphocytes	0	0.00822	IDO2,ITGB1,KRAS,MAP2K4,ZBTB12
CD28 Signaling in T Helper Cells	0	0.00387	IKBKB,MAP2K4
IL-15 Signaling	0	0.00379	KRAS,RPS6KB2
Dendritic Cell Maturation	0	0.00671	IKBKB,MAP2K4,TLR2,ZBTB12
Factors Promoting Cardiogenesis in Vertebrates	0	0.0131	MAP2K4,MYH6
ICOS-ICOSL Signaling in T Helper Cells	0	0.00394	IKBKB,PTEN
FLT3 Signaling in Hematopoietic Progenitor Cells	0	0.0122	KRAS
Human Embryonic Stem Cell Pluripotency	0	0.00995	KRAS,MAP2K4
Antiproliferative Role of Somatostatin Receptor 2	0	0.013	KRAS
Role of NANOG in Mammalian Embryonic Stem Cell Pluripotency	0	0.00806	KRAS
CREB Signaling in Neurons	0	0.0132	CACNA1I,CRHR2,GNAQ,GNAZ,GPR83,GRID1,KRAS,POLR2A
Type I Diabetes Mellitus Signaling	0	0.00393	IKBKB,MAP2K4
Bladder Cancer Signaling	0	0.00862	KRAS
Non-Small Cell Lung Cancer Signaling	0	0.0106	KRAS
p70S6K Signaling	0	0.00516	EEF2,GNAQ,KRAS
G Protein Signaling Mediated by Tubby	0	0.00427	GNAQ,GNAZ
Communication between Innate and Adaptive Immune Cells	0	0.00214	TLR2,ZBTB12
Crosstalk between Dendritic Cells and Natural Killer Cells	0	0.011	ACTC1
Systemic Lupus Erythematosus Signaling	0	0.00281	C5,KRAS,PRPF38A
CDC42 Signaling	0	0.00694	ITGAD,ITGB1,LLGL1,MAP2K4
FAK Signaling	0	0.0125	BCAR1,CAPN3,CRHR2,EFNB2,GPR83,IL17RC,ITGAD,ITGB1,KRAS,MAP2K4,MAPK7,PCDH12,PTEN

Role of Osteoblasts, Osteoclasts and Chondrocytes in Rheumatoid Arthritis	0	0.0132	IKBKB,MAP2K4,Naip1 (includes others)
Phospholipase C Signaling	0	0.00446	GNAQ,ITGAD,ITGB1,KRAS,PLA2G4D
Altered T Cell and B Cell Signaling in Rheumatoid Arthritis	0	0.00106	TLR2
Estrogen-Dependent Breast Cancer Signaling	0	0.012	KRAS
Glioma Invasiveness Signaling	0	0.0137	KRAS
Breast Cancer Regulation by Stathmin1	0	0.00842	ANKHD1/ANKHD1-EIF4EBP3,CRHR2,GNAQ,GPR83,KRAS
Neuroprotective Role of THOP1 in Alzheimer's Disease	0	0.00826	SERPINA3
Regulation of IL-2 Expression in Activated and Anergic T Lymphocytes	0	0.00649	IKBKB,KRAS,MAP2K4
Granzyme A Signaling	0	0.0133	HMGB2
NUR77 Signaling in T Lymphocytes	0	0.00585	MAPK7,NR4A1,ZBTB12
PKCθ Signaling in T Lymphocytes	0	0.00717	CACNA1I,IKBKB,KRAS,MAP2K4
OX40 Signaling Pathway	0	0.00209	MAP2K4
PI3K Signaling in B Lymphocytes	0	0.00677	IKBKB,IRS2,KRAS,PTEN
Cyclins and Cell Cycle Regulation	0	0.0118	ATR
Dopamine-DARPP32 Feedback in cAMP Signaling	0	0.0108	GNAQ,KCNJ3
Telomerase Signaling	0	0.00926	KRAS
Mouse Embryonic Stem Cell Pluripotency	0	0.00962	KRAS
Transcriptional Regulatory Network in Embryonic Stem Cells	0	0.0061	KRAS
eNOS Signaling	0	0.00641	GNAQ
Netrin Signaling	0	0.0139	CACNA1I
Heparan Sulfate Biosynthesis	0	0.0115	HS3ST5

Heparan Sulfate Biosynthesis (Late Stages)	0	0.0125	HS3ST5
Regulation of the Epithelial-Mesenchymal Transition Pathway	0	0.0103	KRAS,MAP2K4
TEC Kinase Signaling	0	0.0104	ACTC1,GNAQ,GNAZ,ITGAD,ITGB1,MAP2K4
SAPK/JNK Signaling	0	0.00598	KRAS,MAP2K4,MAP4K4
Nitric Oxide Signaling in the Cardiovascular System	0	0.00833	PDE3B
Xenobiotic Metabolism Signaling	0	0.0137	HS3ST5,KRAS,MAP2K4,MAPK7
IL-4 Signaling	0	0.0121	COL24A1,COL6A2,COL7A1,IRS2,KRAS,RICTOR,RPS6KB2
B Cell Receptor Signaling	0	0.00945	IKBKB,INPP5B,KRAS,MAP2K4,PTEN,RPS6KB2
WNT/β-catenin Signaling	0	0.00575	GNAQ
cAMP-mediated signaling	0	0.0127	PDE11A,PDE3A,PDE3B
NF-κB Signaling	0	0.00876	IKBKB,IRAK3,KRAS,MAP4K4,TLR2
Hypoxia Signaling in the Cardiovascular System	0	0.0132	PTEN
T Cell Receptor Signaling	0	0.00812	IKBKB,ITGB1,KRAS,MAP2K4,ZBTB12
GPCR-Mediated Integration of Enteroendocrine Signaling Exemplified by an L Cell	0	0.0133	GNAQ
Sirtuin Signaling Pathway	0	0.0102	ABCA1,MAPK7,TOMM40
Iron homeostasis signaling pathway	0	0.00725	SLC48A1
Th17 Activation Pathway	0	0.00207	IRAK3
Apelin Adipocyte Signaling Pathway	0	0.011	MAPK7
Apelin Cardiomyocyte Signaling Pathway	0	0.0101	MAPK7
BAG2 Signaling Pathway	0	0.0119	PSMD13
T Cell Exhaustion Signaling Pathway	0	0.00353	KRAS,MAP2K4

Systemic Lupus Erythematosus In T Cell Signaling Pathway	0	0.00622	KRAS,MAP2K4,RPS6KB2,ZBTB12
Systemic Lupus Erythematosus In B Cell Signaling Pathway	0	0.00552	Il3,INPP5B,KRAS,MAP4K4
White Adipose Tissue Browning Pathway	0	0.00725	CACNA1I
Xenobiotic Metabolism CAR Signaling Pathway	0	0.0104	HS3ST5,MAP2K4
Xenobiotic Metabolism PXR Signaling Pathway	0	0.00518	HS3ST5
Tumor Microenvironment Pathway	0	0.0112	IDO2,KRAS

Table S2: Genes associated to each MP

MP1	MP2	MP3	MP4
2010110K18Rik	4930533B01Rik	1700006J14Rik	0610005C13Rik
2810408I11Rik	9530026P05Rik	1700025G04Rik	4930405A10Rik
4930503L19Rik	AC149090.1	6030407O03Rik	4930453C13Rik
4930558J18Rik	Acacb	8030451A03Rik	9330175E14Rik
4930579G24Rik	Acvr1c	Abhd2	9930111J21Rik2
5430427M07Rik	Appl2	Abtb2	A530032D15Rik
Alms1	Bhlhe41	Acss3	A730085K08Rik
Anapc15	Bnc2	Adamts1	A930037H05Rik
Ankle1	C1ql3	Adamts12	AC168977.2
Anln	Cdh1	Adamts5	Aida
Anp32e	Cdk15	Adgrl2	Ankrd34a
Arhgap11a	Cdk2	Ahr	Apol6
Arhgap19	Cfap54	Aldh1a3	Apol9a
Arhgap33	Chsy3	Ano6	Apol9b
Arhgef39	Daam1	Antxr1	Atp8b4
Asf1b	Dennd5b	Aopep	Axl
Aspm	Disp1	Apobec2	B2m
Aspn	Ehbp1	Aqp1	Batf2
Atad2	Eps8	Arhgap10	Bst2
Atad5	Fmn1	Arhgap24	C1ra
Aunip	Gk	Arhgap29	Casp12
Aurka	Gm13963	Arih1	Ccl2
Aurkb	Gm2115	Arl15	Cfap100
BC030867	Lyst	Atp2b4	Cfb
BC055324	Man1a	Atxn1	Clec2d
Bard1	Man2a1	Baiap2l1	Cmpk2
Batf3	Met	Bcar3	Csf1
Baz1b	Mgat5	Bcas3	Csprs
Birc5	Nceh1	Bche	Csta2
Blm	Nedd4l	Bgn	Cxcl10
Bora	Nhs	C030034L19Rik	Cxcl9
Brca1	Oca2	Cacna1d	Ddx58
Brca2	Osbpl6	Cacnb3	Ddx60
Brd8	Padi2	Cadps	Dhx58
Brip1	Pde10a	Cblb	Dtx3l
Bub1	Ppargc1a	Cdk14	Eif2ak2
Bub1b	Ralgapa2	Cdk6	F830016B08Rik
C230066G23Rik	Sfi1	Col15a1	Flacc1
Camk2n2	Slc24a4	Col28a1	Gbp10
Casp8ap2	Slc7a5	Col3a1	Gbp2
Cbx5	St3gal6	Col5a2	Gbp3
Ccdc18	Sytl2	Col6a1	Gbp4
Ccdc34	Tex2	Col6a2	Gbp5
Ccdc77	Tmod1	Col8a1	Gbp6
Cchcr1	Tspan5	Cped1	Gbp7
Ccna2	Tyr	Cspg4	Gbp8

Ccnb1	Tyrp1	Ctnnal1	Gbp9
Ccnb2	Ubl3	Dact1	Gm10827
Ccne1		Diaph2	Gm11747
Ccne2		Dip2c	Gm12185
Ccnf		Dkk2	Gm13822
Ccsap		Dmd	Gm15893
Cdc20		Dock10	Gm19684
Cdc25b		Dst	Gm20559
Cdc25c		Eefsec	Gm26789
Cdc45		Efna5	Gm4070
Cdc6		Efnb1	Gm42517
Cdc7		Egflam	Gm43727
Cdca2		Eln	Gm44091
Cdca3		Etv5	Gm44148
Cdca5		Ext1	Gm4841
Cdca7		Fam110b	Gm4951
Cdca7l		Fam178b	Gm50237
Cdca8		Farp1	Gm5148
Cdk1		Fgfr1	Gm7030
Cdkn2d		Fign	Gm8773
Cdkn3		Fkbp5	Gpr149
Cdt1		Frmd6	Gpr65
Cenpa		Gli3	Gvin1
Cenpc1		Gm13919	H2-D1
Cenpe		Gm20754	H2-K1
Cenpf		Gm35188	H2-Q10
Cenph		Gm4117	H2-Q4
Cenpi		Gnaq	H2-T22
Cenpk		Hapln1	H2-T23
Cenpl		Hdac9	Herc6
Cenpm		Hivep2	Ifi203
Cenpn		Hmga2	Ifi204
Cenpp		Hs2st1	Ifi205
Cenpq		Hspb2	Ifi206
Cenps		Htr2a	Ifi207
Cenpu		Ica1	Ifi211
Cenpw		Igfbp4	Ifi27
Cep128		Il1rap	Ifi35
Cep192		Insr	Ifi44
Cep295		Itgbl1	Ifi47
Cep55		Itprid2	Ifih1
Cep57l1		Jmjd1c	Ifit1
Cep72		Kank4	Ifit2
Cep89		Kcnn2	Ifit3
Cfap97d2		Kif13a	Ifit3b
Cgas		Kif26b	Ifitm3
Chaf1a		Klf4	Igtp
Chaf1b		L1cam	Iigp1
Chek1		Lama4	Irf1

Chek2		Large1	Irf7
Chgb		Ldlrad3	Irgm1
Chtf18		Lgr4	Irgm2
Cip2a		Limch1	Isg15
Cit		Lmcd1	Isg20
Ckap2		Lpar3	Ky
Ckap2l		Lrch1	Lgals9
Ckap5		Lrch3	Lrfn1
Cks1b		Lrp1	Ly6e
Cks2		Maml2	Map3k19
Clspn		Map2	Mlkl
Cmc2		Map4	Mndal
Cnih2		Map4k3	Nlrc5
Cntrob		Mcam	Nmi
D430018E03Rik		Megf10	Oas1a
Dbf4		Mgp	Oas1g
Dcdc2a		Mir100hg	Oas2
Dck		Mllt3	Oas3
Dctpp1		Moxd1	Oasl1
Ddias		Mpz	Oasl2
Ddx11		Myo5b	Olfr56
Dek		Myof	Parp10
Depdc1a		Nav3	Parp11
Depdc1b		Ndst3	Parp12
Dhfr		Neat1	Parp14
Diaph3		Nebl	Parp9
Dlgap5		Nes	Phf11a
Dna2		Ngfr	Phf11b
Dnaaf2		Nhsl1	Phf11d
Dnajc9		Nxn	Pml
Dnmt1		P3h2	Psmb10
Dnph1		Pam	Psmb8
Dscc1		Pcdh9	Psmb9
Dsn1		Pcgf5	Psme1
Dtl		Pcsk6	Psme2
Dtymk		Pdgfb	Rnf19b
Dut		Pdgfra	Rnf213
Dynlt1a		Pdgfrb	Rsad2
Dynlt1f		Pdgfrl	Rtp4
E2f1		Pdlim4	Samd9l
E2f2		Pdlim5	Samhd1
E2f7		Pdzrn3	Slc2a6
E2f8		Pitpnc1	Slfn8
Ect2		Plcb1	Slfn9
Efcab11		Plekha6	Socs1
Eldr		Plpp1	Sp100
Eme1		Ppp1r1c	Sp110
Emp1		Prelp	Sp140
Ercc6l		Ptpn13	Stat1

Eri1		Ptprj	Stat2
Eri2		Rab27b	Styk1
Esco2		Ramp3	Tap1
Espl1		Rapgef2	Tap2
Exo1		Raph1	Tapbp
Exosc8		Rasgrp2	Tapbpl
Ezh2		Rbms1	Tgtp1
Fam111a		Rere	Tgtp2
Fam83d		Rgs16	Tnfsf10
Fanca		Rnd3	Tomm6os
Fancb		Robo1	Tor3a
Fancd2		Robo2	Trafd1
Fanci		Rock2	Trim12a
Fbxo48		Ror1	Trim12c
Fbxo5		S100a6	Trim21
Fen1		Samd4	Trim25
Fignl1		Samd5	Trim30a
Fkbp2		Sdc3	Trim34a
Fn3k		Sec14l5	Ube2l6
Foxg1		Sema3a	Usp18
Foxm1		Sema3b	Wnt2b
Fzr1		Sema5a	Xaf1
G2e3		Sema6a	Xdh
Gabrb3		Serpinf1	Ypel4
Gas2l3		Serping1	Zbp1
Gemin6		Sertad4	Znfx1
Gen1		Sh3rf1	
Gins1		Sipa1l1	
Gins2		Sipa1l3	
Gins3		Slc35f1	
Gins4		Slc9a3r2	
Gm14091		Sntb1	
Gm20628		Sorcs2	
Gm20667		Taf4b	
Gm3550		Tanc1	
Gm38037		Tbck	
Gm41555		Tcf20	
Gm42031		Tcim	
Gm42047		Tead1	
Gm44238		Tecrl	
Gm47207		Tenm3	
Gm4737		Tfap2b	
Gm48646		Thbs2	
Gm49014		Thsd4	
Gm550		Tiam2	
Gmnn		Tln2	
Gpsm2		Tnc	
Grm1		Trio	
Gtse1		Tslp	

H2afx		Ttc39b	
H2afz		Ube2e2	
Haspin		Wnt4	
Hat1		Wnt6	
Haus4		Xirp1	
Haus6		Zbtb38	
Haus8		Zeb1	
Hdgf		Zfc3h1	
Hells		Zfp532	
Hid1			
Hirip3			
Hist1h1a			
Hist1h1b			
Hist1h1c			
Hist1h1d			
Hist1h1e			
Hist1h1t			
Hist1h2ab			
Hist1h2ac			
Hist1h2ad			
Hist1h2ae			
Hist1h2af			
Hist1h2ag			
Hist1h2ah			
Hist1h2ai			
Hist1h2ak			
Hist1h2an			
Hist1h2ap			
Hist1h2bb			
Hist1h2be			
Hist1h2bf			
Hist1h2bg			
Hist1h2bh			
Hist1h2bj			
Hist1h2bk			
Hist1h2bl			
Hist1h2bm			
Hist1h2bn			
Hist1h2bp			
Hist1h2br			
Hist1h3a			
Hist1h3b			
Hist1h3c			
Hist1h3e			
Hist1h3f			
Hist1h3g			
Hist1h3h			
Hist1h3i			
Hist1h4a			

Hist1h4b			
Hist1h4c			
Hist1h4d			
Hist1h4f			
Hist1h4h			
Hist1h4j			
Hist1h4k			
Hist1h4n			
Hist2h2aa1			
Hist2h2ab			
Hist2h2ac			
Hist2h2bb			
Hist2h3b			
Hjurp			
Hmgb2			
Hmgb3			
Hmgn2			
Hmgn5			
Hmgxb4			
Hmmr			
Hmx2			
Hyls1			
Il1rapl2			
Impa2			
Incenp			
Iqgap3			
Jpt1			
Kctd18			
Kif11			
Kif14			
Kif15			
Kif18a			
Kif18b			
Kif20a			
Kif20b			
Kif22			
Kif23			
Kif24			
Kif2c			
Kif4			
Kifc1			
Kifc5b			
Knl1			
Knstrn			
Kntc1			
Kpna2			
Lbr			
Lig1			
Lin54			

Lin9			
Lmnb1			
Lockd			
Lrfn1			
Lrr1			
Lsm2			
Lsm5			
Mad2l1			
Mastl			
Mcm10			
Mcm2			
Mcm3			
Mcm4			
Mcm5			
Mcm6			
Mcm7			
Mdc1			
Melk			
Mis18a			
Mis18bp1			
Mki67			
Mlf1			
Mms22l			
Mnd1			
Mns1			
Mtbp			
Mtfr2			
Mthfd2			
Mxd3			
Myb			
Mybl1			
Mybl2			
Nasp			
Ncapd2			
Ncapd3			
Ncapg			
Ncapg2			
Ncaph			
Ndc1			
Ndc80			
Nde1			
Neil3			
Nek2			
Nell1			
Nemp1			
Neurl1b			
Nfatc2ip			
Nmral1			
Nrm			

Nsd2			
Nsl1			
Nt5dc2			
Nucks1			
Nuf2			
Nup107			
Nup155			
Nup205			
Nup35			
Nup37			
Nup43			
Nup85			
Nusap1			
Nxt1			
Odf2			
Ogn			
Oip5			
Omd			
Orc6			
Otx2			
Parpbp			
Pask			
Pbk			
Pclaf			
Pcna			
Phf19			
Pif1			
Pimreg			
Pkmyt1			
Pla2g4c			
Plk1			
Plk4			
Pmf1			
Pola1			
Pola2			
Pold1			
Pold2			
Pold3			
Pole			
Pole2			
Polh			
Polq			
Prc1			
Prim1			
Prim2			
Prr11			
Psmc3ip			
Racgap1			
Rad18			

Rad21			
Rad50			
Rad51			
Rad51ap1			
Rad51b			
Rad54b			
Rad54l			
Rangap1			
Rbbp8			
Rbl1			
Rccd1			
Reep4			
Rfc1			
Rfc2			
Rfc3			
Rfc4			
Rfc5			
Rfwd3			
Rif1			
Rmi2			
Rnaseh2c			
Rnf168			
Rpa2			
Rpa3			
Rrm1			
Rrm2			
Rtkn2			
Sapcd2			
Sass6			
Scml2			
Selenoh			
Serpinb8			
Sgo1			
Sgo2a			
Shcbp1			
Siva1			
Ska1			
Ska2			
Ska3			
Skp2			
Slbp			
Slc30a10			
Slc43a3			
Slc9a5			
Slf1			
Slfn9			
Smc2			
Smc4			
Snrnp25			

Spag5			
Spc24			
Spc25			
Spdl1			
Stbd1			
Stil			
Stmn1			
Suv39h1			
Tacc3			
Tagln2			
Tbc1d31			
Tcf19			
Tedc1			
Terf1			
Tex30			
Tfdp1			
Ticrr			
Timeless			
Tipin			
Tk1			
Tmpo			
Tnfaip8l1			
Top2a			
Topbp1			
Tpx2			
Traip			
Trim59			
Trip13			
Troap			
Ttk			
Tuba1c			
Tubb4b			
Tubb6			
Tube1			
Tubg1			
Tyms			
Ube2c			
Ube2s			
Ube2t			
Uevld			
Uhrf1			
Ulbp1			
Ung			
Usp1			
Usp37			
Vrk1			
Wdhd1			
Wdr76			
Wee1			

Xkr5			
Xndc1			
Zfand4			
Zfp367			
Zfp993			
Zgrf1			
Zranb3			
Zwilch			

MP5	MP6	MP7
1110008P14Rik	1700016K05Rik	Acaca
2310009B15Rik	1700025G04Rik	Acacb
Abracl	2610035D17Rik	Aph1c
Ak6	4930517O19Rik	Bri3
Akr1a1	4930554G24Rik	Chpt1
Akr1b3	Adam12	Cited1
Anp32b	Adamts5	Cox17
Anp32e	Adamts6	Cox8b
Anxa2	Adgrl3	Cryab
Ap2m1	Aff3	Cst6
Ap2s1	Agap1	Cyba
Apex1	Akap12	Cystm1
Aprt	Arap2	Dct
Arf1	Asap1	Eif3f
Arhgdib	Atrnl1	Fabp3
Arpc3	B4galt6	Fabp5
Arpp19	Cd200	Fam104a
Asna1	Cd9	Foxp2
Atp5c1	Cdh10	Fundc2
Atp5d	Cdk5rap2	Gm3776
Atp5f1	Chl1	Gng8
Atp5g1	Col23a1	Gsk3b
Atp5h	Csad	Gsta1
Atp5j	Ctsh	Gsta2
Atp5k	Cttnbp2	Gstp1
Atp5o	Dkk3	Mlana
Atp6v0e	Dock3	Mtss1
Atpif1	Eno3	Myo5a
Aurkaip1	Erbb3	Ndufs2
Bag1	Etv1	Oat
Banf1	Fam184b	Oca2
Bax	Fap	Pmel
Bex3	Fbxl7	Ptgds
Bola2	Fxyd1	Ptprs
Btf3	Gjc3	Ralgapa2
Bud31	Gm15594	Reep5
Bzw1	Gm49267	Rgs10
C1qbp	Gpm6b	Rhoa
Cacybp	Gulp1	Rnasek
Ccdc124	Hecw2	Rnf7
Cct3	Hpgds	S100a1
Cct5	Ikbkb	S100b
Cct6a	Il16	Sec11c
Cct8	Inpp5f	Selenos
Cdk2ap1	Iqgap2	Sgcd
Cdk4	Itga2	Slc37a2

Cenpx	Klf12	Smpd1
Cetn3	Lgi4	Traf5
Chchd1	Lima1	Tspan10
Chchd4	Lmo4	Tyrp1
Chchd7	Map4k3	Uqcrfs1
Chmp2a	Mbp	Vegfb
Churc1	Mecom	Vps29
Ciao2b	Mef2c	
Cisd1	Megf9	
Clic1	Metrn	
Cnbp	Mmd	
Cnih4	Mprip	
Coa3	Mpzl1	
Commd1	Mtss1	
Cope	Mxra8	
Cops6	Myzap	
Cops9	Ndrg2	
Coq7	Nrn1	
Cox20	Ntn4	
Cox5a	P3h2	
Cox5b	Pde1c	
Cox6a1	Plat	
Cox7b	Plpp1	
Creld2	Ppm1l	
Cryab	Prickle2	
Cstb	Prkca	
Cuedc2	Prss23	
Cyc1	Psd3	
Cycs	Ptprm	
Dctn3	Rasal2	
Dctpp1	Rasgrp3	
Ddt	Rbfox2	
Ddx21	Rbm20	
Ddx39	Rnf152	
Denr	Sema3d	
Dynll1	Serpinb1a	
Ebna1bp2	Sgcd	
Eef1d	Slc12a2	
Eef1e1	Slc4a8	
Eif1ad	Snx25	
Eif2s1	Sort1	
Eif2s2	Sox5	
Eif3b	Sox5os4	
Eif3c	Sox6	
Eif3g	Stard13	
Eif3i	Tcf7l1	
Eif3j1	Tgfb2	
Eif4a1	Tnik	
Eif4e2	Tom1l2	

Eif4g2	Unc5c	
Eif5a	Zbtb7c	
Eif6	Zfhx4	
Elob	Zfp608	
Elof1	Zfp704	
Emc6		
Emg1		
Eno1		
Erh		
Esd		
Etfb		
Fabp5		
Fam162a		
Fbl		
Fkbp11		
Fkbp1a		
Fkbp3		
Fkbp4		
G3bp1		
Gadd45gip1		
Galk1		
Gapdh		
Gemin6		
Glrx3		
Gm2000		
Gnai2		
Gnb2		
Gnl3		
Gpx1		
Gspt1		
Gtf2h5		
Higd1a		
Hint1		
Hmgn1		
Hnrnpa3		
Hnrnpab		
Hnrnpd		
Hnrnpf		
Hras		
Hsp90aa1		
Hspa5		
Hspa8		
Hspd1		
Hspe1		
Idh2		
Idh3a		
Ier3ip1		
Ifitm2		
Impdh2		

Jpt1		
Kmt5a		
Lamtor1		
Lamtor4		
Lamtor5		
Ldha		
Llph		
Lrrc59		
Lsm12		
Lsm2		
Lsm4		
Lyar		
Magoh		
Mak16		
Manf		
Mbd3		
Mdh1		
Metap2		
Micos10		
Micos13		
Mien1		
Morf4l1		
Mpc2		
Mrpl12		
Mrpl13		
Mrpl14		
Mrpl17		
Mrpl18		
Mrpl20		
Mrpl21		
Mrpl23		
Mrpl27		
Mrpl28		
Mrpl30		
Mrpl34		
Mrpl35		
Mrpl36		
Mrpl52		
Mrpl53		
Mrpl54		
Mrpl57		
Mrpl58		
Mrps14		
Mrps16		
Mrps21		
Mrps24		
Mrps36		
Mrps7		
Mrto4		

Mvb12a		
Mybbp1a		
Mydgf		
Myl12a		
Myl6		
Naa38		
Nap1l1		
Ncl		
Ndufa10		
Ndufa11		
Ndufa12		
Ndufa3		
Ndufa5		
Ndufa8		
Ndufab1		
Ndufb2		
Ndufb3		
Ndufb6		
Ndufb7		
Ndufb8		
Ndufs3		
Ndufs5		
Ndufs6		
Ndufs7		
Ndufs8		
Ndufv2		
Ndufv3		
Nhp2		
Nifk		
Nme1		
Nol7		
Nolc1		
Nop10		
Nop56		
Nop58		
Npm3		
Nsa2		
Nudc		
Nudcd2		
Oaz1		
Pa2g4		
Pabpc1		
Park7		
Pcbp1		
Pdap1		
Pdcd5		
Pebp1		
Pet100		
Pfdn2		

Pfdn6		
Pfn1		
Pgam1		
Pgk1		
Pgls		
Phb2		
Phf5a		
Pin1		
Pkm		
Pole3		
Polr1d		
Polr2e		
Polr2f		
Polr2g		
Polr2j		
Polr2k		
Polr2l		
Pomp		
Pop5		
Pop7		
Ppa1		
Ppdpf		
Ppp1ca		
Ppp1r14b		
Prdx6		
Prelid1		
Prelid3b		
Prkar1a		
Prmt1		
Psenen		
Psma2		
Psma3		
Psma4		
Psma5		
Psma6		
Psma7		
Psmb1		
Psmb2		
Psmb3		
Psmb4		
Psmb5		
Psmb6		
Psmc2		
Psmc3		
Psmc4		
Psmc5		
Psmd12		
Psmd6		
Psmd7		

Psmd8		
Psmg4		
Ptges3		
Rab5if		
Rad23a		
Ran		
Ranbp1		
Rbis		
Rbm8a		
Rer1		
Rhoa		
Rhoc		
Rpl12		
Rpl23a		
Rpl31		
Rps17		
Rps19bp1		
Rps25		
Rps26		
Rsl1d1		
Ruvbl1		
Rwdd1		
S100a10		
Sap18		
Sdhb		
Sdhd		
Serbp1		
Set		
Sf3b5		
Sf3b6		
Sh3bgrl3		
Skp1a		
Slc25a39		
Slc25a5		
Slirp		
Smarca5		
Snrnp27		
Snrpb		
Snrpc		
Snrpd1		
Snrpd2		
Snrpd3		
Snrpf		
Snrpg		
Snu13		
Snx3		
Sparc		
Spcs1		
Sra1		

Srm		
Srp19		
Srsf3		
Ssb		
Ssr4		
Strap		
Sub1		
Suclg1		
Sumo2		
Svbp		
Swi5		
Taf10		
Taldo1		
Tbcb		
Timm10		
Timm10b		
Timm13		
Timm23		
Timm8a1		
Tmed9		
Tmem126a		
Tmem14c		
Tmem208		
Tmem258		
Tomm22		
Tomm5		
Tpi1		
Tpm3		
Tpm4		
Trappc2l		
Trir		
Trmt112		
Tspo		
Txn2		
Txndc17		
Txnl1		
Txnl4a		
U2af1		
Ube2m		
Ufc1		
Uqcc2		
Uqcr10		
Uqcrb		
Vdac1		
Vdac2		
Vdac3		
Wdr83os		
Xbp1		
Ybx3		

Ywhab		
Ywhaq		
Ywhaz		
Zc3h15		
Zmat2		
Znhit1		

Table S3. Flow cytometry immune cell annotations

Population	Abbreviation	Primary markers used for identification
Infiltrating cells	$CD45^{hi}$	$^{a}Lin^{neg}CD45.2^{hi}CD44^{pos/hi}CD49d^{pos/hi}$
Microglia	Mg	$CD45^{low/+}CD44^{low}CD49d^{low}TMEM119^{+/hi}P2RY12^{low/hi}SiglecH^{low/hi}CX3CR1^{+/hi}CD11b^{+}$
Total T cells	T cells	$^{a}Lin^{neg}CD45.2^{hi}SSC\text{-}A^{low}NK1.1^{neg}CD19^{neg}CD3^{+}$
CD8 T cells	CD8 T	$^{a}Lin^{neg}CD45.2^{hi}SSC\text{-}A^{low}NK1.1^{neg}CD19^{neg}CD3^{+}CD8^{+}CD4^{neg}$
CD4 T cells	CD4 T	$^{a}Lin^{neg}CD45.2^{hi}SSC\text{-}A^{low}NK1.1^{neg}CD19^{neg}CD3^{+}CD8^{neg}CD4^{+}$
$CD8^{+}CD4^{+}$ T cells	DP T	$^{a}Lin^{neg}CD45.2^{hi}SSC\text{-}A^{low}NK1.1^{neg}CD19^{neg}CD3^{+}CD8^{+}CD4^{+}$
$CD8^{-}CD4^{-}$ T cells	DN T	$^{a}Lin^{neg}CD45.2^{hi}SSC\text{-}A^{low}NK1.1^{neg}CD19^{neg}CD3^{+}CD8^{neg}CD4^{neg}$
Natural killer	NK	$^{a}Lin^{neg}CD45.2^{hi}SSC\text{-}A^{low}CD19^{neg}CD3^{neg}NK1.1^{hi}$
Natural killer T cells	NKT	$^{a}Lin^{neg}CD45.2^{hi}SSC\text{-}A^{low}CD19^{neg}CD3^{+}NK1.1^{hi}$
Innate lymphoid cells	ILCs	$^{a}Lin^{neg}CD45.2^{hi}SSC\text{-}A^{low}NK1.1^{neg}CD19^{neg}CD3^{neg}CD11b^{neg}CD11c^{neg}$
B cells	B cells	$^{a}Lin^{neg}CD45.2^{hi}CD3^{neg}NK1.1^{neg}CD19^{+}MHCII^{+}$
Neutrophils	Neu	$^{b}Lin^{neg}CD45.2^{hi}SSC\text{-}A^{int}CD11b^{+}Ly6C^{int}Ly6G^{+}$
Mononuclear phagocytes	Mononuclear phagocytes	$^{b}Lin^{neg}CD45.2^{hi}CD44^{+/hi}CD49d^{hi}Ly6G^{neg}CD11b^{+}$ $^{b}Lin^{neg}CD45.2^{hi}CD44^{+/hi}CD49d^{hi}Ly6G^{neg}CD11c^{+}$
Classical Monocytes	$Ly6C^{hi}$ Monocytes	$^{b}Lin^{neg}Ly6G^{neg}CX3CR1^{+}CD44^{hi}F4/80^{neg\text{-}low}CD11c^{neg}MHCII^{neg}Ly6C^{hi}$
Non-classical Monocytes	$Ly6C^{low}$ Monocytes	$^{b}Lin^{neg}Ly6G^{neg}CX3CR1^{+}CD44^{hi}F4/80^{low/int}CD11c^{low}MHCII^{neg}Ly6C^{low}$
Monocyte-derived	Monoderived	$^{b}Lin^{neg}CD45.2^{hi}Ly6G^{neg}CD11b^{int/hi}CD11c^{neg\text{-}low\text{-}int}SiglecH^{neg}CD24^{neg}MHCII^{+/hi}MertK^{pos/hi}$ $F4/80^{pos/hi}$
Dendritic cells	DC	$^{a}Lin^{neg}Ly6G^{neg}CD11c^{+}MHCII^{+}F4/80^{neg}CD24^{+}$
Dendritic cells 1	DC1	$^{a}Lin^{neg}Ly6G^{neg}CD11c^{hi}MHCII^{+}F4/80^{neg}CD11b^{neg}CD24^{hi}CD103^{hi}$
Dendritic cells 2	DC2	$^{a}Lin^{neg}Ly6G^{neg}CD11c^{+}MHCII^{hi}F4/80^{neg}CD11b^{+}CD24^{neg}CD103^{neg}$
Dendritic cells 3	DC.pop3	$^{a}Lin^{neg}Ly6G^{neg}CD11c^{+}MHCII^{+}F4/80^{neg}CD11b^{neg}CD24^{hi}CD103^{neg}$
Plasmacytoid DC	pDC	$^{a}Lin^{neg}Ly6G^{neg}CD11c^{int}MHCII^{lo}Ly6C^{+}SiglecH^{+}$

$^{a}Lin^{neg}$: $TMEM119^{neg}P2RY12^{neg}$
$^{b}Lin^{neg}$: $TMEM119^{neg}P2RY12^{neg}NK1.1^{neg}CD3^{neg}CD19^{neg}$

Table S4: CD8 T cell cluster defining genes

p_val	avg_log 2FC	pct.1	pct.2	p_val_adj	cluster	cluster name	gene
1.95E-68	1.931	0.983	0.550	5.11E-64	0	sc.5	S100a6
2.54E-66	1.235	1.000	0.817	6.67E-62	0	sc.5	Cd3g
2.61E-65	1.362	1.000	0.788	6.85E-61	0	sc.5	Nkg7
9.43E-62	1.314	1.000	0.790	2.47E-57	0	sc.5	AW112010
9.58E-62	1.411	1.000	0.581	2.51E-57	0	sc.5	Cxcr6
1.55E-60	2.079	0.991	0.658	4.05E-56	0	sc.5	Ccl5
2.26E-59	1.733	0.945	0.396	5.92E-55	0	sc.5	S100a4
3.96E-59	1.364	0.766	0.162	1.04E-54	0	sc.5	Gm36723
6.75E-52	1.044	0.830	0.254	1.77E-47	0	sc.5	Fgl2
2.33E-49	1.852	0.770	0.223	6.10E-45	0	sc.5	Gzmb
2.16E-48	0.979	0.996	0.750	5.67E-44	0	sc.5	Cd8a
1.43E-47	1.160	0.689	0.175	3.75E-43	0	sc.5	Tcrg-C2
7.43E-47	1.383	0.923	0.406	1.95E-42	0	sc.5	Ccl4
6.27E-46	1.055	0.953	0.642	1.64E-41	0	sc.5	S100a11
2.05E-43	1.104	0.983	0.565	5.36E-39	0	sc.5	Id2
4.23E-43	1.288	0.932	0.633	1.11E-38	0	sc.5	Klrd1
7.42E-42	0.948	0.987	0.571	1.95E-37	0	sc.5	Rbpj
1.46E-41	0.941	0.932	0.429	3.84E-37	0	sc.5	Pdcd1
1.95E-41	1.196	0.983	0.681	5.12E-37	0	sc.5	Lgals1
1.06E-39	1.087	0.677	0.202	2.78E-35	0	sc.5	Trgv2
1.23E-37	0.933	0.783	0.292	3.24E-33	0	sc.5	Lag3
2.82E-37	0.949	0.685	0.192	7.39E-33	0	sc.5	Havcr2
2.16E-35	0.935	0.647	0.200	5.66E-31	0	sc.5	Cd200r1
3.43E-35	1.140	0.651	0.192	9.00E-31	0	sc.5	Ccl3
1.97E-33	0.941	0.877	0.467	5.16E-29	0	sc.5	Cdk6
1.02E-30	1.011	0.728	0.294	2.68E-26	0	sc.5	Prf1
7.87E-28	1.052	0.553	0.181	2.06E-23	0	sc.5	Klre1
1.80E-27	1.007	0.685	0.277	4.72E-23	0	sc.5	Ifng
1.69E-22	0.955	0.749	0.375	4.44E-18	0	sc.5	Ctla4
1.20E-16	0.956	0.677	0.419	3.14E-12	0	sc.5	Plac8
7.42E-22	1.600	0.639	0.290	1.95E-17	1	sc.3	Ly6c2
1.22E-20	0.629	0.614	0.241	3.20E-16	1	sc.3	Cxcr3
1.91E-16	0.638	0.975	0.791	5.02E-12	1	sc.3	Hcst
1.07E-15	0.617	0.772	0.425	2.82E-11	1	sc.3	Gramd3
1.96E-15	0.561	0.810	0.564	5.15E-11	1	sc.3	Smap1
1.33E-14	0.537	0.709	0.392	3.48E-10	1	sc.3	Hopx
2.46E-14	0.454	1.000	0.993	6.46E-10	1	sc.3	Rpl13a
3.79E-14	0.457	0.994	0.700	9.95E-10	1	sc.3	Ccl5

6.85E-14	0.732	0.854	0.621	1.80E-09	1	sc.3	Zfp36l2
1.04E-13	0.795	0.918	0.794	2.72E-09	1	sc.3	Itgb1
2.79E-13	0.490	1.000	0.992	7.31E-09	1	sc.3	Rps27
3.63E-13	0.593	0.962	0.844	9.52E-09	1	sc.3	Gimap4
1.11E-11	0.497	0.956	0.901	2.92E-07	1	sc.3	Ly6e
1.56E-11	0.526	1.000	0.987	4.09E-07	1	sc.3	Tmsb10
6.09E-11	0.449	0.981	0.814	1.60E-06	1	sc.3	Ptpn18
6.78E-11	0.581	0.892	0.786	1.78E-06	1	sc.3	Ifngr1
1.30E-10	0.561	0.949	0.841	3.41E-06	1	sc.3	Epsti1
2.28E-10	0.531	0.842	0.595	5.98E-06	1	sc.3	Gm2682
4.01E-10	0.490	0.880	0.626	1.05E-05	1	sc.3	Gimap7
6.25E-10	0.528	0.570	0.298	1.64E-05	1	sc.3	Gzmk
8.08E-10	0.440	0.506	0.260	2.12E-05	1	sc.3	Rtp4
1.18E-09	0.563	0.627	0.410	3.09E-05	1	sc.3	Slfn1
1.70E-09	0.451	0.709	0.513	4.46E-05	1	sc.3	Sorl1
3.38E-09	0.437	0.728	0.516	8.85E-05	1	sc.3	Sp110
4.12E-09	0.436	0.905	0.797	0.000	1	sc.3	Gimap3
1.01E-08	0.453	0.994	0.945	0.000	1	sc.3	Ms4a4b
3.58E-08	0.709	0.772	0.591	0.001	1	sc.3	Ly6a
3.98E-08	0.461	0.753	0.538	0.001	1	sc.3	Txnip
6.03E-08	0.495	0.684	0.471	0.002	1	sc.3	Slco3a1
1.31E-55	1.145	0.866	0.186	3.45E-51	2	sc.2	Cd81
1.62E-54	1.324	0.843	0.170	4.25E-50	2	sc.2	Sparc
2.40E-49	1.119	0.827	0.180	6.29E-45	2	sc.2	Sparcl1
1.28E-45	1.068	0.764	0.161	3.35E-41	2	sc.2	Ctsl
1.06E-41	1.374	0.858	0.304	2.78E-37	2	sc.2	Mt1
6.87E-40	1.173	0.835	0.272	1.80E-35	2	sc.2	Ckb
1.37E-38	1.117	0.906	0.346	3.60E-34	2	sc.2	Qk
2.72E-38	1.808	0.984	0.973	7.13E-34	2	sc.2	mt-Nd1
5.42E-37	1.498	1.000	1.000	1.42E-32	2	sc.2	mt-Co1
7.78E-37	1.540	1.000	0.984	2.04E-32	2	sc.2	mt-Nd2
1.05E-36	1.736	1.000	0.994	2.76E-32	2	sc.2	mt-Nd4
1.10E-36	1.084	0.819	0.245	2.89E-32	2	sc.2	Cd63
1.61E-36	1.578	1.000	1.000	4.21E-32	2	sc.2	mt-Atp6
2.87E-35	1.566	1.000	1.000	7.52E-31	2	sc.2	mt-Cytb
5.45E-35	1.099	0.874	0.336	1.43E-30	2	sc.2	C1qb
6.74E-35	1.676	1.000	1.000	1.77E-30	2	sc.2	mt-Co2
4.97E-33	1.568	1.000	1.000	1.30E-28	2	sc.2	mt-Co3
9.81E-33	1.282	0.984	0.682	2.57E-28	2	sc.2	Apoe
1.76E-32	1.027	0.866	0.374	4.61E-28	2	sc.2	C1qa
7.42E-32	1.477	0.992	0.846	1.95E-27	2	sc.2	Ttr
6.28E-31	1.314	0.992	0.811	1.65E-26	2	sc.2	Macf1
2.72E-26	1.213	0.992	0.954	7.14E-22	2	sc.2	AY036118

4.96E-21	1.076	0.984	0.893	1.30E-16	2	sc.2	Cst3
6.15E-21	1.237	0.969	0.667	1.61E-16	2	sc.2	Zbtb20
1.67E-20	1.218	0.992	0.978	4.38E-16	2	sc.2	Camk1d
4.60E-17	1.064	0.992	0.900	1.21E-12	2	sc.2	Elmo1
6.89E-17	1.055	0.969	0.775	1.81E-12	2	sc.2	Gphn
4.70E-15	1.165	0.843	0.621	1.23E-10	2	sc.2	Nr3c1
9.94E-15	1.090	0.945	0.868	2.61E-10	2	sc.2	mt-Nd5
1.21E-10	1.043	0.976	0.882	3.17E-06	2	sc.2	Xist
#######	2.066	0.886	0.043	1.15E-109	3	sc.1	Sell
1.23E-90	1.827	0.927	0.111	3.23E-86	3	sc.1	Cmah
2.59E-89	1.253	0.740	0.035	6.78E-85	3	sc.1	Ccr7
2.08E-84	2.628	0.984	0.209	5.45E-80	3	sc.1	Lef1
1.12E-83	2.250	0.959	0.139	2.93E-79	3	sc.1	Klf2
1.74E-77	1.778	0.967	0.188	4.55E-73	3	sc.1	Tcf7
1.28E-73	2.291	0.943	0.220	3.36E-69	3	sc.1	Satb1
1.62E-65	1.349	0.862	0.150	4.24E-61	3	sc.1	S1pr1
1.66E-65	1.829	0.935	0.241	4.35E-61	3	sc.1	Txk
1.12E-64	1.471	0.837	0.139	2.95E-60	3	sc.1	Klf3
3.84E-60	1.448	0.959	0.220	1.01E-55	3	sc.1	Aff3
2.27E-58	1.832	0.821	0.185	5.95E-54	3	sc.1	Fam241a
1.24E-55	1.273	0.854	0.166	3.26E-51	3	sc.1	Slamf6
1.78E-53	1.676	0.951	0.301	4.68E-49	3	sc.1	Bach2
1.67E-49	1.126	1.000	1.000	4.37E-45	3	sc.1	Rps29
5.83E-49	1.556	0.984	0.710	1.53E-44	3	sc.1	Foxp1
3.10E-47	1.844	0.927	0.391	8.12E-43	3	sc.1	Il7r
2.97E-46	1.667	0.967	0.483	7.78E-42	3	sc.1	Ripor2
9.54E-46	1.450	0.870	0.231	2.50E-41	3	sc.1	Fgf13
3.22E-45	1.426	0.943	0.337	8.45E-41	3	sc.1	Emb
7.15E-44	1.712	0.862	0.323	1.88E-39	3	sc.1	Sidt1
8.78E-44	1.197	0.919	0.421	2.30E-39	3	sc.1	Dgka
5.35E-43	1.623	0.992	0.579	1.40E-38	3	sc.1	Gm2682
1.00E-41	1.081	0.992	0.994	2.62E-37	3	sc.1	Rps19
3.64E-40	1.329	0.764	0.236	9.55E-36	3	sc.1	Rras2
1.96E-38	1.346	0.902	0.380	5.14E-34	3	sc.1	Scml4
1.56E-34	1.231	0.959	0.642	4.09E-30	3	sc.1	Crlf3
1.80E-33	1.154	1.000	0.967	4.72E-29	3	sc.1	Arhgap15
2.79E-31	1.080	0.959	0.616	7.32E-27	3	sc.1	Ssh2
1.23E-26	1.110	0.902	0.419	3.23E-22	3	sc.1	Gramd3
4.72E-47	3.287	0.838	0.166	1.24E-42	4	sc.4	Xcl1
1.73E-34	1.333	0.865	0.236	4.53E-30	4	sc.4	Cd160
2.83E-17	1.037	0.878	0.476	7.41E-13	4	sc.4	Ybx3
9.62E-14	0.921	0.716	0.338	2.52E-09	4	sc.4	Bcl2a1d
3.24E-12	1.158	0.716	0.407	8.50E-08	4	sc.4	Il18r1

1.53E-11	0.918	0.649	0.292	4.02E-07	4	sc.4	Tnfrsf9
3.20E-11	0.729	0.635	0.276	8.40E-07	4	sc.4	Il18rap
3.24E-11	0.584	0.689	0.338	8.49E-07	4	sc.4	Fam162a
5.44E-11	0.800	0.649	0.294	1.43E-06	4	sc.4	Alcam
6.70E-11	0.587	0.878	0.540	1.76E-06	4	sc.4	Elk3
1.05E-10	0.846	0.622	0.302	2.74E-06	4	sc.4	Phactr2
2.15E-10	0.645	0.986	0.809	5.63E-06	4	sc.4	Cd8a
2.55E-10	0.964	0.959	0.758	6.69E-06	4	sc.4	Ifi27l2a
2.85E-10	0.746	0.824	0.496	7.48E-06	4	sc.4	Bcl2a1b
1.11E-09	1.041	0.797	0.499	2.90E-05	4	sc.4	St6galnac3
1.19E-09	0.759	0.838	0.562	3.12E-05	4	sc.4	Nfat5
1.22E-09	0.627	0.757	0.417	3.21E-05	4	sc.4	Cd44
1.53E-09	0.667	0.838	0.512	4.01E-05	4	sc.4	Adamts6
2.57E-09	0.611	0.757	0.411	6.74E-05	4	sc.4	Lag3
4.27E-09	0.679	0.986	0.863	1.119E-04	4	sc.4	Rabgap1l
4.79E-09	0.704	0.932	0.675	1.255E-04	4	sc.4	Rbpj
7.63E-09	0.589	1.000	0.993	2.001E-04	4	sc.4	Hsp90ab1
8.38E-09	0.795	0.608	0.285	2.198E-04	4	sc.4	Rgs16
9.43E-09	0.789	0.649	0.385	2.474E-04	4	sc.4	Nrp1
2.13E-08	0.595	0.959	0.812	5.592E-04	4	sc.4	Eif5a
3.04E-08	0.581	0.824	0.592	7.972E-04	4	sc.4	Trps1
3.80E-08	0.684	0.986	0.802	9.962E-04	4	sc.4	Itgb1
1.80E-07	0.603	0.568	0.297	4.729E-03	4	sc.4	Gpm6b
2.91E-07	0.600	0.824	0.537	7.634E-03	4	sc.4	Mdfic
7.11E-96	3.221	1.000	0.043	1.87E-91	5	sc.6	Hist1h3c
1.57E-94	3.143	0.974	0.040	4.11E-90	5	sc.6	Hist1h2ab
5.21E-78	2.336	1.000	0.063	1.37E-73	5	sc.6	Birc5
7.01E-76	2.096	1.000	0.066	1.84E-71	5	sc.6	Cdca8
1.60E-72	2.753	1.000	0.074	4.20E-68	5	sc.6	Pclaf
3.11E-72	2.367	0.974	0.067	8.16E-68	5	sc.6	Nusap1
7.96E-69	2.104	0.921	0.064	2.09E-64	5	sc.6	Hist1h3f
7.78E-65	2.006	0.974	0.081	2.04E-60	5	sc.6	Kif11
4.16E-56	2.658	0.974	0.117	1.09E-51	5	sc.6	Hist1h3e
2.28E-55	2.500	0.789	0.054	5.99E-51	5	sc.6	Cenpf
3.95E-52	2.195	0.974	0.117	1.04E-47	5	sc.6	Prc1
1.04E-49	2.671	0.816	0.074	2.73E-45	5	sc.6	Ube2c
5.00E-49	2.215	0.974	0.142	1.31E-44	5	sc.6	Hist1h4h
5.70E-49	2.465	0.974	0.148	1.50E-44	5	sc.6	Hist2h2ac
7.13E-48	4.304	1.000	0.169	1.87E-43	5	sc.6	Hist1h1b
5.15E-46	2.696	1.000	0.165	1.35E-41	5	sc.6	Mki67
1.73E-44	4.493	1.000	0.191	4.55E-40	5	sc.6	Hist1h2ae
2.73E-40	1.990	1.000	0.209	7.16E-36	5	sc.6	Smc2
1.39E-38	2.888	1.000	0.229	3.64E-34	5	sc.6	Stmn1

7.12E-37	2.137	0.947	0.185	1.87E-32	5	sc.6	Tubb4b
7.40E-37	3.210	1.000	0.264	1.94E-32	5	sc.6	Top2a
8.30E-37	2.115	0.921	0.183	2.18E-32	5	sc.6	H2afx
6.29E-36	4.842	1.000	0.290	1.65E-31	5	sc.6	Hist1h2ap
1.43E-31	2.358	1.000	0.365	3.76E-27	5	sc.6	Tuba1b
7.01E-29	3.416	1.000	0.497	1.84E-24	5	sc.6	Hist1h4d
6.92E-27	2.571	1.000	0.540	1.82E-22	5	sc.6	Hist1h1e
6.78E-26	2.500	1.000	0.656	1.78E-21	5	sc.6	Tubb5
3.00E-25	3.335	1.000	0.706	7.87E-21	5	sc.6	Hmgb2
5.01E-25	1.976	1.000	0.494	1.32E-20	5	sc.6	Ube2s
2.55E-24	2.124	1.000	0.859	6.69E-20	5	sc.6	H2afz

Table S5: CD4 T cell cluster defining genes

p_val	avg_log2FC	pct.1	pct.2	p_val_adj	cluster	cluster name	gene
2.70E-74	2.4658	0.972	0.382	7.09E-70	0	CD4.sc1	Lef1
4.65E-70	2.2771	0.983	0.299	1.22E-65	0	CD4.sc1	Klf2
1.81E-66	2.4356	0.932	0.312	4.75E-62	0	CD4.sc1	Satb1
2.37E-62	1.4292	0.864	0.151	6.21E-58	0	CD4.sc1	Sell
2.69E-62	2.1106	1	0.497	7.04E-58	0	CD4.sc1	Gm2682
4.68E-62	2.0159	0.994	0.59	1.23E-57	0	CD4.sc1	Foxp1
9.41E-62	1.8122	0.909	0.246	2.47E-57	0	CD4.sc1	Txk
1.29E-58	1.5158	0.938	0.281	3.39E-54	0	CD4.sc1	S1pr1
2.65E-58	1.92	0.926	0.354	6.95E-54	0	CD4.sc1	Bach2
6.09E-55	1.0629	1	1	1.60E-50	0	CD4.sc1	Rps29
2.41E-52	0.9964	0.67	0.078	6.33E-48	0	CD4.sc1	Pik3ip1
2.75E-51	1.5112	0.926	0.374	7.20E-47	0	CD4.sc1	Tcf7
5.81E-48	1.1393	0.71	0.133	1.52E-43	0	CD4.sc1	Actn1
9.80E-48	1.4496	0.972	0.698	2.57E-43	0	CD4.sc1	Crlf3
2.28E-47	1.2499	0.812	0.214	5.99E-43	0	CD4.sc1	Klf3
5.35E-46	1.1001	0.591	0.058	1.40E-41	0	CD4.sc1	Rflnb
3.98E-45	1.4041	0.972	0.636	1.04E-40	0	CD4.sc1	Ripor2
1.43E-44	1.3212	1	0.965	3.74E-40	0	CD4.sc1	Arhgap15
2.40E-44	1.6137	0.506	0.03	6.29E-40	0	CD4.sc1	Igfbp4
8.62E-44	1.143	0.545	0.048	2.26E-39	0	CD4.sc1	St8sia6
6.04E-43	1.0328	0.71	0.136	1.58E-38	0	CD4.sc1	Ccr7
1.23E-42	1.1636	0.932	0.497	3.23E-38	0	CD4.sc1	Dgka
1.35E-40	1.2443	0.858	0.364	3.55E-36	0	CD4.sc1	Scml4
9.21E-40	1.3161	0.778	0.249	2.42E-35	0	CD4.sc1	Cmah
6.09E-35	1.2343	0.835	0.397	1.60E-30	0	CD4.sc1	Tmem71
1.56E-34	1.1863	0.955	0.678	4.09E-30	0	CD4.sc1	Prkcq
8.82E-34	1.0426	0.977	0.907	2.31E-29	0	CD4.sc1	Rapgef6
1.68E-33	1.1313	0.761	0.266	4.41E-29	0	CD4.sc1	St6gal1
2.80E-27	1.0327	0.943	0.751	7.34E-23	0	CD4.sc1	Ikzf1
1.48E-26	1.0186	0.688	0.271	3.88E-22	0	CD4.sc1	Ugcg
1.45E-69	2.6831	0.981	0.296	3.79E-65	1	CD4.sc5	Ikzf2
6.35E-65	1.5118	0.786	0.077	1.66E-60	1	CD4.sc5	Foxp3
6.43E-53	1.8706	0.78	0.14	1.69E-48	1	CD4.sc5	Tnfrsf9
6.99E-47	1.6338	0.761	0.154	1.83E-42	1	CD4.sc5	Il2ra
2.77E-46	1.833	0.95	0.361	7.26E-42	1	CD4.sc5	Tnfrsf4
1.39E-45	1.5504	0.969	0.513	3.65E-41	1	CD4.sc5	Tnfrsf18
3.04E-44	1.208	0.629	0.087	7.97E-40	1	CD4.sc5	Neb
1.90E-38	1.6722	0.962	0.448	5.00E-34	1	CD4.sc5	Ctla4
1.32E-35	1.4683	0.78	0.318	3.46E-31	1	CD4.sc5	Arl5a
4.44E-35	1.3279	0.824	0.34	1.16E-30	1	CD4.sc5	Izumo1r
2.70E-32	1.0323	0.547	0.089	7.08E-28	1	CD4.sc5	Itgb8

3.08E-32	1.1847	0.874	0.414	8.09E-28	1	CD4.sc5	Capg
7.62E-31	1.0991	0.792	0.318	2.00E-26	1	CD4.sc5	Tnfrsf1b
4.00E-30	1.0045	0.906	0.407	1.05E-25	1	CD4.sc5	Il2rb
7.21E-29	1.3823	0.824	0.402	1.89E-24	1	CD4.sc5	Itgav
1.83E-28	1.1439	0.855	0.508	4.79E-24	1	CD4.sc5	Gimap7
1.02E-27	1.2783	0.736	0.323	2.67E-23	1	CD4.sc5	Ighm
4.78E-27	1.3767	0.975	0.848	1.25E-22	1	CD4.sc5	Ifi27l2a
1.40E-26	0.9938	0.906	0.571	3.66E-22	1	CD4.sc5	Pim1
2.49E-23	1.0318	0.881	0.525	6.53E-19	1	CD4.sc5	Samsn1
3.30E-21	1.1678	0.717	0.337	8.66E-17	1	CD4.sc5	Hopx
2.02E-20	0.9867	0.811	0.431	5.29E-16	1	CD4.sc5	Maf
6.45E-20	1.0151	0.969	0.798	1.69E-15	1	CD4.sc5	Rabgap1l
8.10E-19	1.0454	0.912	0.713	2.12E-14	1	CD4.sc5	Sdf4
1.59E-18	1.1913	0.818	0.453	4.17E-14	1	CD4.sc5	S100a6
1.14E-17	0.9536	0.566	0.214	3.00E-13	1	CD4.sc5	Iigp1
1.60E-17	0.9873	0.748	0.373	4.21E-13	1	CD4.sc5	Odc1
1.91E-15	0.9527	0.893	0.672	5.01E-11	1	CD4.sc5	Ly6a
2.28E-15	0.9349	0.881	0.646	5.98E-11	1	CD4.sc5	Icos
2.97E-12	0.9491	0.836	0.677	7.80E-08	1	CD4.sc5	Vim
1.04E-13	0.69	0.672	0.345	2.73E-09	2	CD4.sc2	Arhgap26
6.88E-09	0.5019	0.513	0.262	0.00018	2	CD4.sc2	Cd63
1.06E-07	0.6665	0.807	0.582	0.00277	2	CD4.sc2	Itgb1
2.40E-07	0.7834	0.756	0.582	0.006293	2	CD4.sc2	Emb
4.60E-07	0.635	0.697	0.519	0.012059	2	CD4.sc2	Pde7a
6.15E-07	0.4858	0.958	0.879	0.016137	2	CD4.sc2	Celf2
2.18E-06	0.6497	0.723	0.569	0.05709	2	CD4.sc2	Btg2
3.53E-06	0.7988	0.605	0.378	0.092528	2	CD4.sc2	C1qb
4.44E-42	2.1955	0.965	0.203	1.16E-37	3	CD4.sc3	Cxcr6
6.45E-30	2.1697	0.965	0.311	1.69E-25	3	CD4.sc3	Nkg7
3.56E-25	3.0164	0.895	0.331	9.35E-21	3	CD4.sc3	Ccl5
8.47E-24	1.6638	0.544	0.085	2.22E-19	3	CD4.sc3	Ifng
1.25E-21	1.1158	0.579	0.104	3.29E-17	3	CD4.sc3	Tmem163
1.65E-21	1.5962	0.912	0.427	4.33E-17	3	CD4.sc3	Id2
9.99E-21	1.3405	0.86	0.294	2.62E-16	3	CD4.sc3	Pdcd1
2.02E-18	1.081	1	0.954	5.31E-14	3	CD4.sc3	Cd3g
8.21E-18	1.2564	0.93	0.538	2.15E-13	3	CD4.sc3	Rbpj
5.91E-17	1.6558	0.877	0.414	1.55E-12	3	CD4.sc3	S100a4
6.78E-17	1.3834	1	0.814	1.78E-12	3	CD4.sc3	AW112010
2.36E-15	1.0615	0.825	0.346	6.20E-11	3	CD4.sc3	Hip1
2.96E-15	1.3437	0.772	0.304	7.78E-11	3	CD4.sc3	Dusp2
9.25E-15	0.8408	0.684	0.244	2.43E-10	3	CD4.sc3	Tnfsf10
1.25E-14	1.9371	0.509	0.13	3.27E-10	3	CD4.sc3	Ccl4
4.34E-14	0.9849	0.561	0.159	1.14E-09	3	CD4.sc3	Rgs16
4.95E-14	1.3471	0.86	0.453	1.30E-09	3	CD4.sc3	Rgs1
7.77E-14	1.032	0.947	0.578	2.04E-09	3	CD4.sc3	AU020206

6.53E-13	1.2485	0.947	0.511	1.71E-08	3	CD4.sc3	S100a6
1.62E-12	0.9067	1	0.662	4.26E-08	3	CD4.sc3	S100a11
5.45E-12	0.8826	1	0.973	1.43E-07	3	CD4.sc3	Cd52
6.76E-12	0.9882	0.684	0.273	1.77E-07	3	CD4.sc3	Bhlhe40
1.43E-11	0.972	0.982	0.677	3.75E-07	3	CD4.sc3	Lgals1
7.31E-11	0.7638	0.877	0.507	1.92E-06	3	CD4.sc3	Gng2
6.32E-10	0.7972	0.544	0.193	1.66E-05	3	CD4.sc3	Lgals3
7.11E-10	0.9605	0.807	0.472	1.86E-05	3	CD4.sc3	Cd226
7.43E-10	0.7606	1	0.901	1.95E-05	3	CD4.sc3	Arl6ip1
7.47E-08	1.1071	0.649	0.338	0.001958	3	CD4.sc3	Ctla2a
1.15E-07	0.7851	0.965	0.865	0.003019	3	CD4.sc3	Sub1
1.62E-07	0.7853	0.649	0.354	0.004261	3	CD4.sc3	Ctsw
6.60E-39	1.395	0.775	0.079	1.73E-34	4	CD4.sc4	Gm49180
1.69E-29	2.5873	0.95	0.257	4.44E-25	4	CD4.sc4	Tnfsf8
1.13E-25	1.6995	0.8	0.157	2.96E-21	4	CD4.sc4	Tnfsf11
7.07E-20	1.4357	0.875	0.272	1.85E-15	4	CD4.sc4	Bhlhe40
7.14E-20	1.9977	0.925	0.378	1.87E-15	4	CD4.sc4	Eea1
1.70E-17	1.7789	0.975	0.515	4.47E-13	4	CD4.sc4	Trps1
2.27E-17	1.5468	0.825	0.303	5.96E-13	4	CD4.sc4	Tbc1d4
5.60E-17	1.6436	0.95	0.446	1.47E-12	4	CD4.sc4	Gm15283
6.28E-17	1.3698	0.75	0.2	1.65E-12	4	CD4.sc4	Mir155hg
1.03E-16	1.4134	0.825	0.281	2.71E-12	4	CD4.sc4	Phactr2
9.60E-16	1.5897	0.95	0.566	2.52E-11	4	CD4.sc4	Arap2
4.14E-15	1.5608	0.95	0.691	1.09E-10	4	CD4.sc4	Hif1a
1.06E-13	1.1862	0.8	0.264	2.77E-09	4	CD4.sc4	Kcnq5
1.57E-13	1.1136	0.675	0.202	4.12E-09	4	CD4.sc4	Cd200
4.69E-13	1.1912	0.925	0.537	1.23E-08	4	CD4.sc4	Itpr1
5.07E-13	1.3477	0.9	0.446	1.33E-08	4	CD4.sc4	Odc1
7.10E-13	1.1081	0.925	0.545	1.86E-08	4	CD4.sc4	Jak2
7.71E-13	1.2137	0.95	0.624	2.02E-08	4	CD4.sc4	Ostf1
2.00E-12	1.0762	0.9	0.478	5.24E-08	4	CD4.sc4	Etv6
2.17E-12	1.2973	0.975	0.547	5.69E-08	4	CD4.sc4	Rbpj
2.60E-12	1.1922	0.875	0.459	6.82E-08	4	CD4.sc4	Cd82
5.42E-12	1.2641	0.95	0.755	1.42E-07	4	CD4.sc4	Sdf4
1.69E-11	1.0617	0.95	0.605	4.42E-07	4	CD4.sc4	Itgb1
1.73E-11	1.288	0.625	0.221	4.54E-07	4	CD4.sc4	Gpm6b
2.00E-11	1.0825	0.925	0.479	5.24E-07	4	CD4.sc4	Nfat5
1.60E-10	1.195	0.9	0.513	4.19E-06	4	CD4.sc4	Slamf6
1.80E-10	1.3157	0.975	0.717	4.71E-06	4	CD4.sc4	Stat4
2.92E-10	1.1008	0.775	0.375	7.67E-06	4	CD4.sc4	Kdm2b
7.90E-09	1.1523	0.95	0.764	0.000207	4	CD4.sc4	Prkca
3.18E-07	1.1287	0.675	0.363	0.008349	4	CD4.sc4	Nrp1
1.43E-74	2.8862	1	0.031	3.76E-70	5	CD4.sc6	Hist1h2ab
6.56E-68	2.311	1	0.038	1.72E-63	5	CD4.sc6	Nusap1
5.05E-63	1.9574	0.957	0.038	1.33E-58	5	CD4.sc6	Tpx2

5.27E-61	2.8896	1	0.049	1.38E-56	5	CD4.sc6	Hist1h3c
3.61E-60	2.0618	1	0.049	9.48E-56	5	CD4.sc6	Kif11
1.30E-53	2.0623	0.87	0.038	3.41E-49	5	CD4.sc6	Cenpf
4.48E-49	2.1381	0.957	0.062	1.17E-44	5	CD4.sc6	Cdca8
2.30E-47	2.8141	1	0.08	6.02E-43	5	CD4.sc6	Pclaf
2.46E-45	2.1941	0.913	0.064	6.45E-41	5	CD4.sc6	Birc5
3.76E-43	2.3881	0.913	0.067	9.87E-39	5	CD4.sc6	Ube2c
1.27E-40	2.1334	1	0.098	3.34E-36	5	CD4.sc6	Hist1h4h
4.34E-40	2.2946	0.957	0.089	1.14E-35	5	CD4.sc6	Prc1
8.40E-38	2.1106	1	0.111	2.20E-33	5	CD4.sc6	Diaph3
1.16E-37	4.2177	1	0.122	3.05E-33	5	CD4.sc6	Hist1h1b
2.68E-35	2.3752	0.957	0.116	7.03E-31	5	CD4.sc6	Hist1h3e
4.67E-34	3.9954	1	0.142	1.22E-29	5	CD4.sc6	Hist1h2ae
5.19E-34	3.1412	1	0.138	1.36E-29	5	CD4.sc6	Mki67
6.56E-28	2.124	0.957	0.16	1.72E-23	5	CD4.sc6	Hist2h2ac
2.16E-27	3.3427	1	0.205	5.66E-23	5	CD4.sc6	Top2a
2.22E-26	2.0812	1	0.212	5.81E-22	5	CD4.sc6	Smc2
2.63E-25	1.9485	0.957	0.16	6.91E-21	5	CD4.sc6	Rad51b
1.17E-24	4.4356	1	0.247	3.06E-20	5	CD4.sc6	Hist1h2ap
1.38E-23	2.9391	1	0.26	3.62E-19	5	CD4.sc6	Stmn1
1.53E-19	2.034	1	0.365	4.01E-15	5	CD4.sc6	Lmnb1
8.97E-19	2.045	1	0.408	2.35E-14	5	CD4.sc6	Tuba1b
2.74E-18	3.2597	1	0.497	7.18E-14	5	CD4.sc6	Hist1h4d
8.10E-17	2.4069	1	0.675	2.13E-12	5	CD4.sc6	Tubb5
8.39E-16	3.1063	1	0.793	2.20E-11	5	CD4.sc6	Hmgb2
1.23E-15	2.6079	1	0.833	3.23E-11	5	CD4.sc6	H2afz
3.83E-15	2.2363	1	0.519	1.01E-10	5	CD4.sc6	Hist1h1e

Table S6: Patient T cell, BR1 and BR3 genes signatures

Wischnewski_2023 (BrM pTRT CD8)	VanderLeun_2020	Caushi_2021	Lowery_2022	Hanada_2022	Oliviera_2021
CXCL13	CXCL13	ZNF683	ATP10D	ENTPD1	KRT86
RGS1	ENTPD1	GEM	GZMB	CXCL13	RDH10
CCL4L2	ITGAE	TOX2	ENTPD1	HMOX1	TYMS
GZMB	PDCD1	BATF	KIR2DL4	PDCD1	HMOX1
DUSP4	HAVCR2	GBP5	LAYN	LAYN	GNG4
IFNG	LAG3	MIR4435-2HG	HTRA1	CD27	CXCL13
TRBV28	TNFRSF18	TNS3	CD70	HAVCR2	AFAP1L2
GAPDH	TNFRSF9	GNA15	CXCR6	TNFRSF9	ACP5
CTLA4		CXCL13	HMOX1	MIR155HG	MYO1E
CCL3		RBPJ	ADGRG1	BATF	LAYN
LAG3		ENTPD1	LRRN3	TIGIT	TNS3
CD7		LINC02195	ACP5	AD000671.2	TNFSF4
TIGIT		GPR25	CTSW	GZMH	AKAP5
CCL4		ITGAE	GALNT2	CD70	HAVCR2
ITGAE		GNLY	LINC01480	TMEM121	ENTPD1
		PDCD1	CARS	LRRN3	SLC2A8
		CTLA4	LAG3	NHS	AC243829.4
		PRDM1	TOX	TTN	ZBED2
		TNFRSF9	PTPRCAP	LINC01281	MCM5
		TIGIT	ASB2	ASB2	CAV1
		HAVCR2	ITGB7	SIRPG	GOLIM4
			PTMS	ANKS1B	TRAV21
			CD8A		VCAM1
			GPR68		PON2
			NSMCE1		MTSS1
			ABI3		CD38
			SLC1A4		TRBV11-2
			PLEKHF1		MS4A6A
			CD8B		TOX2
			LINC01871		CSF1
			CCL4		GALNT2
			NKG7		FXYD2
			CLIC3		PLPP1
			NDFIP2		LMCD1
			PLPP1		MYL6B
			PCED1B		LAG3
			CXCL13		HLA-DRA
			PDCD1		IGFLR1

			PRF1		CCDC50
			HLA-DMA		CD27
					KIAA1324
					CDKN2A
					CD70
					ABHD6
					CTLA4
					PDCD1
					GEM
					NUSAP1
					TOX
					CXCR6
					NMB
					HOPX
					CLIC3
					INPP5F
					SNAP47
					TSHZ2
					HLA-DMA
					SIT1
					HLA-DRB1
					TUBB
					PYCARD
					ADGRG1
					HLA-DQA1
					PRF1
					HLA-DPA1
					PTMS
					CKS1B
					HIPK2
					CHST12
					LSP1
					FAM3C
					SLC1A4
					NUDT1
					DNPH1

MP4	MP6	BR1 pro-inflammatory	T_CD8	BR1 chemokine L-R	BR3 Neuro
AIDA	C1orf21	HLA-DRB5	CD8A	CCL3	SEMA3A
ANKRD34A	ADAM12	HLA-DQA1	CD8B	CCL4	SEMA6C
APOL6	ADAMTS5	CD74	CD3E	CCL5	SEMA6B
APOL1	ADAMTS6	TAP1		CCR5	SEMA6A
APOL2	ADGRL3	HLA-DQB2		CXCR6	
APOL1	AFF3	HLA-DQB1		CXCR3	
APOL2	AGAP1	HLA-E		CXCL16	
ATP8B4	AGAP11	B2M		CXCL9	
AXL	AGAP5	CCL5			
B2M	AGAP7P	CCL7			
BATF2	AGAP9	CCL2			
BST2	AKAP12	CXCL10			
C1R	ARAP2	CXCL16			
CASP12	ASAP1	CXCL9			
CCL13	ATRNL1	CCL1			
CCL2	B4GALT6	ISG15			
CFAP100	CD200	IFIT3			
CFB	CD9	IFIT2			
CLEC2D	CDH10	IFI35			
CMPK2	CDK5RAP2	IFI27L2			
CSF1	CHL1	SPP1			
CSTA	COL23A1	IFNB1			
CXCL10	CSAD	TNF			
CXCL9	CTSH	S100A6			
DDX60	CTTNBP2	S100A4			
DHX58	DKK3	ITGAX			
DTX3L	DOCK3	LGALS1			
EIF2AK2	ENO3	LGALS3			
FLACC1	ERBB3	CD86			
GBP6	ETV1	MKI67			
GBP1	FAM184B	CENPF			
GBP2	FAP	BIRC5			
GBP4	FBXL7	TOP2A			
GBP7	FXYD1	CCNB2			
GBP6	GJC3				
GBP5	GPM6B				
GBP6	GULP1				
GBP7	HECW2				

GBP6	HPGDS				
GBP6	IKBKB				
GPR149	IL16				
GPR65	INPP5F				
GVINP1	IQGAP2				
HLA-A	ITGA2				
HLA-B	KLF12				
HLA-C	LGI4				
HLA-E	LIMA1				
HLA-F	LMO4				
HLA-G	MAP4K3				
HLA-H	MBP				
HLA-A	MECOM				
HLA-B	MEF2C				
HLA-C	MEGF9				
HLA-E	METRN				
HLA-F	MMD				
HLA-G	MPRIP				
HLA-A	MPZL1				
HLA-B	MTSS1				
HLA-C	MXRA8				
HLA-E	GCOM1				
HLA-F	MYZAP				
HLA-G	POLR2M				
HLA-A	NDRG2				
HLA-B	NRN1				
HLA-C	NTN4				
HLA-E	P3H2				
HLA-B	PDE1C				
HLA-C	PLAT				
HLA-E	PLPP1				
HLA-F	PPM1L				
HLA-G	PRICKLE2				
HLA-E	PRKCA				
HERC6	PRSS23				
IFI16	PSD3				
IFI16	PTPRM				
MNDA	RASAL2				
PYHIN1	RASGRP3				
IFI16	RBFOX2				
MNDA	RBM20				
PYHIN1	RNF152				
IFI16	SEMA3D				

IFI16	SERPINB1				
IFI16	SGCD				
MNDA	SLC12A2				
PYHIN1	SLC4A8				
IFI27	SNX25				
IFI27L1	SORT1				
IFI27L2	SOX5				
IFI35	SOX6				
IFI44	STARD13				
IFIH1	TCF7L1				
IFIT1	TGFB2				
IFIT1B	TNIK				
IFIT2	TOM1L2				
IFIT3	UNC5C				
IFIT3	ZBTB7C				
IFITM3	ZFHX4				
IRGM	ZNF608				
IRF1	ZNF704				
IRF7	Zfp704				
IRGM					
IRGM					
ISG15					
ISG20					
KY					
LGALS9					
LGALS9B					
LGALS9C					
LRFN1					
LY6E					
MAP3K19					
MLKL					
IFI16					
NLRC5					
NMI					
OAS1					
OAS1					
OAS2					
OAS3					
OASL					
OASL2P					
PARP10					
PARP11					
PARP12					

PARP14					
PARP9					
PHF11					
PHF11					
PHF11					
PML					
PSMB10					
PSMB8					
PSMB9					
PSME1					
PSME2					
RNF19B					
RNF213					
RSAD2					
RTP4					
SAMD9L					
SAMHD1					
SLC2A6					
SLFN11					
SLFN13					
SLFN11					
SLFN13					
SOCS1					
SP100					
SP110					
SP140					
SP140L					
STAT1					
STAT2					
STYK1					
TAP1					
TAP2					
TAPBP					
TAPBPL					
TNFSF10					
TOR3A					
TRAFD1					
TRIM5					
TRIM5					
TRIM21					
TRIM25					
TRIM5					
TRIM34					

TRIM6-TRIM34					
UBE2L6					
USP18					
USP41P					
WNT2B					
XAF1					
XDH					
YPEL4					
ZBP1					
ZNFX1					